THESIS FOR THE DEGREE OF DOCTOR OF PHILOSOPHY

Design and Assessment of Battery Electric Vehicle Powertrain, with Respect to Performance, Energy Consumption and Electric Motor Thermal Capability

EMMA ARFA GRUNDITZ

Department of Energy and Environment
Division of Electric Power Engineering
CHALMERS UNIVERSITY OF TECHNOLOGY
Göteborg, Sweden 2016

Design and Assessment of Battery Electric Vehicle Powertrain, with Respect to Performance, Energy Consumption and Electric Motor Thermal Capability
EMMA ARFA GRUNDITZ
ISBN 978-91-7597-412-5

Doktorsavhandlingar vid Chalmers Tekniska högskola
Ny serie nr. 4093
ISSN 0346-718X

Department of Energy and Environment
Division of Electric Power Engineering
Chalmers University of Technology
SE–412 96 Göteborg
Sweden
Telephone +46 (0)31–772 1000

Chalmers Bibliotek, Reproservice
Göteborg, Sweden 2016

To Daryoush and Faraz . . .

Design and Assessment of Battery Electric Vehicle Powertrain, with Respect to
Performance, Energy Consumption and Electric Motor Thermal Capability
EMMA ARFA GRUNDITZ
Department of Energy and Environment
Chalmers University of Technology

Abstract

In this thesis, various drive cycles, legislative, official real-world and measured, have been studied and characterized based on their speed and acceleration content. Three reference vehicles (a City car, a Highway car and a Sport car) were conceptualized after performance requirements, with data on existing battery electric cars as a frame of reference. The acceleration performance, energy consumption and efficiency of the powertrain, comprising a traction motor, a power electronic module and a battery, was determined and analyzed for the various drive cycles. Furthermore, the consequence on acceleration performance, drive cycle fulfilment and energy consumption during re-scaling of the electric drive system was studied. Moreover, the electromagnetic losses for four different slot areas were compared, along with the thermal steady state and transient over load as well as temperature development during drive cycles.

Through comparison between official and measured drive cycles, it was found that even though the measured cycles reach higher peak acceleration levels for a certain speed level, on an average they still spend only slightly more time at higher levels of acceleration compared to the official cycles. The resulting cycle average powertrain efficiencies were fairly similar for both the official and measured cycles, and showed to be slightly higher for cycles that spend more time at higher speed levels.

During the powertrain sizing regarding torque and power, the acceleration requirement turned out to dominate over other requirements such as top speed, and grade levels. It was found that a down scaling of the electric power train resulted in an energy consumption down to 94% of the original powertrain size.

Finally, the small slot geometry had the highest peak losses during the drive cycles, however, on a cycle average it had the lowest losses for many cycles. This fact, in combination with the highest peak torque and lowest material cost, makes it a very interesting option as an electric vehicle traction motor.

Index Terms: Battery Electric Vehicle, Drive Cycles, Electric Motor, Sizing, Energy Efficiency, Energy Consumption, Thermal Modelling, Thermal Capacity.

Acknowledgements

The financial support through Chalmers Energy Initiative (CEI) is gratefully appreciated.

I would here like to take the opportunity to thank all of those that had a positive impact during the execution of this work.

Foremost, I want to thank my main supervisor and examiner Torbjörn Thiringer for his endless commitment to give vital support, feedback, and encouragement, which he did through all these years. Furthermore, I would like to express my gratitude towards my co-supervisors: Mikael Alatalo for many fruitful discussions and for sharing his knowledge and opinions, and Sonja Lundmark for all her help during this project, e.g. by collecting driving data, and particularly for giving detailed feedback during the finalizing of this thesis.

Additionally, I am very grateful for all of the friendly colleagues at the division of Electric Power Engineering, which together contribute to a very pleasant working environment. Specifically, I would like to thank my long term room-mates over the years: Christian Du-bar, Ali Rabiei and Andreas Andersson for their professional insights, as well as for their kindness and humor.

Finally, I give my warmest thanks to my family whose support after all is the most essential.

Emma Arfa Grunditz
Göteborg, Sweden
May, 2016

Contents

Abstract **v**

Acknowledgements **vii**

Contents **ix**

1 Introduction **1**
- 1.1 Background 1
- 1.2 Previous work 2
- 1.3 Purpose of the thesis and contributions 2
- 1.4 List of Publications 3

2 BEV Dynamics, Powertrain Component Modeling, and Heat Transfer Modelling **5**
- 2.1 Battery electric vehicle (BEV) powertrain 5
- 2.2 Vehicle dynamics 6
  - 2.2.1 Aerodynamic drag 7
  - 2.2.2 Rolling resistance 8
  - 2.2.3 Grading force 10
  - 2.2.4 Wheel force 10
  - 2.2.5 Wheel power and energy 11
- 2.3 Permanent Magnet Synchronous Machine (PMSM) 12
  - 2.3.1 Equivalent electric circuit model 12
  - 2.3.2 Mechanical output 12
  - 2.3.3 PMSM power losses 13
  - 2.3.4 PMSM control 14
  - 2.3.5 PMSM steady state modeling with regard to core losses 15
- 2.4 DC-AC Converter loss modeling 15
- 2.5 Battery modeling 17
- 2.6 Transmission 18
- 2.7 Auxiliary loads 19
- 2.8 Heat transfer modeling in electric machines 19
  - 2.8.1 Heat transfer modes 19
  - 2.8.2 Lumped-parameter modelling 21

3 Road Type Driving Patterns, Road Grade and Daily Driven Distances 25
3.1 Driving patterns 25
3.1.1 Legislative cycles 26
3.1.2 Non-legislative cycles 30
3.1.3 Driving pattern characterization parameters 31
3.2 Road type specification based on speed levels 32
3.2.1 Urban 32
3.2.2 Rural 35
3.2.3 Highway 37
3.3 Acceleration distributions 39
3.3.1 Urban 39
3.3.2 Rural 42
3.3.3 Highway driving 45
3.4 Acceleration duration 47
3.5 Road grade levels 47
3.5.1 Measured road grades 48
3.6 Average daily driving/traveling distance 50

4 Performance Requirements and Wheel Load Analysis of Studied Concept Vehicles 53
4.1 Performance requirements based on data of existing BEVs 53
4.1.1 Speed and acceleration performance 54
4.1.2 Gradability 55
4.1.3 Driving range and curb weight 56
4.1.4 Area, C_d and C_r 56
4.1.5 Summary of requirements on chosen vehicle concepts 57
4.2 Wheel load analysis of chosen concepts 57
4.2.1 Road load and grade 58
4.2.2 Acceleration 60
4.3 Wheel load analysis for selected drive cycles 64
4.3.1 Peak wheel power per cycle 64
4.3.2 Wheel energy per distance for the Test cycles 65
4.3.3 Wheel energy per distance for the Logged cycles 68
4.3.4 Change in potential energy per driven distance for the Logged cycles 69

5 Powertrain Component Sizing, Modeling and Vehicle Simulation 71
5.1 Components used for modeling 71
5.1.1 Converter 72
5.1.2 Battery cell 72
5.1.3 Electric machine 73
5.2 Components sizing process 75
5.3 Implemented battery models 76
5.4 Implemented EM models including transmissions 78
5.5 Implemented converter model 81
5.6 Simulator structure 82

5.7 Simulated time to accelerate $0 - 100\, km/h$ 84
5.8 Simulated time to accelerate $0 - 100\, km/h$ with grade 85
5.9 Fulfillment of reference cycle speed in simulation 87
5.10 Simulated component efficiency per cycle 89
5.11 Simulated energy per driven distance, per cycle 92
5.12 Simulated driving range 96

6 V-Shaped Reference PMSMs for CityII and HighwayII Concept BEVs 99
6.1 CityII and HighwayII concept BEVs 99
6.2 Design, material and mass of machine parts 100
  6.2.1 Frame 103
  6.2.2 Core lamination 103
  6.2.3 Magnets 103
  6.2.4 Other machine parts and material summary 105
  6.2.5 Mass of machine parts 105
6.3 FEA evaluation of performance and losses 106
  6.3.1 Losses and efficiency of the HighwayII motor 108
6.4 CityII and HighwayII motor efficiency with different dc voltage limits . 110
6.5 CityII and HighwayII motor efficiency at 50%, 100% and 200% of stack length 111
6.6 HighwayII motor losses at three magnet and copper temperatures 113
6.7 HighwayII motor losses for four slot areas 115

7 Effects of CityII and HighwayII Motor and Inverter Re-scaling on Performance and Energy Efficiency 121
7.1 Performance 122
7.2 System Efficiency and Cycle Energy Consumption 123

8 Lumped-Parameter Thermal Model of HighwayII V-shaped Reference PMSM 129
8.1 Implemented thermal network 129
  8.1.1 Frame and cooling 130
  8.1.2 Stator yoke 133
  8.1.3 Stator teeth 134
  8.1.4 Stator winding 135
  8.1.5 Air gap 136
  8.1.6 Rotor core and magnets 138
  8.1.7 Shaft 139
  8.1.8 Bearings 140
  8.1.9 Internal air 141
  8.1.10 Thermal capacitances 142
  8.1.11 Summary of thermal network node resistances 144
8.2 Calculation set-up of lumped-parameter thermal model 144
8.3 Steady state comparison of lumped network and FEA 145
8.4 Steady state sensitivity analysis for selected parameters 147
8.5 Transient thermal response to load step 149

9 Thermal Performance for HighwayII PMSM with Four Different Slot Areas 151
9.1 Steady state performance 151
9.2 Transient over load 153
9.3 Performance during drive cycles 155

10 Conclusions and Future Work 159
10.1 Conclusions 159
10.2 Future Work 161

References 163

Appendices 187

A Sales and Specification BEV data 189
A.1 Top selling BEVs 2014 and 2015 189
A.2 Specification BEV data 189
A.2.1 Brand, model and miscellaneous data 190
A.2.2 Dimensional specifications 190
A.2.3 Powertrain specifications 193
A.2.4 Performance specifications 193
A.2.5 Terminated and coming BEV models 193
A.3 Comments on selected data 193
A.3.1 Area and aerodynamic drag coefficient, C_d 193
A.3.2 Rolling resistance coefficient, (C_r) 193
A.3.3 Wheel radius estimation from tire dimensions 198
A.3.4 Traction Electric Machine data 198

B GPS-accelerometer Measurement System 201
B.1 Description of the measurement system 201
B.2 Filtering of measurement Data 202
B.3 Ambiguity of measurements 203
B.4 Logged vehicles 204

C Speed and Acceleration Dither 207

D Temperature Dependence of some Material Parameters 211

E Cooling Channel Modelling 215

Chapter 1

Introduction

1.1 Background

One of the major challenges in the global society today is to reduce the negative impacts that road transportation has on the environment due to toxic and green-house-gas emissions. As a consequence, these type of emissions from vehicles are legally regulated on national and sometimes regional levels. In order to comply with expected near future more stringent regulations, vehicle manufacturers are forced to invest in various fuel saving technologies. This has led to an increased interest in vehicle electrification, foremost hybrid electric vehicles (HEVs) which can reduce fuel consumption compared to conventional vehicles, but also battery electric vehicles (BEVs). BEVs offer high powertrain efficiency and no tailpipe emissions, which is why they are so far considered CO2 neutral in the regulations [1]. If charged with electricity that is produced by fossil free and renewable sources, BEVs have the potential to offer an emission free use phase [2].

Today a large part of the major automotive manufacturers in the world have developed their own BEV model, and BEV sales have seen increased annual growth rates, as high as 54%-87% during 2012-2014 [3]. Still, the battery related drawbacks of relatively short driving range (mainly due to prize constraints) combined with long charging time, prohibit BEVs from taking up the commercial competition with fuel energized cars on a large scale just yet [4, 5].

In this light, it becomes important to investigate the effect on energy efficiency as well as performance that different design choices have, both when it comes to design of the different components in the powertrain, but also regarding the design of the drive system as a whole. Another interesting research aspect is to investigate the possibility to design the drive system according to a specific type of usage, and then to assess the consequence on energy efficiency and performance. Moreover, due to the often limited space for drive system components in vehicles, the choice of peak torque versus thermal capability for a certain electric machine size also becomes highly important.

1.2 Previous work

In order to evaluate tailpipe emissions and fuel consumption of conventional combustion vehicles, various drive cycles have been developed over the last few decades. Numerous studies have been conducted that relate different types of cycles and their speed and acceleration characteristic to the resulting levels of fuel consumption [6], [7], [8] and [9]. However, the influence of speed and acceleration measures on the energy consumption of a BEV is lacking in available literature.

Moreover, since the often used official drive cycles were developed decades ago and vehicle performance have increased from that time, and since they have a relatively low time resolution compared to vehicle dynamics, there is a need for having access to updated cycles with a higher time resolution.

Several interesting publications report measured or simulated results regarding BEV energy consumption per driven distance, range and efficiency during different drive cycles, such as [10–18]. Still, often only a few illustrative well-known official drive cycles are used, e.g. the European NEDC or US FTP(UDDS), HWFET and US06 [10–15]. A few publications utilize several different cycles [16, 17], however an extensive analysis of the influence of driving has not been found in literature so far. Unfortunately, the two just mentioned references also lack in documentation and description of some or all of the component models, thus making them less transparent. An interesting review is given in [18], along with the general relationship between measured battery power and measured speed, acceleration and road grade, for a specially constructed BEV. Additionally, cycle average powertrain efficiencies based on measurements are reported in [10,12,15], however the resulting discrepancy is quite large (60-80%, 90% and 83-91% respectively), even though the former two are based on the same BEV model. In addition, simulated and measured cycle average powertrain component efficiencies are found in [11], [15], but only for two different drive cycles in each.

Furthermore, numerous publications suggest lumped parameter transient thermal models of the electric machine with a varying degree of complexity, e.g [19, 20]. In many cases, the modeled temperature development in a certain machine is compared with experimental results in a few operating points [21,22], and sometimes even during one load cycle [23]. However, the objective is seldom to broadly evaluate the thermal capability of the motor with an electrified vehicle application in mind.

To conclude, many valuable contributions have been made in the theme of relating drive cycles with BEV energy consumption and powertrain energy efficiency. However, a broad compilation of the topic, using transparent and traceable models has not been found in publicly available literature. Furthermore, there is a lack of published evaluations of electric motor thermal capability during both steady state and transient loads for vehicular applications.

1.3 Purpose of the thesis and contributions

The purpose of this thesis is to investigate and quantify the relation between vehicle performance, component size, and energy consumption, while accounting for both a fairly full coverage of drive cycles as well as considering vehicles designed based on an extensive number of existing BEVs. Moreover, a target was to account for the performance requirements in an adequate way, which brought a need to collect high frequency drive cycles where also the acceleration was determined using an accelerometer in addition to just deriving it from a GPS speed signal. An aim was also to investigate the consequence on acceleration performance, drive cycle fulfillment, and cycle energy consumption due to powertrain re-scaling. A final goal was to evaluate the effect that various slot sizes have on the steady state and transient thermal capability of an electric motor when the external size is unaltered.

The main contributions of this work are:

- Sorting and parameterized characterization of official drive cycles, put in relation with own measured cycles
- BEV powertrain component sizing after three differently put performance requirements, with numerous existing BEVs as a frame of reference
- A determination of powertrain component cycle average efficiencies, during various drive cycles using fairly highly detailed and transparent models
- Quantification of the consequence in energy consumption per distance for different cycles, as well as acceleration performance, while the electric drive system max output is varied through active length scaling
- Establishing the consequence on electric machine continuous and peak intermittent torque for four different slot sizes
- Determination of the influence that four different slot sizes has on the total losses and max temperatures reached during various drive cycles

1.4 List of Publications

I E. Grunditz; T. Thiringer, "Performance Analysis of Current BEVs - Based on a Comprehensive Review of Specifications" accepted for publication in *IEEE Transactions on Transportation Electrification*, 2016

II A. Rabiei; T. Thiringer; M. Alatalo; E. Grunditz, "Improved Maximum Torque Per Ampere Algorithm Accounting for Core Saturation, Cross Coupling Effect and Temperature for a PMSM Intended for Vehicular Applications," in *IEEE Transactions on Transportation Electrification* , vol.PP, no.99, pp.1-1, 2016

III E. Grunditz; T. Thiringer, "Characterizing BEV Powertrain Energy Consumption, Efficiency and Range during Official and Drive Cycles from Gothenburg/Sweden," in *IEEE Transactions on Vehicular Technology* , vol.PP, no.99, pp.1-1, 2015

Some contributions are also made in the following publications, however, their content is not directly related to the content of this thesis.

I B. Sandén, P. Wallgren, Editors of E-book: "Systems Perspectives on Electromobility", S. T. Lundmark, M. Alatalo,T. Thiringer, E. Grunditz, B-E Mellander, Chapter 3 "Vehicle Components and Configurations",

II S. Haghbin, A. Rabiei and E. Grunditz, "Switched reluctance motor in electric or hybrid vehicle applications: A status review," *2013 IEEE 8th Conference on Industrial Electronics and Applications (ICIEA)*, Melbourne, VIC, 2013, pp. 1017-1022.

III S. T. Lundmark, A. Rabiei, T. Abdulahovic, S. Lundberg, T. Thiringer, M. Alatalo, E. Grunditz, C. Du-bar, "Experiences from a distance course in electric drives including on-line labs and tutorials," *Electrical Machines (ICEM), 2012 XXth International Conference on*, Marseille, 2012, pp. 3050-3055.

IV S. T. Lundmark, M. Alatalo, E. Grunditz, "Electric Machine Design for Traction Applications Considering Recycling aspects -Review and New Solution," *IECON conference*, Melbourne, November 2011

Chapter 2

BEV Dynamics, Powertrain Component Modeling, and Heat Transfer Modelling

This chapter deals with basic concepts and what is considered to be necessary information for taking part of the rest of the report.

2.1 Battery electric vehicle (BEV) powertrain

The powertrain of a Battery Electric Vehicle (BEV) consists of an electric drive system with a battery serving as an energy buffer. Often there is only one electric machine, typically of three phase AC type, connected to the wheel shaft via a gearbox and a differential. However some applications may utilize several electric machines, e.g. hub wheel motors. The energy is stored chemically in a battery, which is electrically connected to the machine via a DC/AC power electronic converter accompanied by a control system. The control system controls the frequency and magnitude of the three phase voltage that is applied to the electric machine, and these are depending on the driver's present request, which is communicated via the acceleration and/or brake pedal.

In vehicle applications, it is usually desirable to keep the physical volume of the electric machine down. This can be done by designing it for higher speed levels. A reasonable compromise is a maximum speed between $12\,000$ to $16\,000\,rpm$ [24], since it serves as a good compromise between volume and performance. Still, during normal on road driving the speed range of a vehicle may vary between zero to about 130 km/h or even higher at times. This means that the wheels will spin up to around $1200\,rpm$ or higher. Therefore a reduction gear ratio towards the wheels, is inherently needed. Additionally, in order to give the left and right traction wheels a chance to spin at slightly different speeds during turning, there is also a need for a differential to be connected between the wheels. Sometimes the differential also includes a final gear ratio. A typical BEV drive system, which is also the type of system studied in this theses, is depicted in Figure 2.1.

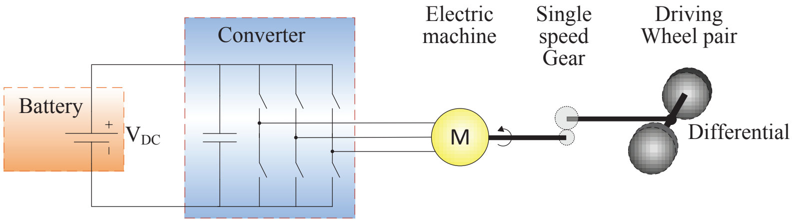

Figure 2.1 Simple schematic sketch of a BEV powertrain.

2.2 Vehicle dynamics

Vehicle dynamics aim to describe how a vehicle moves on a road surface while it is under the influence of forces between the tire and the road, as well as aerodynamics and gravity.

During the powertrain design phase, basic knowledge in vehicle dynamics is essential since it reveals what loads and load levels that the powertrain needs to cope with during driving. The understanding of vehicle dynamics is equally important while evaluating the powertrain's impact on the vehicle's performance (usually assessed through simulations), whether it may be time to accelerate, or average energy consumption per driven distance.

As with modeling of any object, a rolling vehicle can be modeled with various levels of detail depending on what main phenomena that is targeted to be studied. For the type of dynamical studies in this thesis, where powertrain load levels and energy consumption will be analyzed, it is reasonable to assume that the vehicle body is rigid, hence it can be modeled as a lumped mass at the vehicle's center of gravity [25]. Furthermore, only dynamics in one direction, the longitudinal forward direction, is of interest while under the assumption that vehicle stability is not under any circumstances violated.

According to Newton's second law of mechanics, the dynamical movement of a vehicle in one coordinate axis is entirely determined by the sum of all the forces acting on it in that same axis of direction, as described in the translational form

$$m\,a = m\,\frac{d}{dt}\,v(t) = F_{tractive}(t) - F_{resistive}(t) \tag{2.1}$$

where $m\ (kg)$ is the equivalent mass to be accelerated including possible rotating inertias in the powertrain, $a\,(m/s^2)$ and $\frac{d}{dt}v(t)$ is the time rate of change of vehicle speed $v(t)\,(m/s)$, i.e. acceleration $a\,(m/s^2)$, $F_{tractive}(t)\,(Nm)$ is the sum of all the tractive forces acting to increase the vehicle speed and $F_{resistive}(t)$ is the sum of the resistive forces acting to decrease the speed.

The main tractive force is the one exerted from the powertrain via the gear, differential and the wheel shaft to the contact area between the wheels and the road. During downhill driving gravity may also serve as a major tractive force, however during uphill driving it may instead be a large resistive force. Other major resistive forces are aerodynamic drag and rolling resistance, as well as regenerative braking using the electric power train and braking using conventional friction brakes.

IN short, a vehicle will accelerate when the sum of the tractive forces is larger than the sum of the resistive forces, and thus will decelerate when the opposite applies. To keep a constant speed the net resistive force must be exactly matched by the net tractive force.

2.2.1 Aerodynamic drag

The aerodynamic drag that any vehicle unavoidably is exposed to during driving, springs from the flow of air around and through the vehicle which are also often referred to as external and internal flows.

Due to the complex shape of automobiles, and to the even more complex nature of fluid dynamics, accurate and reliable analytical models of aerodynamical drag are very difficult to develop, even with advanced CFD softwares at hand. A compromise that is often used to model the aerodynamical drag force, F_a, is partly empirical, and partly based on the expression of dynamical pressure, which is showing a strong dependance on the square of the vehicle speed as

$$F_a = \frac{1}{2}\,\rho_a\,C_d\,A_f\,(v_{car} - v_{wind})^2 \tag{2.2}$$

where ρ_a (kg/m^3) is the air density, C_d the aerodynamic drag coefficient, A_f (m^2) is the effective cross sectional area of the vehicle, v_{car} (m/s) is the vehicle speed and v_{wind} (m/s) is the component of wind speed moving in the direction of the vehicle [25].

The aerodynamical drag thus increases with head **wind** speeds. A head wind speed of $10\,m/s$ gives an added drag equal to a vehicle driving $36\,km/h$ in no wind, and one of $25\,m/s$ gives a drag equal to a vehicle speed of $90\,km/h$. Still, the direction of the wind that hits the vehicle is rather random, and non-head winds increase not only the vehicle's effective cross sectional area, but also the aerodynamic drag coefficient by around 5 to $10\,\%$ for passenger cars in common wind conditions (slightly more for family sedans and slightly less for sports cars), according to [25].

Air density varies depending on temperature, humidity and pressure, where the later indicates an altitude dependance. For comparative studies, often the density value of $1.225\,(kg/m^3)$ is used, which represents standardized conditions such as dry air at $15\,^{\circ}\mathrm{C}$ at standard atmospheric pressure $(1013.25\,Pa)$ i.e. at sea level [25]. For temperatures between -30 to $50\,^{\circ}\mathrm{C}$ the density of dry air may be 80 to $110\,\%$ of the standard air density, while an increase in altitude of about $300\,m$ above sea level leads to a decrease in the dry air density of about $3\,\%$ relative to the standard air density [26].

The effective cross sectional **area** of the vehicle varies depending on the vehicle size and shape. For auto manufacturers, the value of a certain car model's area can be found through detailed drawings or perhaps wind tunnel tests, yet the resulting value is not always communicated in official vehicle specifications. Therefore external parties are often forced to make rough estimations which relate the area to the product of a vehicle's height and width or track width. Various such estimations can be found in literature; $79 - 84\ \%$ in [27], $81\ \%$ in [28] and $90\ \%$ of the product of track width and height in [29].

The **drag coefficient**, C_d is a dimensionless parameter that represents all the drag effects that are active on the vehicle, i.e. both external and internal. To acquire an accurate estimate it has to be measured. Therefore, automotive manufacturers measure the total drag force, F_a in wind tunnels or coast down tests as well as the cross sectional area, air density and vehicle speed. Then, the drag coefficient can be found via (2.2). In comparison to area, this parameter is often made official and communicated in car model specifications. Typically the C_d value is in the range 0.25-0.35 in today's passenger cars [27], yet it may vary between 0.15 for a more streamlined shape up to 0.5 or higher for open convertibles, off-road vehicles or other rough shaped vehicles. Furthermore, the C_d value will change if the airflow around and through the vehicle is altered during driving, for instance an open side window may increase the C_d value by about 5 $\%$ [27]. During the last few decades the general trend has been decreasing C_d values on new passenger cars [28], much due to the increased interest in fuel efficiency and emissions. In order not to compromise too much on the design and compartment comfort for the passengers, most work on aerodynamical drag reduction is likely to be focused on the C_d value [28] rather than on the area.

2.2.2 Rolling resistance

Rolling resistance is caused by a number of different phenomena taking place in and around the car tires during rolling. One of the major effects is that the repeated deflection of the tire causes a hysteresis within the tire material, which gives rise to an internal force resisting the motion [27]. Still, according to [25, p.110] rolling resistance depends on more than seven different phenomena, which makes estimation of rolling resistance through analytical modeling very difficult. Therefore, the rolling resistance force, F_r acting on a vehicle in the longitudinal direction, is usually expressed as the effective normal load of the vehicle multiplied by the dimensionless rolling resistance coefficient, C_r as

$$F_r = C_r\, m\, g\, cos(\alpha) \tag{2.3}$$

where $m\,(kg)$ is the vehicle mass, $g\,(m/s^2)$ is the gravity constant, $\alpha\,(rad)$ is the road inclination angle. Often the $cos(\alpha)$ term is neglected since even a large grade such as $10\,\%$ ($\alpha \approx 0.1\ rad$), means that $cos(\alpha) \approx 0.995$ i.e. an error of less than $0.5\,\%$ of the rolling resistance force.

Empirical studies show that the C_r value depends on factors such as; tire material and design, but also tire working conditions such as inflation pressure (C_r decrease with increasing pressure), tire temperature (C_r decrease with increasing temperature), road surface (structure, wet or dry) and speed (C_r increase with increasing speed) [27].

For low speed levels, C_r increases only slightly with speed, while at higher speed levels, C_r increases with almost the square of the speed [25]. At even higher speed levels a standing wave appears in the tire which greatly increases the energy loss and temperature rise in the tire, a condition that may eventually lead to tire failure [27], [25].

The rolling resistance coefficient's dependency on speed also varies with tire temperature, where higher temperature causes a weaker speed dependency [27]. During operation, it may take over 30 minutes of driving at a constant speed level, before the tire temperature reaches its steady-state value [30]. Then the rolling resistance coefficient may be somewhat smaller compared to the initial value at the same speed level. For tires found to have a relatively small positive speed dependency by non thermal steady-state measurements: a measurement made after reaching thermal steady-state may even show a small negative speed dependency of the rolling resistance coefficient, according to [30].

Various published suggested speed dependencies of C_r are shown in Figure 2.2, where some of the information represent data found in *Bosch Automotive Handbook* [29] and Guzzella's *Vehicle Propulsion Systems* [31], both of which are here assumed to be based on measurements of typical available tires. The notations from Bosch stand for design speed limits of the tires: $180 km/h$ for S, $190\, km/h$ for T, $210\, km/h$ for H, $240\, km/h$ for V, $270\, km/h$ for W, above $240\, km/h$ for Z, and finally the ECO tires are low rolling resistance tires that come in various speed ranges. In addition, Figure 2.2 shows three often referred to analytical estimations; one linear found in [32] (Ehsani), one that is weakly dependant on the square of the speed found in [27] (Wong), and one strongly depending on the square of the speed found in [25] (Gillespie). From the comparison in the figure, it is clear that the analytical expressions deviate quite a lot from the typical tire data. It can also be seen that C_r is slightly larger for tires of higher speed rating, and that the increase of C_r with speed is somewhat smaller compared to tires of the lower speed ratings.

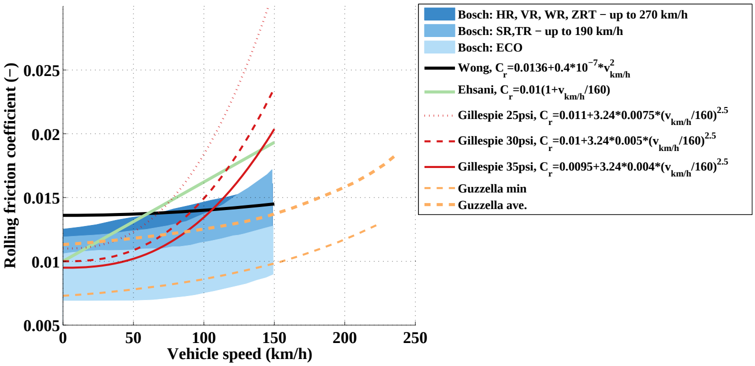

Figure 2.2 Rolling resistance coefficient as a function of speed from different literature sources; Bosch: [29], Wong: [27], Gillespie: [25], Ehsahni: [32] and Guzzella: [31].

During estimations of vehicle performance or fuel economy, C_r is often assumed to be constant, with typical values around 0.011 to 0.015 for radial types representing passenger car tires on dry concrete or asphalt [29], [24] and [25]. Due to increased environmental concerns in recent years, low rolling resistance tires are now also available, thus C_r values as low as 0.007 to 0.009 may also be applicable [24]. In addition, according to [33] most tires sold in the USA have measured C_r values between 0.007 to 0.014. Furthermore, [33] states that there are few sources with published data on rolling resistance coefficients of presently common passenger car tires, nevertheless a review of published data is provided, covering some of the main tire manufacturer's most sold models. The format of the data is; rolling resistance coefficients of new tires, measured under standardized circumstances, according to the SAE J1269 or J2452. The first standard measures the tire's C_r at a speed of $80\, km/h$, but after the tire has reached thermal steady state. The second standard measures C_r during a $180\, s$ stepwise coast down test from $115\, km/h$ to $15\, km/h$, but only after the tire initially has reached thermal steady-state at $80\, km/h$. Most of the data presented in [33], adhere to the first standard (J1269). Even data deduced with the second standard (J2452) are presented as average values.

According to [33], based on tire manufacturer data of new tires from 2005, the average C_r of low speed tires (up to $180 - 190\,km/h$) is 0.0098, for high speed tires (up to $210 - 240\,km/h$) it is 0.0101, while for very high speed tires (above $240\,km/h$) it is 0.0113.

2.2.3 Grading force

In case of a road grade (or inclination), the vehicle's dynamics will be affected by the component of the gravitational force F_g that is parallel with the road as

$$F_g = m\,g\,sin(\alpha) \tag{2.4}$$

where $\alpha\,(rad/s)$ is the angle between the level road and the horisontal plane as in

$$\alpha = arctan(\frac{rise}{run}) \;=\; arctan(\frac{\%grade}{100}) \tag{2.5}$$

where *rise* is the vertical rise and *run* is the horisontal distance. Road slope is often expressed in terms of $\%$ *grade*, hence this terminology will be used throughout the thesis.

Since the vehicle may be traveling uphill or downhill this force may either be resisting or contributing to the net tractive force on the vehicle, i.e. it will either be positive or negative.

From an energy perspective, driving on a non level road will cause buffering and draining of potential energy in the vehicle. However, since passenger cars are usually displaced only temporarily over a day or so, from it's starting position (e.g. at home), whatever the route traveled the potential energy remains the same when coming back to the starting point. As with deceleration, a BEV is normally able to recuperate some of the energy from going downhill.

Grade and acceleration force comparison

Both acceleration force and grading force are products of vehicle mass, thus it follows that for any vehicle a certain acceleration level causes the same wheel force as a certain road grade level. Typical acceleration and grade levels which have an equivalent wheel force, are shown in Table 2.1.

Table 2.1 Equivalent force for certain acceleration and grade levels.

a (m/s^2)	1	2	3	4	5	6
Grade $(\%)$	10.3	20.8	32.1	44.7	59.2	77.3
Grade $(\%)$	5	10	15	20	25	30
a (m/s^2)	0.49	0.98	1.46	1.92	2.38	2.82

2.2.4 Wheel force

The tractive force, F_{wheel} that has to come to the wheels from the powertrain in order to sustain a certain speed level, road grade and acceleration can be found as in

$$F_{wheel}(t) = F_{acc}(t) + F_a(t) + F_r(t) + F_g(t) \tag{2.6}$$

where $F_{acc}\,(Nm)$ is the force required to accelerate the vehicle mass at a certain magnitude of acceleration ($F_{acc} = m\,a$), see (2.1).

A positive value of F_{wheel} then strives to accelerate the vehicle, while a negative value can represent either a regenerative braking force from an electric motor or friction braking. Finally, if $F_{wheel}(t) = 0$ and the friction brake is disengaged, the vehicle is said to be coasting, that is only F_a, F_r and possibly F_g are acting on the vehicle.

The maximum tractive force on the driving wheels can be limited by either the powertrain's maximum force capability or the maximum adhesive capability between tire and ground that is possible to be applied on the wheel without loosing the grip to the road, i.e. starting to spin or slide [25] p. 35. The later is limited by the current normal force on the driving wheels, F_N and the coefficient of friction between the tire and the road, μ [24] as

$$F_{wheel,max} = \mu\, F_N \tag{2.7}$$

The normal load on the driving wheels or wheel pair is affected by the weight distribution in the car, hence it varies from car to car, and even from occasion to occasion for the same car since the loading may vary, and finally by the change in weight distribution during an acceleration or deceleration, [24, 25].

The friction coefficient depends nonlinearly on the longitudinal tire slip, which is caused by deformation of the tire during acceleration and decelerations [24]. The slip is defined as

$$slip = (1 - \frac{v_{car}}{\omega\, r})100\ (\%) \tag{2.8}$$

and it leads to a non unity relation between the car speed, $v_{car}\,(m/s)$ and the product of wheel speed $\omega\,(rad/s)$ and wheel radius $r\,(m)$, which would otherwise be valid.

Starting from zero slip and friction, the friction coefficient increases with increasing slip, up to slip values of about 15 to 20 $\%$ where the coefficient peaks at values around 0.8 to 1, depending on type of tire and road condition, [24] and [32]. At even higher slip values, the friction coefficient decreases, but at a lower rate than before. Moreover, high slip values means that the wheels, hence also the electric machine will spin faster than calculated directly from the vehicle speed while ignoring the tire slip.

2.2.5 Wheel power and energy

The instantaneous tractive power that has to come to the wheels, P_{wheel} from the powertrain in order to sustain a certain speed level, road grade and acceleration is determined by the tractive force and the vehicle speed as

$$P_{wheel}(t) = F_{wheel}(t)\, v_{car}(t) \tag{2.9}$$

The total consumed energy at the wheel can be found from the time integral of the power as

$$E_{wheel} = \int P_{wheel}(t)\, dt \tag{2.10}$$

During regenerative braking while F_{wheel} is negative also P_{wheel} will be negative, hence the total consumed energy over time will be reduced.

2.3 Permanent Magnet Synchronous Machine (PMSM)

A PMSM consist of a rotor with permanent magnets and a wound stator which is energized by an external AC voltage source, typically of three phase type. The stator core and the rotor is made of laminated steel plates that serve as conduction paths for the magnetic flux.

2.3.1 Equivalent electric circuit model

An often used representation is the circuit equivalent dynamic *dq*-model of a PMSM which is shown in Figure 2.3, where *dq* implies the rotor frame of reference, or synchronous coordinates. The *direct* or *d*-axis physically represent a radial axis crossing the centerline of the magnets, i.e. directed in the direction of the magnetic flux from a magnet, while the *quadrature* or *q*-axis represent an axis crossing in between two magnets, (i.e. two magnetic poles), and that is 90 electrical degrees ahead of the *d*-axis.

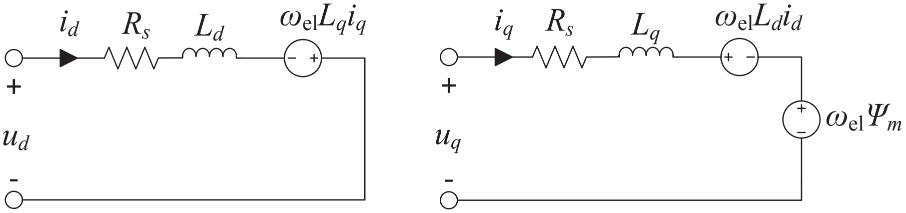

Figure 2.3 Circuit equivalent model of a PMSM.

The dynamic *d*- and *q*-axis stator voltage equations as functions of the *d*- and *q*-axis stator currents (i_d and i_q) are;

$$u_d = L_d \frac{di_d}{dt} + R_s i_d - w_{el} L_q i_q \tag{2.11}$$

$$u_q = L_q \frac{di_q}{dt} + R_s i_q + w_{el} L_d i_d + w_{el} \Psi_m \tag{2.12}$$

where R_s is the stator winding resistance, w_el is the electrical angular speed ($w_el = n_p w_r$ where w_r is the rotor angular speed and n_p is the number of pole pairs), L_d and L_q are the *d*- and *q*-axis winding inductances, and Ψ_m is flux linkage related to the permanent magnet.

When considering electrical steady state, the di/dt-terms may be omitted.

2.3.2 Mechanical output

For salient machines the produced electromechanical torque can be expressed as

$$T_e = \frac{3n_p}{2K^2}(\Psi_d i_q - \Psi_q i_d) = \frac{3n_p}{2K^2}(\Psi_m i_q + (L_d - L_q)\, i_d\, i_q) \tag{2.13}$$

where Ψ_d and Ψ_q are flux linkage in the *d*- and *q*-axis, and K is the scaling constant for transformation between three phase to two phase space vectors. For amplitude invariant scaling, K should be set to unity.

The stator inductance relates a change in current with a change in flux linkage (as $\Psi = L\,i$), and for low current levels (i.e. low torque levels) the relation is close to linear, but at higher current levels the iron becomes magnetically saturated, thus an equally large increase in current will then only cause a minor increase in the flux linkage (i.e. only a minor increase of the torque). In order for this effect to be represented in the circuit diagram, both the *d*- and the *q*-axis inductance could be modeled as functions of current. The saturation also limits the magnet flux linkage, hence this could also be modeled as a function of current.

The part of the *electromagnetic torque* production that is caused by the right part of (2.13) is called *reluctance torque*. In salient machines, often L_d is smaller than L_q, due to a higher reluctance of magnetic material compared to iron. Thus, to be able to produce a positive reluctance torque, the *d*-axis current must be negative.

Ideally the mechanical output of an electric motor, in terms of torque and power as a function of speed, can be divided into two main areas of operation; the *constant torque* region and the *constant power* region. In the constant torque region starting from zero speed, the machine is capable of producing its max torque given that it can be fed by the same level of max current. As the speed increases, so does the induced voltage, hence the applied voltage must also increase, until the maximum voltage limit is hit. At this point the machine is operating at its maximum power limit. The speed level where this occurs is referred to as *base speed*. To be able to reach still higher speeds, the effect of the induced voltage must be decreased. This is done by reducing the flux-linkage in the *d*-axis, by utilizing the *d*-axis current. Therefore, the same level of maximum torque can no longer be provided. Instead the torque becomes inversely proportional to the speed. The power, however is ideally kept constant up to the top speed of the motor, hence the name constant power region.

For a certain machine, the maximum transient low speed torque is often limited by the maximum converter current, which in turns is set by thermal limitations. The base speed depends on the maximum available voltage from the voltage source. Naturally both the current and voltage will affect the maximum available power.

2.3.3 PMSM power losses

The two largest losses in a PMSM are the resistive losses in the copper windings in the stator, and the iron losses mainly in the stator core, where the copper losses are usually the larger of the two [34]. Other causes of power loss are the mechanical; windage and friction.

Copper losses:

Copper losses depend on the number of phases, the stator winding phase resistance, R_s, and the square of the *RMS* phase current, $I_{s,RMS}$. In the *dq*-reference frame it can be expressed as

$$P_{cu} = 3\,R_s\,{I_{s,RMS}}^2 = \frac{3}{2}\,R_s\,({i_d}^2 + {i_q}^2) \tag{2.14}$$

The stator resistance increases with temperature, such that for every 25 °C increase in wire temperature, the resistance increases by about $10\,\%$. This means that, for the same magnitude of current, the copper losses will increase by the same factor.

Another factor that may increase the resistance during operation is the frequency of the supply voltage, through the so called **skin effect** or by the **proximity effect**. These effects are however fairly small.

Iron (core) losses:
Iron losses or core losses depend mainly on two phenomena; magnetic hysteresis and induced eddy currents. The mean losses can be described as

$$P_{fe} = k_h\, f\, {B_{pk}}^{n} \, + \, k_c\, f^2\, {B_{pk}}^{2} \tag{2.15}$$

where

k_h	a hysteresis parameter
f	frequency of the flux
B_{pk}	the peak flux density in the B-H hysteresis curve
n	depends on B_{pk}, f_r, and steel material (typically 1.6-2.2)
k_c	an eddy current parameter

The core losses are generally very difficult to estimate correctly. Even with advanced FEM softwares the error may be quite large. One of the complexities is that, induced voltages in machines which are fed by switched inverters contain harmonics beside the base frequency, hence the flux linkage will also contain harmonics that causes excess core losses. Both the characteristics of the harmonics and their effect in the material are difficult to predict correctly.

The rotor losses are usually rather small in PMSM machines, and mainly caused by eddy current losses in the iron core and the magnets, which can be reduced by certain design choices such as thinner laminations, core material with higher resistivity and by segmentation of the magnets.

2.3.4 PMSM control

As stated above, the PMSM losses depend on the operating conditions, i.e. the torque and speed. Moreover, the operating conditions depend on the control method used, since any given torque and speed operating point, can be realized with a range of combinations of *d*- and *q*-axis currents. One control strategy that is rather simple to implement in theoretical calculations, is the so called Maximum Torque Per Ampere (MTPA) method, where the angle ϕ between the *d*- and *q*-axis currents is found such that the highest torque for a certain magnitude of current, I_s, is produced (where $I_d = I_s\, sin(\phi)$ and $I_q = I_s\, cos(\phi)$). This method thus also minimizes the copper losses. The MTPA angel can be found as

$$sin(\phi) = -\frac{\Psi_m}{4(L_d - L_q)I_s} - \sqrt{\left(\frac{\Psi_m}{4(L_d - L_q)I_s}\right)^2 + \frac{1}{2}} \tag{2.16}$$

where I_s is the stator current magnitude [35]. The MTPA strategy is valid until the voltage limit is hit, after which another strategy has to be implemented, e.g. Maximum Torque Per Voltage.

2.3.5 PMSM steady state modeling with regard to core losses

Since core losses are rather difficult to estimate with a high level of accuracy, an alternative method may be to introduce a core loss resistance, R_c as was done in [35] and [36], see Figure 2.4.

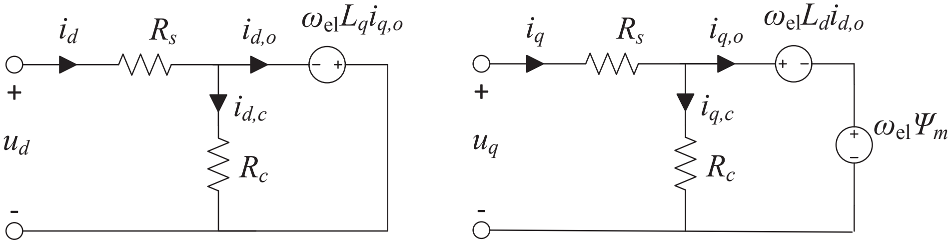

Figure 2.4 Steady state model of a PMSM, taking no load losses into account.

Then the stator voltage equations becomes

$$u_d = R_s i_d - w_{el} L_q i_{q,o} \tag{2.17}$$

$$u_q = R_s i_q + w_{el} L_d i_{d,o} + w_{el} \Psi_m \tag{2.18}$$

The electromechanical torque can be expressed as

$$T_e = \frac{3n_p}{2}(\Psi_m i_{q,o} - (L_d - L_q) i_{d,o} i_{q,o}) \tag{2.19}$$

2.4 DC-AC Converter loss modeling

A DC-AC converter typically utilizes power electronic switching devices in order to convert between the battery DC voltage and the three phase AC voltage which is demanded by the electric machine. In automotive application each switch normally consist of one or a few paralleled IGBT chips in parallel with one or a few diode chips, depending on current rating.

During operation, the main losses in the converter are due to *conduction* and *switchings* both in the transistor and the diode. The losses can be modeled as in [37] where an ideal sinusoidal Pulse Width Modulated (PWM) three phase voltage is assumed. Losses dissipated in the driver and snubber circuits, as well as due to capacitive and inductive parasitics, are assumed negligible. For the IGBTs, on-state, turn-on and turn-off losses are considered, while the reverse blocking losses are assumed negligible. Similarly for the diodes, on-state and turn-on losses are considered, but the turn-on losses are neglected due to an assumed fast diode turn-on process.

According to [37] the average on-state losses in the IGBTs in one switch can be estimated according to

$$P_{cond.\,IGBT} = \Big(\frac{1}{2\pi} + \frac{m\cos\varphi}{8}\Big) V_{CE0}\,\hat{I_s} + \Big(\frac{1}{8} + \frac{m\cos\varphi}{3\pi}\Big) R_{CE}\,\hat{I_s}^{\,2} \tag{2.20}$$

and the average (per switching period) turn-on and turn-off switching losses as

$$P_{sw.\,IGBT} = f_{sw}\,E_{(on+off)}\,\frac{1}{\pi}\,\frac{\hat{I}_s}{I_{ref}}\left(\frac{V_{DC}}{V_{ref}}\right)^{K_v} \tag{2.21}$$

where the following parameters are component dependent (most are extractable from the semiconductor component data sheet)

V_{CE0}	IGBT threshold voltage of the on-state characteristics, temperature dependent
R_{CE}	IGBT on-state resistance, temperature dependent
E_{on+off}	Energy dissipated during turn-on and turn-off
I_{ref}	Reference current, to which switching losses in data sheet correlate
V_{ref}	Reference DC voltage, to which switching losses in data sheet correlate
K_v	Parameter describing voltage dependency of switching losses, typically 1.3 to 1.4

while the others are operation dependent

m	PWM modulation index
φ	phase angle between voltage and current
$\hat{I}_s$	Amplitude of AC phase current
f_{sw}	switching frequency
V_{DC}	DC voltage level

The average diode on-state losses can be estimated as

$$P_{cond.\,diode} = \left(\frac{1}{2\pi} - \frac{m\cos\varphi}{8}\right)V_{F0}\,\hat{I}_s + \left(\frac{1}{8} - \frac{m\cos\varphi}{3\pi}\right)R_F\,\hat{I}_s^{\,2} \tag{2.22}$$

and the average turn-off losses as

$$P_{sw.\,diode} = f_{sw}\,E_{rr}\left(\frac{1}{\pi}\,\frac{\hat{I}_s}{I_{ref}}\right)^{K_i}\left(\frac{V_{DC}}{V_{ref}}\right)^{K_v} \tag{2.23}$$

where

V_{F0}	diode threshold voltage of the on-state characteristics, temperature dependent
R_F	diode on-state resistance, temperature dependent
E_{rr}	Energy dissipated during turn-off (due to the reverse recovery process)
K_i	Parameter describing current dependency of switching losses, typically 0.6
K_v	Parameter describing voltage dependency of switching losses, typically 0.6

Due to symmetry in operation, it is enough to model the losses in a single switch, and to attribute the same power loss in the other switches in order to find the total converter losses.

According to [38], by utilizing the so called *third harmonic injection* operation of the converter, the output amplitude of the AC phase voltage, $\hat{U}_{ph}$, ideally depends on the present DC voltage, V_{DC}, and the controlled PWM modulation index, m_a as

$$\hat{U}_{ph} = m_a\,\frac{V_{DC}}{\sqrt{3}} \tag{2.24}$$

In order to maintain controllability of the current a maximum m_a of 0.9 is recommended in [38]. This then sets the limit of the possible output AC voltage relative to the DC voltage.

IGBT converter modules are typically designed to withstand specific voltage levels of around $600\,V$, $1200\,V$ etc. Then at each voltage level, a number of slightly different modules are normally available, with various current ratings, such as $200\,A$, $400\,A$ etc. Since the losses to a large part depend on the magnitude of current, the current ratings implies how large temperature rise due to losses that the cooling system is able to handle without risking overheating of the transistor or diode chips.

2.5 Battery modeling

A very simple equivalent circuit model of an electrochemical battery is shown in Figure 2.5, where V_{OC} represent an ideal no load battery voltage, R_{dis} and R_{ch} represent the internal resistances during discharge and charge of the battery by the current I_b, leading to a load dependent terminal voltage V_t, [39], [31] and [32].

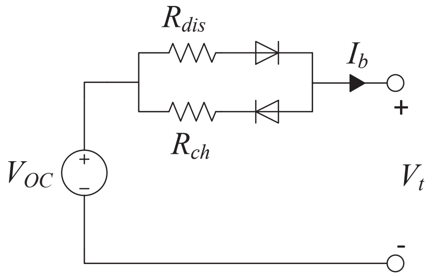

Figure 2.5 Simple battery model, with separate internal resistance for discharge and charge, with ideal symbolic diodes.

The terminal voltage equation during discharge is thus

$$V_t = V_{OC} - R_{dis}\, I_b \tag{2.25}$$

The charge content in the battery is often described by the term *state-of-charge* (SOC) which changes with battery current over time as

$$SOC(t) = SOC_{init} - \frac{\int_{t_0}^{t} I_b\,(\tau)\, d\tau}{Q_{tot}} \tag{2.26}$$

where SOC_{init} is the initial SOC level, Q_{tot} (Ah) is the total charge capacity of the battery.

In order to make the model in Figure 2.5 a bit more advanced the no load voltage can be modeled as a function of the battery's state of charge. During operation the battery energy content is drained which leads to a decrease in the no load voltage, down to a certain point at a very low SOC level where the no load voltage suddenly drops very rapidly.

The main power losses in the battery are due to the internal resistance and can be modeled as RI^2 conduction losses.

Normally a lithium ion battery cell has a maximum and minimum allowed terminal voltage level, and a maximum and minimum allowed current, or *C-rate*, where a discharge rate of 1C means that the current is such that the battery will be discharged in one hour. According to [40] the test to determine a battery's energy content is usually done for a constant current discharge at a $C/3$ discharge rate.

With the battery model as in Figure 2.5, the maximum power that can be transferred to the load is $P_{max,theoretic} = \frac{1}{4} \frac{{V_{OC}}^2}{R_{dis}}$, however according to [40], for practical reasons the limit is rather set as

$$P_{max,theoretic} = \frac{2}{9} \frac{{V_{OC}}^2}{R_{dis}} \tag{2.27}$$

The output power may also be limited by either a minimum voltage as

$$P_{max,V_{min}} = V_{min} \frac{V_{OC} - V_{min}}{R_{dis}} \tag{2.28}$$

or by a maximum current limit, which may be due to lifetime or thermal issues, as

$$P_{max,I_{max}} = I_{max}(V_{OC} + R_{dis}\, I_{max}) \tag{2.29}$$

Both the no load voltage and internal resistances vary depending on SOC level and battery temperature.

According to [39], a more dynamical representation of the terminal voltage is achieved with one or more RC-links in the model, where the main capacitive effects within the battery are also represented.

2.6 Transmission

Automotive gearbox losses generally depend on various operating conditions, where the main factors are; speed, load level and temperature, resulting in typical vehicle gearbox efficiencies of $95 - 97\,\%$ [31]. According to [41] the losses spring from phenomena that are both load independent (spring losses; oil churning and air windage) and load dependent (mechanical losses; rolling and sliding), where sliding losses may be the dominating contributor. The load independent losses cannot easily be modeled accurately with general analytical expressions. Instead experimental results are required in order to develop empirical loss models whose validity naturally will be rather limited. A number of these types of models have been suggested by various researchers. For the load dependent losses, physical expressions can be utilized in the loss modeling, however accurate parameter estimation can still be difficult.

In a BEV the transmission is typically of single-speed spur gear type, which according to [42] and [43] can be assumed to have an efficiency of 95%, in energy consumption assessments.

2.7 Auxiliary loads

During normal vehicle operation, not only the propulsion will drain the battery of energy, but also a number of secondary loads, which are often fed by a low voltage circuit. These loads may be air-conditioner, radiator fan, pumps, wipers, windows, lights, radio as well as various control systems in the vehicle [44]. Apart from an overall increased energy consumption, these types of loads may also demand relatively high peak power levels from the battery, e.g. $1.5\,kW$ for compact cars and $2.8\,kW$ for a mid-size car, according to [24]. Furthermore, according to [24], an electrical air conditioning system is designed for a peak power of $6.5\,kW$ and a continuous power of $4\,kW$.

2.8 Heat transfer modeling in electric machines

In electric machines, temperature differences and gradients arise due to the inherent internal heat sources that are the loss mechanisms. The regional temperature differences give rise to transfer of heat, or thermal energy, from warmer regions to colder through the three processes (or modes): conduction, convection and radiation [45].

At high loads, even for short periods of time, there is a risk to violate the electric machine thermal limits with immediate failure or shortage of lifetime as a result [19, 46]. Therefore, in order to predict the temperature distribution in an electric machine during varying load situations such that typically arise in BEVs, the heat transfer rates for the different modes must be estimated and incorporated into a thermal model of the machine. A lumped-parameter thermal network is known to give a reasonable accuracy in temperature distribution, even with a relatively low number of nodes [19, 47].

2.8.1 Heat transfer modes

Heat **conduction** is caused by thermal diffusion via atomic level randomized interactions in solids, as well as in stationary fluids and gases [45]. In solids the mechanisms are molecular lattice vibrations and movement of free electrons, and in fluids and gases with randomly moving molecules, the mechanisms are molecular collisions and diffusion [48]. In electric machines conduction thus occurs between the solid machine parts. In the case of a planar layer of a single material over which a temperature gradient exist the conductive heat transfer rate, q_{cond} $(W or J/s)$, is proportional to: the material's thermal conductivity λ (W/mK); the temperature gradient dT (K) over the layer; and to the cross sectional area A (m^2) that is perpendicular to the heat transfer, whereas it is inversely proportional to the heat transfer distance dx (m) (or thickness l_{thick}), as in (Fouriers Law)

$$q_{cond} = -\lambda A \frac{dT}{dx} = -\lambda A \frac{\Delta T}{l_{thick}} \tag{2.30}$$

The **convection** heat transfer mode occurs between a surface and a moving fluid. The process incorporates both conduction close to the surface interface where the fluid motion approaches zero speed, and heat transfer by the moving fluid where the heat transfer rate increases with increasing fluid motion rates [45, 48]. If the fluid is set in motion by an external factor such as a fan, pump, or even wind, it is called *forced convection*, otherwise it is called *natural convection*. The convection heat transfer rate q_{conv} (W) is proportional to: the surface area A (m^2) in contact with the fluid medium; the temperature difference between the surface T_{surf} (K) and the fluid T_{fl} (K); and the *convection heat transfer coefficient* h (W/m^2K), as in

$$q_{conv} = hA(T_{surf} - T_{fl}) \tag{2.31}$$

For electric machines, *natural convection* (or *free* convection) occurs between the housing/exterior and the surrounding air, where fins can be used to enlarge the surface area thus enhance the heat transfer rate. In order to improve the heat transfer rate even further, *forced convection* can be utilized, often realized by a fan, e.g. attached to the shaft on one side of the machine. For highly loaded machines, liquid cooling can be used where the cooling media can be a water or oil mixture, and the cooling ducts can be placed inside the frame, or sometimes even inside the machine close to the windings.

Convection heat transfer is also present in the machine's air gap, as well as in the internal air between the housing endcaps and the lamination core, where the rotor's rotations cause the air to move [49].

The convection heat transfer coefficient depend on many factors such as: the surface geometry; the nature of fluid motion; the thermodynamic and transport properties of the fluid; and on the flow rate. Hence, it has to be experimentally or empirically determined [22, 45, 48]. As a rough guidance, there are published ranges of typical values of the heat transfer coefficient depending on the type of convection and media. By combining the range data in [45, 48, 50, 51], the heat transfer coefficient for natural convection is typically $2 - 25$ W/m^2K for gases, and $10 - 1000$ W/m^2K for liquids, whereas for forced convection it is typically $10 - 300$ W/m^2K for gases and $50 - 20,000$ W/m^2K for liquids.

In practice, the seeking of a convection heat transfer coefficient is often replaced by the seeking of the dimensionless *Nusselt* number Nu, which is the ratio of the convective and conductive heat rates. It is thus proportional to the heat transfer coefficient and the characteristic length (or fluid layer) l_c, and inversely proportional to the thermal conductivity, as in [48]

$$Nu = \frac{q_{conv}}{q_{cond}} = \frac{hA\Delta T}{\lambda A \Delta T / l_{thick}} = \frac{hl_c}{\lambda} = f(geometry, Re, Pr) \tag{2.32}$$

The Nusselt number depends on the specific geometry as well as on the two dimensionless parameters: the *Prandtl* number Pr, and the *Reynolds* number Re [45]. The Prandtl number is the ratio of a fluids momentum to heat diffusivity, and depend only on a medium's material parameters. It is proportional to the fluid specific heat capacity c_p (J/kgK) and to the dynamic viscosity μ $(kg/m\,s)$ and inversely proportional to the thermal heat conductivity [45, 48], as in

$$P_r = \frac{c_p \mu}{\lambda} \tag{2.33}$$

For $Pr \ll 1$ conductive heat transfer dominates, and for $Pr \gg 1$ convective heat transfer dominates. According to [48], Pr is typically 0.12-1 for gases, 1.12-13.7 for water, and

50-100,000 for oils. There is also a temperature dependence of all of the three material parameters.

The Reynolds number is the ratio of the fluid inertia to the viscous forces, and is proportional to the mass density ρ (kg/m^3), the fluid velocity v (m/s), and the characteristic length l_c (m), and inversely proportional to the dynamic viscosity [45,48], as in

$$R_e = \frac{\rho v l_c}{\mu} \tag{2.34}$$

For high Re the flow easily becomes *turbulent*, and for low Re the turbulence is more damped and may even give a *laminar* flow. Since a high Re usually gives a higher Nu, a turbulent flow thus gives a higher convection heat transfer coefficient. The transitions from laminar to turbulent flow may occur at a specific critical Re value. This value depend on many factors, such as the type of fluid medium, surface geometry and roughness and temperature of medium and surface, hence it is difficult to predict analytically. However, historically conducted experiments for a range of often used geometries and fluids can offer reasonable estimation methods and some times approximated values.

Thermal radiation is heat transfer in the form of electromagnetic waves or photons that are emitted by a surface to its colder surroundings or to another surface [45,48]. The radiated heat transfer rate q_{rad} (W) is proportional to the surface *emissivity* ε, surface area A (m^2), and difference between surface temperature T_{surf} and surrounding temperature T_{surr} (K) both to the power of four, as in (Stefan-Boltzman's equation)

$$q_{rad} = \varepsilon \sigma A (T_{surf}^4 - T_{surr}^4) \tag{2.35}$$

where $\sigma = 5.670\,10^{-8}$ $(W/m^2\,K^4)$ is Stefan-Boltzmann's constant [48]. The maximum rate of radiation that can be emitted is that of a *black body* which has an emissivity equal to one. For other surfaces the emissivity is a measure of the effectiveness of radiation compared to that of a black body, and range between 0-1 [45,48]. When forced convection cooling is used the radiation is often assumed negligible [48,52]. It is also possible to define a heat transfer coefficient h_{rad} for radiation and form an equation similar to (2.31) [45,48], as in

$$q_{rad} = h_{rad} A (T_{surf} - T_{surr}) \tag{2.36}$$

where the heat transfer coefficient is

$$h_{rad} = \varepsilon \sigma (T_{surf} - T_{surr})(T_{surf}^2 - T_{surr}^2) \tag{2.37}$$

2.8.2 Lumped-parameter modelling

Heat transfer in electrical machines is inherently three dimensional. It is, however, often modeled in fewer dimensions under the assumption of dimensional interdependence [19]. A reasonably accurate thermal model must capture the main flows of heat transport in the machine. This can be done analytically in a lumped-parameter network, or numerically using FEA (Finite Element Analysis) and CFD (Computational Fluid Dynamics) methods.

With the lumped-parameter method, execution is fast, and a wide range of load points e.g. vehicle load cycles, can be analyzed in a relatively short period of time. The primary effort lies in forming a relevant network where the main heat transfer paths are represented, and to find suitable estimates of the heat transfer rates. With FEA and CFD software, highly detailed and complex machine geometries can be analyzed, however both model set-up and load point execution can be time consuming. CFD software is especially competent in analyzing convection problems. Thermal FEA software programs are usually limited to improving the accuracy of conduction estimation, whereas for convection and radiation the same approximations must be used as those in a lumped-parameter network.

In a lumped-parameter thermal model, bulk regions of the electric machine are lumped together where it is reasonable to assume spatially uniform material properties, thermal energy storage capacity, internal heat generation, and thus temperature. Different lumped regions are then interconnected using thermal impedances which are primarily determined by geometrical and material properties. In this way, the thermal network is analogous to an electrical network, but with thermal resistances and heat energy storing capacitances instead, where the heat transfer rate has the same role as current, and temperature the role of voltage.

In thermal steady state, the temperature T difference between the two adjacent nodes i and j (in an n-node system) can be described by the relation [49]

$$T_i - T_j = \mathbf{G}^{-1}\mathbf{P} \tag{2.38}$$

where **P** is a vector that represent internal heat sources i.e. machine losses in selected nodes, and is defined as

$$\mathbf{P} = \begin{bmatrix} P_1 \\ P_2 \\ \vdots \\ P_n \end{bmatrix} \tag{2.39}$$

and **G** is the thermal conductance matrix defined as

$$\mathbf{G} = \begin{bmatrix} \sum_{i=1}^{n} \dfrac{1}{R_{1,i}} & -\frac{1}{R_{1,2}} & \cdots & -\frac{1}{R_{1,n}} \\ -\frac{1}{R_{2,1}} & \sum_{i=1}^{n} \dfrac{1}{R_{2,i}} & \cdots & -\frac{1}{R_{2,n}} \\ \vdots & \vdots & \ddots & \vdots \\ -\frac{1}{R_{n,1}} & -\frac{1}{R_{n,2}} & \cdots & \sum_{i=1}^{n} \dfrac{1}{R_{n,i}} \end{bmatrix} \tag{2.40}$$

The net thermal resistance R_{th} (K/W) of a region due to heat **conduction** is proportional to the temperature difference over the region and inversely proportional to the heat transfer rate as in

$$R_{th} = \frac{1}{G} = \frac{\Delta T}{q_{cond}} = \frac{l}{\lambda A} \tag{2.41}$$

For a region with a varying area perpendicular to the direction of heat flow, the net thermal resistance instead becomes a line integral as in

$$R_{th} = \int_0^l \frac{1}{\lambda A(x)}\,\mathrm{d}x \tag{2.42}$$

Due to the typically cylindrical shape of rotating electric machines, a few specific geometries are often modeled, such as a hollow cylinder and a segment of a hollow cylinder as in Figure 2.6. For radial heat transfer in a segment of a hollow cylinder, the thermal resistance, as resulting from (2.42), is

$$R_{th} = \frac{ln(\frac{r_{out}}{r_{in}})}{\phi \lambda l_{thick}} \tag{2.43}$$

where r_{out} (m) and r_{in} (m) are the outer and inner radii, ϕ (rad) is the segment angle, and l_{thick} is the segment thickness. For a whole hollow cylinder, the segment angle is 2π.

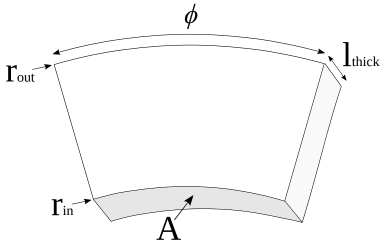

Figure 2.6 Segment of a hollow cylinder, for calculation of radially thermal conductive material.

For axial heat transfer in a hollow cylinder the thermal resistance is

$$R_{th} = \frac{l_{thick}}{\lambda \pi (r_{out}^2 - r_{in}^2)} \tag{2.44}$$

The thermal resistance due to heat **convection** is inversely proportional to the convection heat transfer coefficient and the surface area, as in

$$R_{th} = \frac{T_{surf} - T_{fl}}{q_{conv}} = \frac{1}{hA} \tag{2.45}$$

Similarly, the thermal resistance due to heat **radiation** is inversely proportional to the radiation heat transfer coefficient and the surface area, as in

$$R_{th} = \frac{T_s - T_{surf}}{q_{rad}} = \frac{1}{h_{rad}A} \tag{2.46}$$

The heat energy storage or thermal capacitance of a region is the product of material density ρ, volume V (m^3), (i.e. mass m (kg)) and specific heat c_p $(J/kg\,K)$. The net thermal capacitance in a node C_{th} (J/K) is the sum of capacitances connected to the node, as in

$$C_{th} = \rho \sum_{i=1}^{n} V_i c_{p,i} = \sum_{i=1}^{n} m_i c_{p,i} \tag{2.47}$$

A capacitance matrix similar to the conductance matrix can then be formed, as

$$\mathbf{C} = \begin{bmatrix} C_{th,1} & 0 & \dots & 0 \\ 0 & C_{th,2} & \dots & 0 \\ \vdots & \vdots & \ddots & \vdots \\ 0 & 0 & \dots & C_{th,n} \end{bmatrix} \tag{2.48}$$

For transient thermal analysis, the node increase in temperature from a reference value, can be found from [49] [53]

$$\frac{d\mathbf{T}}{dt} = \mathbf{C}^{-1}(\mathbf{P} - \mathbf{GT}) \tag{2.49}$$

or, expressed differently as in

$$\mathbf{C}\frac{d\mathbf{T}}{dt} + \mathbf{GT} = \mathbf{P} \tag{2.50}$$

2.8.2.1 "T-equivalent" network node configuration

As discussed in [19, 20, 54, 55] for one dimensional radial heat flow in a hollow cylinder with no internal heat generation, the node that represent the mean temperature can readily be placed in the middle of two thermal resistances $R_0/2$ that each represent half of the total radial conduction thermal resistance, R_0.

However, if there is also an internal heat generation, that can be considered uniform, then the same middle node would no longer represent the mean temperature, but a somewhat higher temperature.

Instead, a small negative thermal resistance $-R_0/6$, can be connected between the central node and the internal heat source and thermal capacitance, so called "T-equivalent" network node configuration. A derivation can be found in [54].

One alternative approach is to introduce "compensation thermal elements" on each side of the central node, as described in [56].

$$t_{comp.,i} = \frac{P_{loss,i}}{4}\frac{R_{th,i}}{2} \tag{2.51}$$

Chapter 3

Road Type Driving Patterns, Road Grade and Daily Driven Distances

For a successful vehicle design, as with the design of any product, knowledge of the use phase is essential. Vehicles are used in various environments, by different types of drivers and for numerous purposes. Each of these circumstances put their specific capability requirements on the vehicle in terms of static and dynamic road load levels.

Through the years much research has been conducted, especially in Europe and the US, aiming to identify typical *driving patterns* on different *road types*. The main reason has then been to assess in which way, and to what degree, vehicle pollutant emissions and fuel consumption are effected by different driving patterns and situations.

This chapter attempts to identify typical levels of **speed**, **acceleration** and **road grade** attributed to different road types, such as urban (or city) driving and high speed motorway driving, for the purpose of finding suitable BEV powertrain design criteria regarding torque speed and power. Additionally, typical daily driving distances will be investigated, since range is an important design factor for a BEV.

3.1 Driving patterns

Normal on-road driving is thus affected by many different factors such as: driver behavior, weather conditions, street type, traffic conditions, journey type as well as vehicle type and specifications [6]. This makes it a quite challenging task to identify and to specify typical driving characteristics.

Many studies have been done under the sponsorships of American and European national emission regulatory organizations, such as the US Environmental Protection Agency (EPA), the California Air Resources Board (CARB) and the United Nations Economic Commission for Europe (UN/ECE). The purpose has then been to develop test procedures which describe repeatable standardized laboratory tests on light duty vehicles, i.e. passenger cars, as a part of the type approval procedure. Then legally regulated emissions as well as fuel economy/efficiency are measured while the vehicle is driven according to a reference speed over time: a so called *drive cycle*. In order to make sure that the legally set emission targets are not exceeded in typical real-world traffic, it is highly desired that the laboratory test fallout is fairly close to that. Another important outcome of the test is that they represent a fair estimation of fuel economy/efficiency for customers.

However as recognized by EPA most test drive cycles were developed a few decades ago, and both legal speed limits and vehicle power specifications thus performance have increased since, [7], the later which has also been noted in Sweden by [57]. It was to account for this that EPA updated the fuel economy test procedure in 2008 to also include two more aggressive cycles.

In recent years, several extensive studies have been conducted all around the world, targeting investigation and identification of typical driving patterns and their effect on fuel consumption and emissions. As a fact, apart from the added cycles, EPA has also considered such studies in order to find other causes of fuel consumption during real-world driving, such as fuel energy density, wind, tire pressure and road roughness [7]. But instead of expanding the test procedure to include such factors, EPA has developed an intricate formula where the city and highway fuel economy label data are calculated based on certain weighting factors on sections of each test cycle.

So far, the test procedures in Europe are the same since the year 2000. Yet, several large projects have been conducted where driving data has been collected by using instrumented vehicles, and corresponding drive cycles have been developed. The most known studies are the INRETS, HYZEM, ARTEMIS and the latest is the WLTC.

Due to the large interest in gathering information of local driving patterns, a wide range of real-world cycles have been developed to capture the specific circumstances of driving on a certain type of road, in a particular city, or region of the world. Cycles of this type can be found from regions such as; (Pune) India, China, Hong Kong, Tehran Iran, (Melbourne, Perth) Australia, Manila Filipines, Edingburgh UK, Latvia, Athens Greece and Vietnam.

In the Chalmers initiated, *The Swedish Car Movement Data Project*, 714 cars have been instrumented during the years 2010-2012, in the south west of Sweden and the data is gathered in a data base [58]. As a researcher, access to the data base can be granted, however it has not been used within the scope of this project.

Instead, in this project sample in-house-measurements have been conducted, mostly covering the area in and around Göteborg, but also longer highway sections, e.g. between Göteborg and Jönköping and Torslanda-Stenungsund. Data regarding speed and acceleration has been measured with a GPS and an accelerometer, see Appendix B.

3.1.1 Legislative cycles

During the standardized tests, the vehicle is driven on a chassis dynamometer with the driving wheel pair on a roller, attempting to, within specified limits, follow the time series speed trace of a specified drive cycle. The vehicle's rolling resistance and air drag is estimated and added as an extra load on the roller. Traditionally, there are separate test procedures for measuring pollutant emissions like (CO, HC, NOx, and PM) compared to measuring CO_2 emissions together with fuel economy/consumption. The differences in procedures may be; the used drive cycle/-s, or at which ambient temperature the test is run. European and Japanese test procedures include only one specified drive cycle (NEDC) and (JC08) for both test procedures including BEVs, while the US test procedures utilize five dissimilar drive cycles, each aiming to represent various types of driving on different road types.

Here follows a short review of the history of the development of the legislative drive cycles in the US, Europe and Japan, many of which are used in this thesis.

3.1.1.1 Test drive cycles in the US

Vehicle driving patterns and emissions were studied in Los Angeles, USA, in the 1950s, due to the strong suspicion that the city's smog was to a large part caused by motor vehicles. In the end of the 1950s one of the first test cycles was developed. Input data was collected by driving with seven different cars on different types of roads around Los Angeles, and recording the amount of time spent in certain bins of engine speed and manifold pressure, as well as time spent to accelerate between the speed levels. The resulting cycle was a so called *modal drive cycle* with sixteen modes of constant speed and acceleration, where the relative duration of each mode served as a reflection of the measurements. The top speed was $80\,km/h$ and the maximum acceleration was $1.34\,m/s^2$ [59]. But it wasn't until about a decade later, in 1966, that a shortened version of it, a seven-mode cycle, (same top speed but lower maximum acceleration $0.8\,m/s^2$ representing 24 hours average conditions) was adopted in Californians first test procedure to measure vehicle emissions (HC and CO) and fuel economy in a standardized manner [60], [59]. In 1968 the procedure was adopted in the rest of the USA [59].

However already in 1969 the work continued towards an updated test cycle which could better represent typical morning traveling in Los Angeles, and more measurements were done. Finally the new cycle was taken from direct speed measurements from a vehicle driving on a specific route (the LA-4 route) around Los Angeles, as the one out of six runs which was closest to the average [59]. The cycle distance was then shortened to represent the typical driving distance in Los Angeles at the time, $12\,km$ [59]. The maximum acceleration and deceleration rate of the cycle was limited to $1.48\,m/s^2$ ($3.3\,mph/s$), due to a limited measuring range of the lab chassis dynamometer [59], [60]. The cycle was called the Urban Dynamometer Driving Schedule (**UDDS**), but it is also known as the LA4-S4 cycle or **FTP-72**, and was adopted as a new test cycle in the US in 1972 [60]. Test runs in labs measuring HC, CO and CO2 showed a very good correspondence with the real route emissions. In 1975 the cycle was somewhat modified such that the initial cycle was followed by a 10 min long stand still (soak), after which the initial 505 seconds were repeated, thus forming the **FTP-75** cycle, which is still used today to represent urban/city driving.

As EPA started to publish fuel economy data of new cars based on the city cycle FTP in the 1970s, the interest rose in similar data also for highway driving, [60]. Therefore, EPA started a "chase car" measurement series and drove over $1\,690\,km$ on non-urban roads in the area of Michigan, Ohio and Indiana, where the maximum speed limit was $88.5\,km/h$ ($55\,mph$), as in most of the USA at the time. The collected data was analyzed and resulted in the Highway Fuel Economy Test cycle (**HWFET**). Also in this cycle, acceleration and deceleration rates were limited to $1.48\,m/s^2$, due to belt slippage during chassis dynamometer tests, however, these modifications were considered to have only minor influence since they were limited to the fist ten and last twenty seconds of the cycle [59].

According to a study by CARB in 1990, large accelerations could have dramatic effects on emission levels, but these events were missing in the FTP cycle [61]. As EPA found a lack of data on the occurrence frequency of such accelerations during normal driving, they initiated a new study. Hence in 1992 EPA together with CARB and two manufacturer organizations[1] conducted a vast real-world-driving study based on 100-150 instrumented vehicles in each of the three cities, Baltimore, Spokane and Atlanta [61]. Data was also recorded using the "chase car" method on routes in Baltimore, Spokane and Los Angeles [61]. The recorded driving data showed that during almost $13\,\%$ of the time, the vehicle was experiencing higher speed and acceleration levels than what was represented in the FTP cycle [61]. Based on the measured data from Baltimore together with the collected data from Los Angeles, Sierra Research which was contracted by EPA, divided the time traces into micro-trips, i.e. cutting the cycle at each stand still. A software was then developed which sampled different micro-trips together to form a drive cycle, according to certain cycle targets. In this way thousands of cycles were created. Finally those few with the best match to targeted speed-acceleration-distribution were chosen to be continued with [61]. One of the most famous ones is the **REP05** which represents aggressive highway driving where about $70\,\%$ of the time is spend at higher speed and acceleration levels compared to the FTP cycle [61]. Other known cycles are the **ARB02** and **LA92** also called the Unified Cycle (**UC**).

Later in the mid 1990s the EPA emission test procedure was updated, the so called Supplemental Federal Test Procedure (SFTP), to also include two new cycles which represents more aggressive driving and rapid speed fluctuations. One of them was the **SC03**, which is a low speed cycle, but contains rapid speed fluctuations. The other one was the **US06** cycle, which is developed as a shortened combination of the REP05 and the ARB02 cycles, representing high speed and acceleration levels.

Today EPA's test procedure for emissions comprise of the FTP-75, SC03, UDDS (FTP-72), US06 and the LA92 cycles, regulated under $Tier1 - 3$. For fuel economy and CO_2 emission labeling (regulated since 2012 on a fleet average basis), the FTP and HWFET were the only cycles used until vehicle model year 2008, when also the US06, SC03 (run at $35\,^{\circ}\mathrm{C}$) and a cold version of the FTP ($-6.7\,^{\circ}\mathrm{C}$, instead of $23.9\,^{\circ}\mathrm{C}$ as for HWFET and hot FTP) were added.

When it comes to certifying driving range and fuel economy of BEVs, either the FTP and HWFET cycles can be used, or the five cycles used for conventional vehicle fuel economy can be used, until EPA's rules are updated for BEVs [62].

Another cycle which has been developed by the EPA, is the New York City Cycle (**NYCC**), which represents congested traffic in a large city. Even though it is not utilized in any regulatory test procedure, it can be seen in many published articles regarding Hybrid Electric Vehicles (HEV) and Plug-In Hybrid Electric Vehicles (PHEV).

---

[1] The American Automobile Manufacturers Association (AAMA) and the Association of International Automobile Manufacturers (AIAM)

3.1.1.2 Test drive cycles in Europe

Smog was also an increasing problem in larger cities in Europe during the 1950s and 1960s, especially in London. According to [59], a modal cycle was developed in the mid 1960s, which was based on measurements in Paris of engine speed, pressure, brake pedal activity and selected gear position, (very much like the work previously done in Los Angeles), i.e. with modes of constant speed and accelerations. Furthermore, according to [59], this cycle was then modified into the first **ECE 15** cycle (15 modes), based on additional measured driving patterns in ten European cities. The cycle was adopted in the European Community's first vehicle emission regulation in 1970 (directive 70/220/EEC) as a part of a vehicle's type approval, with limits on gaseous pollutants depending on the vehicle weight [63].

In 1990 EU test procedures, the **EUDC** part was added after four ECE-15 cycle repetitions, aiming to also represent more aggressive and high speed driving. This combination formed a cycle called ECE+EUDC, or MVEG-A, which was also initiated by a $40\,s$ period of engine idling [64]. From the year 2000, the idling period was removed, thus it became an engine cold start cycle, called New European Driving Cycle (**NEDC**), or MVEG-B [64].

Today the NEDC cycle is utilized in test procedures of both pollutant emissions (regulated in $Euro\,1-6$) and for testing fuel consumption and CO_2 emissions. The later is regulated since 2012. NEDC is also utilized when determining the driving range and energy consumption of BEVs. The temperature during the test may be between between $20-30\,°\mathrm{C}$.

3.1.1.3 Test drive cycles in Japan

In Japan a modal cycle was developed 1969. It was replaced 1973 by an early version of the 10-mode cycle simulating driving in Tokyo with max speed of $40\,km/h$ used in emission certifications, and 1975 an 11-mode was developed simulating suburban driving with a top speed of $60\,km/h$ [59] however this part was not added to the test procedure. Not until 1991 was a high speed mode added to the Japanese test; the 15-mode cycle, still with a moderate top speed of $70\,km/h$ [65]. During recent years, from 2008 to 2011 the latest and current test cycle was introduced in the regulations; the **JC08** cycle, which is a step away from the earlier modal cycles, yet still representing congested city driving with the relatively low top speed of $80\,km/h$ [64]. As in Europe, the same cycle is used for measuring both pollutant emissions as well as fuel economy and CO_2 emissions.

3.1.1.4 Test drive cycles in the world

Since the 1970s many more countries around the world have adopted emission regulations (for light duty vehicle emissions of CO, HC, NOx and PM in gram per driven km) and related test procedures, often based on either the US *Tier* or European *Euro* [64, 65]. Today Australia[1], half of south America and most of Asia[2], including China and India, but not Japan, have adopted the European regulations, while North America and about half of south America have adopted the US emission regulations [29].

3.1.2 Non-legislative cycles

Many of the non-legislative cycles are not easily accessible for external parties, still it can be assumed that the majority of the automotive industry has gained access in order to develop their final products.

This work is based on cycles from Artemis, WLTC as well as own in-house measurements in the area around Göteborg.

3.1.2.1 Artemis

The Artemis project involved 40 European research laboratories and was founded by the European Commission, to develop new European methods, tools, models and databases for accurate estimation of pollutant emissions from transport [66]. Within the project, a set of real world driving cycles for passenger cars were developed, categorized as *urban*, *rural* and *motorway*, each with sub-cycles representing various driving conditions such as traffic density.

The Artemis cycles are based on data from 77 instrumented vehicles in France, UK, Germany and Greece collected in 1990s in the previous research projects *DRIVE-MODEM* and *HyZem*, each in which a number of cycles were also developed (in the categories: urban, congested urban, road and motorway) [66].

The Artemis Urban cycle has sub-cycles of congested, dense and free flow traffic, where the speed level differs between about $10 - 60\,km/h$ as well as the number of and duration of stops. The Rural cycle has sections of steady and unsteady speeds at rural secondary to main roads at speed levels around $50 - 100\,km/h$. Finally the Motorway cycle also has sub-cycles of steady and unsteady speed at speed levels between about $90 - 150\,km/h$ [66]. There is also a modified version of the Motorway cycle, which has a top speed of about 130 km/h.

3.1.2.2 WLTC

Since 2008, the United Nations Economic Commission for Europe (UN-ECE) are presently working on finalizing a proposal for a new Worldwide harmonized Light duty driving Test Cycle (WLTC), which can be used for type approval fuel consumption and emission tests. The cycle is aimed to represent typical driving on a global scale. Vehicle data has been collected from instrumented vehicles in USA, Japan, India, Korea and the European countries Belgium, Germany, Spain, France, Italy, Poland, Slovenia, Switzerland, United Kingdom and Sweden. The logged data has then been chopped into micro trips which in turn have been categorized for further analysis [67].

Three classes of drive cycles have been developed, where Class 1 is to be used by vehicles with power-to-mass ratio of $\leq\ 22\,W/kg$, Class 2 by vehicles with power to mass

---

[1] Australian emission regulations are based on European regulations but with some additional selected parts from US and Japanese standards [64].

[2] In South Korea the diesel engine vehicles are under European regulation while the gasoline engine vehicles are under US regulations [64].

ratios > 22 and $\leq 34\,W/kg$, and finally Class 3 by vehicles with ratios $> 34\,W/kg$ [67]. Each class consist of 2 to 4 cycles called: Low, Middle, High, ExtraHigh, which are refereing to speed levels. They have different characteristics such as speed and acceleration levels, and cover scenarios like congestion or free flow traffic.

3.1.2.3 Electric Power Engineering, Chalmers

At the beginning of this work, there was a lack of awareness of and access to real-world cycles, except those used as test cycles. Another important aspect was the desire to attain vehicle operation information at a higher time resolution than what is typically available from the official test cycles, which are mainly second based. Therefore a measurement system was purchased and a few different cars were instrumented during typical driving in the area of Göteborg. The measurement system consists of a $5\,Hz$ GPS receiver and a $20\,Hz$ 3D acceleratorer, thus giving a higher time resolution than what can be found in most official real-world cycles. Apart from vehicle speed and acceleration, also the road grade has been estimated with this system, while this is often omitted in official real-world cycles. See Appendix B for a more detailed description of the measurement system, as well as filtering of measured data.

The selected data represent collected logs mostly in the area of Göteborg, by a limited set of car models, drivers, and routes. Some routes represent typical home-to-work routes, others only typical driving in the city or on the highway.

3.1.3 Driving pattern characterization parameters

Research on the topic of driving patterns have traditionally been focused on identifying specific events during driving that may have an effect on fuel consumption and emissions, as well as on quantifying this effect through empirical field studies with instrumented vehicles. In several such studies, it has been found that high acceleration levels in general, and in combination with high speed in particular, have a major effect on both emissions and fuel consumption, even though the frequency of occurrence of these events is rather small i.e. only a few percent of the total driving time, [8] and [9]. Still these findings belong to conventional vehicles with internal combustion engines, it is likely that similar measures will also have an important impact on electrically powered vehicles. Power demanding measures are especially interesting in this study since the maximum demanded powertrain power is sought.

The analysis is often based on a set of calculated parameters related to time, speed and acceleration. According to [8], the parameters can be divided into; **level parameters** such as *max., average and standard deviation of speed and acceleration*, **distribution measures** like *relative time spent in bins of speed and acceleration*, and by **oscillatory measures** considering for example *changes of speed levels per distance or time*. It is not evident, which parameters that are relevant when considering the power demand and energy consumption of a BEV, however 15 parameters have been chosen to be used for all of the discussed drive cycles in this thesis. As level parameters; total time, driven distance, maximum speed, average speed, average running speed (i.e. without stops) and standard deviation of speed, have been used as well as maximum, average, and standard deviation of positive and negative acceleration. As distribution measures; relative time spent standing still, and in certain speed levels have been used, as well as relative time spent during positive and negative acceleration, and within certain acceleration level intervals. Finally an oscillatory measure is also used; Relative Positive Acceleration (RPA), defined as

$$RPA = \frac{\int speed(t)\ positive\,acceleration(t)\ dt}{\int speed(t)\,dt = total\,driven\,distance}. \tag{3.1}$$

RPA is an indicator of accelerations which demand high power, since a large acceleration may demand a high torque but not necessarily a high power, unless it is combined with a high speed [8] [6].

3.2 Road type specification based on speed levels

The speed levels experienced by vehicles are of great interest for finding necessary top speed of the vehicles. It is also interesting to know what speed levels that typically occur on which road type.

In this thesis, all used cycles have been assigned to either of the three road type categories; *Urban*, *Rural* or *Highway*, mainly based on share of time spent at speed levels up to $60\,km/h$, between $60-90\,km/h$, and above $90\,km/h$, respectively, as can be seen in Table 3.1. With this general rule, many cycles could be categorized both as Urban and Rural, due to the ambiguous data. However, for cycles that were categorized as Urban, the time share at speed levels above $90\,km/h$ was nil or only a few percent, otherwise they were categorized as Rural.

As already stated, the purpose of this categorization is to find typical driving characteristics for the chosen road types, therefore the majority of the time spent at certain speed levels is dominating the categorization.

Table 3.1 General categorization of cycles based on time share at speed levels.

	$60-90\,km/h$	$> 90\,km/h$
Urban:	$< 20\,\%$ of the time	$\approx 0\,\%$ of the time
Rural:	$> 20\,\%$ of the time	$< 20\,\%$ of the time
Highway:	-	$> 20\,\%$ of the time

3.2.1 Urban

The time series of speed and acceleration for the Urban Test cycles can be seen in Figure 3.1, and for the Logged Urban cycles in Figure 3.2. Three logged urban cycles were excluded from the figure, since two of them represent already displayed routes, and one was similar to the others.

Cycle data regarding time duration, driven distance and speed levels can be seen in Table 3.2, for both Test cycles and Logged cycles. In order to account for non zero measured speed from the GPS, the average running speed as well as the time share standing are based on speed levels at $3\,km/h$ and below, for all cycles, i.e. including the test cycles.

Regarding the time shares within certain speed intervals, the selected logs match the test cycles quite well. The main difference is a longer mean time share standing for the test cycles (27 % compared to 17 %), and thus a shorter time share at low speed, compared to the logs. Most certainly some of the test cycles represent more dense traffic conditions than what was experienced in the Logged cycles.

For the test cycles, the maximum speed varies between 45 km/h for the NYCC cycle to 91 km/h for the FTP cycles, while the difference is smaller for the logged cycles; 49 for the V774 120312 log to 78 km/h for the Prius 120403 log. Still, the logged cycles have a somewhat higher mean average speed value compared to the test cycles, while the average running speed is rather similar. The spread in speed levels seen by the speed standard deviation is a bit larger for the test cycles, especially for those with the highest top speed.

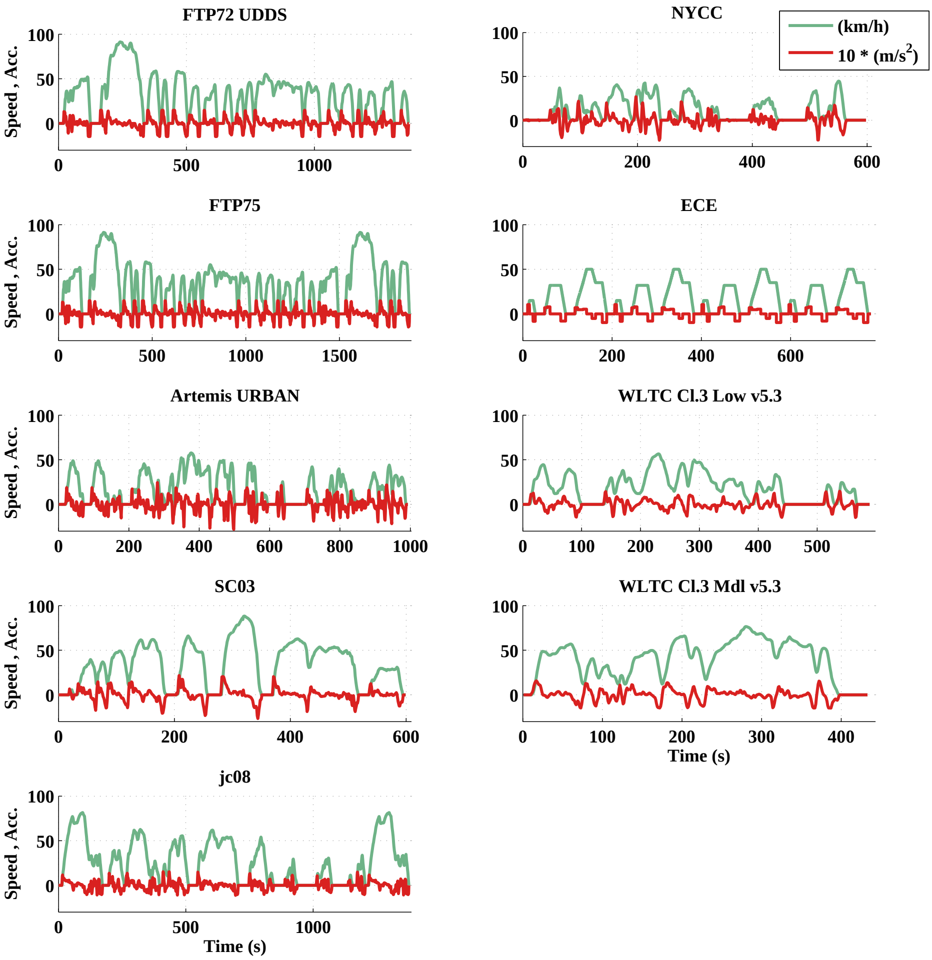

Figure 3.1 Acceleration and speed over time for Urban test cycles, [68], [64], [1] and [69].

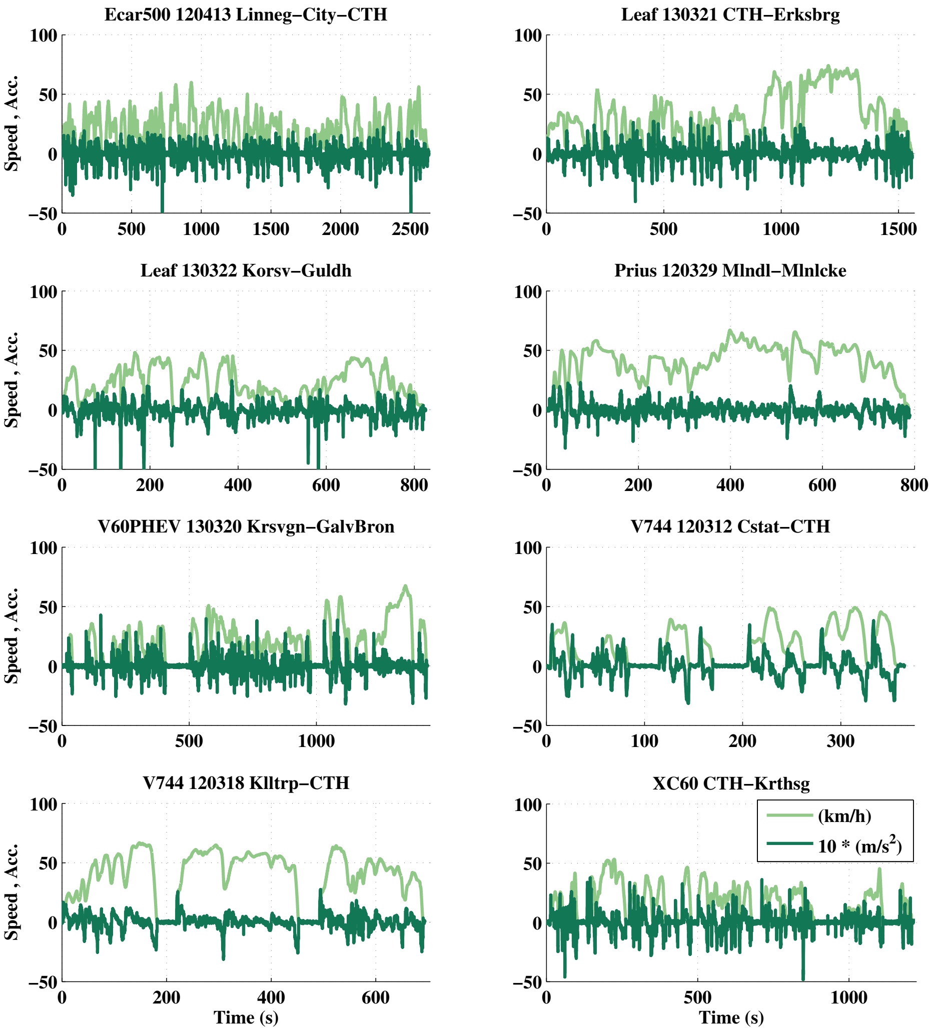

Figure 3.2 Acceleration and speed over time for Logged Urban cycles.

Table 3.2 Cycle data for Urban Test cycles, and Logged Urban cycles.

Urban Test Cycles	Cycle duration (s)	Driven distance (m)	Max. speed (km/h)	Average speed (km/h)	Average running speed (km/h)	Std. speed (km/h)	Time share standing (%)	Time share <60 km/h (%)	Time share 60-90 km/h (%)	Time share > 90 km/h (%)
Artemis URBAN	993	4 870	58	18	25	17	33	66	0	0
ECE	780	4 058	50	19	27	17	34	66	0	0
NYCC	598	1 898	45	11	18	13	44	56	0	0
WLTC Cl.3 Low	589	3 095	57	19	25	16	28	72	0	0
FTP72 UDDS	1 369	11 990	91	32	39	24	21	71	7	1
FTP75	1 874	17 769	91	34	42	26	21	67	11	2
SC03	599	5 761	88	35	43	25	21	65	14	0
jc08	1 376	10 317	82	27	37	24	28	60	12	0
WLTC Cl.3Mdl v5.3	433	4 756	77	40	44	22	12	70	18	0
MEAN	**957**	**7 168**	**71**	**26**	**33**	**20**	**27**	**66**	**7**	**0**

Logged Urban Cycles	Cycle duration (s)	Driven distance (m)	Max. speed (km/h)	Average speed (km/h)	Average running speed (km/h)	Std. speed (km/h)	Time share standing (%)	Time share <60 km/h (%)	Time share 60-90 km/h (%)	Time share > 90 km/h (%)
Ecar500 120413 Linneg-City-CTH	2 633	12 927	60	18	24	15	28	72	0	0
Leaf 130321 CTH-Erksbrg	1 558	13 130	74	30	35	21	14	71	14	0
Leaf 130322 Korsv-Guldh	826	4 959	48	22	24	13	10	90	0	0
Prius 120329 Mlndl-Mlnlcke	790	9 098	67	41	42	14	2	94	4	0
Prius 120329 Mlnlcke-Mlndl	866	9 773	75	41	44	20	8	76	16	0
Prius 120403 Mlnlcke-CTH	1 036	11 585	78	40	43	20	7	73	20	0
V60PHEV 130320 Krsvgn-GalvBron	1 437	7 454	68	19	26	17	29	69	2	0
V744 120312 Cstat-CTH	365	1 608	49	16	25	16	37	63	0	0
V744 120318 Klltrp-CTH	694	7 762	67	40	46	20	13	75	12	0
V744 120327 CTH-Klltrp	806	7 932	64	35	39	18	9	83	8	0
XC60 CTH-Krthsg	1 213	5 246	53	16	23	14	33	67	0	0
MEAN	**1 111**	**8 316**	**64**	**29**	**34**	**17**	**17**	**76**	**7**	**0**

3.2.2 Rural

The time series of speed and acceleration for the Rural Test cycles can be seen in Figure 3.3, and for the Logged Rural cycles in Figure 3.4. One logged cycle was excluded from the figure, since the same route was already displayed in the opposite direction. However the graphs show the same route at three different occasions, which illustrates the deviation between different runs on the same route.

Cycle data for both Logged Rural and Rural Test cycles can be seen in Table 3.3. Also in this case the mean time share standing is larger for the test cycles compared to the logs (13 % respective 9 %). Then the time share on medium to high speed levels are somewhat higher for the test cycles compared to the logs. This is also reflected in the maximum speed levels which are larger for the test cycles. In the same time, the mean average speed as well as the average running speed are very similar between the test and logged cycles. The UCLA has the lowest average speed of only 39 km/h, while the EUDC has the highest at 63 km/h, followed by the Artemis Rural and WLTC High. It is also EUDC and NEDC that have the highest maximum speed levels. For the logs there are four cycles with maximum speed levels around 100 to 110 km/h. It can be seen that a high maximum speed is not necessarily linked with a high average speed, instead cycles with lower max. speed may have similar level of average speed.

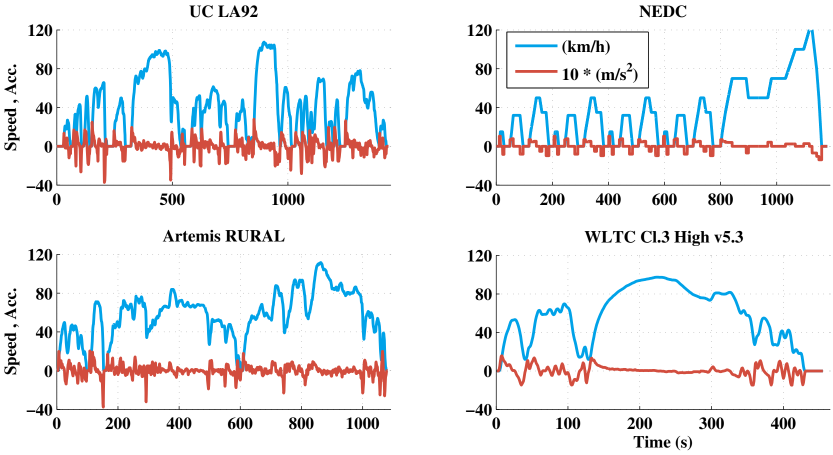

Figure 3.3 Acceleration and speed over time for Rural test cycles, [68], [64], [1] and [69].

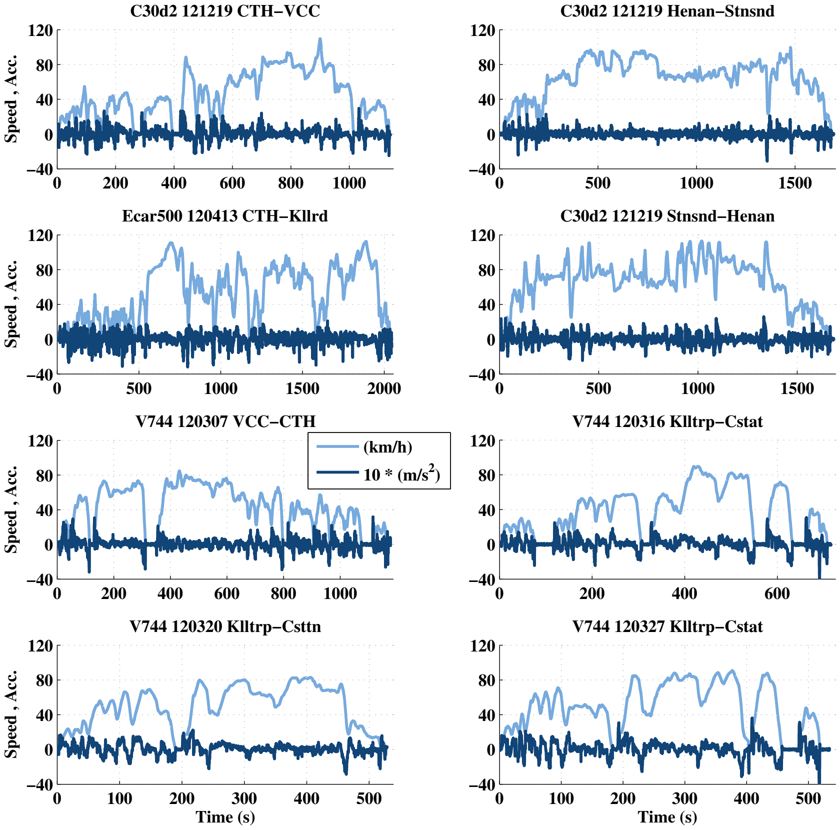

Figure 3.4 Acceleration and speed over time for Logged Rural cycles.

Table 3.3 Cycle data for Rural Test cycles, and Logged Rural cycles.

Rural Test Cycles	**Cycle duration (s)**	**Driven distance (m)**	**Max. speed (km/h)**	**Average speed (km/h)**	**Average running speed (km/h)**	**Std. speed (km/h)**	**Time share standing (%)**	**Time share <60 km/h (%)**	**Time share 60-90 km/h (%)**	**Time share > 90 km/h (%)**
UC LA92	1 435	15 706	108	39	47	32	19	56	14	11
EUDC	400	6 955	120	63	70	31	10	31	37	21
NEDC	1 180	11 013	120	34	44	31	26	55	13	7
Artemis RURAL	1 082	17 272	112	57	59	25	4	47	42	7
WLTC Cl.3 High v5.3	455	7 162	97	57	61	29	7	42	36	15
MEAN	**910**	**11 622**	**111**	**50**	**56**	**30**	**13**	**46**	**28**	**12**

Logged Rural Cycles	**Cycle duration (s)**	**Driven distance (m)**	**Max. speed (km/h)**	**Average speed (km/h)**	**Average running speed (km/h)**	**Std. speed (km/h)**	**Time share standing (%)**	**Time share <50 km/h (%)**	**Time share 50-90 km/h (%)**	**Time share > 90 km/h (%)**
C30d2 121219 CTH-VCC	1 141	14 349	110	45	49	26	8	60	29	3
C30d2 121219 Henan Stnsnd	1 696	30 541	100	65	66	22	2	26	60	12
C30d2 121219 VCC-CTH	1 340	13 726	84	37	41	25	10	64	26	0
Ecar500 120413 CTH-Kllrd	2 046	30 557	112	54	58	32	7	45	36	12
C30d2 121219 Stnsnd Henan	1 684	30 879	113	66	68	26	3	27	55	15
V744 120307 VCC-CTH	1 178	13 899	85	42	49	25	13	55	32	0
V744 120316 Klltrp-Csttn	716	7 574	90	38	47	27	19	59	22	0
V744 120320 Klltrp-Csttn	529	7 191	83	49	51	24	4	52	44	0
V744 120327 Klltrp-Cstat	534	7 164	91	48	55	28	12	51	37	0
MEAN	**1 207**	**17 320**	**96**	**49**	**54**	**26**	**9**	**49**	**38**	**5**

3.2.3 Highway

The time series of speed and acceleration for the Highway Test cycles can be seen in Figure 3.5, and for the Logged Highway cycles in Figure 3.6. Cycle data regarding time duration, driven distance and speed levels can be seen in Table 3.4, for both Logged and Test cycles.

Here it can be seen that the time share standing is only a few percent for both test and logged cycles, while the time shares at high speed are in general higher for the test cycles (58 %) compared to the logged (41 %). The max. speed levels are higher for the test cycles with one exception; the HWFET cycle. Consequently, also the average speed levels are higher for the test cycles, with the Artemis cycles at the highest levels. The highest average speed is logged for the V70 120515 cycle, followed by the C30d2 121219 Vcc-Stnsnd log.

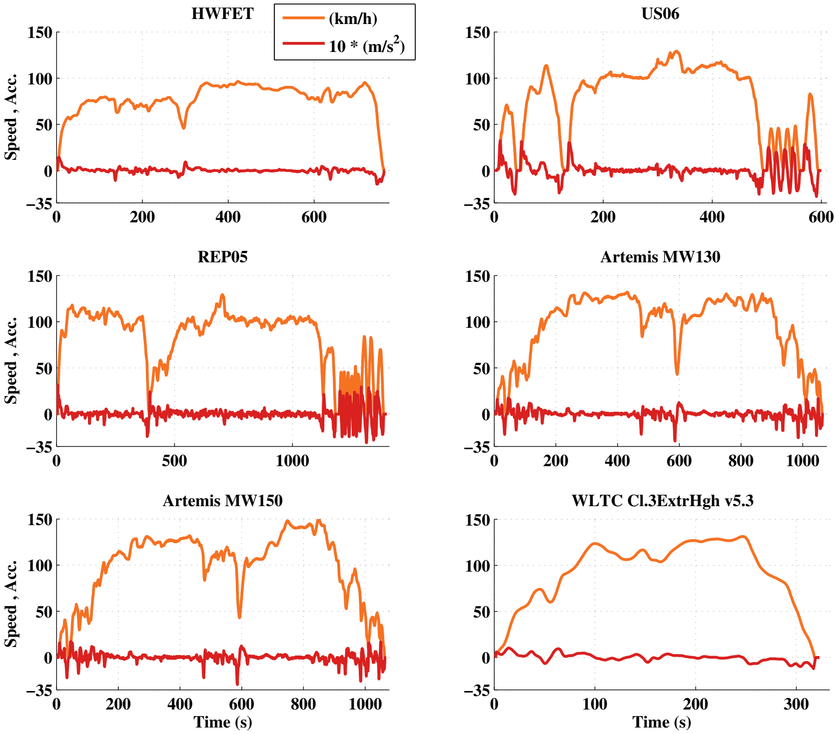

Figure 3.5 Acceleration and speed over time for Highway cycles, [68], [64] and [69].

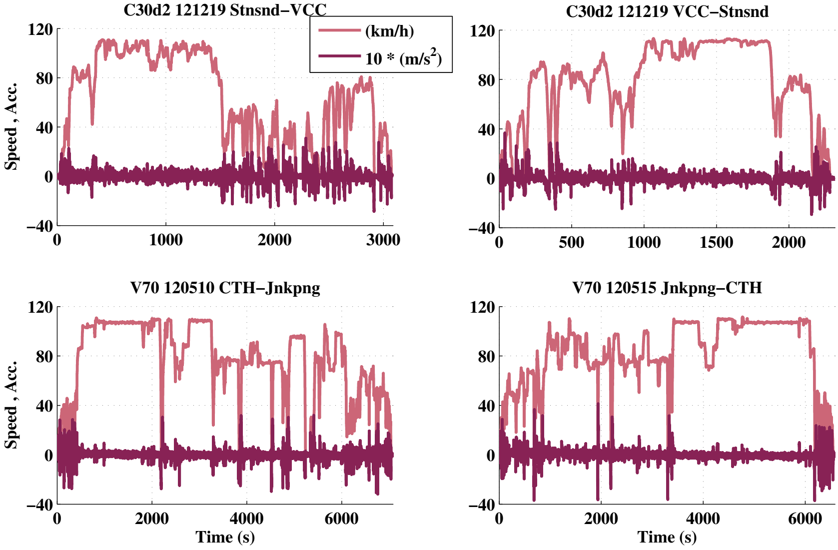

Figure 3.6 Acceleration and speed over time for Logged Highway cycles.

Table 3.4 Cycle data for Highway test cycles, and logged Highway cycles.

Highway Test Cycles	Cycle duration (s)	Driven distance (m)	Max. speed (km/h)	Average speed (km/h)	Average running speed (km/h)	Std. speed (km/h)	Time share standing (%)	Time share <60 km/h (%)	Time share 60-90 km/h (%)	Time share > 90 km/h (%)
HWFET	765	16 507	96	78	78	16	1	10	66	23
US06	600	12 888	129	77	83	40	9	20	15	56
REP05	1 400	32 253	129	83	86	32	4	19	13	65
Artemis MW130	1 068	28 736	132	97	98	35	2	18	10	70
Artemis MW150	1 068	29 545	150	100	101	38	2	18	10	70
WLTC Cl.3ExtrHgh v5.3	323	8 254	131	92	94	36	2	17	18	63
MEAN	**871**	**21 364**	**128**	**88**	**90**	**33**	**3**	**17**	**22**	**58**

Logged Highway Cycles	Cycle duration (s)	Driven distance (m)	Max. speed (km/h)	Average speed (km/h)	Average running speed (km/h)	Std. speed (km/h)	Time share standing (%)	Time share <60 km/h (%)	Time share 60-90 km/h (%)	Time share > 90 km/h (%)
C30d2 121219 Stnsnd-VCC	3 080	54 194	111	63	69	36	9	36	21	34
C30d2 121219 VCC-Stnsnd	2 309	50 426	113	79	81	32	3	21	32	44
V70 120510 CTH-Jnkpng	7 075	149 402	111	76	79	31	4	20	36	40
V70 120515 Jnkpng-CTH	6 576	149 413	112	82	83	27	2	16	36	46
MEAN	**4 760**	**100 859**	**112**	**75**	**78**	**32**	**5**	**23**	**31**	**41**

3.3 Acceleration distributions

Since the peak force and power on the wheels often is due to the vehicle's acceleration, it is vital to study what levels of acceleration that are to be expected to occur during normal driving in the different three road types.

In this section acceleration levels will be studied as a function of speed and time. Logged real-world cycles will be compared with official test cycles.

For official test cycles the speed time series is given, usually as one value per second. Acceleration has been calculated while considering one time step forward and one backward as

$$a(k) = \frac{dv}{dt} = \frac{v(k+1) - v(k-1)}{t(k+1) - t(k-1)}, \tag{3.2}$$

since it is proven to minimize the estimation error, compared to only considering one time step in the forward or backward direction (Euler forward or Euler backward).

3.3.1 Urban

Cycle data regarding acceleration levels can be seen in Table 3.5, for Urban Logged and Test cycles. It can be seen that the time share of positive and negative acceleration are similar for both the test and logged cycles, where they are shorter for the test cycles due to the longer time share standing. Regarding the time shares at certain acceleration levels, the mean values are very similar for the test and the logged cycles.

The main difference between test cycles and the logged cycles are the much larger maximum acceleration levels seen in the logs, both positive and negative. Amongst the test cycles, it is the NYCC and Artemis Urban that have the highest levels of peak acceleration, at $2.7\,m/s^2$ and $2.4\,m/s^2$ respectively, while many of the logs have maximum values over $3\,m/s^2$. Still the average positive and negative acceleration levels are similar for all cycles, while the standard deviations are slightly higher for the logs. Another interesting point is that ECE has the lowest maximum acceleration level between the test cycles, yet in the same time it has the highest average acceleration, both positive and negative.

Finally the mean RPA values are similar for the test and logged cycles. Many test cycles have RPA values around 0.17 to $0.20\,m/s^2$. However two cycles stand out; Artemis Urban and NYCC, with RPA values of 0.30 and 0.29 respectively. The spread in RPA values seem to be larger for the logged cycles. The largest values are seen for the V744 120312 (0.37) and XC60 $.0.32\,m/s^2$.

Table 3.5 Acceleration cycle data for Urban test and Logged cycles.

Urban Test Cycles	Max. pos. acc. (m/s^2)	Max. neg. acc (m/s^2)	Average pos. acc. (m/s^2)	Average neg. acc. (m/s^2)	Std. pos. acc. (m/s^2)	Std. neg. acc. (m/s^2)	RPA (m/s^2)	Time share pos. acc. (%)	Time share neg. acc. (%)	Time share $a<1\ m/s^2$ (%)	Time share $1<a<2\ m/s^2$ (%)	Time share $2<a<3\ m/s^2$ (%)	Time share $a>3\ m/s^2$ (%)
Artemis URBAN	2.4	-2.8	0.6	-0.7	0.5	0.6	0.30	38	35	92	8	0	0
ECE	1.0	-0.9	0.7	-0.7	0.2	0.2	0.14	19	19	98	2	0	0
NYCC	2.7	-2.3	0.6	-0.5	0.5	0.5	0.29	34	35	94	5	1	0
WLTC Cl.3 Low	1.5	-1.5	0.5	-0.4	0.4	0.3	0.20	35	40	96	4	0	0
FTP72 UDDS	1.5	-1.5	0.5	-0.5	0.4	0.5	0.17	41	37	94	6	0	0
FTP75	1.5	-1.5	0.5	-0.5	0.4	0.5	0.17	40	37	93	7	0	0
SC03	2.2	-2.7	0.5	-0.6	0.5	0.6	0.20	43	37	94	5	1	0
jc08	1.5	-1.1	0.4	-0.5	0.3	0.3	0.17	39	34	97	3	0	0
WLTC Cl.3Mdl v5.3	1.6	-1.5	0.4	-0.5	0.4	0.5	0.20	49	39	94	5	0	0
MEAN	**1.8**	**-1.7**	**0.5**	**-0.6**	**0.4**	**0.4**	**0.21**	**38**	**35**	**95**	**5**	**0**	**0**

Logged Urban Cycles	Max. pos. acc. (m/s^2)	Max. neg. acc (m/s^2)	Average pos. acc. (m/s^2)	Average neg. acc. (m/s^2)	Std. pos. acc. (m/s^2)	Std. neg. acc. (m/s^2)	RPA (m/s^2)	Time share pos. acc. (%)	Time share neg. acc. (%)	Time share $a<1\ m/s^2$ (%)	Time share $1<a<2\ m/s^2$ (%)	Time share $2<a<3\ m/s^2$ (%)	Time share $a>3\ m/s^2$ (%)
Ecar500 120413 Linneg-City-CTH	2.2	-5.2	0.5	-0.5	0.4	0.6	0.26	50	50	93	7	0	0
Leaf 130321 CTH-Erksbrg	3.0	-4.0	0.5	-0.5	0.6	0.6	0.24	50	50	92	7	1	0
Leaf 130322 Korsv-Guldh	2.5	-8.5	0.5	-0.6	0.4	0.7	0.21	45	55	94	6	0	0
Prius 120329 Mlndl-Mlnlcke	2.3	-3.2	0.4	-0.4	0.4	0.4	0.17	42	58	95	5	0	0
Prius 120329 Mlnlcke-Mlndl	3.4	-4.1	0.5	-0.5	0.6	0.6	0.22	49	51	91	8	1	0
Prius 120403 Mlnlcke-CTH	3.1	-2.7	0.4	-0.4	0.5	0.5	0.19	48	52	93	7	1	0
V60PHEV 130320 Krsvgn-GalvBron	4.3	-3.2	0.5	-0.5	0.6	0.5	0.27	47	53	93	5	1	0
V744 120312 Cstat-CTH	3.8	-3.2	0.6	-0.6	0.7	0.7	0.37	48	52	88	9	2	1
V744 120318 Klltrp-CTH	2.8	-3.1	0.4	-0.4	0.4	0.6	0.21	55	45	96	4	0	0
V744 120327 CTH-Klltrp	3.0	-2.7	0.4	-0.4	0.4	0.5	0.21	54	46	95	4	1	0
XC60 CTH-Krthsg	3.8	-4.8	0.5	-0.5	0.6	0.6	0.32	52	48	92	6	2	0
MEAN	**3.1**	**-4.1**	**0.5**	**-0.5**	**0.5**	**0.6**	**0.24**	**49**	**51**	**93**	**6**	**1**	**0**

The maximum acceleration as well as second based operating points, for the Test cycles can be seen in Figure 3.7 and for the Logged cycles in Figure 3.8. As can be seen, the largest acceleration levels are experienced at the lower speed levels.

For the test cycles, at speed levels up to around $40\,km/h$ Artemis Urban, NYCC and SC03 have the highest levels of positive and negative acceleration at $1.7 - 2.5\,m/s^2$ and -2.3 to $-2.8\,m/s^2$. At higher speeds it is SC03, FTP75 and WLTC Middle that have the highest positive acceleration levels, although strongly descending with increasing speed. At about $50\,km/h$ the peak acceleration levels are around $0.4 - 1.4\,m/s^2$, while at about $80\,km/h$ they are around $0.2 - 0.5\,m/s^2$.

As already noted from the cycle parameter data, the peak acceleration levels of the logged cycles are higher compared to the test cycles, also when considering the different speed levels. For the logged cycles, at about $50\,km/h$ the peak acceleration levels are around $1 - 2.5\,m/s^2$, while at about $80\,km/h$ the cycles have already reached their top speed.

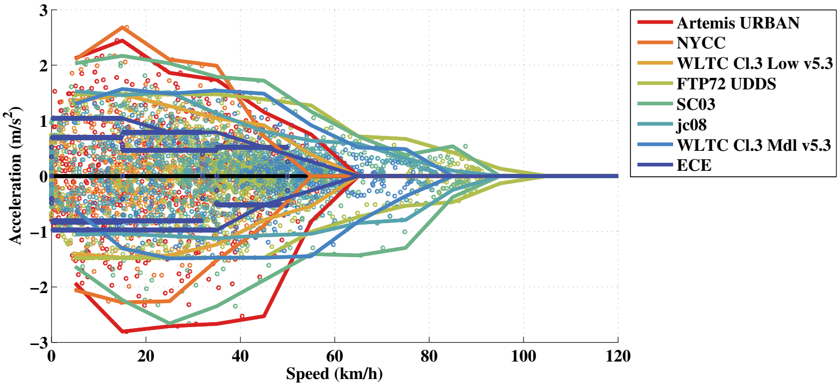

Figure 3.7 Maximum acceleration over speed along second with operation points per second, for Urban Test cycles.

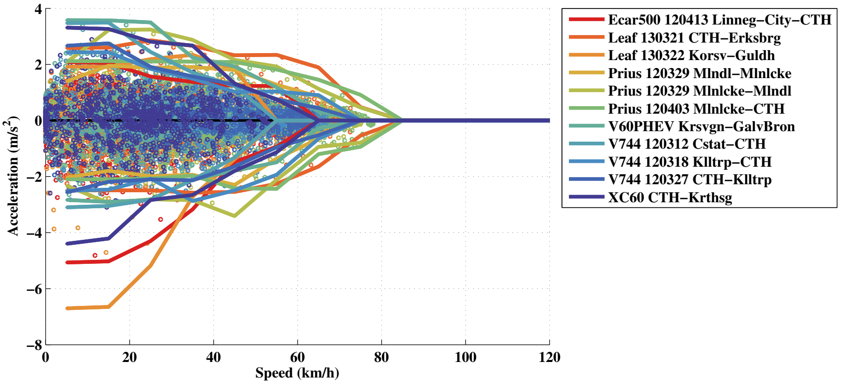

Figure 3.8 Maximum acceleration over speed along second with operation points per second, for Logged Urban cycles.

In order to compare the distribution of acceleration over the speed range, between Urban test cycles and Logged Urban cycles, the relative time spent in bins of $0.5\,m/s^2$ and $5\,km/h$ is depicted in Figure 3.9, along with the highest reached acceleration level at each speed. When creating the plots, to each speed and acceleration operating point a gaussian noise was added, which was later compensated for in the final result. The benefit is smoother contour lines, however a small error is also introduced, it can be regarded as negligible. Hence the contour lines outside of the maximum acceleration graph should be disregarded. The method is further illustrated in Appendix C.

As was also indicated by the standard deviations, the logged cycles spend a somewhat larger share at slightly larger acceleration levels, compared to the test cycles. This can be seen by comparing the acceleration levels for the same time share contour line.

The figures show that for the test cycles, most of the time is spent around zero speed at very low levels of accelerations (less than $1\,m/s^2$), due to frequent stops. For the logged cycles, most time is spent at speed levels around 5 to 10 km/h, but also within 1 m/s^2. Furthermore, the test cycles spend a somewhat larger time share at higher speed levels compared to the logged cycles.

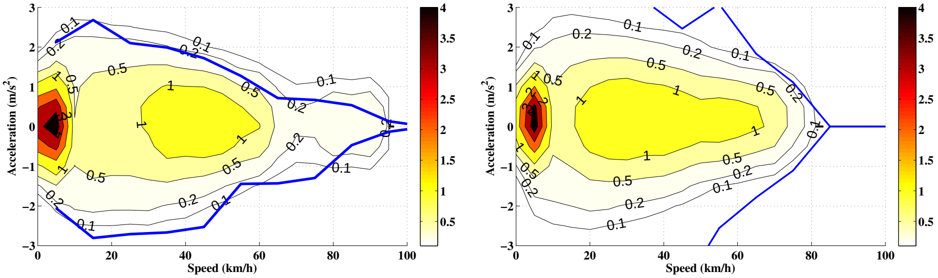

(a) Urban Test cycles.

(b) Logged Urban cycles.

Figure 3.9 Share of total time $(\%)$ of operation in acceleration bins of $0.5\ m/s^2$ and speed bins of $5\ km/h$, with added noise, for all Urban Test and Logged cycles.

3.3.2 Rural

Cycle data regarding acceleration levels can be seen in Table 3.6, for Rural Logged and Test cycles. Also for the Rural cycles, the logs show higher peak acceleration levels and standard deviations compared to the test cycles, while the average values are similar. The test cycles have a slightly larger time share below 1 m/s^2, while the logs have slightly a higher time share for acceleration levels between 1 to 2 m/s^2. Furthermore, high RPA values are more frequent amongst the logs.

For the test cycles it is the UC (LA92) cycle that has the highest peak acceleration both positive and negative, as well as the highest RPA value. On the contrary, EUDC and NEDC have the lowest peak acceleration levels and the lowest RPA value.

Amongst the logs, two cycles have similar peak acceleration levels; C30d2 121219 VCC-CTH and V744 120327 Klltrp-Cstat, however the later have a slightly higher average acceleration, and a much larger RPA value (0.34 compared to 0.19 m/s^2).

The maximum acceleration as well as second based operating points, for the Test cycles can be seen in Figure 3.10 and for the Logged cycles in Figure 3.11.

In Figure 3.10 it is clearly seen that the two cycles UC LA92 and Artemis Rural differs quite a bit from the others since the levels of acceleration are larger over the whole speed range, and even more so for negative accelerations. Also when comparing with the Urban test cycles, these two cycles stand out. For the logged cycles it can be seen in Figure 3.11 that the highest peak accelerations only occur at very low speed levels (below 20 km/h). Around 40 km/h most cycles have peak accelerations between 1.5 to 2.5 m/s^2, while for higher speed levels the difference between the cycles increase.

Table 3.6 Acceleration cycle data for Rural test and Logged cycles.

Rural Test Cycles	**Max. pos. acc. (m/s^2)**	**Max. neg. acc (m/s^2)**	**Average pos. acc. (m/s^2)**	**Average neg. acc. (m/s^2)**	**Std. pos. acc. (m/s^2)**	**Std. neg. acc. (m/s^2)**	**RPA (m/s^2)**	**Time share pos. acc. (%)**	**Time share neg. acc. (%)**	**Time share a<1 m/s^2 (%)**	**Time share 1<a<2 m/s^2 (%)**	**Time share 2<a<3 m/s^2 (%)**	**Time share a>3 m/s^2 (%)**
UC LA92	3.1	-3.9	0.7	-0.7	0.5	0.7	0.24	38	34	91	9	1	0
EUDC	0.8	-1.4	0.4	-0.9	0.2	0.3	0.09	26	11	100	0	0	0
NEDC	1.0	-1.4	0.6	-0.8	0.3	0.2	0.11	21	16	99	1	0	0
Artemis RURAL	2.4	-4.1	0.5	-0.5	0.4	0.6	0.18	41	40	96	3	0	0
WLTC Cl.3 High v5.3	1.7	-1.5	0.4	-0.4	0.4	0.4	0.14	47	41	96	4	0	0
MEAN	**1.8**	**-2.5**	**0.5**	**-0.7**	**0.3**	**0.4**	**0.15**	**35**	**28**	**96**	**4**	**0**	**0**

Logged Rural Cycles	**Max. pos. acc. (m/s^2)**	**Max. neg. acc (m/s^2)**	**Average pos. acc. (m/s^2)**	**Average neg. acc. (m/s^2)**	**Std. pos. acc. (m/s^2)**	**Std. neg. acc. (m/s^2)**	**RPA (m/s^2)**	**Time share pos. acc. (%)**	**Time share neg. acc. (%)**	**Time share a<1 m/s^2 (%)**	**Time share 1<a<2 m/s^2 (%)**	**Time share 2<a<3 m/s^2 (%)**	**Time share a>3 m/s^2 (%)**
C30d2 121219 CTH-VCC	2.9	-2.5	0.5	-0.5	0.5	0.5	0.24	53	47	93	6	1	0
C30d2 121219 Henan Stnsnd	2.3	-3.1	0.3	-0.3	0.3	0.3	0.13	48	52	97	3	0	0
C30d2 121219 VCC-CTH	3.6	-2.8	0.5	-0.4	0.5	0.4	0.19	44	56	93	6	1	0
Ecar500 120413 CTH-Kllrd	2.1	-3.2	0.5	-0.5	0.4	0.5	0.23	56	44	93	7	0	0
C30d2 121219 Stnsnd Henan	2.6	-2.4	0.5	-0.4	0.5	0.4	0.24	48	52	93	7	0	0
V744 120307 VCC-CTH	3.2	-3.2	0.4	-0.4	0.4	0.5	0.20	53	47	95	5	1	0
V744 120316 Klltrp-Csttn	3.1	-4.2	0.5	-0.5	0.5	0.6	0.25	54	46	93	7	1	0
V744 120320 Klltrp-Csttn	2.2	-2.9	0.5	-0.5	0.4	0.5	0.25	57	43	93	7	0	0
V744 120327 Klltrp-Cstat	3.6	-4.3	0.6	-0.6	0.6	0.7	0.34	56	44	87	12	1	0
MEAN	**2.8**	**-3.2**	**0.5**	**-0.5**	**0.5**	**0.5**	**0.23**	**52**	**48**	**93**	**7**	**1**	**0**

At about $50\,km/h$ the peak acceleration levels are around $1 - 2.5\,m/s^2$ for the logs and 0.5 to $1.5\,m/s^2$ for the test cycles, while at about $80\,km/h$ they are $0.5 - 2\,m/s^2$ for the logs and 0.3 to $1\,m/s^2$ for the test cycles.

As for the Urban cycles, the relative time spent in acceleration bins of $0.5\,m/s^2$ and $5\,km/h$ is depicted in Figure 3.12, along with the highest reached acceleration level at each speed.

Also for the Rural cycles, the logged cycles spend slightly more time at somewhat higher acceleration levels over the whole speed range. I can also be seen that apart from the time spent at stand still and very low speed, also much of the time is spent around $40\,km/h$ for both test and logged cycles, $55\,km/h$ for the test cycles, and finally around $70\,km/h$ for both test and logged cycles.

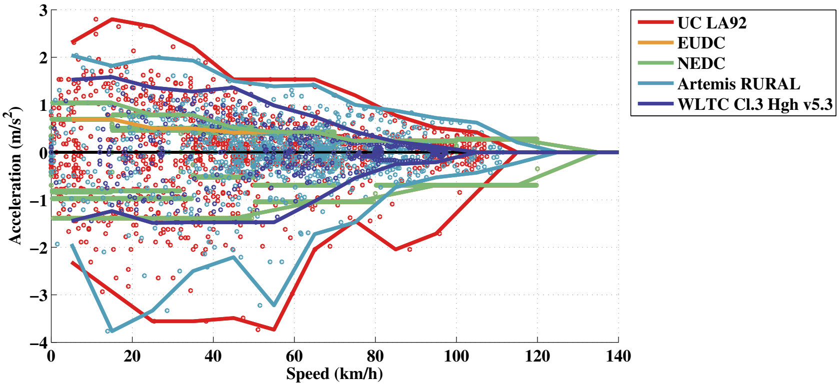

Figure 3.10 Maximum acceleration over speed along second with operation points per second, for Rural Test cycles.

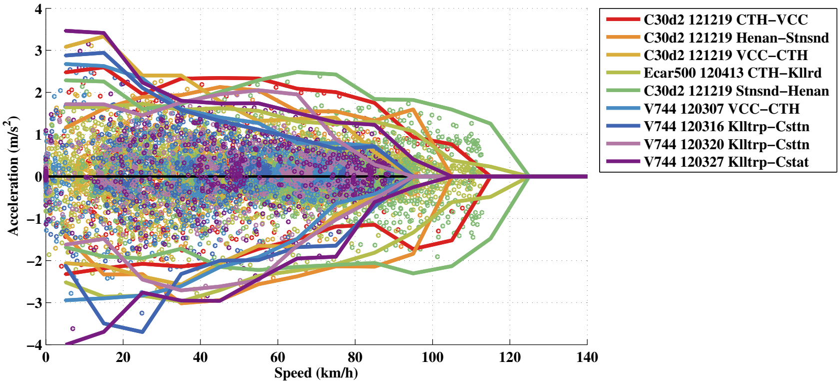

Figure 3.11 Maximum acceleration over speed along second with operation points per second, for Logged Rural cycles.

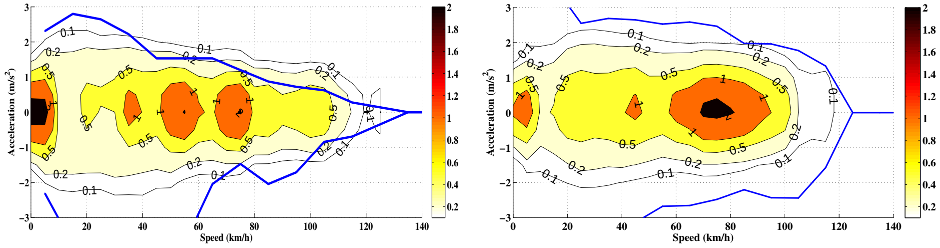

(a) Rural Test cycles.

(b) Logged Rural cycles.

Figure 3.12 Share of total time $(\%)$ of operation in acceleration bins of $0.5\ m/s^2$ and speed bins of $5\ km/h$, with added noise, for all Rural Test and Logged cycles.

3.3.3 Highway driving

Cycle data regarding acceleration levels can be seen in Table 3.7, for Highway Logged and Test cycles. As for the Urban and Rural cycles, the peak accelerations of the logged Highway cycles are higher compared to the test cycles, while the average, standard deviations and the time shares at different acceleration levels are similar. In this case the test cycles have higher RPA values.

Amongst the test cycles, the US06 and REP05 have the highest peak acceleration levels, however the average and standard deviation of acceleration as well as the RPA value is higher for US06.

The acceleration parameters of the logged cycles are rather similar to one another.

Table 3.7 Acceleration cycle data for Highway test and Logged cycles.

Highway Test Cycles	**Max. pos. acc. (m/s^2)**	**Max. neg. acc (m/s^2)**	**Average pos. acc. (m/s^2)**	**Average neg. acc. (m/s^2)**	**Std. pos. acc. (m/s^2)**	**Std. neg. acc. (m/s^2)**	**RPA (m/s^2)**	**Time share pos. acc. (%)**	**Time share neg. acc. (%)**	**Time share a<1 m/s^2 (%)**	**Time share 1<a<2 m/s^2 (%)**	**Time share 2<a<3 m/s^2 (%)**	**Time share a>3 m/s^2 (%)**
HWFET	1.4	-1.5	0.2	-0.2	0.2	0.3	0.07	47	42	99	1	0	0
US06	3.2	-2.8	0.7	-0.7	0.8	0.7	0.19	45	44	90	5	5	1
REP05	3.2	-3.1	0.4	-0.5	0.6	0.6	0.14	52	45	94	4	2	0
Artemis MW130	1.7	-2.9	0.3	-0.4	0.3	0.5	0.12	48	37	97	3	0	0
Artemis MW150	1.7	-2.9	0.3	-0.4	0.3	0.5	0.12	47	37	97	3	0	0
WLTC Cl.3ExtrHgh v5.3	1.0	-1.2	0.3	-0.3	0.2	0.3	0.12	51	46	99	1	0	0
MEAN	**2.1**	**-2.4**	**0.4**	**-0.4**	**0.4**	**0.5**	**0.13**	**48**	**42**	**96**	**3**	**1**	**0**

Logged Highway Cycles	**Max. pos. acc. (m/s^2)**	**Max. neg. acc (m/s^2)**	**Average pos. acc. (m/s^2)**	**Average neg. acc. (m/s^2)**	**Std. pos. acc. (m/s^2)**	**Std. neg. acc. (m/s^2)**	**RPA (m/s^2)**	**Time share pos. acc. (%)**	**Time share neg. acc. (%)**	**Time share a<1 m/s^2 (%)**	**Time share 1<a<2 m/s^2 (%)**	**Time share 2<a<3 m/s^2 (%)**	**Time share a>3 m/s^2 (%)**
C30d2 121219 Stnsnd-VCC	3.1	-2.9	0.4	-0.3	0.4	0.4	0.14	48	52	96	4	0	0
C30d2 121219 VCC-Stnsnd	3.7	-2.9	0.3	-0.3	0.4	0.4	0.13	49	51	96	3	1	0
V70 120510 CTH-Jnkpng	3.2	-3.2	0.2	-0.2	0.3	0.4	0.09	51	49	98	2	0	0
V70 120515 Jnkpng-CTH	4.1	-3.7	0.3	-0.2	0.4	0.3	0.09	46	54	98	2	0	0
MEAN	**3.5**	**-3.2**	**0.3**	**-0.3**	**0.4**	**0.4**	**0.11**	**49**	**52**	**97**	**3**	**0**	**0**

The maximum acceleration as well as second based operating points, for the Test cycles can be seen in Figure 3.13 and for the Logged cycles in Figure 3.14.

As could be noted in the cycle parameters, the US06 and REP05 cycles have higher levels of acceleration over the speed interval than the other test cycles, with many operating points above $2\,m/s^2$ up to a speed level of $60\,km/h$. Next to US06 and REP05, the Artemis Motorway cycles have the highest acceleration levels over the speed range, and a particulary strong braking acceleration at high speed (about 2 to $3\,m/s^2$).

As can be seen in Figure 3.14, the peak acceleration over the speed range of the logged Highway cycles are close to one another, but also fairly close to those of the US06 and REP05.

The relative time spent in bins of $0.5\,m/s^2$ and $5\,km/h$ is depicted in Figure 3.15, along with the highest reached acceleration level at each speed.

When comparing the distribution of logged cycles with the test cycles, the differences in time spent at various acceleration levels over the speed range is rather small. The main difference that can be seen is the relatively larger time spent at higher speed levels in the test cycles compared to the logged cycles. It can be seen that in the test cycles most time is spent at speed levels close to 80 to $130\,km/h$ ($110\,km/h$ in particular), while for the logged cycles most time is spent at $50\,km/h$ and between 70 to $120\,km/h$.

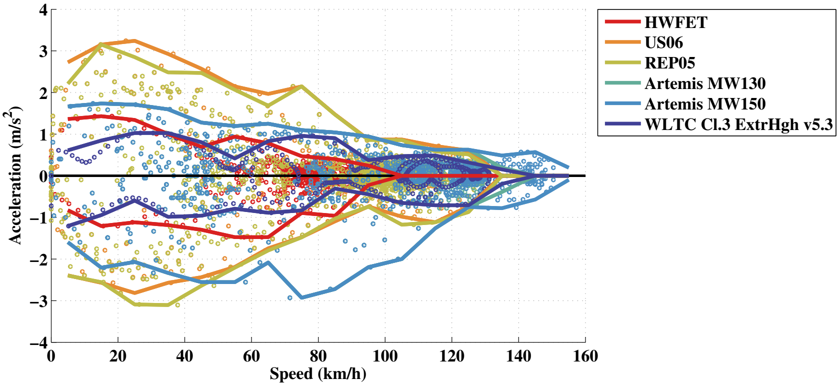

Figure 3.13 Maximum acceleration over speed along second with operation points per second, for Highway Test cycles.

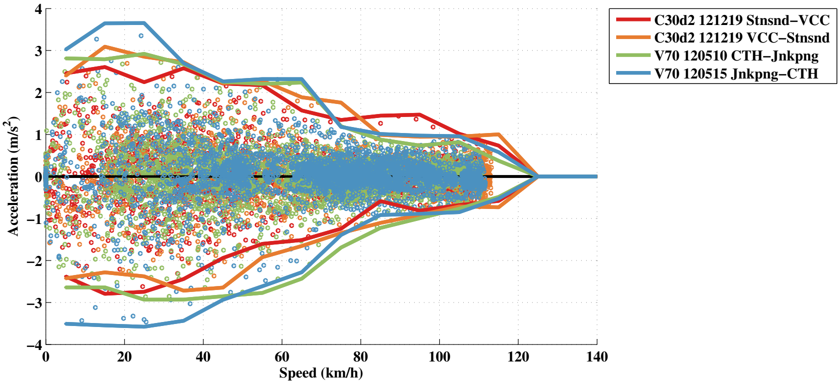

Figure 3.14 Maximum acceleration over speed along second with operation points per second, for Logged Highway cycles.

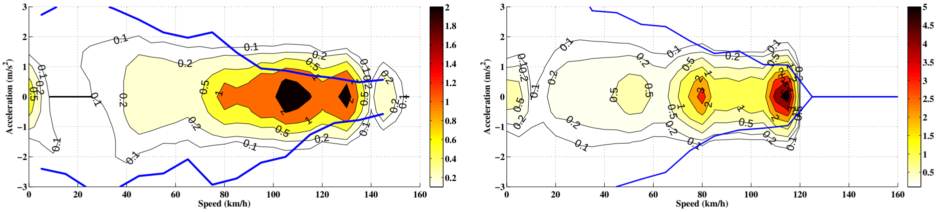

(a) Highway Test cycles.

(b) Logged Highway cycles.

Figure 3.15 Share of total time $(\%)$ of operation in acceleration bins of $0.5\ m/s^2$ and speed bins of $5\ km/h$, with added noise, for all Highway Test and Logged cycles.

3.4 Acceleration duration

The time duration of all accelerations and decelerations are calculated for both the Test and Logged cycles. The resulting cumulative frequency distribution is presented in Figure 3.16. In general, the duration of accelerations are longer than the duration of decelerations. Typically, 80% of all accelerations are 12s-13s or shorter for the Test cycles, and around 9s or shorter for the Logged cycles. Furthermore, 50% of all Test cycle accelerations are 5s-6s or shorter, and for the Logged cycles they are around 4s or shorter.

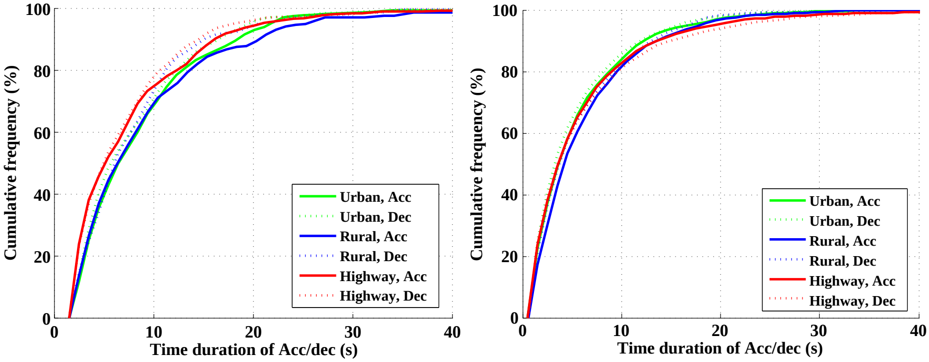

(a) Test Cycles.

(b) Logged typical cycles.

Figure 3.16 Cumulative frequency distribution of the time duration of each acceleration and deceleration, counted between zero-crossings, for the Test and Logged cycles.

3.5 Road grade levels

As with speed and acceleration, common levels of road grade are of great interest when seeking typical vehicle load levels.

The Swedish office of traffic (Trafikverket) has specified recommended maximum road grade levels for new roads to 6 %, and for improved roads to 8 %, in their guidelines for how roads are to be designed [70].

Similarly, according to [71] the National System of Interstate and Defence Highways in the US are designed after guidelines that state a recommended maximum grade level depending on the road's speed limit. For speeds up to 90 km/h, maximum grade levels of 5 % are recommended, while it is 6 % for mountainous areas. At higher speed levels the recommended max grade is 4 %. According to [25] p. 13, grade levels on US primary and secondary roads may reach 10 to 12%.

Trafikverket also provide a searchable database called PMSV3 [72], that contains measured road data covering different roads in Sweden, which are gathered from several occasions over the last decades via a special measurement van. Amongst other data, road grade, road speed limit and speed of measurement vehicle have been recorded. It is possible to make combined searches in the data base on one or more parameters. A search on speed limit of at least 110 km/h and grades of at least 6% but maximum 12%, results in three hits, i.e. three different highways in Sweden has sections of grade 6% or larger. One is on E6 Bohuslän between Munkedal and Tanum, one in Dalarna between Borlänge and Falun, and one in Skåne south of Skottorp across Hallandsåsen with grades of $6-7\%$ over a distance of $1.8\ km$. Another steep slope with a grade of about 7 %, is west of Jönköping on road 40 along a section of about 1 km at a speed limit of 90 km/h. Further searches leads to about a 170 hits on sections with speed limits of $100\,km/h$ and grades of at least 6% but maximum 12%, and $1\,330$ hits on sections with speed limits of $90\,km/h$ and grades of at least $6\,\%$ but maximum $12\,\%$, for $70\,km/h$ the number of hits is $31\,638$, and for $50\,km/h$ it is 5905. These numbers are however not to be blindly trusted, since some of the later measurements are not coherent with the previous ones and thus indicates much larger grades than previously.

At low speed levels, e.g. in cities or on drive ways the road grade can be even larger, perhaps up to and above $30\,\%$ as indicated by [73] for several streets is San Francisco in the US.

3.5.1 Measured road grades

Road grade levels have also been estimated from the logged data, see histogram representation in Figure 3.17. A fair accuracy of the estimation proved to be rather difficult with the used measurement system at hand, especially at low speed levels. Nevertheless, the resulting data corresponds rather well to expected values with respect to the information in the previous section.

Analysis showed only a small dependence on speed, i.e. that higher grade levels are relatively less common for the Highway cycles.

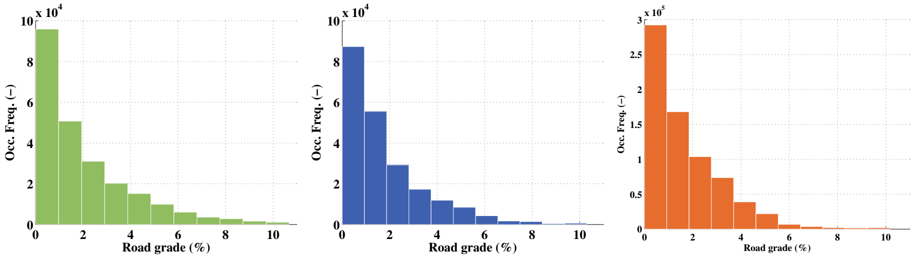

(a) Urban.

(b) Rural.

(c) Highway.

Figure 3.17 Road grade histogram of all Logged Urban, Rural and Highway cycles.

Figure 3.18 presents the difference in altitude between the end and start of the Logged cycles, as well as the difference between maximum and minimum reached altitudes. For a cycle with a large positive difference between the end and the start altitude, a significant part of the energy that is consumed during driving is due to the increases in potential energy. For those cycles that adhere to the same driving route and are driven in opposite directions, it can be seen that the difference between end and start altitude is similar but with opposite signs. Thus, the total energy consumption may be different for the two cycles.

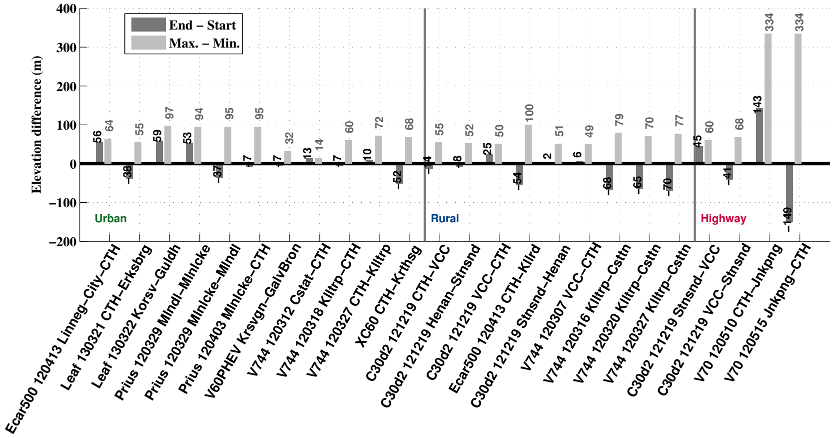

Figure 3.18 The net altitude difference between the cycle end and start points, as well as the difference between maximum and minimum altitude that is experienced during the Logged cycles.

The time duration of all uphill and downhill cycle segments are calculated for the Logged cycles. The resulting cumulative frequency distribution is presented in Figure 3.19. It can be noted that the time duration is generally longer for the Highway cycles. For 80% of the uphill occasions in the Urban and Rural cycles, the time duration is around 25s or shorter, and it is 38s or shorter for the Highway cycles. Furthermore, for 50% of the uphill cycle segments, the time duration is 10s-14s or shorter. To conclude, the time duration of grade climbing is generally more than twice the time duration of acceleration.

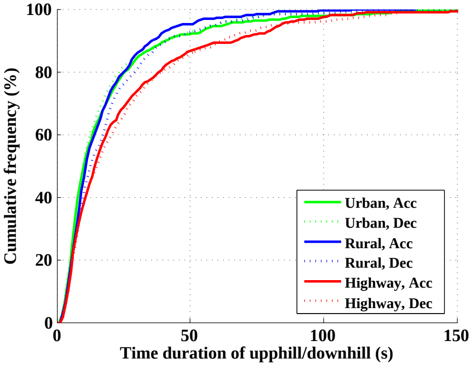

Figure 3.19 Cumulative frequency distribution of the time duration of each uphill and downhill, counted between zero-crossings, for the Test and Logged cycles.

3.6 Average daily driving/traveling distance

In order to find suitable driving ranges for electric cars it is essential to gain knowledge of how far drivers usually travel. By assuming that the only definite time to charge is over night, one can consider information regarding traveled distances per day.

Many countries around the world try through surveys, to map typical mobility habits of people traveling by different commodities. In these surveys respondents are asked to keep a traveling or driving journal usually for a single specified day, thus regarded to be typical, or in the case of some studies for a number of consecutive days. The main drawbacks with these kinds of studies (when it comes to estimating necessary EV driving range) are that the results are strictly related to mobility of persons, who may use different vehicles during the same day, but also that the quality of the results highly depend on the estimates done by the respondents as stated in [58]. More preferably, single vehicles are tracked and studied during a much longer period, e.g. The Swedish Car Movement Data Project or an American study in the Atlanta region [74].

The type of information gained may be average daily commuting distances, average daily driving over a whole population studied. It may also be a cumulative distribution of share of daily distances that at least has been covered.

According to National Household Travel Survey in the US(NHTS) [75], the average commuting distance by private vehicles in US was 19.5 km, and the average driven distance per driver in 2001 and 2009 respectively were 55 and 49 km on a weekday and 46 and 40 km on a Saturday or Sunday.

According to the latest major National Travel Survey in Sweden, the average driven distance per day with private car in 2005/2006 range between 20 to 36 km depending on region, with a national average of 30 km [76]. However according to another report from the same period (Körsträckor 2006) which is based on data from vehicle trip meter (checked during yearly car check up at Bilprovningen), the average total driven distance per vehicle during 2006 was 14 390 km, which gives an average daily driving distance of about 39 km [77].

A survey in Europe finds that the average driven distance in six European countries (France, Germany, Italy, Poland, Spain and UK) vary between 40 km (UK) to 80 km (Poland) per day, and shows no important difference between the days in a week [78].

Various sources have been found that present the needed type of data, [79], [80], [81], [82], [83], [84], [85] and [74]. However the results differ between countries, and studies, and even between the same studies depending on how the answers are chosen to be analyzed, which makes general conclusions difficult to make, see Figure 3.20. For more details on the different studies, see the related references mentioned here.

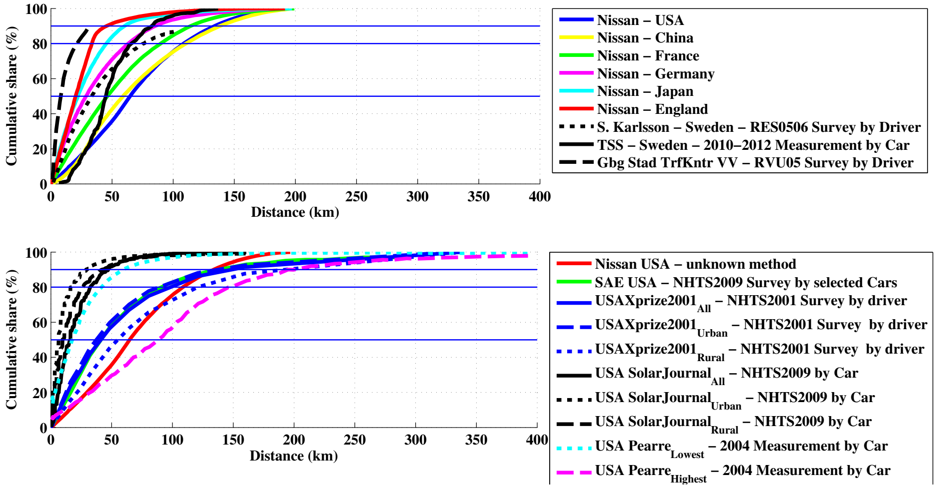

Figure 3.20 Daily driving distances in various countries, for either drivers or cars, extracted by different methods.

According to [79], $90\,\%$ of the people in European countries drive less than about $120\,km$ per day on an average, while $90\,\%$ of the people in USA drive less than $135\,km$ per day. It is also seen that Japan seem to have similar driving patterns as EU and that China seem to have similar driving patterns as US.

As can be seen the information regarding Sweden differs a bit between the different sources, perhaps this is due to different methods used, see [80], [81] and [82]. Based on results from The Swedish Car Movement Data Project which cover cars in the south west of Sweden, $90\,\%$ of the cars travel less than about $70\,km$ per day on average.

In the US the spread between different published data is relatively large. As a summery of all presented graphs, $50\,\%$ of the average daily driving distances are shorter than 6 to $89\,km$, and $80\,\%$ of them are shorter than $16\,km$ to $148\,km$. One study indicate that larger distances are covered during rural driving compared to urban driving, [85].

Chapter 4

Performance Requirements and Wheel Load Analysis of Studied Concept Vehicles

Vehicle performance can be summarized in single quantitative measures such as: top speed, minimum time to accelerate from $0 - 100\,km/h$, and specifically for BEVs, driving range. The work in this chapter and the next is concentrated to three concept light duty BEVs, i.e. passenger cars, each with their own targeted qualitative specification which can be seen in Table 4.1. Apart from the qualitative targets, all vehicles should be able to manage highway driving in most countries around the world.

In this section the stated qualitative targets will be further specified into quantitative performance requirements for each of the concept cars, with collected data on over 30 existing light duty BEV models as a frame of reference.

Table 4.1 Qualitative design targets for the three concept BEVs.

	Seats	**Size**	**Speed and acceleration**	**Range**
City	4-5	Small	Medium	Medium
Highway	5	Medium	High	Long
Sport	2	Small	Very high	Very long

4.1 Performance requirements based on data of existing BEVs

The performance requirements of the three concept vehicles are mainly based on data found on currently top selling BEV models. Car data that is relevant for this chapter is: curb weight, height and width in order to estimate effective vehicle area, drag coefficient C_d, top speed, time to accelerate, certified driving range as well as energy consumption per driven distance.

Data on top selling light duty BEV models (including concepts) has been gathered mainly from vehicle manufacturers. The full list of vehicle models along with the collected data and their associated references is presented in Appendix A.

For some of the data there exists a level of uncertainty on the correctness and reliability, since it is not specified in a standardized way, and many sources do not declare under which conditions the data is valid.

For example, mass for vehicles are often given as *curb weight*, which is usually defined as the mass of the specific model with standard equipment and neither passengers nor extra cargo. However, in manufacturer's mass specifications it is not always evident what is included in the presented value. Moreover, the cross sectional area is very seldom stated, thus it has to be estimated, e.g. by a method such as the ones suggested in Chapter 2, i.e. as a weighted product of vehicle height and width.

Lastly, the vehicle driving range given is usually specified as the certified range gained by driving according to either American EPA cycles or the European NEDC cycle, however in some sources this is not declared. The same issue is also valid for energy consumption per distance.

For further ease of benchmarking, the existing vehicle models are sorted into the four categories: small, medium-large, high performing and sport, where the former two are based on vehicle external volume calculation while assuming a rectangular block. The sport category consists of high acceleration capable 2-seat models. The high performing category also consists of high acceleration capable models, but with five seats.

4.1.1 Speed and acceleration performance

All three concept vehicles should be able to handle highway driving in most countries, which is typically between $110 - 130\,km/h$, as stated in [86]. Only a few countries have speed limits above this, where the highest limit is $150\,km/h$.

Data on top speed is available for all of the studied BEV models, and it shows a rather wide variety. However the majority of the small-large models have top speeds around 120-160 km/h. The top speed of the small cars ranges from $120 - 145\,km/h$, while it is $122 - 161\,km/h$ for the medium-large cars, and $190 - 249\,km/h$ the high performing models. The top speed of the sport models varies between $170 - 305\,km/h$.

Based on this, the top speed of the **City car** is settled to $135\,km/h$ on a flat road in order to manage highway driving in most countries with a small margin included. This speed is somewhat higher compared to the lowest speed models, yet it is not as high as for the fastest small cars. The top speed of the **Highway car** is set to $150\,km/h$ to handle highway driving in all countries. This speed level matches the fastest small size BEVs. The top speed of the **Sport car** is chosen to be $210\,km/h$ on a flat road, which matches two of the existing sport cars, but not the fastest ones.

Acceleration performance is usually stated as the minimum time to accelerate from $0 - 100\,km/h$ or $0 - 60\,mph$ (which corresponds to $0 - 96.5\,km/h$), i.e. while using the maximum torque from the powertrain. This type of data is available for almost all of the studied BEVs.

The top speed and acceleration time of the three concept vehicles along with specified data of the existing BEVs can be seen in Figure 4.1.

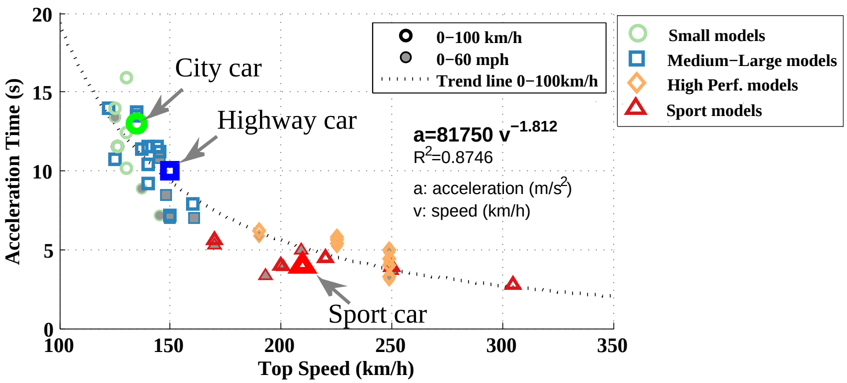

Figure 4.1 Top speed vs. acceleration for the three concept BEVs and for the existing BEVs. Additionally, a suggested trend line is provided, which represent 0-100km/h acceleration data.

It can be noted that those models with the highest top speed levels, are also those with the shortest time to accelerate. For the sport and the high performing models the time is around 3s-6s. For the small cars, the spread in acceleration time is relatively large: around 7s-16s, and for the medium-large cars it is 7s-14s.

For the three concept vehicles, only the time to accelerate from $0 - 100\,km/h$ is specified. For the **City car**, the time is decided to be maximum $13\,s$, which corresponds to a medium performance small car. For the **Highway car**, it is decided to be $10\,s$, which is also somewhat of a medium value for the category. Finally the chosen $0 - 100 km/h$ acceleration time for the **Sport car** is set to $4\,s$, in order to match the sport cars with the highest performance.

4.1.2 Gradability

A vehicle's *gradability* is the maximum grade that a vehicle can climb at a certain speed while using the maximum power from the powertrain. Data on gradability for the concept vehicles is not based on typical values from existing BEVs, since this type of data is rare.

There are however a few sources that present general gradability design goals. In [87] for example, the requirements are that the cars should be able to start in a $25\,\%$ uphill grade, drive at a speed of $88.5\,km/h$ in a $3\,\%$ grade, and in $72.4\,km/h$ in a $6\,\%$ grade.

When considering typical grade levels on highways there are relatively few passages with grade levels larger than $6\,\%$, unless perhaps considering mountainous areas. There are even fewer sections with grade levels of $12\,\%$ or higher.

Based on the above, as well as the quantitative requirements in Table 4.1, it is decided that the **Highway car** should be able to sustain a speed of $130\,km/h$ at a grade 6%, and that the **Sport car** is to be able to sustain a highway speed of $130\ km/h$ even in steep grades of $12\,\%$. The **City car**, on the other hand, should have a maximum speed of at least $90\,km/h$ at the grade of $6\,\%$. Furthermore it is decided that, in coherence with the minimum goals stated in [87], all three concept vehicles should be able to **start** in a uphill gradient of at least $25\,\%$.

4.1.3 Driving range and curb weight

The NEDC driving range for the small cars is between $85 - 160\,km$, and for the medium-large cars it is $162 - 250\,km$. For the high performing models it is $390 - 528\,km$, and for the sport cars it is $200 - 600\,km$, or up to $450\,km$ when excluding the Rimac Concept One.

It is decided that the concept **City car** is to have a NEDC range of about $160\,km$, which is as long as for the two top models in the category. As seen in Figure 3.20, this distance covers over $90\,\%$ of the average daily driven distances in many countries in the world, although real world driving will most likely lead to a different driving range. For the **Highway car** the NEDC range should be around $200\,km$, in order to match the models with the longest range, still not as long as for the Model S models. The NEDC range of the **Sport car** is to be $300\,km$, which is longer than for two of the sport models, but much shorter than than the one with the longest range.

Data on curb weight is available for all BEV models. In general the small cars have the lowest masses: around $900 - 1355\,kg$, and the medium-large cars' weights are $1195 - 1725\,kg$ (when excluding BYD e6 which has a weight of $2380\,kg$). The high performing models weigh around $2100\,kg$, and the sport models between $1200 - 2110\,kg$.

Based on the reference data, it is decided that the curb weight of the concept **City car** is to be $1200\,kg$, which is in the higher range for the small car category. The weight of the **Highway car** is set to $1700\,kg$, which also reflects a value in the higher range for the medium-large cars. Finally the concept **Sport car** is to have a curb weight of $1900\,kg$, i.e. a rough mean value.

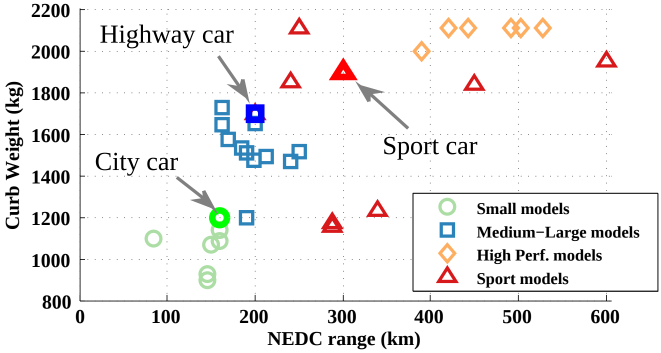

Figure 4.2 NEDC driving range vs. curb weight for the three concept BEVs as well as for the existing BEVs.

4.1.4 Area, C_d and C_r

Data on vehicle front area was found for nine of the existing vehicles. Based on the information in Table A.7, the area for the rest of the vehicles is estimated as $86\,\%$ of the product of height and width. For simplicity it is here assumed that the same weighting factor can be used for all cars.

The areas of the concept vehicles are mainly determined based on the estimated areas of the existing BEVs, as presented in Figure A.2. The area of the **City car** is chosen to be $2.05\,m^2$, which resembles a small car, the **Highway car** area is chosen to be $2.3\,m^2$ which takes after the large cars, while the **Sport car** area is chosen to be $2.0\,m^2$.

With the published C_d values of existing BEV's as a reference the C_d value of the **City car** is chosen to be 0.3, for the **Highway car** 0.28, and finally the C_d value of the **Sport car** is chosen to resemble that of the Roadster, 0.35.

Data on tire radius of existing BEVs is not available, instead it has been estimated based on tire size, see Figure A.3. Based on this, the tire radius of concept models are chosen accordingly: the **City car** $0.31\,m$, the **Highway car** $0.32\,m$, and the **Sport car** $0.34\,m$.

inally, the tire rolling resistance coefficient C_r should be set for all of the concept vehicles. Even though the rolling resistance is known to be speed dependent, there is no clear consensus on how this should be modeled (as shown in Figure 2.2) unless perhaps tire specific data is available, which it is not in this case. Another aspect is that the type of study in this thesis is of comparative nature, hence a possible speed dependence of the rolling resistance is expected to have a rather small impact on the final result. With these aspects as a background as well as the information presented on the topic in Chapter 2 and Appendix A, it is assumed that the rolling resistance of the concept BEVs can be estimated by the mean values: 0.009 for both the **City car** and the **Highway car** representing low rolling resistance tires, while for the **Sport car** the tires are expected to be optimized for performance rather than energy efficiency, leading to a value of 0.012.

4.1.5 Summary of requirements on chosen vehicle concepts

A summary of the stated requirements of the three concept cars presented in Table 4.2.

Table 4.2 Performance requirements of the three concept cars.

	City	**HW**	**Sport**	
Seats	4-5	5	2	kg
Mass	1200	1700	1900	kg
Acceleration 0-100 km/h	13	10	4	s
Top speed	135	150	210	km/h
NEDC Range	160	200	300	km
Aearod. drag coeff. C_d	0.3	0.28	0.35	$-$
Area	2.05	2.3	2.0	m^2
Wheel radius	0.31	0.32	0.34	m
Rolling resist. coeff. C_r	0.009	0.009	0.012	$-$
Starting gradability	25 %	25 %	25 %	$\%$
Gradability (Speed at grade)	90 at 6%	130 at 6%	130 at 12%	km/h, $\%$

4.2 Wheel load analysis of chosen concepts

In the wheel load analysis of the concept vehicles the levels of force, speed and power at the wheels, are estimated based on the above stated quantitative vehicle requirements.

With help of the information in Chapter 2 regarding vehicle dynamics, the forces due to aerodynamic drag (2.2), rolling resistance (2.3), road grade (2.4) as well as acceleration (2.1) are calculated for all of the concept vehicles, assuming a gravitational constant, $g = 9.81\,m/s^2$ and an air density of $\rho = 1.2\,kg/m^3$. At this point no regard is taken to time duration of any of the operating points, only to the level of magnitude. The analysis is also based on finding information that is of interest for a BEV with a single speed gearbox.

4.2.1 Road load and grade

The road load wheel forces (aerodynamic drag and rolling resistance) for each of the concept BEVs have been estimated at speed levels within their specified speed ranges, as can be seen in the left part of Figure 4.3. Due to the aerodynamic drag, the wheel force shows a strong dependence on speed. The Sport car demands the largest wheel force at a certain speed level compared to the other cars, and the City car demands the lowest. The contour lines represent wheel power for a certain combination of speed and force.

As an illustrative example: if the City car is driving at its top speed, $135\,km/h$ on a level road, this demands a wheel power of about $23\,kW$, while driving at $100\,km/h$ demands roughly half of that. Furthermore, if the City car is driving at $100\,km/h$ i.e. with a wheel power load of about $13\,kW$, while the powertrain is able to deliver up to $23\,kW$, this means that there is a potential excess wheel power of about $10\,kW$ relative to the road load demand. This excess power equals a wheel force of about $400\,N$, which could give an acceleration of about $0.3\,m/s^2$ ($\frac{400\,N}{1200\,kg}$).

In the right part of Figure 4.3, the road load force is normalized to vehicle mass. Then it can be seen that for low speed levels the Sport car has a slightly larger road load per mass, but for speed levels above around $66\,km/h$ it is the City car that has the highest road load, relative to its mass. This reflects the relatively larger aerodynamic drag compared to rolling resistance for small cars. Power level contour lines are also included in the right part of Figure 4.3, however this time each car has their own lines. The excess wheel force and power over the road load at a certain speed level, can in this diagram directly be translated into a possible acceleration. It can thus be seen that, at the same power level, the power lines for the Sport car are the lowest, while the lines for the City car are the highest, and that the deviation increases with increasing power levels. This means that, for the same speed level, a possible wheel power of $50\,kW$ in the City car would give a higher acceleration, compared to having the same power level available in the Sport car.

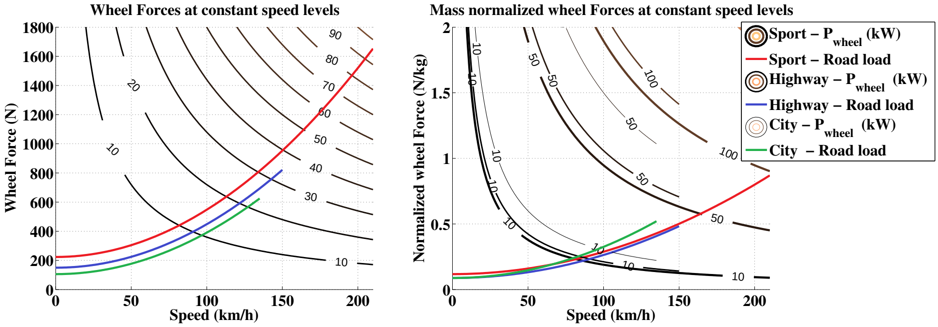

Figure 4.3 Road load wheels force as a function of car speed on a level road, and mass normalized wheel force, for all three concept cars. The contour lines represent wheel power for a certain combination of speed and force, which is the same for all cars in the left part of the figure, however not for the right part.

Figure 4.4 shows both absolute wheel forces and mass normalized wheel forces for each concept car, for road loads at certain grade levels as well as at operating points corresponding to the specified speed and grade performance requirements.

Starting with the **City car**, Figure 4.4(a) shows that the top speed and the grading requirement at high speed, demand about the same levels of wheel power; 23 kW and 26 kW respectively, while the force level at the grading requirement is roughly twice that at the top speed (about 1 kN and 0.6 kN respectively). The takeoff requirement demands the largest force, almost 3 kN but since the speed is low, so is the power demand. In the right part of Figure 4.4(a) it can be seen that the takeoff requirement is equal to an acceleration of almost $2.5\,m/s^2$, as was predicted in Table 2.1, and as is also valid for the other cars. To conclude, if the wheel force is limited to 3 kN at speed levels up to a power limit of 26 kW, above which the wheel force follows the power line, then all three specified operating points will be achievable. As mentioned, the difference between the maximum available wheel force and the road load at a certain grade, equals the vehicle's acceleration capacity. With the above limits, the initial acceleration at takeoff would be about $2.4\,m/s^2$ on a flat road, at 50 km/h it would be about $1.4\,m/s^2$ and at 100 km/h about $0.47\,m/s^2$.

For the **Highway car**, shown in Figure 4.4(b), the top speed demands a force of about 1 kN and a power of 34 kW, while the high speed grading requirement demands a force of about 1.8 kN and a power of 60 kW, i.e. a larger difference between the requirements compared to the City car (it can be seen that also for the Highway car the demanded power at 6 % grade in 90 km/h is almost the same as that at the top speed). For the Highway car an initial force level of about 4.1 kN is required to manage the takeoff requirement, up to about 50 km/h where the power thus can be limited to 60 kW.

The **Sport car**, shown in Figure 4.4(c), evidently demands the highest levels of force and power compared to the other two cars. As for the City car, both the top speed and grading requirements demands roughly the same power levels 96 kW and 108 kW respectively. The takeoff requirement demands an initial force of about 4.8 kN. This force level may be sustained up to about 80 km/h, where the power may be limited to 108 kW.

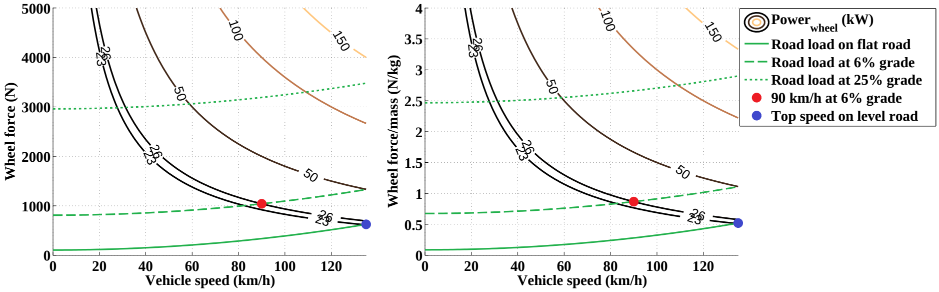

(a) City car.

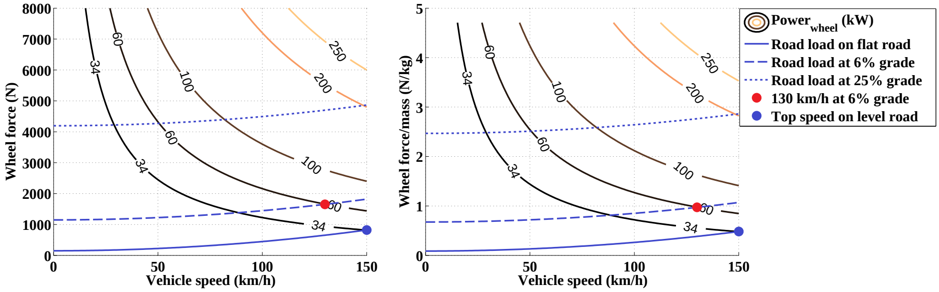

(b) Highway car.

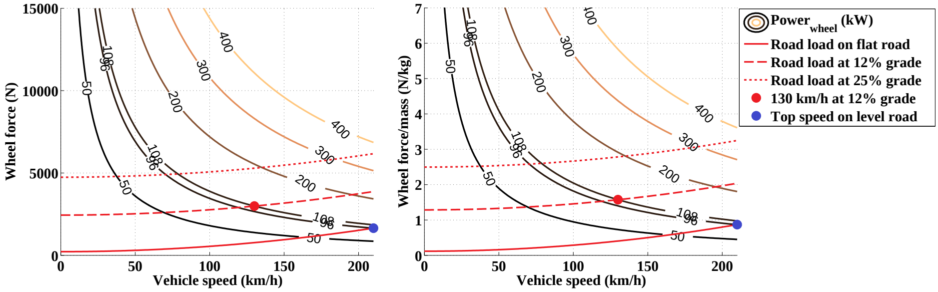

(c) Sport car.

Figure 4.4 Force on wheels due to road load per speed level, and normalized force per vehicle mass, for all three concept cars, along with contour lines representing combinations of wheel force and speed for different levels of wheel power.

4.2.2 Acceleration

Given the above stated demanded levels of force and power versus speed due to the three mentioned requirement; top speed, grade at high speed and take-off at high grade, it can be noted that the implied acceleration capacity of each car would be rather limited. Further investigations must be made to find suitable levels of force and power that will also fulfill the acceleration requirements.

By assuming a torque and speed characteristic that is typical for an electric machine, (i.e. a region of constant torque at low speeds followed by a region of constant power at higher speeds, where the torque is inversely proportional to the speed), various combinations of initial maximum levels of wheel force and wheel power limits can be found, such that they will all fulfill the acceleration requirement. Even though the acceleration time from $0-100\,km/h$ is the same for all combinations, the acceleration time from $0-50\,km/h$, hence also $50-100\,km/h$ differs. It can thus be concluded that the requirement on acceleration time from $0-100\,km/h$ alone, is not enough when seeking to specify a vehicles acceleration performance over the operational speed range. Few data regarding acceleration times between different speed levels are available for the existing BEV models, see Appendix A. Acceleration times for $0-50\,km/h$ are 3s-6s and for $0-60\,km/h$ 3.7s-7.7s.

4.2.2.1 City car

In Figure 4.5, three combinations of initial max force and max power are presented, where the base speed values are set to $1/4$, $1/3$ and $1/2$ of the top speed of the City car, i.e. similar to common ratios for electric machines.

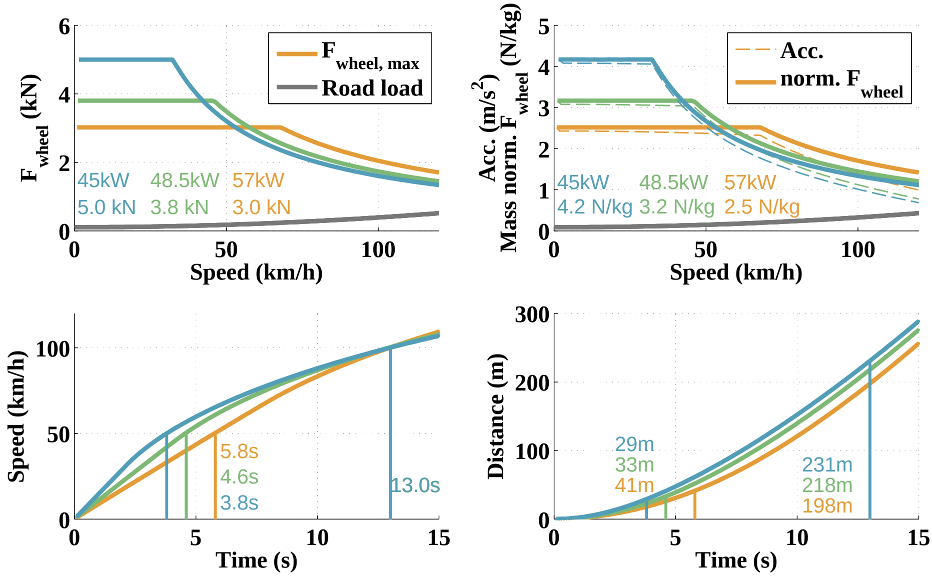

Figure 4.5 Speed and distance over time, as well as wheel force and acceleration, for base speeds that are $1/4$, $1/3$ and $1/2$ of the top speed, during $0-100\,km/h$ acceleration, for the concept City car.

The lowest base speed is related to the largest initial force (**5 kN**), lowest power (**45 kW**), fastest acceleration of $0-50\,km/h$ (just under $4\,s$) along with the shortest driven distance during the acceleration, while the acceleration time of $50-100\,km/h$ is the longest. Given that this is the City car, it can be argued that low speed acceleration performance should be preferred over high speed performance. It is thus decided that the lowest power level should be the design template. Compared to the power levels of existing BEVs with similar acceleration times, the chosen power level is smaller. However the acceleration time $0-50\,km/h$ complies rather well when comparing with some of the existing BEVs.

When comparing the results in Figure 4.5, with the ones found in Figure 4.4(a), the initial force demanded by the acceleration requirement should be around $2\,kN$ higher than that for the takeoff requirement (of $3\,kN$), while the power should be $19\,kW$ higher than that of the high speed gradient requirement (of 26 kW). It is thus the acceleration requirement that will determine the maximum force and power that has to come to the wheels (via the gear box) from the powertrain.

4.2.2.2 Highway car

Combinations of initial force and power limits have been studied in the same manner for the **Highway car** as well, see Figure 4.6.

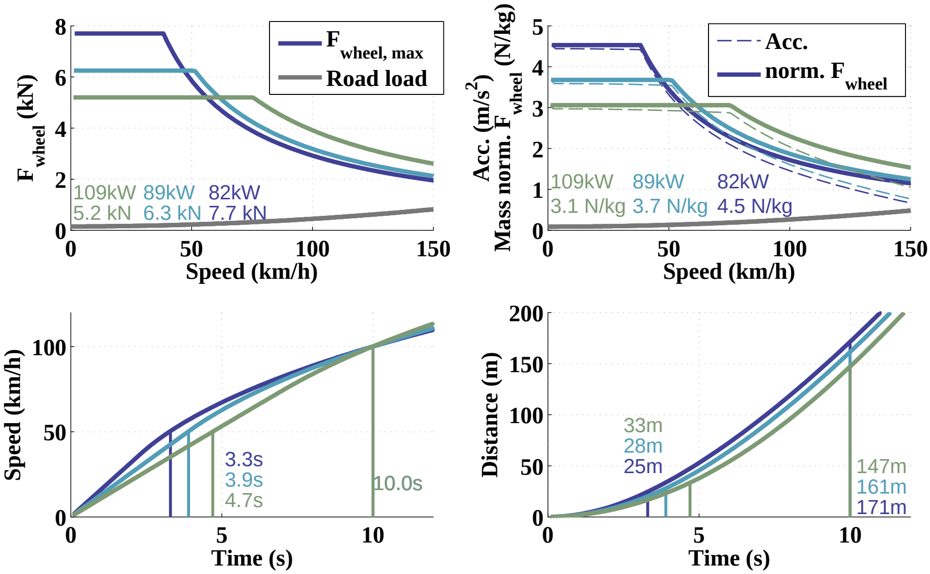

Figure 4.6 Speed and distance over time, as well as wheel force and acceleration, for base speeds that are $1/4$, $1/3$ and $1/2$ of the top speed, during $0-100\,km/h$ acceleration, for the concept Highway car.

Also here the result is that the combination that has the highest initial force ($7.7\,kN$) and lowest power ($82\,kW$) result in the best low speed performance ($3.3\,s$ when accelerating $0-50\,km/h$). However since the $0-50\,km/h$ and $0-60\,km/h$ acceleration times of the few existing BEVs that was found are around $4\,s$, this is here chosen as a targeted value also for the Highway car. Thus targeted initial force is **6.3 kN** and power is **89 kW**. That means that the initial force should be about $2.2\,kN$ more than what was demanded by the takeoff requirement (of $4.1\,kN$), and the power should be $29\,kW$ more than that of the high speed gradient requirement (of 60 kW), as seen in Figure 4.4(b). This would result in an initial acceleration level of about 3.7 m/s^2.

4.2.2.3 Sport car

Finally, for the **Sport car**, see Figure 4.7, an initial force of 16.6 kN and a power of 251 kW result in the best low speed performance with an initial acceleration level of $8.7 m/s^2$ up to a speed of about 50 km/h.

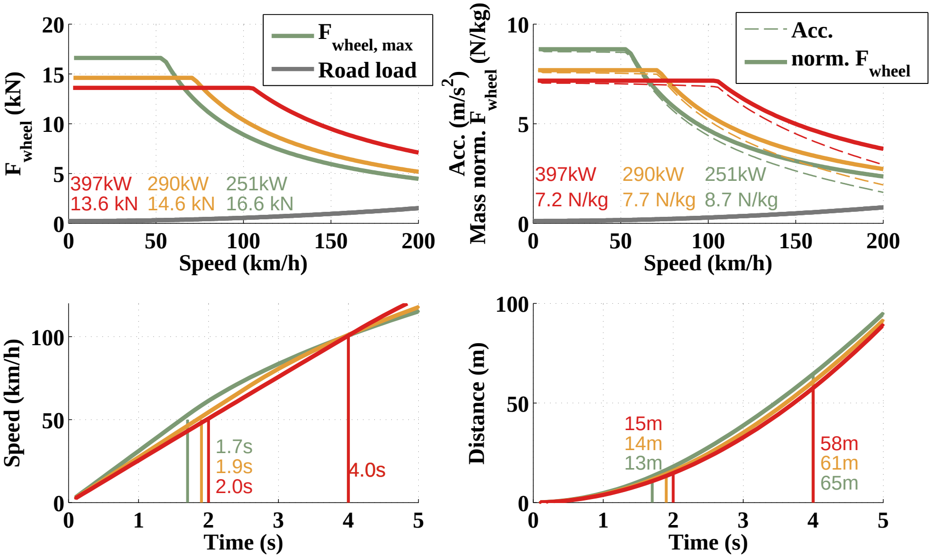

Figure 4.7 Speed and distance over time, as well as wheel force and acceleration, for base speeds that are $1/4$, $1/3$ and $1/2$ of the top speed, during $0 - 100\,km/h$ acceleration, for the concept Sport car.

According to logged acceleration tests of performance vehicles presented in [86], the peak acceleration is kept up to around 80 km/h for an acceleration time which is just above 5 s, hence it is decided that the Sport car should also have a similar base speed. That means that the middle curve is chosen as the desired powertrain capability, with an initial force of **14.6 kN** and a power of **290 kW**.

In this case another aspect needs to be considered; the maximum adhesive capability between the tires and the road, see Section 2.2.4. It might not be physically feasible to sustain such a large force on two wheels without loosing the grip. By assuming that the weight on the driving wheels during the acceleration is about 60 $\%$ of the vehicles weight and that the friction between the tire and the road is unity for dry asphalt and performance tires, then the maximum wheel force becomes 11.2 kN ($0.6 \cdot 1900 \cdot 9.81 \cdot 1 = 11.2\,kN$). Perhaps this value could be larger if another weight distribution was assumed, or if the friction constant was a bit larger. Nevertheless, to be on the safe side, an All-Wheel-Drive (AWD) is here assumed for the Sport car, resulting in a maximum total wheel force of about 18.6 kN.

4.3 Wheel load analysis for selected drive cycles

In this section time traces of speed profiles are used as inputs when calculating demanded wheel power and energy for the three concept cars.

4.3.1 Peak wheel power per cycle

Figure 4.8 shows peak positive and negative wheel power per car, for the Urban, Rural and Highway test cycles. In general, the Sport car demands the largest power levels and the City car the lowest. Similarly, the Urban cycles demand the lowest levels of peak power, while the Highway cycles demand the highest. There are however a few highway cycles with similar peak power levels as some of the Urban and Rural cycles. The relation between peak positive and negative power is rather small for the Urban and most of the Rural cycles, while it is larger for many of the Highway cycles.

For the Urban cycles it is the SC03 and FTP cycles that have the highest wheel power. This can also be seen in Figure 3.7, as these cycles have the highest positive peak accelerations at high speed. The same is also valid for UC LA92 and Artemis Rural for the Rural cycles and REP05 and US06 for the Highway cycles.

With a wheel power of $45\,kW$ for the City car, there may be a problem with the two rather aggressive Highway cycles; REP05 and US06, as well as full regenerative braking in UC LA92, Artemis Rural and the Artemis Motorway cycles. Naturally, the highest speed levels in Artemis150 would not be reached since it exceeds the top speed of the City car. On the contrary, if the Highway car is equipped with a maximum power of $89\,kW$, all cycles should be conceivable, except full regenerative braking in the Artemis Motorway cycles. The Sport car will have no problem following the test cycles, since the highest peak power is only $90\,kW$ compared to the powertrain's peak wheel power of $290\,kW$.

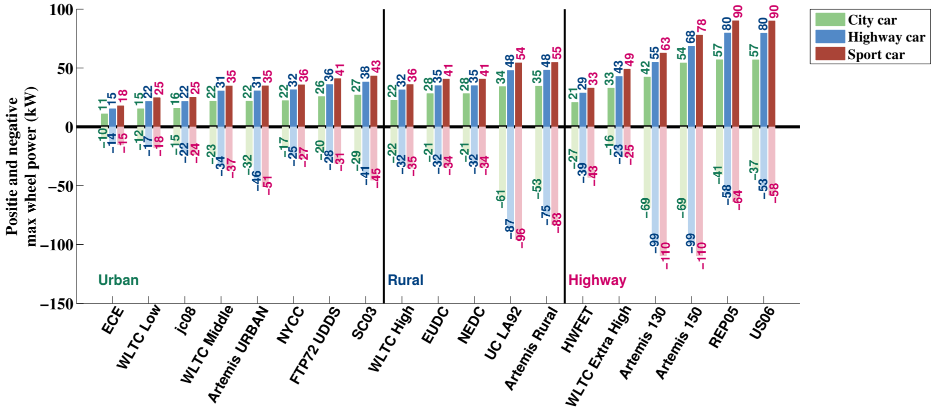

Figure 4.8 Max positive and negative wheel power during Urban, Rural and Highway Test cycles, for all the three concept cars.

The maximum positive and negative wheel power for the logged cycles can be seen in Figure 4.9. It can be seen that the City car may have problem to reach some operating points in 2 of the Urban cycles, 3 of the Rural cycles and 3 of the Highway cycles, while the Highway car may have problem with only one of the Rural cycles, and the Sport car is likely to not have any problem to fulfill all power levels.

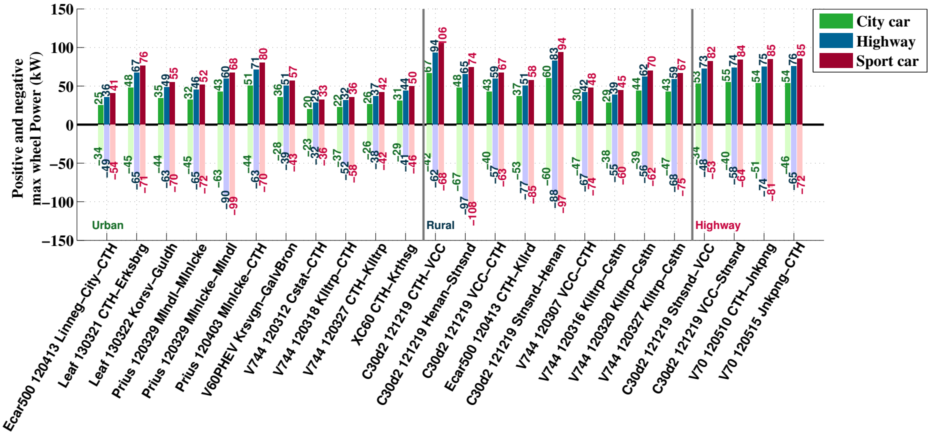

Figure 4.9 Max positive and negative wheel power during Logged Urban, Rural and Highway cycles, for all the three concept cars.

4.3.2 Wheel energy per distance for the Test cycles

In this section both the total positive and negative wheel energy per cycle are calculated and divided by the cycle distance, in order to find the energy consumption for each of the concept cars.

Cycle energy per distance for the three concept cars can be seen in Figure 4.10. Over all, the consumption levels are similar for both Urban and Rural cycles, while they are somewhat higher for the Highway cycles. It is clear that the relative amount of braking energy is much larger for the Urban cycles, and rather limited for the Highway cycles. Furthermore, for the Urban cycles, acceleration and rolling resistance are the main causes of energy consumption, while the aerodynamic drag is rather small. Due to the somewhat higher speed levels in the Rural cycles, the aerodynamic drag becomes larger. Still for the Rural cycles the energy consumption seem to be relatively evenly chaired between the three sources. For the Highway cycles, the aerodynamic drag is the single largest cause of energy consumption, often followed by the rolling resistance. So, even though acceleration is the main force to consider when studying peak power levels: when it comes to energy consumption it is not always the dominating cause, at least not according to the test cycles. For those cycles where acceleration is the main cause of energy consumption (Urban cycles in general, and NYCC, Artemis Urban and UC LA92 in particular), the braking energy is also larger compared to other cycles, thus there is a chance for recuperation.

Amongst the Urban cycles it is the NYCC and Artemis that have the highest levels of energy consumption, while ECE has the lowest. This can be related to Table 3.2 to 3.7, where it can be seen that NYCC, Artemis Urban and ECE have relatively low maximum and average speed values, but ECE have much lower maximum acceleration and RPA value than NYCC and Artemis Urban. For the Rural cycles, UC LA92 has the highest consumption and NEDC the lowest. Both cycles have similar levels of average speed but the UC LA92 has a large time share spent at higher speed levels. It is also the UC LA92 that has the highest maximum acceleration amongst the Urban cycles, as well as the highest RPA value, while NEDC has the lowest. Finally the Artemis motorway cycles have the highest consumption between the Highway cycles, and HWFET the lowest. In this case it is not the cycle with the highest acceleration or RPA values that consume the most energy, but it is that cycle that has the highest average speed and spend the most time at high speed levels.

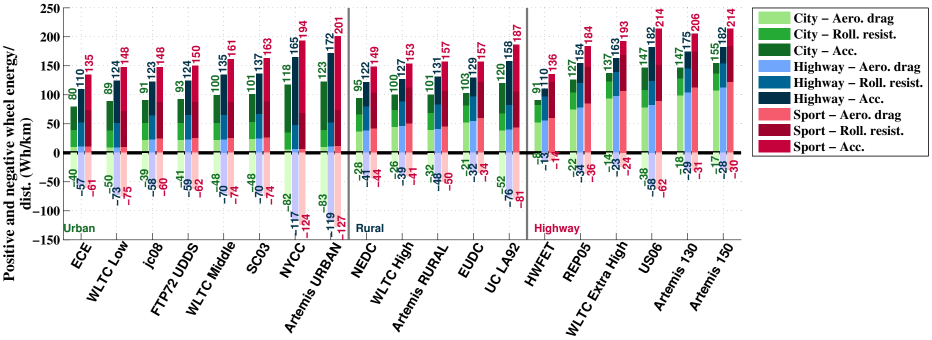

Figure 4.10 Positive and negative wheel energy per driven distance during Urban, Rural and Highway Test cycles, for all of the three concept cars, while acceleration is calculated using the described forward-backward method.

The positive and "negative" values of wheel energy consumption per driven distance, are also illustrated as a function of average running speed for each cycle and car, in Figure 4.11. As a frame of reference, the calculated wheel energy per driven distance while driving at constant speed levels are also included in the figure, i.e. while only considering aerodynamic and rolling resistance. As shown, the energy per distance when driving at constant speed increases with increasing speed, due to the speed dependency of the aerodynamic drag. The deviations between the positive cycle values and constant speed values of energy consumption represent the excess energy consumption due to the acceleration content in each cycle. At the same time, an equally large amount of "negative energy consumption" can potentially be regenerated with the electric powertrain, which would reduce the influence of acceleration on the net battery energy consumption.

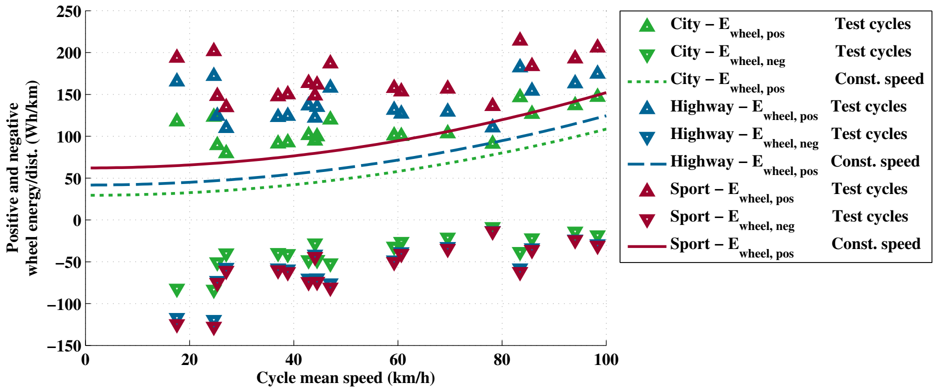

Figure 4.11 Wheel energy per driven distance during Urban, Rural and Highway Test cycles, for all the three concept cars.

4.3.2.1 The problem with 1 Hz speed data and acceleration calculation

It should be noted that the energy consumption per driven distance is sensitive to the method which is used to estimate the acceleration from the reference speed trace. As mentioned, most drive cycles are defined by one speed value per second, hence the associated acceleration must be calculated by differentiating the speed over time. This differentiation may be done using different methods such as the Forward, Backward or Central difference methods, where the acceleration of the current time step is calculated using the change in speed and time between the next and current time step, the current and previous time step, or between the next and previous time step, respectively.

Due to the relatively low time resolution of the cycle speed compared to vehicle dynamics, the resulting accelerations differ for the three methods. Both the Forward and Backward difference methods give exactly the same acceleration levels, but they are shifted one sample period in time and thus attributed to different speed levels. For positive accelerations, the accelerations calculated with the Forward difference method are attributed to lower speed levels, and during braking they are attributed to higher speed levels, while it is the opposite for the Backward difference method. The Central difference method gives the average acceleration between the other two methods at the current time step, and is here regarded as the least erroneous method and has been used throughout this thesis.

It can thus be expected that the Backward method often will over estimate the propulsion power and energy, and under estimate the braking power and energy, compared to the Central method. The percent change in wheel energy consumption per driven distance due to using the Backward difference method compared to using the Central difference method, can be seen in Figure 4.12 for propulsion and braking with the City car. As expected, all cycles show an increase in propulsion energy consumption and most cycles show a decrease in available braking energy per distance, while four cycles show an increase in braking energy (Artemis RURAL, HWFET, REP05, and ArtemisMW130). For most cycles the difference is around 1-6% in both propulsion and braking mode, while it is as much as 13% and 16% for the acceleration intense Artemis URBAN and NYCC in propulsion mode.

The large difference between the acceleration estimation methods is reduced (inverse linearly) when the time resolution is increased. By re-sampling the speed vector through linear interpolation, it was noted that, at 6 Hz the difference is 1% or smaller for all cycles except Artemis URBAN and NYCC, and at 15 Hz the difference is 1% or lower for all cycles.

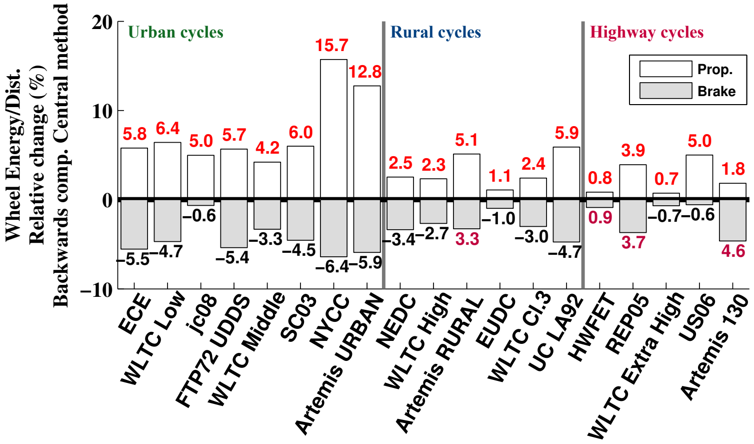

Figure 4.12 Change in wheel energy per distance due to Backwards method compared to Central difference method, during Propulsion and Braking of all Test cycles, for the City car.

4.3.3 Wheel energy per distance for the Logged cycles

The wheel energy consumption per driven distance for the logged cycles can be seen in Figure 4.13. In these cycles, energy consumption referred to acceleration is the major source in both Urban and Rural cycles, although the consumption due to acceleration and to grade can not be separated, thus both are included in these figures. Furthermore, no clear conclusion regarding the comparison of absolute levels between the different types of cycles can be drawn. The spread within the Urban cycles is quite large.

For comparison the energy consumption as a function of running average speed is also presented for the logged cycles in Figure 4.14, showing a rather similar result.

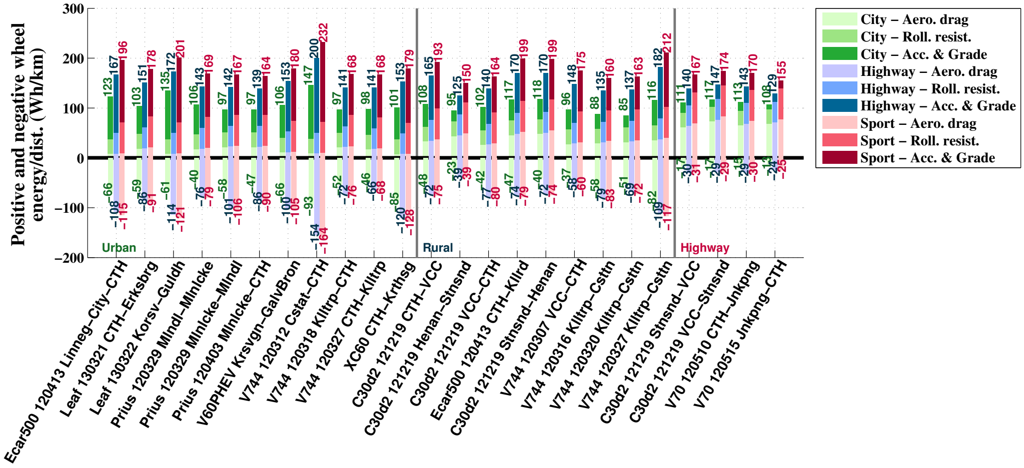

Figure 4.13 Positive and negative wheel energy per driven distance during Urban, Rural and Highway Logged cycles, for all of the three concept cars.

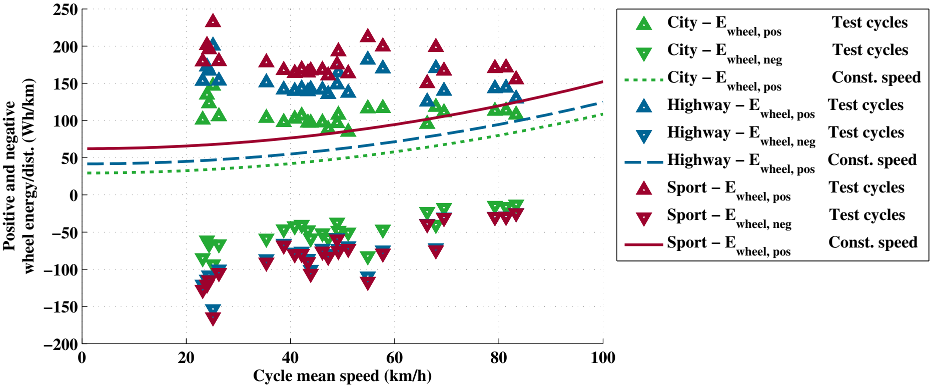

Figure 4.14 Wheel energy per driven distance during Urban, Rural and Highway Logged cycles, for all the three concept cars.

4.3.4 Change in potential energy per driven distance for the Logged cycles

In order to get an indication of the relative energy consumption that road grade causes for the different cycles, the potential energy increase or decrease between the end and the starting altitude level is divided by the total driven distance, and is presented in Figure 4.15. Even though there is a large altitude difference (143 and 149 m) for the two cycles V70 120510 CTH-Jnkpng and V70 120515 Jnkpng-CTH (as seen in3.18), the driven distance is also quite long, 145 km. Hence it is likely that the relative energy consumption due to road grade is fairly small. In practice the energy consumption due to road grade will naturally be larger than these values, due to the looses in the powertrain.

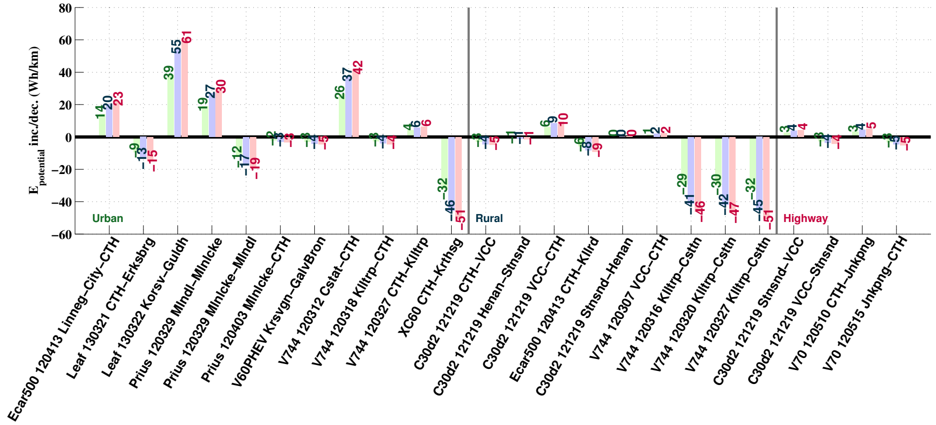

Figure 4.15 Change in potential energy between end point and starting point of the Logged cycles per driven distance, for all the three concept cars; City-green (left), Highway-blue (middle) and Sport-Red (right).

Chapter 5

Powertrain Component Sizing, Modeling and Vehicle Simulation

As was found in Chapter 4, the demanded maximum torque and power from the powertrain can be solely determined by the acceleration requirement for all of the three concept cars. Furthermore, it was found that the acceleration requirements could be satisfied with more than one combination of maximum wheel force and power. This means that the output requirement of the powertrain has some degree of freedom to it. Therefore the final choice will to a large part depend on the characteristics of the chosen components to be used.

In this chapter each of the concept cars will be assigned a base-line powertrain set-up, including sizing of, and models for; the electric machine, converter, battery and transmission.

For simplicity auxiliary loads are excluded from the study, however they are likely to have an important impact on BEV energy consumption, especially in particulary warm and cold conditions.

Furthermore it is decided that the acceleration requirement should be achieved at a $10\,\%$ SOC level, and that the torque and power at higher SOC levels will not be functions of the available DC voltage. This means that the powertrain will be slightly oversized at higher SOC levels.

5.1 Components used for modeling

The analysis is based on the powertrain components described in this section; electric machine, battery and converters. The aim is to use components which are considered to represent typical characteristics for this type of application, rather than state-of-the-art components.

5.1.1 Converter

As can be seen in Appendix A, most commercial BEVs have DC voltage levels of around $300 - 400\,V$. The only exceptions are the sport cars where the voltage levels are higher. Hence an IGBT module with a voltage rating around $650\,V$ is well suited, since then there is a margin for increasing battery voltage during braking, but also to handle other phenomena occurring during operation such as induced voltage peaks during converter switchings caused by stray inductances. Furthermore, it is assumed that the maximum converter RMS phase current $I_{RMS,max}$ can be as high as 2/3 of the current rating in the data sheet. Converter models from Infinieon found at [88] with different current rating are used for all three cars.

5.1.2 Battery cell

The battery cell used is a Lithium-ion (cathode: $LiNiO_2$ cathode active: $LiMn_2O_4$, anode: graphite) cell of laminate type, manufactured by the Japanese company *Automotive Energy Supply Corporation* (AESC), where Nissan Motor Co. is a majority owner [89]. Their batteries have also been used in the Nissan Leaf BEV models (96 in series and 2 in parallel). The *US Idaho National Laboratory* (INL) under the *US Department of Energy* (US DOE) have published measured data on the Nissan Leaf battery pack, including terminal voltage during a full discharge at a C/3 discharge rate, as well as the internal charge and discharge resistances as a function of energy, in [90]. Based on the published data, the cell open circuit voltage, V_{oc} has been estimated by approximating the resistive voltage drop during a C/3 discharge rate, see Figure 5.1. The figure also includes assumed maximum and minimum voltages, as well as denoted voltage levels at 10 and 90 $\%$ SOC. The average open circuit cell voltage within the used SOC window (10 to 90 $\%$) has been estimated to $3.88\,V$, which is slightly higher than the stated nominal voltage by the manufacturer; $3.75\,V$. The mean values of the charge and discharge resistances within 10 to 90 $\%$ SOC are also presented in the figure. The average cell charge capacity is assumed to be $28.8\,Ah$, [90], which can be compared to the manufacturer value of $32.5\,Ah$.

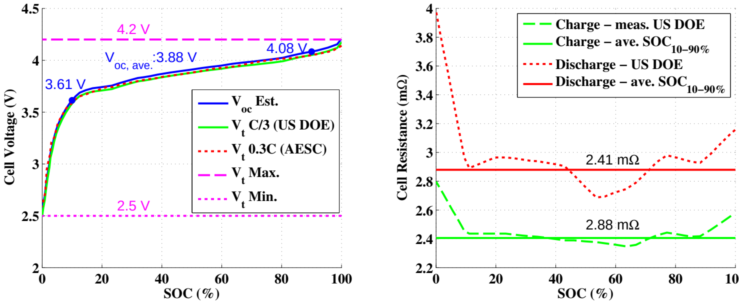

Figure 5.1 Estimated AESC battery cell no load voltage as a function of SOC, and estimated average values of cell resistances, based on data from [US DOE, AESC].

5.1.3 Electric machine

The base for the electric machine used here, is a machine that was designed and built at the division of Electric Power Engineering at Chalmers in the end of the 1990's, and is described in [91] and [53]. It is a four pole PMSM with inset magnets, designed for a series HEV application, with water cooling. Machine voltage and current ratings ([91] and [53]) along with measured machine parameters ([36]) can be seen in Table 5.1.

Table 5.1 PMSM data.

$U_{RMS,max,L-L}$	220 V
$I_{RMS,max}$ $3\,min.$	315 A
Phase resistance, R_s	7.9 mΩ
d-axis inductance, L_d	230 mH
q-axis inductance, L_q $(i_q = 1pu)$	420 mH
Flux linkage related to magnet, Ψ_m	104 mWb
Stator outer diameter	189 mm
Stator inner diameter	110 mm
Stator core length	231 mm
Slot fill factor	0.45
Conductors per slot	3
Conductors in parallel	2

Given the stated peak RMS current (which was a $3\,min.$ value) and winding structure, the maximum current density can be found to be about $12\,A/mm^2$ (with a slot fill factor of about 0.45, three turns per slot and two parallel windings the conductor area is $13.47\,mm^2$). According to [34], a liquid cooled brushless machine can have a current density between 10 to $30\,mm^2$. It is here chosen to increase the machine current density to $20\,A/mm^2$, which leads to a max RMS current of about $540\,A$.

As was done in [36] and [92], the core losses are estimated using the added core resistance R_c described in Chapter 2. The core loss resistance as a function of speed is estimated based on measured no load losses over the machine speed range, presented in [53] (paper E), as

$$R_c \approx \frac{3}{2}\frac{(w_{el}\,\psi)^2}{P_{fe}} \tag{5.1}$$

For each operating point, the machine core losses are then calculated as ([92])

$$P_{fe} = \frac{3}{2}\,R_c(i_{d,o} - i_d)^2 + (i_{q,o} - i_q)^2); \tag{5.2}$$

The efficiency and total losses of the originally sized electric machine (i.e. with unity scaling factors) can be seen in Figure 5.2, as well as maximum torque over speed using the MTPA control strategy as described in [92].

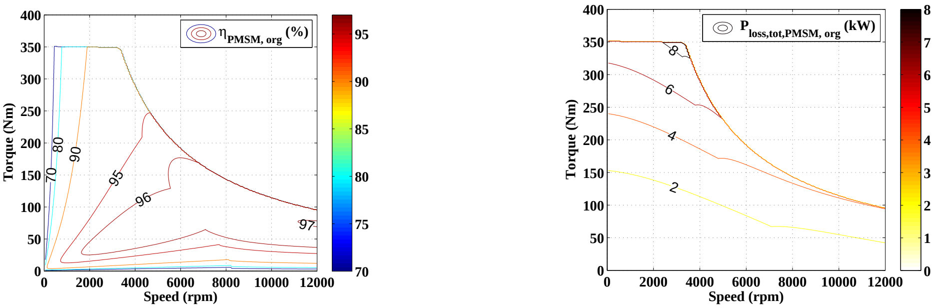

(a) Efficiency (%).

(b) Losses (kW).

Figure 5.2 Efficiency and total power losses for the electric machine with the original size, i.e. unity scaling factors.

5.1.3.1 PMSM active length scaling

During production of electric machines, the iron core laminations are often stamped from core plates [34]. Since the lamination design and stamp tool is rather expensive to develop, electric machine manufacturers often offer different machine sizes that are based on the same stamped laminations, but of different stack lengths. According to [34], the stack length-to-diameter ratio is typically 1 to 3, but it can also be higher. For low length/diameter ratios, the losses in the end windings will become more dominant, and the torque production will be limited since only the stator and rotor package length contributes.

In order to achieve a desired output torque and power, the original machine is here scaled by changing the active length. All machine parameters (that is only the active parts of the winding resistance and inductance) are expected to increase linearly with the length, except the current rating. Also the no load losses used for the R_c estimation are scaled accordingly.

The winding resistance thus needs to be divided into one active part and one that represents the winding overhang. According to [53] paper D p.92, the average conductor length of a half turn, l_{av} can be expressed as

$$l_{av} = l_{active} + l_{passive} = l_{stk} + 1.2\tau_p + 2d_{ext} \tag{5.3}$$

where l_{stk} is the active lamination stack length, τ_p is the winding pole pitch and d_{ext} is the part of the end winding that is estimated to be axially extended outside of the lamination stack. The stack length is $231\,mm$, the pole pitch is $\frac{\pi}{2}\frac{D}{p}$, where D is the stator inner diameter $(110\,mm)$ and p is the pole pair number (two pole pairs), and finally the $2d_{ext}$ is assumed to be $0.05\,m$ as in [53]. This gives a total average conductor length of $384.7\,mm$, where the active part is $231\,mm$ or $60\,\%$ and the over hang is $153.7\,mm$ or $40\,\%$, ([53] paper D p.80). The end winding inductance is assumed to be very small, hence neglected, although as mentioned in [93] it may not be a viable assumption for motors with a low length/diameter ratio.

The length scaling is implemented using the stack length scaling factor, SF_{Lstk}.

5.1.3.2 PMSM rewinding scaling

As described in [35], the machine voltage rating is assumed to be relatively freely adaptable through rewinding of the machine, such that the maximum torque, speed and power remain the same, as well as the losses and hence the efficiency. For simplicity, non-integer winding turns are here allowed.

Then the total stator resistance and both inductances are scaled using the square of the rewinding scaling factor, SF_{rw}, while the magnet flux and applied voltage is linearly scaled, and finally the current is inversely scaled with SF_{rw}.

5.2 Components sizing process

The sizing and modeling process for the City car can be seen in Figure 5.3, and for the Highway and Sport cars in Figure 5.4. As can be seen, two slightly different approaches are utilized, where some steps are independent while others build on previous steps. Each step will be further described in the following sections.

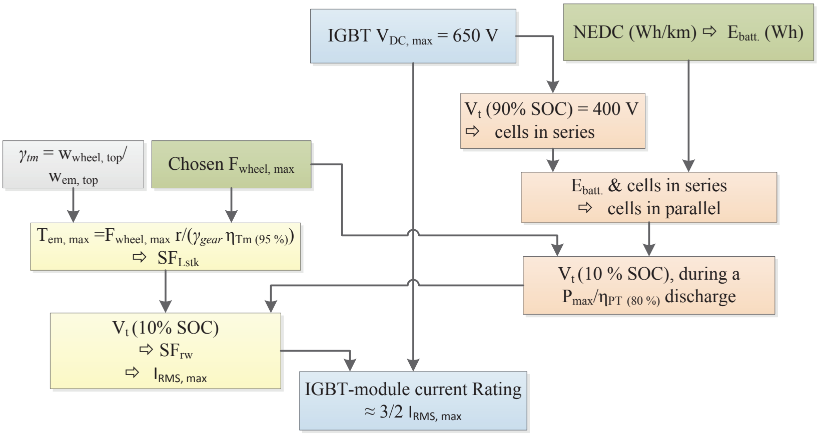

Figure 5.3 BEV powertrain sizing and modeling algorithm for the City car.

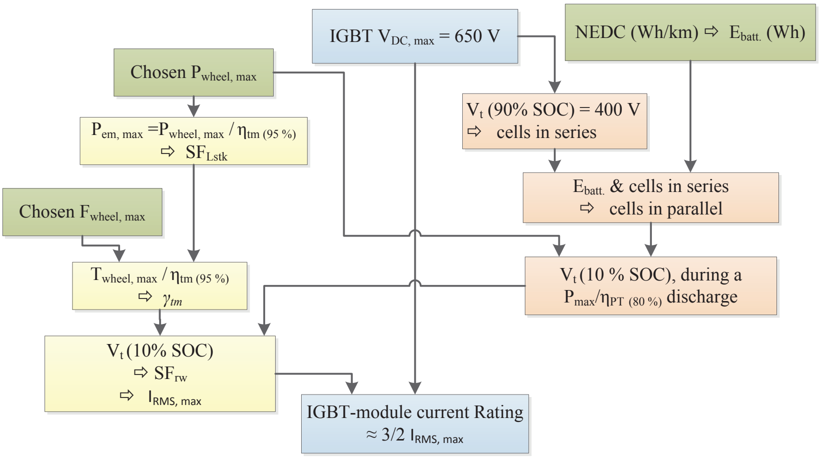

Figure 5.4 BEV powertrain sizing and modeling algorithm for the Highway and Sport cars.

5.3 Implemented battery models

The battery energy content for each car is calculated based on the respective desired NEDC driving range from Table 4.2 and the calculated wheel energy consumption for the NEDC cycle presented in Figure 4.10. It is assumed that all of the available braking energy is recuperated. Additionally, an average powertrain efficiency of $80\,\%$ is assumed, as well as a usable SOC-window of $80\,\%$ (from 10 to $90\,\%$ SOC).

In order to have a good margin to the power electronic component breakdown voltage of $650\,V$, it is chosen that the Open Circuit voltage, V_{oc}, at $90\,\%$ SOC, should be $400\,V$. Given the assumed average AESC battery cell voltage of $4.08\,V$ at $90\,\%$ SOC, the number of needed series connected cells is 98.04, which gives a nominal voltage of $380.4\,V$. The same voltage level is used for all cars, hence the same number of series connected cells are implemented.

The number of cells in parallel can be found in two steps, where the first is to estimate the demanded pack charge capacity as the resulting ratio between the desired energy capacity relative to the pack nominal voltage. In the second step the pack charge capacity is related to the assumed cell capacity.

A summary of the parameters of the implemented batteries in all three cars can be seen in Table 5.2. The assumed pack charge resistance are taken as scaled values of the average cell charge and discharge resistances, within the chosen SOC-window.

The battery open circuit voltage as a function of SOC is modeled according to the left part of Figure 5.5(a), 5.5(b) and 5.5(c), which also includes the assumed maximum and minimum voltage levels. Furthermore, the estimated voltage drops during constant current discharges at $3C$ and $5C$ are presented, as well as the voltage drop during a full constant power discharge of full electric machine power at $10\,\%$ SOC. For the City car this power is close to a $3C$ current rating

In the right part of Figure 5.5(a), maximum charge and discharge power limits, according to the three types (2.27), (2.28), (2.29) in Chapter 2 are presented for the City car.

The theoretical and the voltage limited discharge power limits are rather similar, while the current limited discharge power limits are substantially lower. Also a constant discharge power of 58 kW is depicted, and shows to be just a bit larger than the 3C limit. During charging, only the voltage limited charge power is presented. It shows a stronger dependence on SOC level compared to the discharge power. Similar characteristics are valid for the Highway and Sport cars as well, although not shown here.

Table 5.2 Summary of battery data for all three cars.

	City	**Highway**	**Sport**
NEDC range	160 km	200 km	300 km
Energy	19.3 kWh	29.9 kWh	56.6 kWh
Series cells	98.04	98.04	98.04
Parallel cells	1.76	2.73	5.17
V_t at 90 $\%$ SOC, $P_{EM,max}$	325 V	317 V	283 V
R_{dis}	160.4 $m\Omega$	103.4 $m\Omega$	54.6 $m\Omega$
R_{ch}	134 $m\Omega$	86.4 $m\Omega$	45.6 $m\Omega$

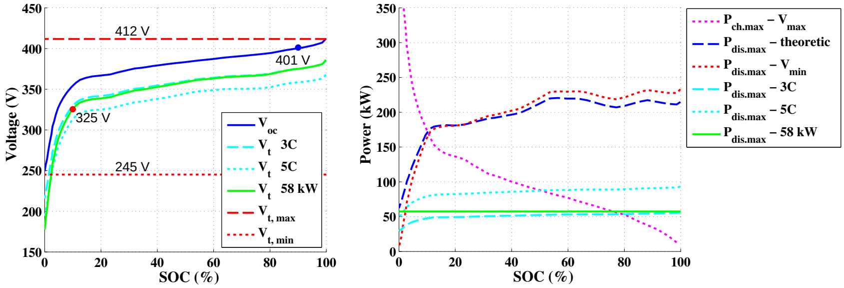

(a) City car.

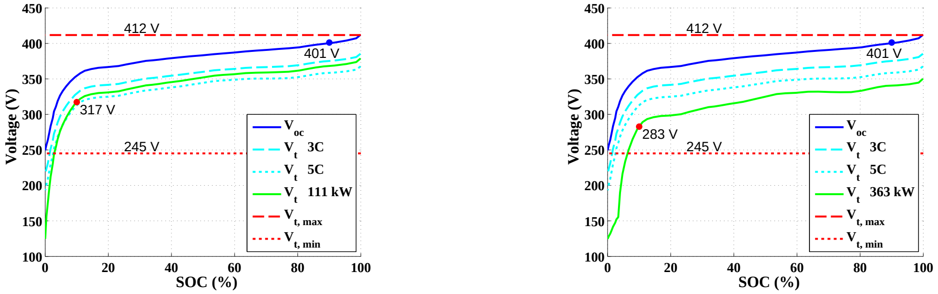

(b) Highway car.

(c) Sport car.

Figure 5.5 No load voltage as a function of SOC-level, max and min terminal voltage, terminal voltage during constant current during 3 and $5C$ discharge rates, as well as during a constant EM max power discharge. In the right part of figure a for the City car: max charge and discharge power related to max voltage see (2.28), theoretical (2.27), current limited at 3 and $5C$ see (2.29), and finally for the EM max power.

5.4 Implemented EM models including transmissions

For the City car it is decided that the total transmission ratio should be based on the direct relationship between the vehicle and machine top speed, as the base speed then is fairly close to the desired one from Figure 4.5, as well as the power level. The wheel radius, the gear ratio γ_{tm} and the desired maximum wheel force (compensated for a transmission efficiency of $95\,\%$) are then used as inputs when finding a suitable length scaling factor. Then a value for the rewinding scaling factor is found such that the DC voltage level is matching the estimated DC voltage level during a full power discharge at SOC level of $10\,\%$. Finally, the resulting maximum RMS phase current, $I_{RMS,max}$ is noted and used as a base for choosing the converter current rating, $I_{c,nom}$. It is assumed that a reasonable current margin is achieved when $I_{c,nom} \approx 3/2\, I_{RMS,max}$.

For the Highway and Sport cars, the transmission ratio is not initially decided. Instead the stack length is scaled until the desired output wheel power is reached. In order to realize the AWD functionality in the Sport car, it is decided that two equally sized electric motors shall work in parallel; one on the rear drive axle, and one on the front. This implementation will also help keeping the length scaling down. Then the transmission ratio is decided as the ratio for which the desired wheel force is achieved (while considering the assumed transmission efficiency). Finally the rewinding scaling factor and resulting maximum RMS phase current is found in the same manner as for the City car, as well as the converter current rating.

The implemented electric machine torque and power levels as well as scaling factors and transmission ratios can be seen in Table 5.3. The transmission ratio,γ_{tm} is defined as in

$$\omega_{em} = \gamma_{tm}\, \omega_{wheel} \tag{5.4}$$

where ω_{em} is the electric machine angular speed (rad/s), ω_{wheel} is the angular speed of the wheel(rad/s).

Table 5.3 Summary of electric machine and transmission data for all three cars, along with vehicle power-to-weight ratio.

	City	Highway	Sport
γ_{tm}	10.3882	7.62	6.22
P_{max}	49 kW	97 kW	153
T_{max}	140 Nm	280 Nm	420 Nm
$F_{wheel,max}$	4750 N	6600 N	7700 N
n_{max}	12,000 rpm	9475 rpm	10,191 rpm
$U_{RMS,max,L-L}$	207 V	202 V	180 V
$I_{RMS,ph,max}$	233 A	468 A	786 A
SF_{Lstk}	0.405	0.795	1.1925
$\frac{L_{stk}}{D_{outer}}$	0.495	0.972	1.458
SF_{rw}	2.32	1.154	0.687
η_{max} at 350 V	96.2 %	96.9 %	97.0 %
Vehicle Power-to-weight ratio	41 W/kg	57 W/kg	153 W/kg

The resulting output torque and power as function of speed for all cars, can be seen in Figure 5.6, and the resulting wheel forces can be seen in Figure 5.7.

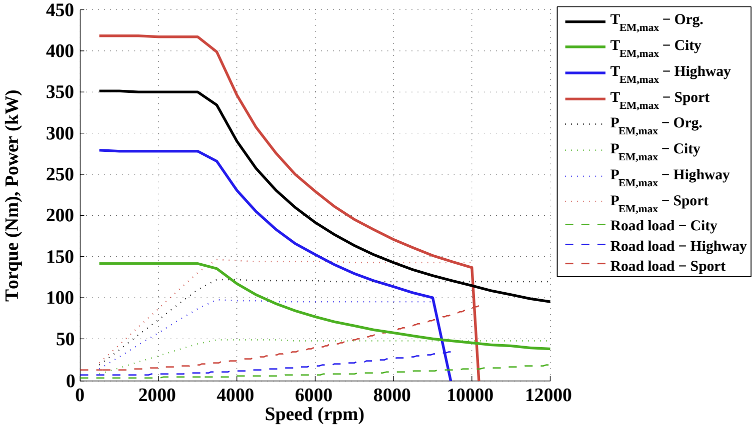

Figure 5.6 Max torque and power as a function of speed for the original electric machine and the scaled machines at a DC voltage level during a full power discharge, at 10 % SOC.

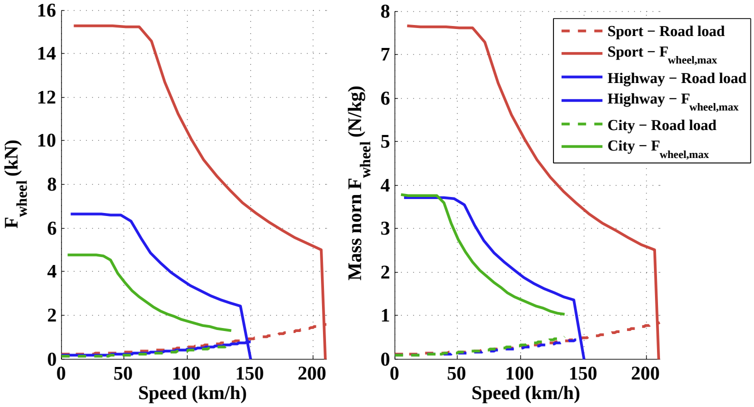

Figure 5.7 Maximum wheel force and power as a function of car speed from the electric machine at a DC voltage level during a full power discharge, at 10 % SOC.

The implemented electric machine total losses (including conduction losses as in (2.14), and core losses as describes above), and associated energy efficiency at two different voltage levels and for all three machines, can be seen in Figure 5.8 and 5.9 for the City and Sport cars, while the characteristics of the Highway machine car lies in between. The losses increase mainly with increasing torque, and somewhat with speed. As can be seen, for each car's machine, the losses and efficiency are exactly the same up to the case of field weakening, where the losses are slightly decreased at lower voltage levels, hence the efficiency is somewhat increased. This means that the average electric machine efficiency during a drive cycle simulation will only vary depending on SOC, if any operating point is outside of the area with similar efficiency.

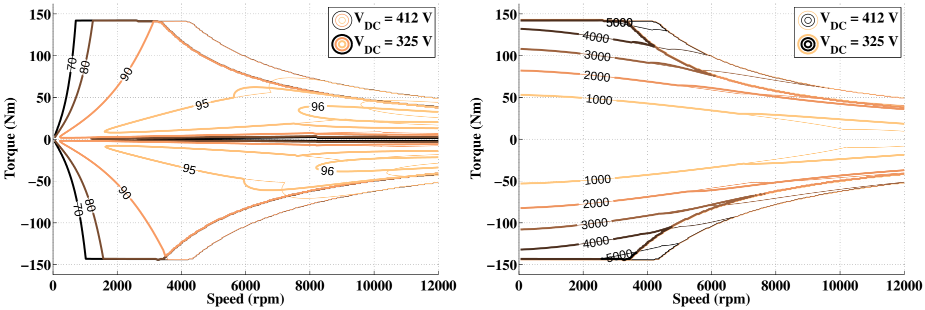

(a) Efficiency (%).

(b) Losses (W).

Figure 5.8 Implemented electric machine efficiency and power loss maps, for the City car.

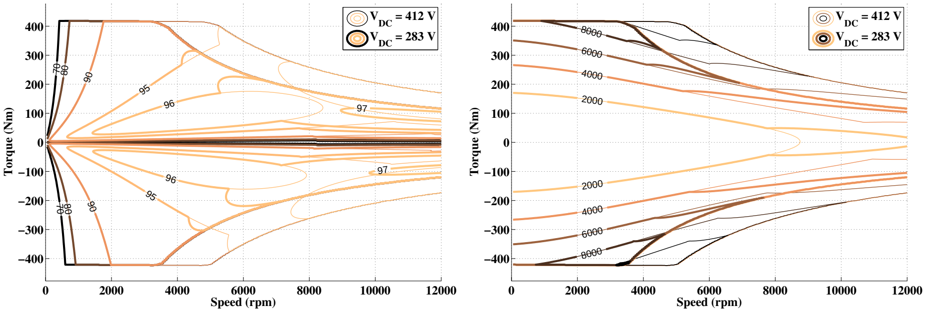

(a) Efficiency (%).

(b) Losses (W).

Figure 5.9 Implemented electric machine efficiency and power loss maps, for the Sport car.

In Figure 5.10, the total powertrain efficiencies (excluding batteries) as a function of mass normalized wheel force and car speed, can be seen. For the same level of speed and acceleration, it shows that the City car powertrain is a bit more efficient compared to the Highway and sport cars's.

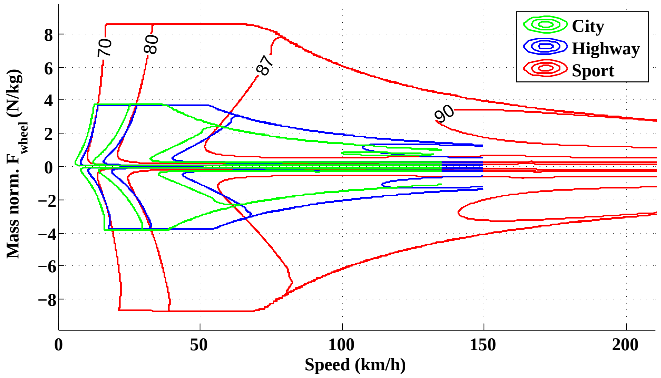

Figure 5.10 Total power train efficiency, including electric machine, converter and transmission, for the three concept cars, as a function of speed and normalized wheel force.

5.5 Implemented converter model

For the City car a converter module with current rating of 400 A (Infineon FS400R07A1E3_H5) is chosen, even though the rating might be a bit too low. For the Highway car a module with current rating of 800 A (Infineon FS800R07A2E3) is implemented. Finally for the Sport car; four modules are used, two in parallel for each of the two machines, where the module current rating is 600 A (Infineon FS600R07A2E3). That will give a total converter current rating of 2.4 kA, which is assumed to be able to withstand an RMS current of 1.6 kA, hence it is viable for the chosen machine size.

The extracted IGBT module parameters can be seen in Table 5.4, and adhere to chip temperatures of $125\,^{\circ}\mathrm{C}$ and a gate voltage of 15 V. The on-state threshold voltage and resistance parameters are estimated under consideration of expected current levels. The switching frequency is set to 10 kHz.

Table 5.4 IGBT module parameters, for all three cars, where the data for the Sport car represent all four modules.

	City car:		Highway car:		Sport car:	
	IGBT	Diode	IGBT	Diode	IGBT	Diode
$I_{c,nom}$	400 A		800 A		4*600 A	
I_{ref}:	400 A		550 A		4*400 A	
V_{ref}:	300 V		300 V		300 V	
On-state threshold voltage	0.709 V	0.803 V	0.673 V	0.761 V	0.66 V	0.775 V
On-state resistance	2.468 $m\Omega$	1.999 $m\Omega$	1.336 $m\Omega$	1.12 $m\Omega$	0.441 $m\Omega$	0.352 $m\Omega$
Turn-on Energy loss	4.2 mJ	-	12 mJ	-	44 mJ	-
Turn-off Energy loss	16.0 mJ	7.25 mJ	25 mJ	9.5 mJ	68 mJ	28 mJ

The total power losses are estimated using (2.20) to (2.23), and can be seen together with energy efficiency in Figure 5.11 for the City car and in Figure 5.12 for the Sport car, in the machine torque and speed frame of reference, while the results for the Highway converter lies in between. The converter losses mainly increase with increasing torque, while the efficiency has a strong speed dependency and increases with increasing speed. Unlike the electric machine, the converter losses vary somewhat depending on the DC voltage level in the whole operating range. The efficiency is mostly higher at lower voltage levels in the same torque and speed operating point, due to lower switching losses.

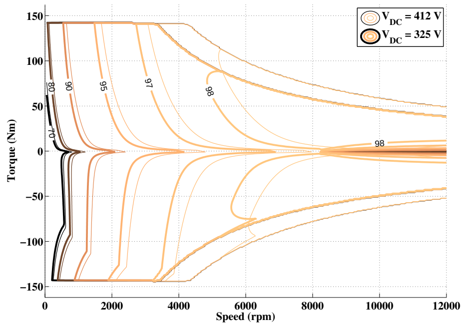

(a) Efficiency (%).

(b) Losses (W).

Figure 5.11 Implemented converter efficiency and power loss maps at three DC voltage levels, for the City car.

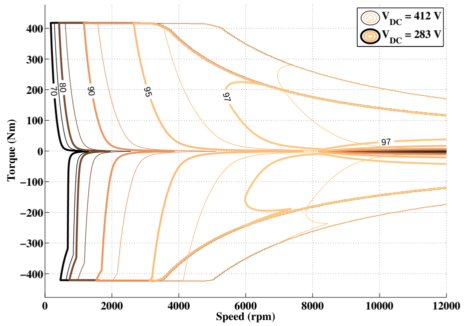

(a) Efficiency (%).

(b) Losses (W).

Figure 5.12 Implemented converter efficiency and power loss maps at three DC voltage levels, for the Sport car.

5.6 Simulator structure

A simplified presentation of the simulation structure, which was implemented in Matlab Simulink, is presented in Figure 5.13. The input to all simulations are the reference speed cycles as functions of time. The time resolution of the Test cycles are all $1\,Hz$, while it is $20\,Hz$ for the Logged cycles. All simulations are executed with a fixed time step of $0.01\,s$, which proved to provide reasonable stability. For the logged cycles, also the estimated road grade levels as a function of time is an input to the simulations.

In order to allow deviation from the speed reference a PI driver model is implemented. Its input is the difference between the reference speed and the simulated speed. The proportional K_p and integral K_i gains are chosen such that the reference speed and associated acceleration are followed fairly close by the simulation output (where $K_p = K_i = 3$). The output of the driver model is a signal between -1 to 1.

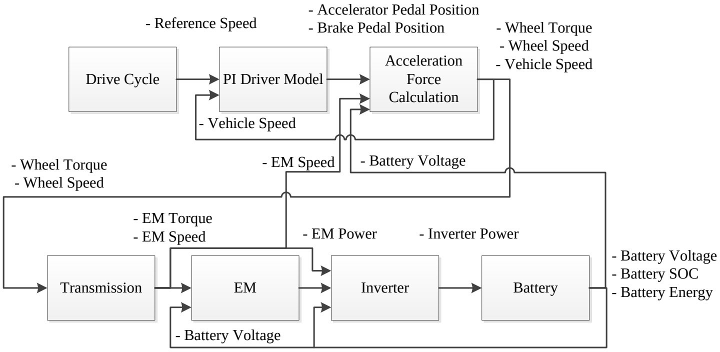

Figure 5.13 Simplified simulation structure.

The positive output from the driver model is regarded as an acceleration pedal signal and the negative part as a brake pedal signal. These signals are then scaled by the maximum torque from the electric machine in motoring and generating mode, which are implemented through look-up tables as functions of machine speed and DC-link voltage. Thus it gives the electric machine torque reference signals, via linear interpolation. It is then assumed that the electric machine can fulfill the torque reference. No wheel slip is assumed, hence the electric machine speed is simply found via the simulated vehicle speed, the wheel radius and the transmission ratio.

At each time step the sum of the resistive forces on the wheel (the vehicle's aerodynamic drag, rolling resistance and possibly also grading force) is converted to a total resistive wheel torque. Given the total resistive torque together with the wheel torque from the electric machine via the transmission, and the vehicles estimated mass inertia, (as the product of the vehicle mass and the square of the wheel radius, while ignoring additional rotating inertias), the resulting vehicle acceleration is calculated (as the rotational form of (2.1)). Furthermore, the simulated speed is then calculated as the time integral of the resulting acceleration.

Both the electric machine and converter power losses are implemented trough look-up tables that are functions of machine torque and speed, as well as DC-link voltage, where the output is found through linear interpolation. The power flow between electric machine and converter is calculated as the added or subtracted losses to the mechanical machine output, depending on mode of operation. Likewise is the DC-link power flow calculated via the additional converter losses. The DC-link power flow is then the input to the battery model, where the current is found from division of the power with the terminal voltage from the previous time step. The current is then used to estimate the

SOC level, (as in (2.26)) as well as battery conduction losses together with the discharge and charge internal resistances. Finally, the terminal voltage is found as the subtracted resistive voltage drop from the SOC dependent open circuit voltage.

Next follows results from the simulations in terms of requirement and drive cycle fulfillment as well as powertrain and energy consumption for the different drive cycles.

5.7 Simulated time to accelerate $0 - 100\,km/h$

The simulation result from the $0 - 100\,km/h$ acceleration test can be seen in Figure 5.14 to 5.16, for the three cars respectively, where the ideal calculations for similar values of the initial maximum force and power, are also presented as a reference. Note that the ideal calculations for the City car is here adjusted to comply with the implemented size of the electric machine. The tests have been conducted for both $10\,\%$ and $90\,\%$ SOC levels, which gave different results as expected.

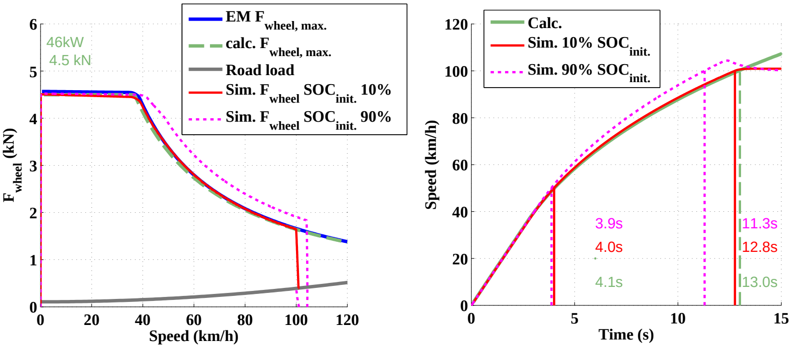

Figure 5.14 Comparison of acceleration test from $0 - 100\,km/h$, between calculation and simulation, as well as maximum force on wheels from the electric machine, for the City car.

For the City car, the time to accelerate from $0 - 100\,km/h$ by simulation was $12.8\,s$, at a battery SOC level of $10\,\%$ see Figure 5.14. This is about $1.5\,\%$ faster than the acceleration requirement for the city car, which was $13\,s$. As can be seen in the figure, above base speed the simulated wheel force is somewhat larger than the ideally calculated force, hence the acceleration will be faster. The simulated wheel force is even larger at the 90% SOC level, resulting in an acceleration time of $11.3\,s$, i.e. $7.8\,\%$ shorter then at $10\,\%$ SOC. The simulated acceleration time to $50\,km/h$ is $4\,s$ at $10\,\%$ SOC and only slightly smaller at the 90% SOC level, $3.9\,s$.

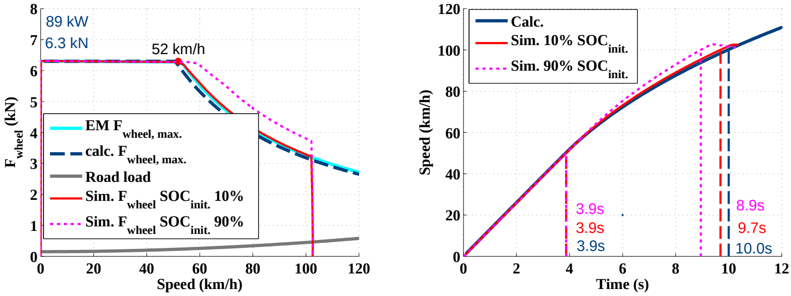

Figure 5.15 Comparison of acceleration test from $0-100\,km/h$, between calculation and simulation, as well as maximum force on wheels from the electric machine, for the Highway car.

Also the Highway car has a slightly shorter acceleration time to $100\,km/h$ compared to the ideal calculation; $9.7\,s$, which is $3\,\%$ faster. The difference between the two SOC levels is even larger than for the City car, where the time for the 90% SOC level is $8.9\,s$ which is $8.2\,\%$ faster than at $10\,\%$ SOC. The time to $50\,km/h$ is the same for all cases.

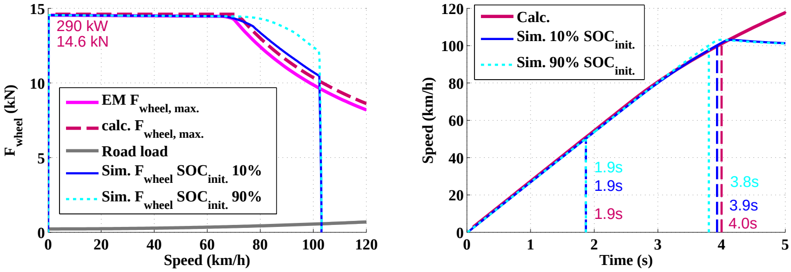

Figure 5.16 Comparison of acceleration test from $0-100\,km/h$, between calculation and simulation, as well as maximum force on wheels from the electric machine, for the Sport car.

Finally for the Sport car the time to $50\,km/h$ is the same for all cases, while the time to $100\,km/h$ is $3.9\,s$ and $3.8\,s$ for the 10 and $90\,\%$ SOC respectively, which means about 2.5 and $5\,\%$ faster then the requirement.

5.8 Simulated time to accelerate $0-100\,km/h$ with grade

Here an acceleration from $0-100\,km/h$ is again simulated, but now for the case of added road grade as a form of controlling the fulfillment of the requirement to be able to handle a grade at high speed. The results can be seen in Figure 5.17 to 5.19.

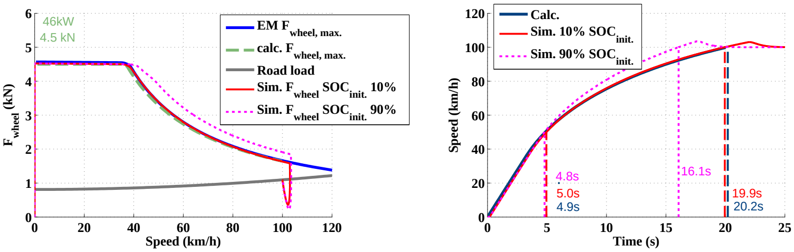

Figure 5.17 Comparison of acceleration test from $0 - 100\,km/h$, between calculation and simulation, as well as maximum force on wheels from the electric machine, for a road grade of $6\,\%$, for the City Car.

The City car was to be able to sustain a speed of $90\,km/h$ in a uphill grade of $6\,\%$, which it does. In this case it takes about $5\,s$ for the City car to reach $50\,km/h$ and about $20\,s$ to reach $100\,km/h$ at $10\,\%$ SOC. The higher SOC level gives only minor effects on the time to $50\,km/h$, while it needs $3.8\,s$ less to reach $100\,km/h$ compared to the $10\,\%$ SOC.

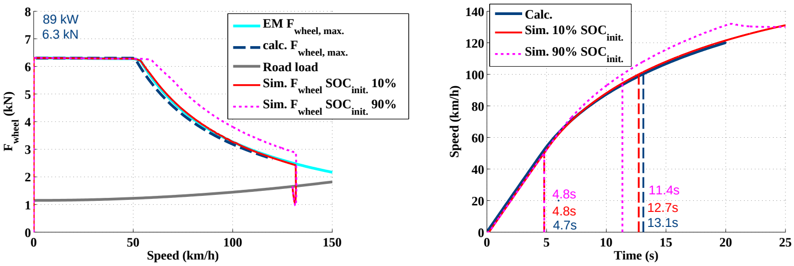

Figure 5.18 Comparison of acceleration test from $0 - 100\,km/h$, between calculation and simulation, as well as maximum force on wheels from the electric machine, for a road grade of $6\,\%$, for the Highway Car.

The Highway car is able to sustain the uphill grade of $6\,\%$ at the speed of $130\,km/h$. In this case the acceleration time difference between the no grade case is much smaller compared to the City car. Also less difference is noted between the two SOC levels, only $1.3\,s$ for $100\,km/h$, and none for $50\,km/h$.

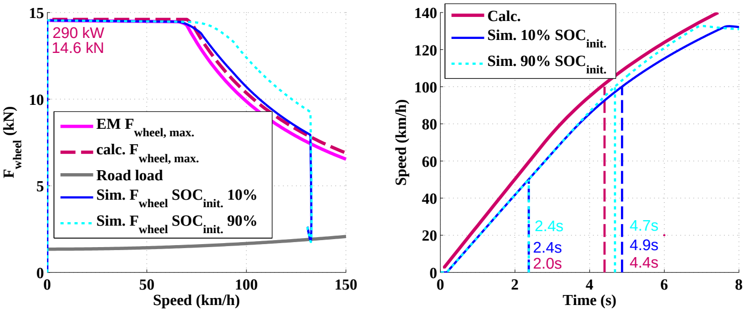

Figure 5.19 Comparison of acceleration test from $0 - 100\,km/h$, between calculation and simulation, as well as maximum force on wheels from the electric machine, for a road grade of 6 %, for the Sport Car.

Finally, the Sport car can handle the $12\,\%$ uphill grade at $130\,km/h$. The time to accelerate to $100\,km/h$ only becomes $0.9\,s$ longer compared to the case with no grade, for both SOC levels.

5.9 Fulfillment of reference cycle speed in simulation

Due to the use of a driver model (i.e. a speed controller) in the simulation, naturally the simulated speed will deviate from the reference speed trace, even for operating points well within the operating area of the powertrain. Hence when analyzing energy consumption and efficiency for a certain cycle, it must be remembered that a slightly different cycle than the reference, is analyzed. As a consequence, typical values of the difference between reference speed and simulated speed have been studied. Another parameter worth studying is the difference in positive and negative average energy at the wheels per driven distance, between the simulation and the reference speed and acceleration. It might happen that there is a large speed difference at a certain time step, but that it's influence on the average energy consumption difference is rather small.

For the Test cycles the speed differences range between $0.1 - 0.4\,km/h$, $0.2 - 0.5\,km/h$ and between $0.2 - 0.6\,km/h$ for the City, Highway and Sport cars respectively. Typical values of the maximum difference between the simulated acceleration and the acceleration of the reference Test cycles are; $0.0 - 0.1\,m/s^2$, $0.0 - 0.2\,m/s^2$ and $0.0 - 0.1\,m/s^2$ for the City, Highway and Sport cars respectively. Worth noting is that the time simulation inherently is a backward calculation, hence the Euler backward method is used for the reference cycle acceleration, instead of the otherwise more accurate forward-backward method described in Chapter 3.

Moreover, during the modal European cycles (ECE, EUDC and NEDC) a minor speed overshoot is noted when the reference speed of the cycle is changing rapidly from a constant acceleration to a constant speed, which gives a relatively small difference of $0.2\,km/h$ between the reference and simulated speed. This also results in a small oscillation in the simulated acceleration of $0.7\,m/s^2$. Nevertheless, these effects are seen to have little influence on the average wheel energy consumption during the cycle, hence they are ignored.

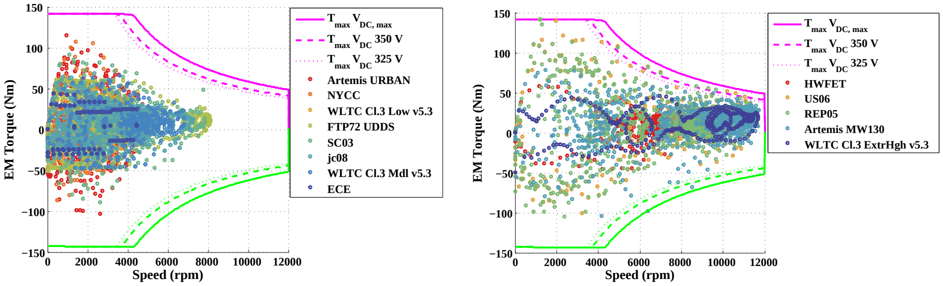

(a) Urban cycles. (b) Highway cycles.

Figure 5.20 EM operating points during the Urban and Highway cycles for the City car.

For the City car, three points in each of the two cycles US06 and REP05 were outside of the powertrain's operational area, causing a maximum deviation of $1.7\,km/h$ from the reference speed, and $0.4\,m/s^2$ from the reference acceleration. These represent speed and acceleration levels of $56\,km/h$ at $3\,m/s^2$, and $80\,km/h$ at $2.2\,m/s^2$, and finally around $120\,km/h$ at $1.3\,m/s^2$. The consequence on the average energy consumption is negligible in these cases. Also one point in the Artemis Motorway cycle during braking at high speed is outside of the operating area of the electric machine, see Figure 5.20. The operating points of the City car electric machine can be seen as gray dots in Figure 5.20 for the Urban and Highway cycles. In the same figure also ideal electric machine operating points for a lossless system is depicted for comparison, and color marked depending on the type of cycle.

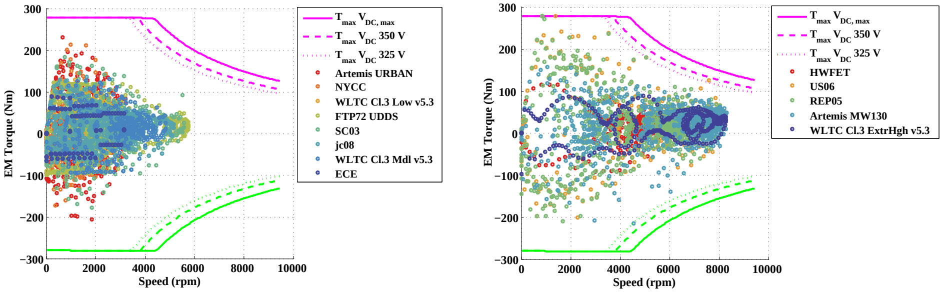

(a) Urban cycles. (b) Highway cycles.

Figure 5.21 EM operating points during the Urban and Highway cycles for the Highway car.

The US06 and REP05 cycles caused some deviations also for the Highway car of maximum $1.5\,km/h$ and $0.2\,m/s^2$, however in this case the operating points that cause problem are those that demand high acceleration (almost $4\,m/s^2$) from stand still, see Figure 5.21. The problem appears twice in REP05 and once in US06. Also here there is no effect on the net average wheel energy.

For the Sport car, the operating points from all Test cycles are well within the limits of the powertrain.

Furthermore, all cars are able to follow the Logged Urban cycles, with typical maximum speed differences between the reference and simulated cycle as $0.3 - 0.8\,km/h$. One Rural cycle for the City car (C30d2 121219 Stnsnd-Henan) and all Highway cycles have single large speed deviations with a relatively large effect on the average net wheel energy. The Highway and Sport cars have no major deviations worthy to mention.

5.10 Simulated component efficiency per cycle

The average Test cycle efficiency separated into propulsion and braking mode can be seen in Figure 5.22 to 5.24, for the City, Highway and Sport cars respectively. Also the average cycle efficiency of each modeled component (electric machine, converter, battery and transmission) is depicted in the figures for comparison.

Although the differences in efficiency between the cycles and cars are quite small (a few units of percent), some trends can be seen when comparing the results between the cycles and cars. One tendency is a slightly higher average total powertrain efficiency for the highway cycles and a somewhat lower efficiency for the Urban cycles, for all of the cars. Also the total powertrain efficiency of the City car is generally a bit higher, and a bit lower for the Sport car. Furthermore, the total powertrain cycle efficiency is normally a few units of percent higher in motoring mode compared to generating mode, which can also be seen in Figure 5.10.

The lowest total efficiency for all cars is achieved in the NYCC cycle where both the electric machine and converter efficiencies are low. The highest efficiencies are seen in the WLTC Extra high and Atermis Motorway cycles. The Sport car converter configuration proves to give a rather poor efficiency for several of the Urban cycles. Perhaps a better strategy is to implement a control system where the extra driving wheel pair is only engaged during higher power and torque demands.

The transmission efficiency is in line with the efficiency of the converter and electric machine. Perhaps a more advanced loss model of the transmission would be preferred here in order to differentiate between the various load cases.

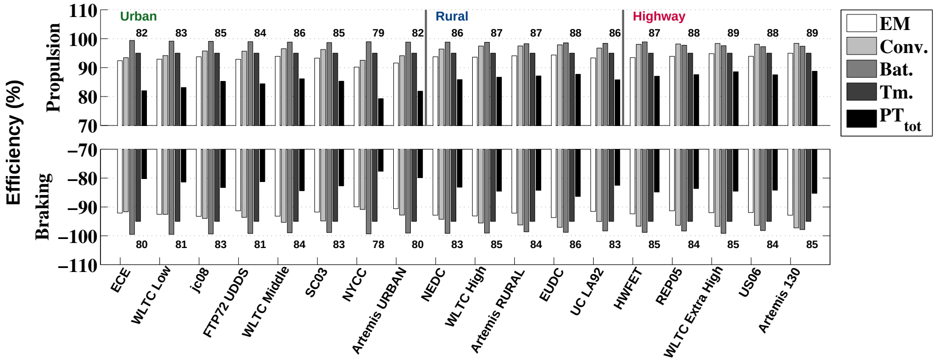

Figure 5.22 Total powertrain efficiency per cycle in propulsion vs. braking mode (negative y-axis), and efficiency broken down per component, from simulation of the City car, with $90\,\%$ initial SOC, for the Test cycles.

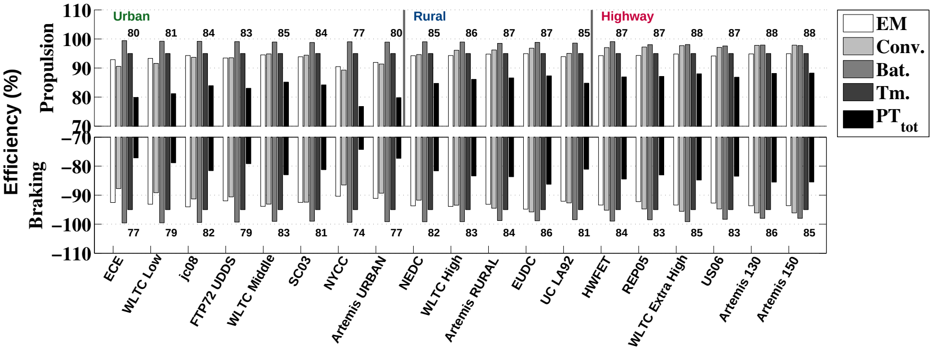

Figure 5.23 Total powertrain efficiency per cycle in propulsion vs. braking mode (negative y-axis), and efficiency broken down per component, from simulation of the Highway car, with 90 % initial SOC, for the Test cycles.

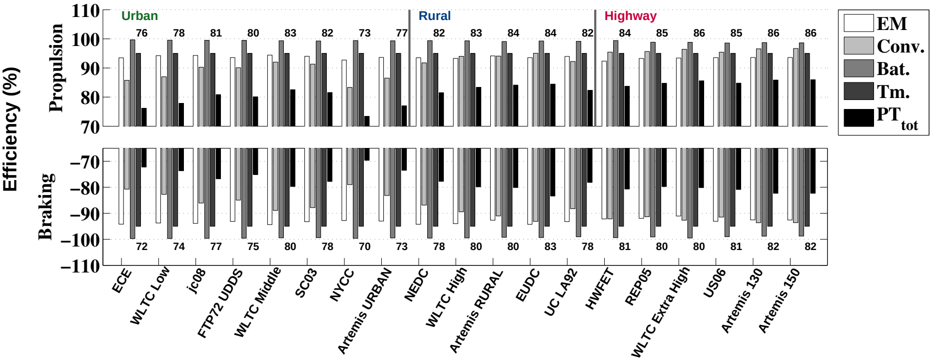

Figure 5.24 Total powertrain efficiency per cycle in propulsion vs. braking mode (negative y-axis), and efficiency broken down per component, from simulation of the Sport car, with 90 % initial SOC, for the Test cycles.

Similarly, the total powertrain efficiency for the Logged cycles can be seen in Figure 5.25 to 5.27, for the City, Highway and Sport cars respectively.

Generally the same trends can also be seen here. Nevertheless, the spread within the Urban and Rural road type categories is here a bit larger. The absolute efficiency values per car, are in line with those for the Test cycles, although a bit lower for the Logged Highway cycles compared to the Highway Test cycles.

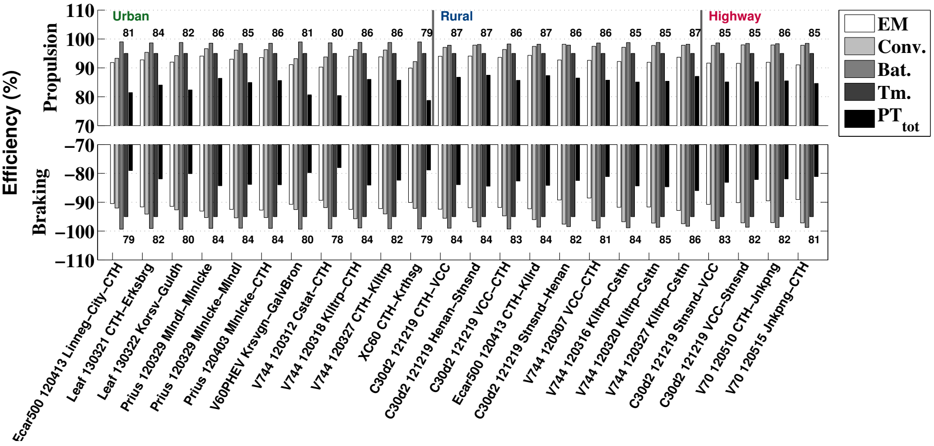

Figure 5.25 Total powertrain efficiency per cycle in propulsion vs. braking mode (negative y-axis), and efficiency broken down per component, from simulation of the City car, with 90 % initial SOC, for the Logged cycles.

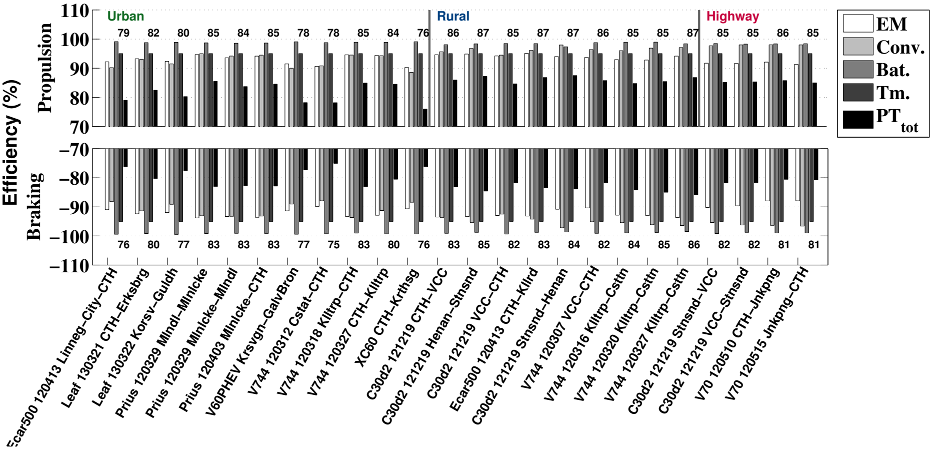

Figure 5.26 Total powertrain efficiency per cycle in propulsion vs. braking mode (negative y-axis), and efficiency broken down per component, from simulation of the Highway car, with 90 % initial SOC, for the Logged cycles.

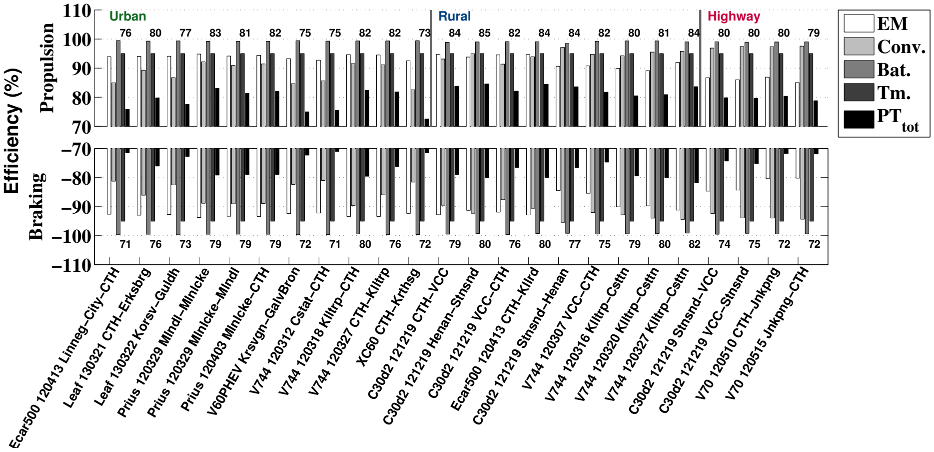

Figure 5.27 Total powertrain efficiency per cycle in propulsion vs. braking mode (negative y-axis), and efficiency broken down per component, from simulation of the Sport car, with 90 % initial SOC, for the Logged cycles.

5.11 Simulated energy per driven distance, per cycle

The resulting battery energy per driven distance of the Test cycles can be seen in Figure 5.28 to 5.30, for the City, Highway and Sport cars respectively. In the figures, data on discharge and charged energy are separated from the net battery energy flow.

Since the average powertrain efficiency is rather similar for all road types, the battery energy consumption per driven distance will to a large part depend on the drive cycle and less on the powertrain. This can also be seen when comparing the relative levels of wheel energy consumption in Figure 4.10, with the simulation results presented here.

There is a rather high coherence between the absolute values of the net energy consumption for the Urban cycles, except for the NYCC and Artemis Urban cycles whom have higher consumption, with the lowest speed levels but the highest acceleration levels. The difference between these two cycles and the rest of the cycles is the smallest for the City car and the largest for the Sport car. The lowest consumption for all cars, can be noted for the ECE cycle, which is explained by its relatively low speed levels and the lowest level of accelerations. This is also despite the relatively low powertrain efficiency for this cycle in all cars.

It can also be seen that the energy consumption of the European test cycle NEDC, is fairly close to the WLTC high and the Artemis Rural, but generally larger than for the Urban cycles and much smaller than for the Highway cycles.

The spread in absolute values is the largest for the Highway cycles, where HWFET has the lowest levels of consumption per distance due to its low speed, while the Artemis Motorway cycles have the highest consumption as well as speed levels. In general, the simulations show a higher energy consumption per driven distance for the Highway cycles.

Those cycles with the highest discharge energy consumption are also those with high or the highest levels of acceleration and RPA value, within the same road type, and in the same time they often have low maximum and average levels of speed. This is valid for NYCC, Artemis Urban, UC LA92 and US06.

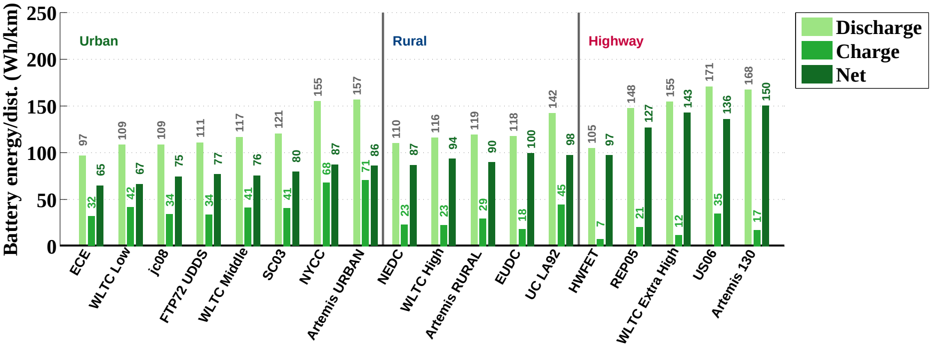

Figure 5.28 Average powertrain propulsion, braking and net energy consumption per driven distance, from simulation of the City car, with 90 % initial SOC, for the Test cycles.

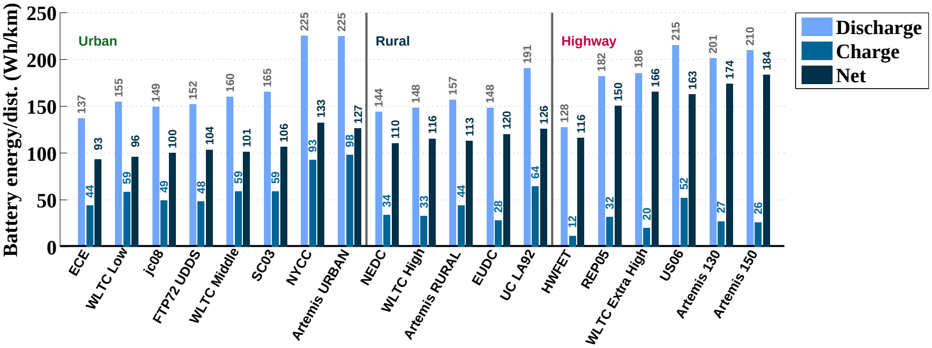

Figure 5.29 Average powertrain propulsion, braking and net energy consumption per driven distance, from simulation of the Highway car, with 90 % initial SOC.

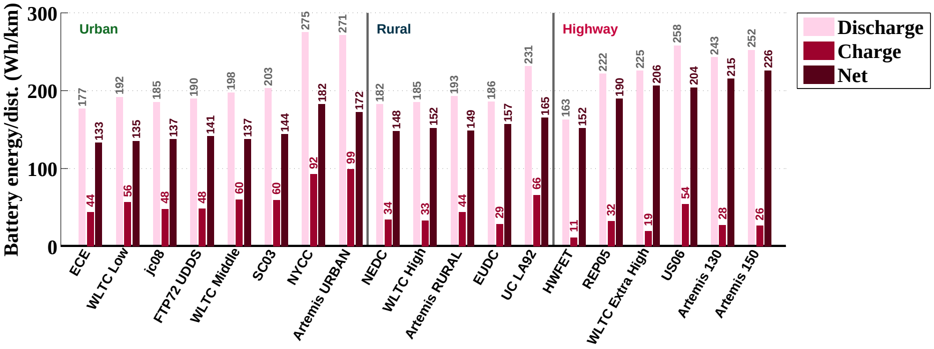

Figure 5.30 Average powertrain propulsion, braking and net energy consumption per driven distance, from simulation of the Sport car, with 90 % initial SOC.

Similarly, the discharge, charged and net battery energy flow for the Logged cycles can be seen in Figure 5.31 to 5.33, for all three cars. Perhaps more examples are needed in order to draw any general conclusions though.

The energy consumption coherence between the Logged road types, is not as high as for the Test cycles, except when it comes to the Highway cycles which are very coherent. Not to forget, for the Logged cycles, not only speed and acceleration but also road grade levels are included in the energy consumption figures shown.

The two cycles with the highest energy consumption for all three cars are the Urban classified cycles; Leaf 130322 Korsv-Guldh and V744 120312 Cstat-CTH. Also the cycle Ecar500 120413 Linneg-City-CTH has a relatively high energy consumption. From Figure 4.15, the reason is a rather long uphill climbing which in these short cycles has a major impact on the energy consumption.

It can also be seen that for the three cycles V744 Klltrp-Csttn at different days, two of them have similar results while the third (120327) have a higher consumption, even though the average powertrain efficiency is somewhat higher for the third case compared to the first two. In Table 3.3 it can be seen that the speed levels are similar, while as seen in Table 3.5 the maximum and average levels of acceleration as well as the RPA value is higher in the third case, hence the higher consumption.

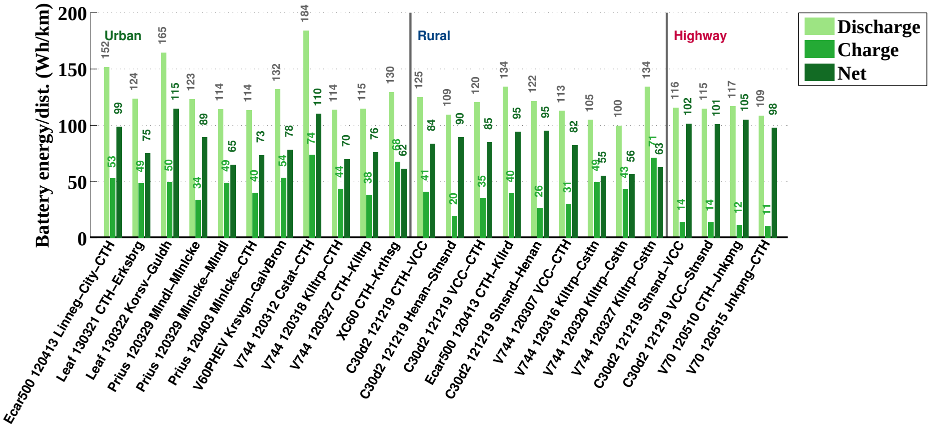

Figure 5.31 Average powertrain propulsion, braking and net energy consumption per driven distance, from simulation of the City car, with 90 % initial SOC, for the Logged cycles

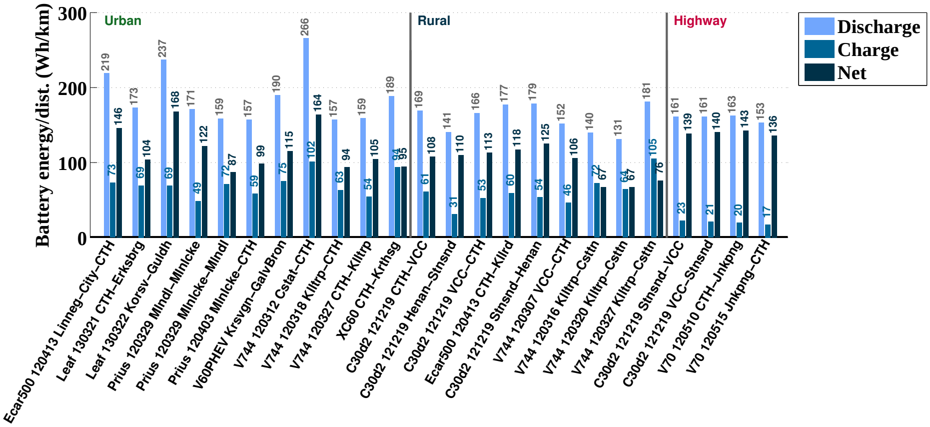

Figure 5.32 Average powertrain propulsion, braking and net energy consumption per driven distance, from simulation of the Highway car, with 90 % initial SOC, for the Logged cycles

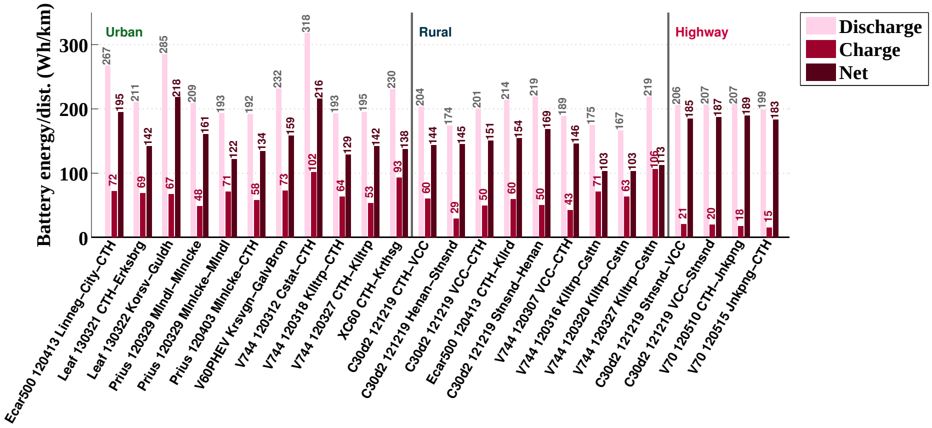

Figure 5.33 Average powertrain propulsion, braking and net energy consumption per driven distance, from simulation of the Sport car, with 90 % initial SOC, for the Logged cycles

5.12 Simulated driving range

Simulation of consecutive NEDC cycles for the City car can be seen in Figure 5.34. The resulting driven distance was $174.7\,km$, which is fairly close to the set requirement of $160\,km$. As can also be seen in the figure, the average powertrain efficiency is consistent over the discharge intervall, which can be expected as the operating points of the NEDC cycle are well within the non field weakening area of the machine even at the lowest level of SOC where the machine efficiency is the same at all voltage levels. The average cycle efficiency is $86\,\%$ in motoring mode and $83\,\%$ in generator mode, which can be compared to the efficiency estimation used ($80\,\%$) when seeking a suitable battery energy content for the range requirement.

The results from the range simulation of the Highway and Sport cars can be seen in Table 5.5. The average powertrain cycle efficiencies are higher than assumed also for the Highway and Sport cars, as can also be seen in the table. The highest average powertrain efficiency is achieved in the City car, as expected from the comparison in Figure 5.10, where the City car showed a higher efficiency for the same speed and acceleration. Given the resulting values of average efficiency, the energy capacity of the batteries could be reduced by about $3 - 10\,\%$.

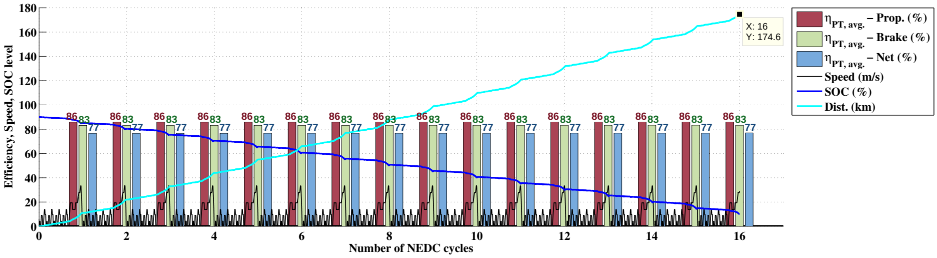

Figure 5.34 Average powertrain propulsion, braking and net efficiency from simulation of City car NEDC driving range.

Table 5.5 NEDC range simulation results compared to requirements.

	City car:	**Highway car:**	**Sport car:**
Requirement	160 km	200 km	300 km
Simulation result	174.6 km	215.7 km	307.2 km
Relative increase	+ 9.2 %	+ 7.9 %	+ 2.4
Propulsion efficiency	86 %	85 %	82 %
Braking efficiency	83 %	82 %	79 %
Net efficiency	77 %	73 %	71 %
Suggested decreased battery size	-1.9 kWh	-1.5 kWh	-1.5 kWh

Based on the simulation results of net battery energy consumption per driven distance, possible driving range has been calculated for all Test cycles with the City and Highway cars, see Figure 5.35 and 5.36. In this illustrative example, the battery energy content is estimated to $80\,\%$ of $19.3\,kWh$, which here results in a NEDC range of $178\,km$. The discrepancy with the value in Table 5.5, may be due to the assumed energy content of the battery which in the simulation varies depending on the load situation. It can be seen that the lower energy consumption for the Urban cycles generally provides $20-50\,km$ more than the NEDC cycle, while the range is shortened by about $50\,km$ for most Highway cycles.

Similarly, for the Highway car, the range increase for most Urban cycles is $10-30\,km$, and the decrease is about $20-90\,km$ for the Highway cycles, see Figure 5.36.

For comparison, the estimated driving range of the Logged cycles for the City car can be seen in Figure 5.37. The ranges are about $130-250\,km$, $160-280\,km$ and $150-160\,km$ for the Logged Urban, Rural and Highway cycles respectively, i.e. a larger variety than for the Test cycles.

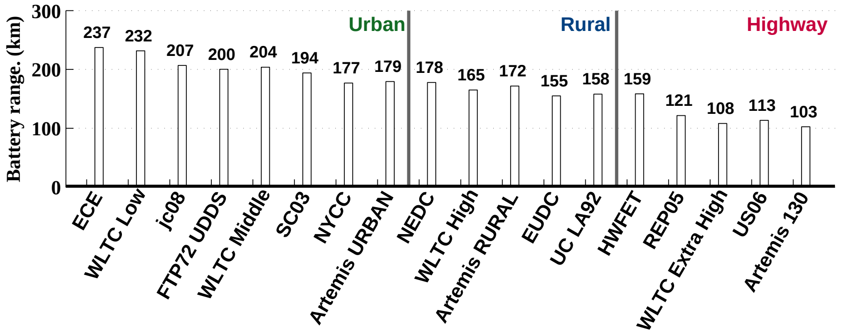

Figure 5.35 Estimated driving range for the Test Cycles with the City car.

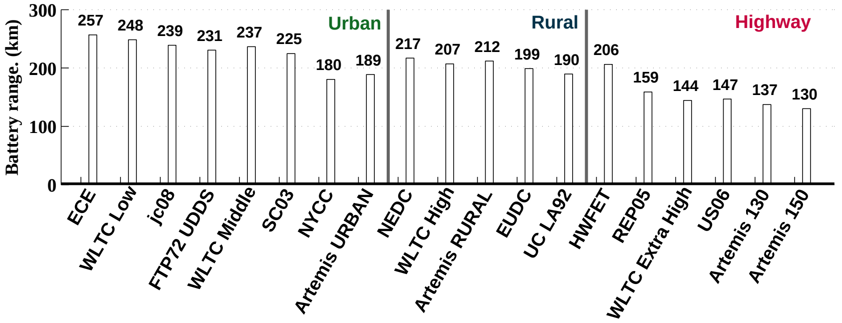

Figure 5.36 Estimated driving range for the Test Cycles with the Highway car.

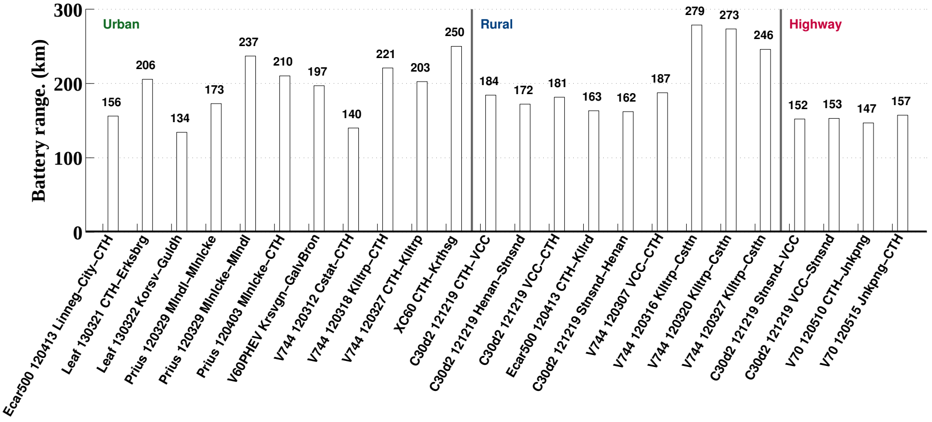

Figure 5.37 Estimated driving range for the Logged Cycles with the City car.

Chapter 6

V-Shaped Reference PMSMs for CityII and HighwayII Concept BEVs

In order to improve the representation of the electromagnetic losses as a function of torque and speed, over those of the inset PMSM used in Chapter 5, a set of new reference electric motors have been designed, evaluated and implemented. They are used in both a re-scaling study (Chapter 7) and in a thermal study (Chapters 8 and Chapter 9). The aim is that the new reference motors are of a representative machine type which can be found in BEVs that are presently available on the market. A thorough market review shows that the PMSM machine is the most widely used motor type in current BEV powertrain's, consequently this type is chosen.

Given the drive system limits, this section further presents the design, material selection and performance of the new reference motors, which are intended for a CityII and a HighwayII concept BEV model that are also presented. Both the CityII and HighwayII BEV motor efficiencies are analyzed at different voltage levels and different stack lengths. Furthermore, the HighwayII BEV motor is analyzed for four different slot areas, while maintaining the same max rms phase current. Each stator geometry is modelled at three different magnet and copper temperatures to account for reduced magnet strength at higher temperatures, as well as increased copper resistivity.

In-depth design optimizations to enhance various performance measures, are however not considered.

6.1 CityII and HighwayII concept BEVs

Similar to what is done in Chapter 4, two new BEVs are conceptualized, based on an updated review of performance data on commercially available BEVs, as presented in Appendix A. Their performance requirements are presented in Table 6.1.

There are only small differences in requirements between the new CityII and HighwayII BEVs compared to the City and Highway BEVs in Chapter 4. They all share the same curb weights, NEDC range, and gradeability requirements. In contrast, both the CityII and HighwayII BEVs have slightly lower top speed values, lower tire rolling resistance coefficients, and a bit larger aerodynamic drag coefficients. Other parameters are subject to only small changes.

As in Chapter 4, three different combinations of max force and power are investigated, in order to reach the required acceleration times; i.e. base speed values that are 1/4, 1/3 and 1/2 of the top speed.

In order to prioritise the low speed performance of the CityII BEV, the relation between base and top speed is chosen to be small: i.e. 1/4. This gives a 0-50km/h acceleration time of 3.9s, and 31m, instead of 4.4s or 5.7s for the other two considered cases. The max wheel power needed is then about 45 kW and the max force about 5 kN, which gives a max wheel torque of about 1.5 kNm.

For the HighwayII BEV, the case of base speed as being 1/3 of the top speed is chosen. This gives a 0-50km/h acceleration time of 3.8s and 34m, instead of 3.3s or 4.7s for the other two cases. The max wheel power needed is then about 87 kW, the max wheel force is 6.5 kN, and the max wheel torque is 2 kNm.

Thus, both the CityII and HighwayII concept BEVs have similar low speed acceleration performances, whereas the HighwayII BEV have better high speed performance. Consequently, the 50-100km/h acceleration time is around 6s for the HighwayII BEV and about 9s for the CityII.

Table 6.1 Prerequisites for the new concept CityII and HighwayII BEVs used in Chapter 7, 8, and 9.

	CityII	**HighwayII**	
Seats	4-5	5	
Curb weight	1200	1700	kg
Acceleration 0-100 km/h	13	11	s
Top speed	130	145	km/h
NEDC Range	160	200	km
Aearod. drag coeff. C_d	0.31	0.29	$-$
Area	2.1	2.3	m^2
Wheel radius	0.30	0.32	m
Rolling resist. coeff. C_r	0.007	0.007	$-$
Starting gradability	25 %	25 %	%
Gradability (Speed at grade)	90 at 6%	130 at 6%	km/h, %

6.2 Design, material and mass of machine parts

PMSM motors can be found in at least 14 out of the 21 most sold highway capable BEV models, as is shown in Appendix A. Other types are IMs found in three of the models, wound rotor SM found in two and HSM (hybrid synchronous) or PM assisted SR (synchronous reluctance) machine found in one of the most sold models.

Detailed data on implemented electric motors in vehicles are seldom published, however there are some publications by Nissan on their 2011 and 2013 Leaf models in [94–97]. Furthermore, there are a number of publications from the US Department of

Energy science and energy laboratory ORNL (Oak Ridge National Laboratory), covering the electric powertrain in HEVs such as Toyota's Prius 2004 and 2010 and Camry 2007, Honda Accord 2014, Lexus LS 600h 2008, as well as the BEV Nissan Leaf 2011, e.g. in [98–100]. Although the motors in these vehicle models are of different power ratings and volumes, they share some common design features. They are all IPM (interior permanent magnet) SM motors with 48 stator slots, 8 poles, and distributed windings. The magnets in the rotor are configured in a V-shape in all models, except in Leaf and LS 600h where also a third magnet is used close to the air gap (forming a ∇-shape). This machine type is known to fulfill design goals such as high torque and power density, high efficiency and wide constant power region, which are all highly desired in EVs [101].

The reference IPM SM stator and rotor core lamination designs are similar to that of the Toyota Prius 2004 motor, with 48 stator slots and 8 poles. However, the stator teeth and yoke are thinner, and a different angle for the V-shaped magnet arrangement is used. Furthermore, the three phase winding is distributed, but with two layers, and four parallel branches. The copper fill factor in the slot area is set to 45%. This is in line with the fill factor of industrial IMs, which are in the range 35%-45%, according to [102].

The reference machine geometry is scalable, both by core length and diameter, hence a suitable machine size can easily be found for any desired peak torque performance and length-to-diameter ratio. One reference machine is designed for the CityII BEV and one for the HighwayII. Both have length-to-diameter ratios around 0.8, which during length scaling between 50-200% of the reference length, gives length-to-diameter ratios between about 0.4-1.6.

The dimensioning is done considering a max dc voltage of 400 V for both motors, and the max speed is limited to 12,000 rpm. The voltage and speed values are in line with what has been found for EMs in current BEVs, as shown in Appendix A. The number of turns per coil is then adjusted in order for field weakening to start at around 3000 rpm for the CityII EM and 4000 rpm for the HighwayII.

The gear ratios, k_{gear} are simply taken as the relation between the top speed of the motor and wheel as in (5.4). With an assumed transmission efficiency of 97%, the max electric motor output torque and power are determined to be about 46 kW and 147.5 Nm for the CityII BEV, and about 89 kW and 214 Nm for the HighwayII BEV.

The max rms current density $J_{rms,max}$ in the slot is initially set to 20 A/mm^2 (28.3 A peak). The max rms phase current is then proportional to: the max rms current density; the slot fill factor k_{ff}; the slot area A_{slot}; and the number of parallel branches n_{npb}, and inversely proportional to the number of layers n_{layer} and turns per coil n_{tpc}, as in

$$I_{ph,rms,max.} = \frac{J_{rms,max}\, k_{ff} A_{slot}}{n_{layer}} \frac{n_{npb}}{n_{tpc}} \tag{6.1}$$

The assumed machine configuration is shown in Figure 6.1, along with an illustration of the active machine parts, i.e. the parts that contribute to torque production. For simplicity, the machine configuration is limited to the main components: active parts, end winding, frame, shaft and bearings. Selected machine data are shown in Table 6.2, for the CityII and HighwayII reference motors.

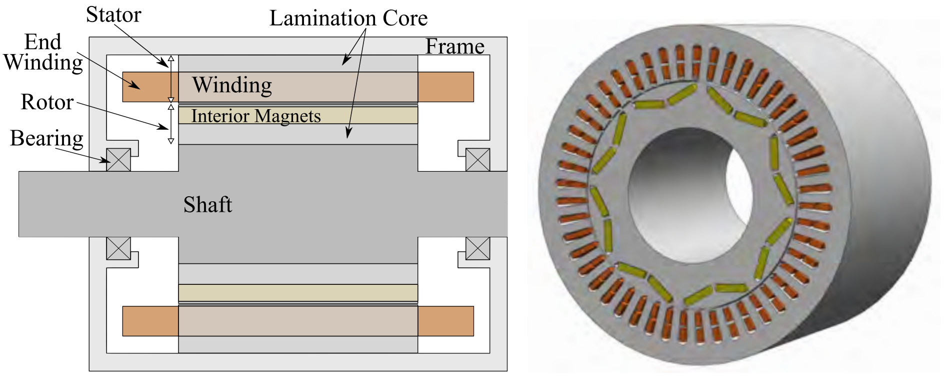

(a) Cross section.

(b) Active parts.

Figure 6.1 Axial cross section of machine configuration, and the active machine parts, of V-shaped reference motors.

Table 6.2 Summary of PMSM data for the CityII and HighwayII BEV motors.

	CityII	**HighwayII**
Peak Power	46 kW	89 kW
Max Torque	147.5 Nm	214 Nm
Base speed	3000 rpm	4000 rpm
Max speed	12,000 rpm	12,000 rpm
Gear ratio	10.440	9.984
Max DC voltage	400 V	400 V
Max rms current density	20 A/mm^2	20 A/mm^2
Max rms phase current	125 A	251 A
Peak Efficiency at 400 V_{dc}	96.4 %	97.1 %
Core length	136 mm	150 mm
Core stacking factor	0.95	0.95
Lamination thickness	0.3 mm	0.3 mm
Number of slots	48	48
Number of poles	8	8
Stator outer diameter	166 mm	182 mm
Stator inner diameter	112.05 mm	122.85 mm
Stator yoke thickness	9.445 mm	10.365 mm
Tooth width	4.33 mm	4.52 mm
Tooth height	17.53 mm	19.21 mm
Slot opening width	1.66 mm	1.82 mm
Slot area	69.67 mm^2	83.74 mm^2
Slot fill factor	45%	45%
Turns per coil	10	6
Coils per pole per phase	4	4
Rotor outer diameter	110.81 mm	121.485 mm
Rotor inner diameter	66.4 mm	72.8 mm
Air gap length	0.62 mm	0.6825 mm
Magnet thickness	3.7765 mm	4.1405 mm
Magnet width	14.94 mm	16.38 mm

6.2.1 Frame

The frame is assumed to be a hollow cylinder with an end cap on each side, all with a thickness of 11 mm, and to be without any complex textures, for simplicity. The outer frame diameter is 102 mm and the length 262 mm. Furthermore, it is assumed to be made of a die cast aluminum alloy (as in Nissan Leaf [94]), for a lightweight yet mechanically strong construction, with good thermal conductivity. It also includes a spiral cooling channel for liquid cooling, see Section 8.1.1.

A number of different aluminum alloys are used for this purpose today, and their net thermal conductivity is less than that of pure aluminum, which is 237 W/mK at 300K [48]. In publications regarding thermal modelling of electric motors, the value of thermal conductivity of the frame's aluminum alloy is seen to vary between 150 to 230 W/mK [20, 49, 53, 103]. It is here assumed that the aluminum alloy 195 is used for the frame, which has a thermal conductivity of 168 W/mK at 300 K, a specific heat of 883 J/kgK, and a density of 2790 kg/m^3, [45, 48].

6.2.2 Core lamination

The chosen lamination material is the 0.3 mm thick NO30 by Tata Cogent [104]. This thickness is in line with published data of Toyota's, Lexus' and Nissan's electric motor laminations; which are 0.28-0.31 mm [94, 100]. The material's B-H curve and loss data are shown in Figure 6.2, along with the resulting approximated loss curves by the FEA software program Ansys Maxwell. The FEA core losses are calculated as in (2.15), where $k_h = 0.0583049\, W/kg$, $k_c = 2.653\, 10^5\, W/kg$, and $n = 2$.

The density of the NO30 grain is taken to be 7540 kg/m^3, the thermal conductivity 31 W/mK, which is a typical value at $100°C$, and the specific heat 557 J/kgK also at $100°C$ [105]. Temperature dependency for thermal conductivity and specific heat is presented in Appendix D.

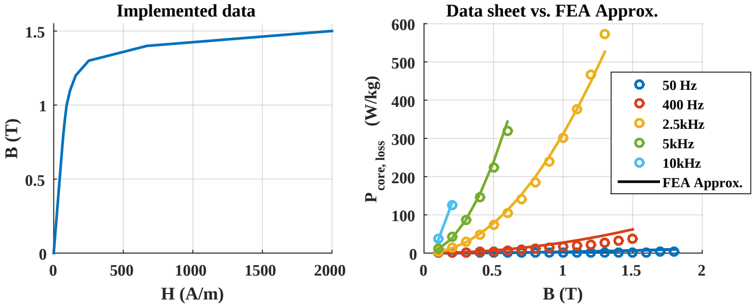

Figure 6.2 Data sheet and implemented data for the chosen lamination material, NO30.

6.2.3 Magnets

A permanent magnet is mainly characterized by its remanent flux density, Br (T), and its ability to withstand demagnetization, or coercivity, Hc (A/m), both of which are temperature dependent. Permanent magnets consisting of NdFeB (neodymium iron boron) are commonly used in today's EVs, so also in Toyotas, Hondas, Lexus' and Nissans models [99]. Published measurements indicate that the Br value for the motors in Prius 2010, LS600h and Camry 2007 are at least 1.3 T at 20°C, and at least 1.1 T at 100°C, whereas Hc is between -1220 to -1440 kA/m at 100°C [100]. Their temperature capability seem to be around 180-200°C, or maybe even as low as 160°C for Prius 2010.

The temperature capability of NdFeB magnets in electric vehicles, is often improved by substituting some of the Nd for Dy (dysprosium). This additive helps to increase Hc, and to maintain high values of Hc at higher temperatures, however it also reduces the Br somewhat. According to [106], typical values of Dy content in EV magnets, during 1985 to 2011, were 8.5-11% of the magnet weight, which represent temperature capabilities around 200-220°C. A similar value is also presented in [107], where a Dy content of 8.7w% is said to be typical for EV drives. However, due to a sudden and substantial price increase of Dy in 2011, which is not yet fully recovered, magnet manufacturers are currently seeking to reduce the amount of Dy [106]. As an example, Nissan claims to have lowered the Dy content by 40% in their 2013 Leaf model compared to the 2011 model [97]. One publication from 2012, indicate that very low Dy contents may be used in EVs, on an average 3.6-4w%, and single values up to 7.7w% [108], which represents temperature capabilities around 150°C and 180°C, according to [106].

For this reason, a magnet with a relatively low Dy content is chosen for the reference motors; Hitachi NEOMAX NMX-37F, which is expected to have around 3.5-4.5w% Dy [109]. The material data is shown in Figure 6.3 [110], which indicate a temperature capability up to 140°C. The Br value is around 1.2 T at 20°C, and drops to 1.1 T at 140°C, whereas the Hc value is about -940 kA/m at 20°C, and -790 kA/m at 140°C. As expected, the Hc values are a bit lower compared to Toyotas and Lexus' magnets, which thus both can be assumed to have a larger Dy content.

The magnet density is taken to be 7500 kg/m^3, the thermal conductivity as 7.5 $W/m\,K$, and the specific heat as 410 $J/kg\,K$, as stated by Hitachi [111]. The electric conductivity is taken to be 1.3 $\mu\Omega m$, and assumed to adhere to 20°C [111]. The temperature coefficient of resistivity is here assumed to be 0.5%/°C, which gives an electrical conductivity of 750 469 S/m at 70°C. The considered magnet material properties at 20°C, 70°C and 120°C are presented in Table 6.6.

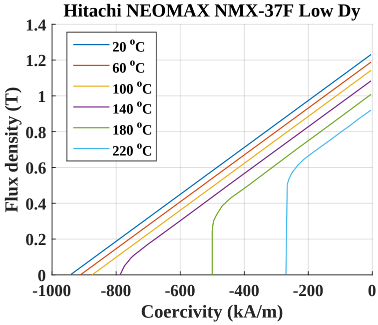

Figure 6.3 Data sheet data for chosen magnet material [110].

6.2.4 Other machine parts and material summary

The windings are made of copper that is assumed to have a density of 8933 kg/m^3, thermal conductivity of 401 $W/m\,K$, and specific heat of 394 $J/kg\,K$, which all adhere to $100°C$ [45]. The copper resistivity at $20°C$, $\rho_{Cu,20}$ is taken to be $1.68\,10^{-8}$ Ωm, and the temperature coefficient α to be 0.3862 $\%/K$. The resistivity, ρ_{Cu} at other temperatures T, are calculated as

$$\rho_{Cu}(T) = \rho_{Cu,20}[1 + \alpha(T - 20)] \tag{6.2}$$

The air is assumed to have a thermal conductivity of 0.03095 W/mK, and density of 0.9458 kg/m^3, which all adhere to $100°C$ [48]. Temperature dependency parameters for air is presented in Appendix D.

The mass density of the winding impregnation is assumed to be 1350 kg/m^3, and the specific heat 1700 $J/kg\,K$, which is also used in [20, 53], and stated as unsaturated polyester.

The shaft is assumed to have a length of 306 mm and a diameter of 40 mm except for the part along the lamination stack, which is assumed to extend to the inner rotor lamination boundary (i.e. a diameter of 72.8 mm). Furthermore, the shaft is assumed to be solid and to be of carbon-silicon steel with the density 7817 kg/m^3, thermal conductivity of 51 $W/m\,K$ [48]. The temperature dependency of the thermal conductivity is presented in Appendix D.

The ball bearings for the HighwayII machine, are assumed to each have a width of 15 mm, and inner and outer diameters of 40 mm and 68 mm respectively. The mass of one unit is assumed to be 190 g, as is commonly found for this size of ball bearings from the bearing manufacturer SKF [112].

Table 6.3 Material properties of motor parts.

	Density (kg/m^3)	**Thermal Conductivity** $(W/m\,K)$	**Specific Heat** $(J/kg\,K)$
Air	0.9458	0.03095	-
Frame	2790	168	883
Laminations	7540	31	557
Winding	8933	401	385
Winding slot impregnation	1350	0.2	1700
Magnets	7500	7.5	410
Shaft	7817	51.9	446

6.2.5 Mass of machine parts

The machine mass is estimated based on the simplified assumed configuration shown in Figure 6.1. For the active components, the mass is a product of density and volume, where volume is a product of cross sectional area and core lamination stack length. The cross sectional area of the end winding is assumed to be the same as that of the active winding. The end winding length is estimated using (5.3), with an assumed axial extent of 35 mm on each side of the lamination stack.

The mass of the different motor parts for the CityII and HighwayII BEV motors are presented in Table 6.4. Information regarding slot impregnation material is given in Section 8.1.4.

Table 6.4 Mass (kg) of selected main motor components for CityII and HighwayII motors.

	CityII	**HighwayII**
Frame	4.7	5.5
Stator Yoke	4.5	6.0
Stator Teeth	3.7	4.9
Active winding	1.8	2.4
Slot impregnation	0.3	0.4
End Winding	1.7	2.2
Magnets	0.9	1.2
Rotor laminations	5.0	6.7
Shaft	4.6	5.8
Bearings	0.4	0.4
Total Lamination	13.3	17.6
Total Copper	3.5	4.6
Total Passive Parts	11.6	14.3
Total Active Parts	16.0	21.2
Total	**27.6**	**35.5**

6.3 FEA evaluation of performance and losses

The reference motors have been simulated in 2D, in the electromagnetic FEM software Ansys Maxwell. The simulated machine geometry and mesh density is shown in Figure 6.4, including a few example results. For simplicity, the lamination stacking factor is ignored in all electromagnetic simulations.

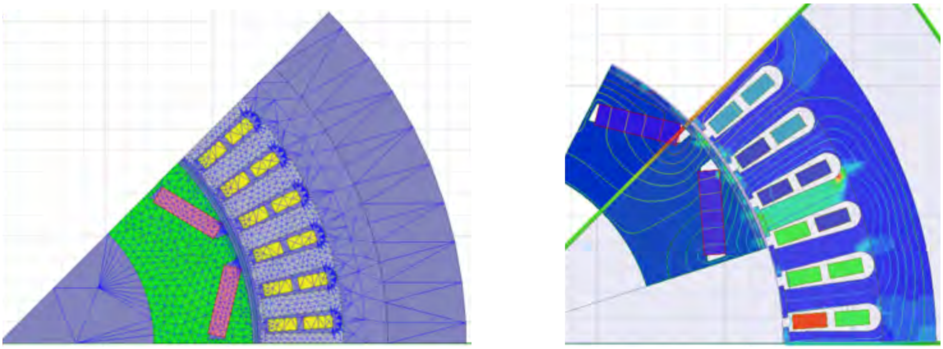

(a) Mesh.

(b) Flux lines, total losses and current density.

Figure 6.4 FEA of one pole of the HighwayII motor at 4000 rpm, 251 A rms, showing mesh, vector potential flux lines, total losses in the core and magnets, as well as current density in the windings, at a certain time instant.

For each machine geometry, at 13 different speed levels (i.e. at 1 rpm, and at every 1000 rpm up to 12,000 rpm), 11 × 11 operating points in the id-iq plane have been evaluated for two electrical periods, with 101 sample points. Sinusoidal current excitation have been used in all operating points. The data resolution in the id-iq-plane is then increased through interpolation, as shown in Figure 6.5(a). From this, the MTPA (Max Torque Per Ampere) operating points as well as the field weakening operation is numerically found for each integer torque level, within the allowed operating current and voltage limits, as exemplified in Figure 6.5(b). A final interpolation in the speed range is then conducted.

Selected data mainly consist of losses in the different machine parts, e.g. lamination losses in the stator yoke, teeth, and rotor, dc resistive losses in the active part of the winding, and eddy current losses in the magnets.

For the HighwayII motor, these motor simulations have been done for three additional slot areas apart from the already presented motor geometry (further treated in section 6.7). For all of the four slot geometries the simulations are done at the three different magnet temperatures; $20°C$; $70°C$ and $120°C$, (section 6.6). For the CityII motor, the simulations are done for a single geometry with magnet and copper temperatures of $70°C$ (section 6.4). Finally, for both the CityII and the original geometry of the HighwayII motors, simulations are done at half and double the stack length with a magnet and copper temperature of $70°C$ (section 6.5).

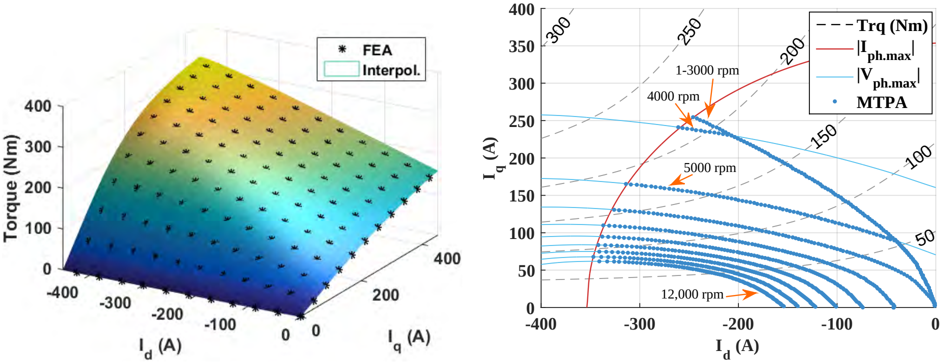

(a) FEA operating points and interpolated torque.

(b) Result of current control algorithm.

Figure 6.5 FEA simulated operating points for each speed level along with resulting interpolated torque, and current control id iq reference values for each integer torque level, at 1 rpm and every 1000 rpm up to max speed.

Both components of the core losses (hysteresis and eddy) increase with increasing machine speed, as shown in Figure 6.6 for the two speed levels 4000 rpm and 12,000 rpm. The figure also shows the transient behaviour of the hysteresis losses in the FEA software program over the two simulated electrical periods, as well as the used mean value over the last period.

Eddy current losses in the magnets arise due to variation of flux density during operation. In the FEA software the magnets are modeled as zero current carrying coils while considering eddy effects. As mentioned, the conductivity values used are presented in Table 6.6.

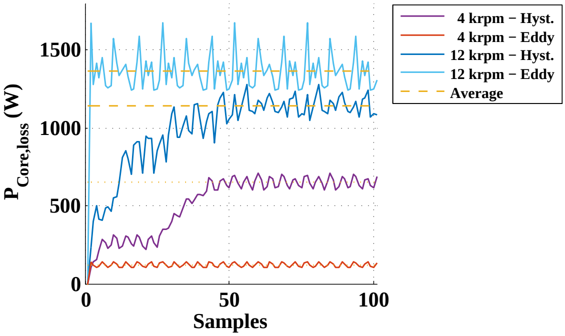

Figure 6.6 Lamination core losses at around 250 A rms, 4000 rpm and 12,000 rpm, for the HighwayII motor.

The copper losses in the active part of the winding are extracted from the FEA software. Skin and proximitys effect is here ignored. Then the total copper losses are found via the relative length of the active part of the winding, by again using (5.3). The end winding losses are simply the difference between the total and the active part. For the HighwayII reference motor, the active part is 52% of the total winding length, thus leaving 48% to the end windings.

6.3.1 Losses and efficiency of the HighwayII motor

The resulting loss components and efficiency for the HighwayII motor are presented for the whole operating area in Figure 6.7, with the magnet and copper temperature of $70°C$.

The magnet losses are the lowest of all losses, only up to 13 W. Thus, the two dominating loss mechanisms are resistive copper losses and lamination core losses.

As the copper losses depend on the square of the current, their torque-speed-dependence resembles that of the current magnitude's. Below base speed there is no speed dependence, but there is thus a strong torque dependence. However, above base speed a larger current is needed (at the same torque level) in order to suppress the magnetic flux from the magnets, i.e. field weakening operation. At any given speed level, the copper losses are the largest at the max torque level.

Both lamination and magnet losses strongly increase with speed, and somewhat with torque. The lamination core losses reach the highest levels in the stator teeth, at least well above base speed. The largest values are reached above 10,000 rpm close to the max torque levels. The rotor core losses are relatively low, yet they also increase rather much at combinations of high torque and speed.

For this reason, the peak total loss of about 6.4 kW is found at the combined max torque and speed operating point. The efficiency is over 90% in a large part of the operating area, and reaches at most above 97.1%.

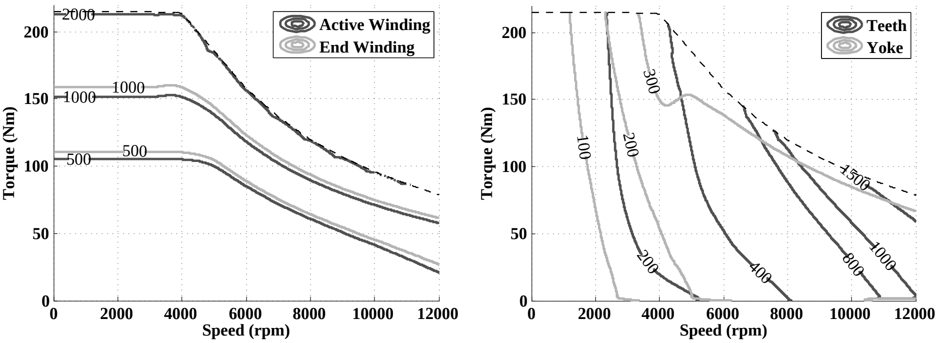

(a) Winding losses in W.

(b) Stator lamination losses in W.

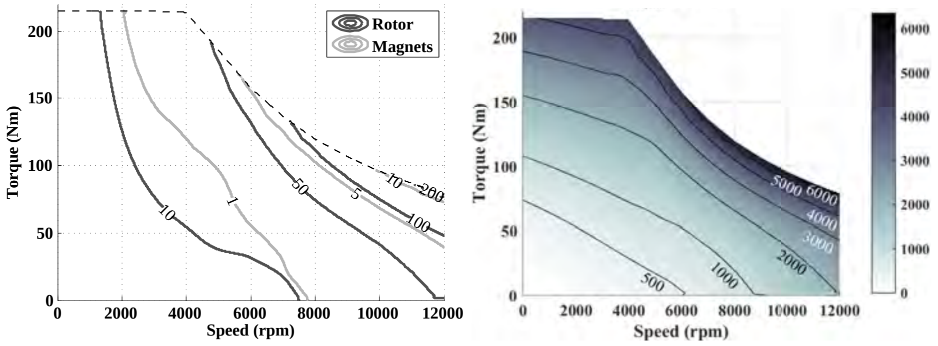

(c) Magnet and rotor lamination losses in W.

(d) Total losses in W.

Figure 6.7 Electromagnetic losses as a function of torque and speed, for the HighwayII V-shaped reference motor.

The percent ratio of total copper losses over total motor losses is presented in Figure 6.8(a). Generally, the copper losses dominate for torque levels above 50 Nm. As copper and core losses are the two main loss components, the rest of the losses in the figure adhere to the core losses. Generally, the core losses are the main loss components for speed levels above about 2000 rpm and torque levels below 50 Nm. Consequently, core losses can be expected to dominate in drive cycles with low acceleration levels and relatively high speed levels, whereas copper losses can be expected to dominate in drive cycles with higher acceleration levels.

Finally, the percent ratio of core losses in the teeth over the total core losses is presented in Figure 6.8(b). At speed levels below 6000 rpm around 50-60% of the core losses are developed in the teeth. At higher speed levels the share increases to about 80% at top speed. A similar study of the rotor reveals that its core losses are essentially well below 10% of the total core losses in the whole operating area. This means that the rest of the loss share shown in Figure 6.8(b) principally adhere to the stator yoke.

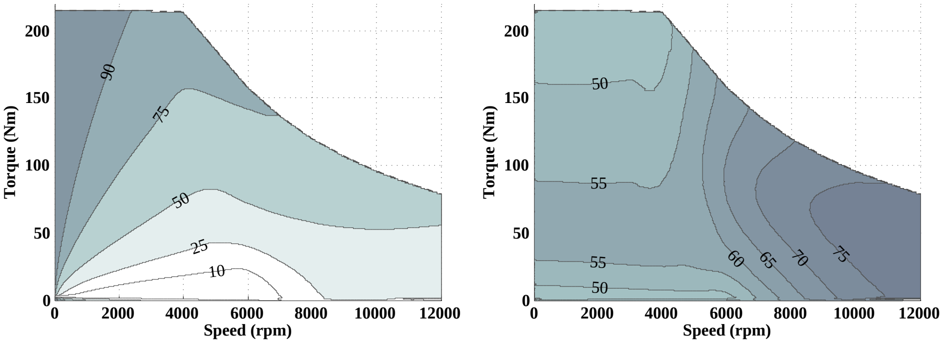

(a) Share of total copper losses to the total electromagnetic losses, in %.

(b) Share of lamination teeth losses to the total stator and rotor lamination losses, in %.

Figure 6.8 Share of total losses as a function of torque and speed, for the HighwayII V-shaped reference motor.

6.4 CityII and HighwayII motor efficiency with different dc voltage limits

Due to the dynamic behaviour of the battery voltage during vehicle operation, the motor losses and efficiency are calculated for different levels of available dc voltage (between 250-450V), as presented in Figure 6.9. In all cases the max rms phase current is unaltered.

If the max available voltage is increased, field weakening control can start at a higher speed level, compared to a lower max voltage. In the same time, with a higher max voltage a lower field weakening current is needed in the same operating point, again compared to the case of a lower max voltage. The result is that a higher max voltage leads to a higher efficiency in the field weakening region.

Also the max power increases with increased available voltage. The max power is linearly proportional to the change in available voltage, and changes about 25 kW per 100 V for the HighwayII motor (or 11%-21%). Specifically, for the HighwayII motor the max power is 114 kW with 450 V, whereas it is 62 kW when 250V is available.

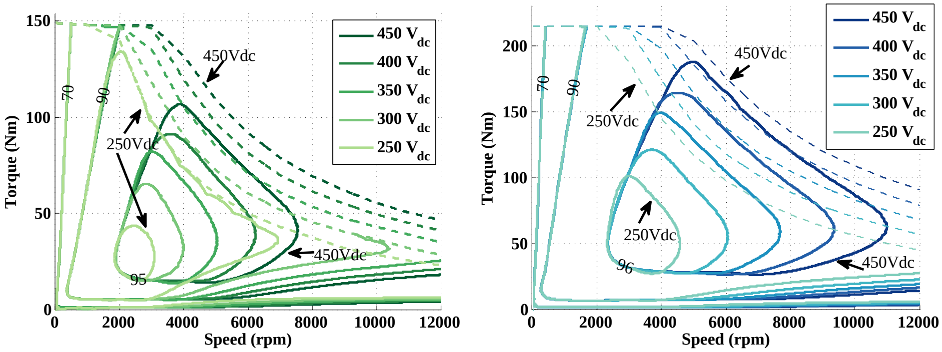

(a) CityII motor.

(b) HighwayII motor.

Figure 6.9 Electromagnetic efficiency contour lines at different levels of max dc voltage, for the CityII and HighwayII V-shaped reference motors.

6.5 CityII and HighwayII motor efficiency at 50%, 100% and 200% of stack length

Similarity as in Section 5.1.3.1, the stack length of the CityII and HighwayII motors are scaled linearly. During the length scaling the cross sectional geometry is unaltered, as is the dc voltage limit of 400 V, as well as the max rms current density of 20 A/mm^2. However, the number of turns per coil are changed in order to keep the same base and max speed. When changing the stack length of the motors under these conditions, the passive end winding losses remains the same, whereas the active losses are linearly proportional to the stack length.

The mass of the motors are estimated as the sum of the parts that scale with the stack length $m_{l_{stk}}$, and those parts that don't m_{ext}. The parts that scale with the stack length are: both the stator and rotor laminations, the magnets, the active part of the winding, as well as those part of the frame and shaft that are within the stack length. The scaling factor $f_{l_{stk}}$ represent the ratio of the scaled stack length and the reference stack length, i.e. it is 0.5 to 2. The mass of a scaled motor is thus

$$m_{EM_{scaled}} = m_{lstk} + f_{l_{stk}} m_{ext} \tag{6.3}$$

The resulting mass of the re-scaled CityII and HighwayII motors are presented in Figure 6.10. Even though the motor masses change from 60% to 180% of the reference motors, the effect on the vehicle mass is less than 1% for the 50% scaling factor and less than 2% for the 200% scaling factor, for both vehicles.

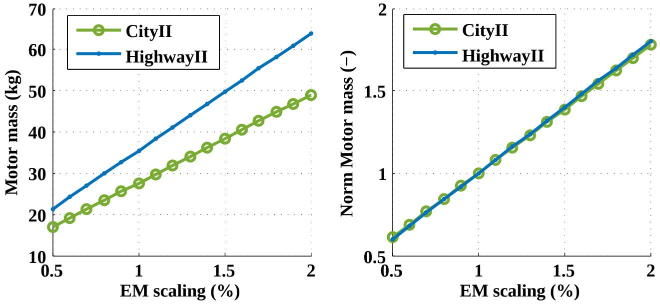

Figure 6.10 Mass of CityII and HighwayII re-scaled motors, and motor masses normalized by the reference motors.

Simulations are done at all three length scalings: 50%, 100% and 200% of original stack length. The losses and efficiency maps from the simulations are essentially identical to the results when simply scaling the active part of the losses with the same factors as the stack length. For simplicity, it therefore the latter method that is used for intermediate length scalings of losses and torque levels, and the resulting efficiencies is presented in Figure 6.11. Additionally, selected data on three scalings for both motors are presented in Table 6.5.

Table 6.5 Selected data on min and max length scaling of CityII and HighwayII V-shaped reference motors.

CityII motor	$L_{stk,min}$	$L_{stk,ref}$	$L_{stk,max}$
Core length	68 mm	136 mm	272 mm
Turns per coil	20	10	5
Max rms phase current	63 A	125 A	251 A
Active winding share	34%	51%	67%
$R_{s,Tot}$	204 $m\Omega$	68 $m\Omega$	26 $m\Omega$
$R_{s,ActWi}$	70 $m\Omega$	35 $m\Omega$	17 $m\Omega$
$R_{s,EndWi}$	134 $m\Omega$	34 $m\Omega$	8 $m\Omega$
Motor mass	16.9 kg (61%)	27.6 kg (100%)	49.1 kg (178%)

HighwayII motor	$L_{stk,min}$	$L_{stk,ref}$	$L_{stk,max}$
Core length	75 mm	150 mm	300 mm
Turns per coil	12	6	3
Max rms phase current	126 A	251 A	502 A
Active winding share	35%	52%	69%
$R_{s,Tot}$	65 $m\Omega$	22 $m\Omega$	8 $m\Omega$
$R_{s,ActWi}$	23 $m\Omega$	11 $m\Omega$	6 $m\Omega$
$R_{s,EndWi}$	42 $m\Omega$	10 $m\Omega$	3 $m\Omega$
Motor mass	21.3 kg (60%)	35.5 kg (100%)	63.9 kg (180%)

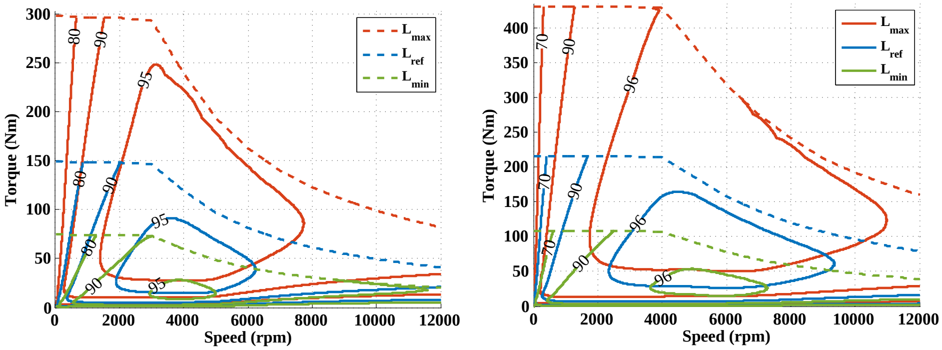

(a) CityII motors.

(b) HighwayII motors.

Figure 6.11 Electromagnetic efficiency contour lines (%) for three different length scalings of the CityII and HighwayII motors.

6.6 HighwayII motor losses at three magnet and copper temperatures

Simulations have been done with magnet and copper temperatures at $20°C$, $70°C$ and $120°C$ using the magnet materia data in Table 6.6. As presented in the table, the magnet strength (B_r) decreases with increasing temperature. Since the max current does not differ between the cases, this thus also lead to a decreased max torque with increasing temperature.

Table 6.6 Magnet simulation input data, phase resistance, and resulting max torque and power at three temperatures of magnets and copper.

	$20°C$	**$70°C$**	**$120°C$**
Remanent flux	1.236 T	1.1824 T	1.1244 T
	(100%)	(95.66%)	(90.96%)
Relative permeability	1.0432	1.0428	1.0446
Coercivity	-942,926 (A/m)	-902,285 (A/m)	-856,586 (A/m)
Conductivity	769,231 (S/m)	750,469 (S/m)	732,601 (S/m)
Phase resistance	18 $m\Omega$	22 $m\Omega$	26 $m\Omega$
	(100%)	(119%)	(139%)
Max torque	220 Nm	215 Nm	210 Nm
	(100%)	(97.7%)	(95.5%)
Max power	5.7 kW	6.4 kW	6.9 kW

Due to the weakening of the magnet, at a certain torque level outside the field weakening area of operation, a larger current is needed at a higher temperature compared to a lower. In contrast, within the field weakening area, the weaker magnet leads to a reduced need for field weakening current, especially at the lower torque levels. Therefore, at a certain torque level a lower current is needed for higher temperatures compared to lower. This is illustrated in Figure 6.12(a).

This reasoning also explains the presented copper losses in Figure 6.12(b), since copper losses are proportional to the square of the rms current. Naturally, also the winding resistance increase with temperature, which further enhances the differences of the copper losses' behaviour in the torque-speed diagram between the studied temperatures. Due to the linear dependency on current for the torque and the quadratic dependency for the winding losses, the difference in losses between the three temperatures increase as the torque becomes higher.

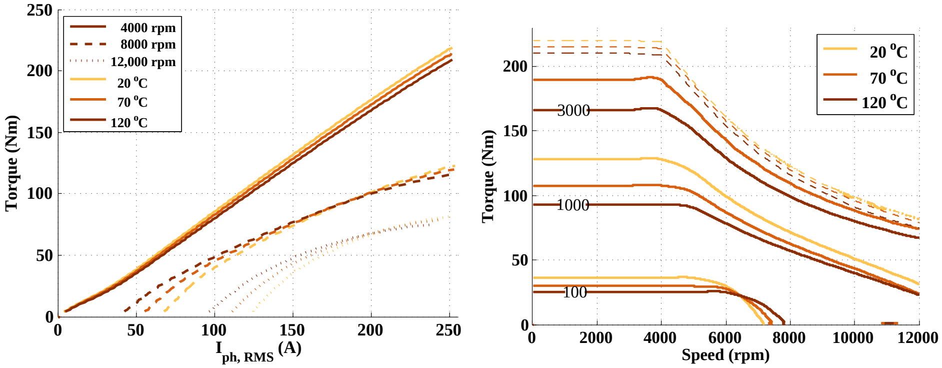

(a) Torque per input phase rms current.

(b) Winding loss contour lines at 100 W, 1000 W and 3000 W.

Figure 6.12 Produced torque per applied rms phase current, and total winding losses as a function of torque and speed, for the HighwayII V-shaped reference motor, at winding and magnet temperature 20°C, 70°C and 120°C.

The lower field weakening current also cause minor deviations in the magnet losses in the torque-speed diagram shown in Figure 6.13(a).

Finally, the resulting total losses for the three different temperatures are presented in Figure 6.13(b).

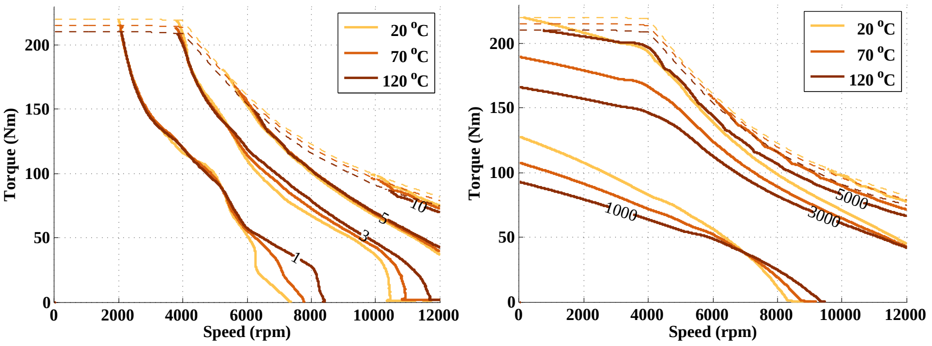

(a) Magnet loss contour lines at 1 W, 3 W, 5 W, and 10 W.

(b) Total losses at 1 kW, 3 kW and 5 kW.

Figure 6.13 Magnet and total losses as a function of torque and speed, for the HighwayII V-shape reference motor, at winding and magnet temperature 20°C, 70°C and 120°C.

6.7 HighwayII motor losses for four slot areas

FEA simulations have been done for the HighwayII motor with four different slot areas: Small, Original, High and Large, shown in Figure 6.14. For the Small and Large slots both the height and width are changed compared to the Original slot, whereas for the High slot only the height is increased. As the inner and outer stator diameters are unaltered, the Small slot has both wider teeth and yoke, whereas the Large slot has a bit thinner teeth and yoke, and the High slot only thinner yoke. Since the copper fill factor is kept essentially the same in all four cases, thus the winding cross sectional area is changed with the slot area. All stator geometries are simulated at the three copper and magnet temperatures 20°C, 70°C and 120°C. In all cases the same max rms current of 251 A and max dc voltage of 400V are used.

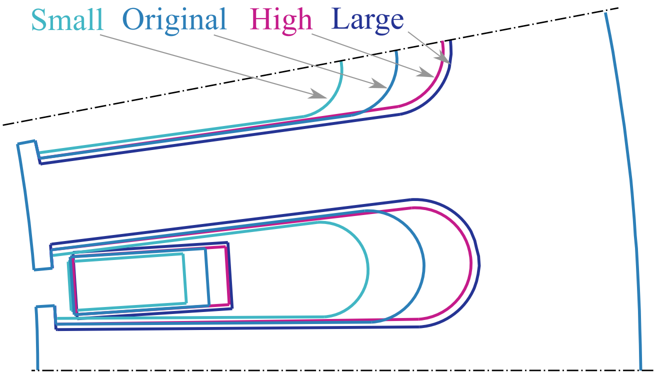

Figure 6.14 The FEA simulated different stator lamination geometries, as well as one of the winding layers.

The numerical values of the different slot areas are presented in Table 6.7, along with percentage ratios compared to the Original. Furthermore, the copper areas are are also presented, and it is the smallest in the Small slot and the largest in the Large slot. Consequently, the current density is the largest in the Small slot and the lowest in the Large slot. Additionally, the phase resistance, and max torque for all slots at the three magnet and copper temperatures are also presented in the table.

It should be noted that the axial extent of the end winding is assumed to be different for the different slot areas. The extent is taken to be linearly proportional to the square root of the change in copper area from the original slot area to the others. For the small slot geometry, the extent is shorter (29.7 mm), for the Large and High slot geometries it is longer (40.2 mm, and 37.2 mm respectively). .

Table 6.7 Parameters for the four stator slot sizes.

	Small	**Original**	**Large**	**High**
Slot Area	60.96 mm^2	83.74 mm^2	109.66 mm^2	94.30 mm^2
	(73%)	(100%)	(131%)	(113%)
Total Copper Area	27.23 mm^2	37.69 mm^2	49.84 mm^2	42.65 mm^2
	(72%)	(100%)	(132 %)	(113 %)
Max rms current density	28 A/mm^2	20 A/mm^2	15 A/mm^2	18 A/mm^2
	(138%)	(100%)	(76%)	(88%)
Share Active part of winding	54.5%	52.3%	50.2 %	51.3 %
R_s at $20^{\circ}C$	24 $m\Omega$	18 $m\Omega$	14 $m\Omega$	17 $m\Omega$
R_s at $70^{\circ}C$	29 $m\Omega$	22 $m\Omega$	17 $m\Omega$	20 $m\Omega$
R_s at $120^{\circ}C$	34 $m\Omega$	26 $m\Omega$	20 $m\Omega$	23 $m\Omega$
	(133%)	(100%)	(79%)	(90%)
T_{max} at $20^{\circ}C$	239 Nm	220 Nm	192 Nm	203 Nm
T_{max} at $70^{\circ}C$	234 Nm	215 Nm	187 Nm	198 Nm
T_{max} at $120^{\circ}C$	228 Nm	210 Nm	182 Nm	193 Nm
	(109%)	(100%)	(87%)	(92%)

The flux linkage from the magnet as a function of q-axis current for the different slot areas is shown in Figure 6.15, for the temperature of $70^{\circ}C$. In general the flux from the magnet decreases with increasing q-axis current due to cross saturation. The saturation effect is the largest in the stator geometry with the thinnest teeth and yoke: the Large slot, whereas it is the smallest for the geometry with the thickest teeth and yoke: the Small slot.

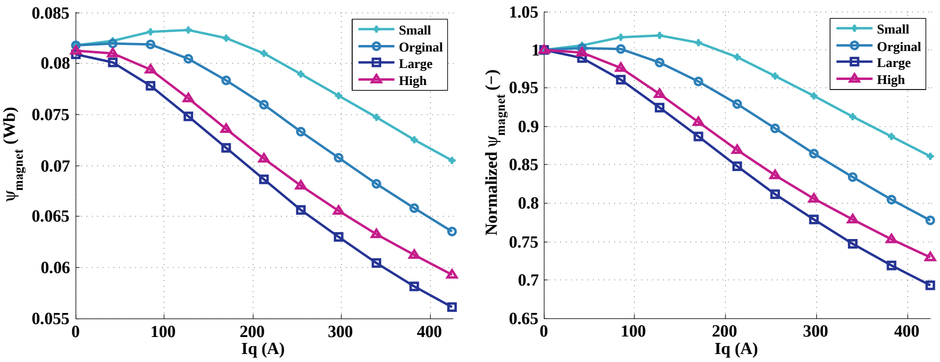

(a) Flux linkage from magnets (Wb).

(b) Flux linkage from magnets normalized by the value at zero q-axis current.

Figure 6.15 Flux linkage from magnets as a function of q-axis current for the different stator slot areas at 70$^\circ C$ copper and magnet temperature.

The four stator geometries also have different dq inductances, where the Small slot geometry have the largest values and the Large slot have the lowest, in the whole id-iq plane. Also the absolute difference between the dq inductances (which is relevant for the reluctance torque production as expressed in (2.13) is the largest for the Small slot and the smallest for the Large slot. These relations are the same at every speed level.

Consequently, both torque components: magnet and reluctance, are the highest for the Small slot geometry in the whole dq current operating area, and the lowest for the Large slot. The net produced torque for the different geometries is presented in the id iq plane in Figure 6.16(a). As shown, the difference in produced torque between the geometries decreases with decreasing current, especially with decreasing q-axis current.

The resulting dq current operating points are presented in Figure 6.16(b), for a few selected speed levels. Outside of the field weakening area the MTPA method result in a somewhat larger share of the q-axis current for the Small slot geometry compared to the others. As a consequence, yet bit higher torque levels can be reached for the same current magnitude. The higher flux from the magnet also result in a stronger speed dependence of the induced voltage, hence the base speed is lower for the Small slot compared to the others. In the field weakening area, instead a larger d-axis current is needed in the Small slot in order to suppress the flux from the magnet, that is even though its d-axis inductance is larger. This counteracts some of the previous torque producing advantage with the Small slot. As noted, the difference between the geometries decreases with increasing speed regarding produced torque and resulting dq current operating points, i.e. when going further into the field weakening area.

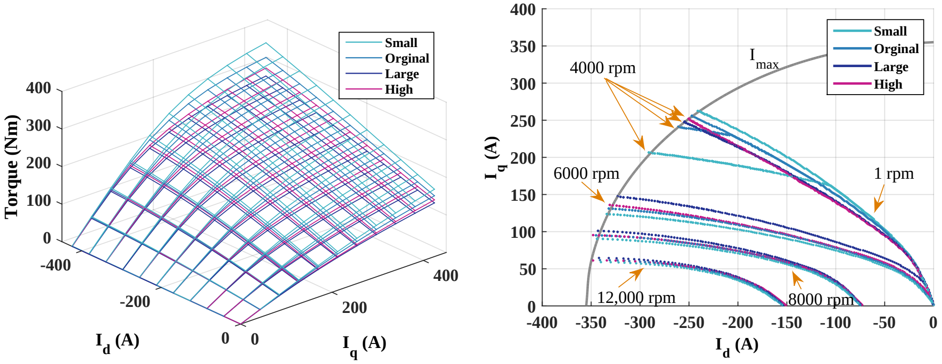

(a) Produced torque for different slot areas.

(b) Result of current control algorithm for different slot areas at 1 rpm, 4000 rpm , 6000 rpm, 8000 rpm and 12,000 rpm.

Figure 6.16 Produced torque and result of current control algorithm as a function of dq current, for the different stator geometries at 70°C copper and magnet temperature.

As a consequence, at low speed levels the largest produced torque per input rms current is given by the Small slot geometry and the lowest by the Large slot. At higher speed levels the difference is quite small. Still, it is then the Large slot that produces somewhat higher torque per input rms current compared to the other slot sizes. the tendency is a bit higher produced torque. The results are shown for a few example speed levels in Figure 6.17(a). The resulting max torque as a function of speed is shown as the dashed line in Figure 6.17(b).

The total lamination core losses are also presented in Figure 6.17(b). As shown, the increase with speed of the core losses is the smallest for the Small slot geometry and the highest for the Large and High slot geometries. Likely, the larger cross sectional lamination area for the Small slot geometry cause somewhat lower flux density levels, and therefore also lower core losses. At low torque levels the core losses are the largest in the Large slot geometry, whereas they are the highest in the High slot at higher torque levels. A similar relation is also noted for both the yoke and teeth losses separately, whereas the opposite order is noted in the rotor (although not shown here), i.e. largest for the Small slot and lowest for the Large. Still, the magnitude of the core losses in the rotor are much lower than in the yoke and teeth, which is why the impact on the total losses is small.

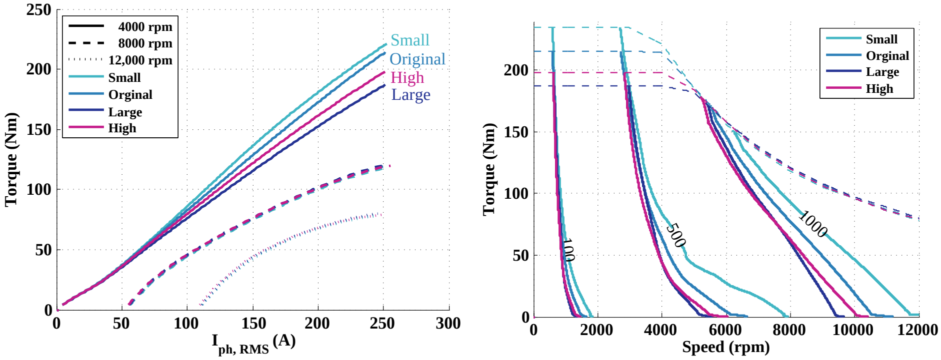

(a) Torque per input rms phase current.

(b) Total lamination core loss contour lines at 500 W and 1000 W.

Figure 6.17 Produced torque per input rms phase current, as well as total core losses as a function of torque and speed, for the HighwayII V-shaped reference motor, for the Small, Original, Large and High slot areas.

In contrast with the core losses, a larger copper cross section leads to a lower winding resistance. Owing to this, the Small slot has the highest winding resistance, and the Large slot the lowest. In the field weakening area the phase current is essentially the same in any speed torque operating point for all slot geometries. Then, the higher winding resistance in the Small slot causes larger copper losses in this region, as shown in Figure 6.18(a). Outside of the field weakening area, at the same torque level, the phase current is the highest in the Large slot and the lowest in the Small. Thus, in this area the resistance and current counteract each other in the loss creation. The result is still that the copper losses are the highest for the Small slot geometry also outside of the field weakening area, and fairly similar between the other geometries.

Nevertheless, the difference in total losses between the four geometries is rather small, as shown in Figure 6.18(b). These small deviation s were a bit unanticipated, but indeed interesting to note. Essentially it is only the losses with the Small slot that deviates notably. In a large part of the operating area the losses with the Small slot are somewhat higher compared to the other slot geometries.

The main difference between the losses in the motors with different slot geometries is thus not the total amount of losses, but the relation between copper and core losses (as shown for the Original slot in Figure 6.8(a)). The motor with the Small slot thus have increased its share of copper losses and decreased the share of core losses, whereas the motors with the Large and High slots have instead increased the share of core losses and decreased the share of copper losses.

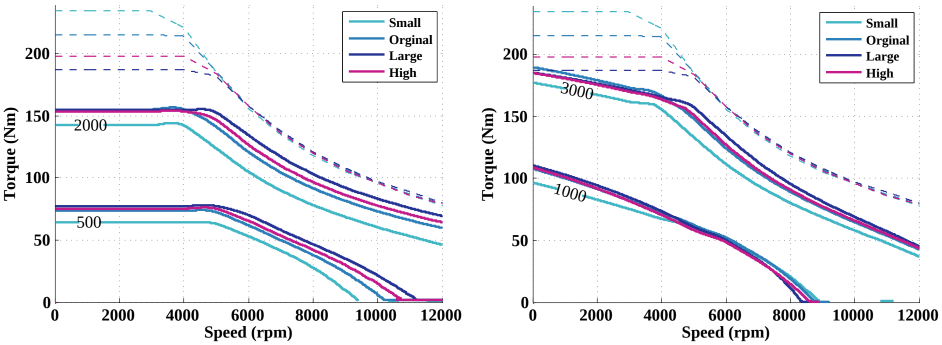

(a) Copper loss contour lines at 500 W and 2000 W.

(b) Total loss contour lines at 1000 W and 3000 W.

Figure 6.18 Copper and total losses as a function of torque and speed, for the HighwayII V-shaped reference motor, for the Small, Original, Large and High slot areas.

The ratio of the copper losses in the Small slot machine over the copper losses in the Original slot is presented in Figure 6.19. As expected, in the field weakening area where the rms currents are almost the same, the ratio is fairly constant (≈1.36). However, outside of the field weakening area the ratio decreases with increasing torque (≈1.1-1.3).

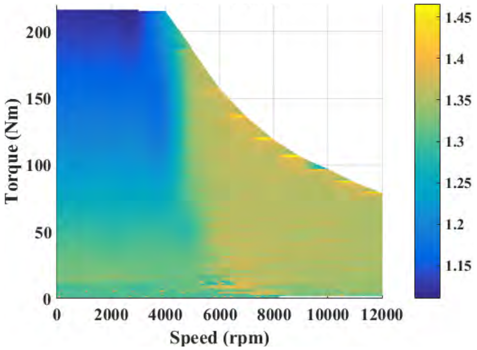

Figure 6.19 The ratio of the Small slot copper losses to the Original slot copper losses.

Chapter 7

Effects of CityII and HighwayII Motor and Inverter Re-scaling on Performance and Energy Efficiency

In this chapter, the electric motor and inverter of the CityII and the HighwayII concept BEVs (described in Section 6.5) are resized in terms of torque and power rating as well as losses and motor mass. After this, the consequence on vehicle performance and energy efficiency for the Test cycles are studied and quantified.

The re-scaling of the motors is simply a linear scaling of the active length, as is described in Chapter 5. The scaling factors are here in steps of 10%, from 50% to 200% of the reference motors.

The inverter which is used in the City car in Chapter 5 (current rating 400 A rms), is here used as a baseline inverter for both the CityII and HighwayII cars, for simplicity. In order for the converter losses to still be reasonably representative, the on-state resistance and switching loss parameters are scaled with the same factors as the motor lengths. The resistances are inversely proportional and the switching loss parameters are linearly proportional, while the constant voltage drop term in the collector-emitter path is left unchanged.

The same simulation structure as in Chapter 5 is here used. Also, the configuration of the gear efficiency and batteries in the CityII and HighwayII cars are identical to the settings in the City and Highway cars. On the other hand, only the losses in motoring mode of the electric machine and inverters are here implemented in the models. It is thus assumed that the loss maps in the generative mode are the same as in motoring mode.

7.1 Performance

As noted in Section 6.5, the initial max torque levels of the re-scaled motors are linearly proportional to the scaling factor. The max mass normalized wheel force for some of the re-scaled electric motors can be seen in Figure 7.1, together with the vehicle's road load, which remains essentially the same in all cases. Even the smallest motor size will be able to sustain the vehicle's top speed requirement.

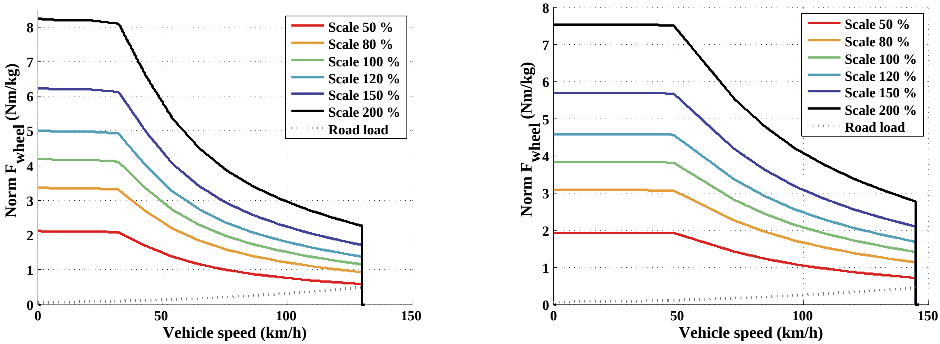

(a) CityII.

(b) HighwayII.

Figure 7.1 Max mass normalized wheel force as a function of vehicle speed (at 400 V DC) along with road load, for the re-scaled CityII and HighwayII powertrains.

The resulting time to accelerate 0-50 km/h and 0-100 km/h, for an initial SOC level of 90% is presented in Figure 7.2, both as a function of max torque and of max power. Naturally, the time to accelerate decreases for increasing max torque and power ratings, and it does so in a nonlinear way. For both cars, the time to accelerate at 50% scale factor is about 1.8-2.1 times longer compared to the reference length, and at 200% scale factor it is 0.5-0.6 times the value of the reference length. Furthermore, it can be noted that at any certain max torque level, the acceleration time is shorter for the CityII car compared to the HighwayII car. This can be expected since the City car is seen to have slightly higher mass normalised wheel force values, compared to the HighwayII car. The difference is even larger when comparing with max power levels, which is due to the different base speed levels of the two cars' motors.

The noted nonlinear dependency means that the effect of a change in stack length is largest for short stack lengths compared to long ones. This effect can be seen since the base speed is kept the same during the scaling. For the acceleration time 0-100km/h, the difference between the scale factors 50% and 80% is 12s for the CityII car, and 8s for the HighwayII. The difference between 120% and 150% is only about 2s for both cars. For the acceleration time 0-50km/h the differences between the same scale factors are a bit smaller: around 3s and less than 1s for both cars.

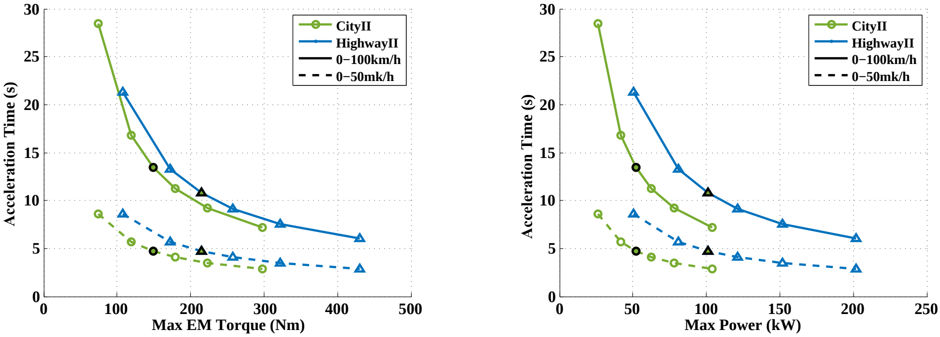

(a) Acceleration time related to max torque.

(b) Acceleration time related to max power.

Figure 7.2 Acceleration time 0-50 km/h and 0-100 km/h, as a function of max torque and max power at 400 V, for the powertrain scale factors: 50%, 80%, 100% (black), 120%, 150%, and 200%.

7.2 System Efficiency and Cycle Energy Consumption

As a comparison, the total powertrain efficiency of the $50\,\%$ down scaled system together with the baseline system, as functions of vehicle speed and mass normalized wheel force, is presented in Figure 7.3 for a DC voltage level of $400\,V$. (For the sake of simplicity when creating the figure, the battery efficiency is here set to the fixed value of 98%, however, this is not used in the simulations.) For the same speed and acceleration operating points, the down-scaled system has a higher efficiency at lower force levels. However, as the force increases so does the copper losses, which are higher in the down-scaled motor. The result is that the system with larger scale factor becomes more and more beneficial with increasing force levels. The transition is gradual for the different scale factors. The same trend can be seen for both the CityII and HighwayII powertrain systems. At the same time, the HighwayII system has a larger operating area with a high efficiency. These results are in line with what was seen for only the motor efficiency in Figure 6.11.

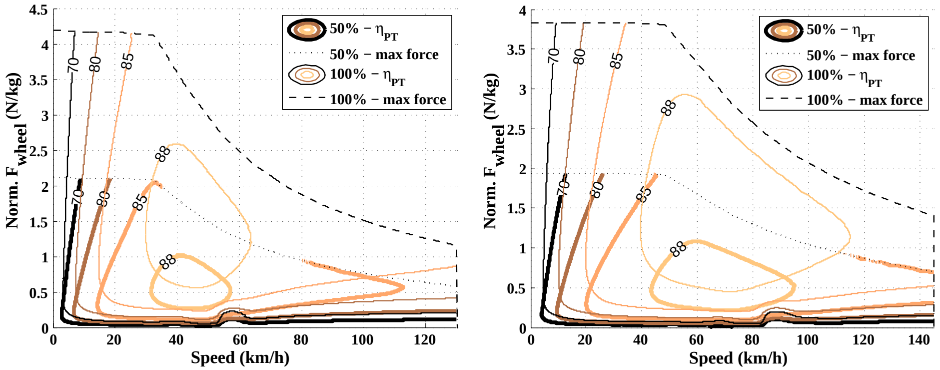

(a) CityII.

(b) HighwayII.

Figure 7.3 Total powertrain efficiency of the 50 % down scaled system and the reference system (100 %) at 400 V DC.

The vehicle energy consumption for all Test cycles has been simulated for the re-scaled powertrain systems, and it was done similarly as described in Chapter 5.

For some cycles, the down-scaled systems were no longer able to sustain all of the operating points in the reference speed's time trace due to the limited acceleration capability. In these cases there may be a rather large difference between the reference speed and the simulated speed. Even though the effect of this deviation on the average cycle energy consumption per driven distance may be relatively small, the max allowed speed deviation is here set to 2 km/h. The same value is also the max allowed deviation between a test vehicle's speed and the reference cycle (within one second) during standardized consumption tests with NEDC in Europe [1]. In the US the max allowed speed deviation is 3.2 km/h (2 mph) [113].

The resulting max speed deviations for the different powertrain systems and test drive cycles are presented in Figure 7.4. As expected, it is the cycles with the highest levels of peak acceleration that give too large speed errors for larger scale factors, especially US06, and REP05, which are too large even for the CityII car with the 120% scale factor. Furthermore, tor the CityII car ArtemisMW130, LA92(UC), WLTC ExtrHgh, NYCC, and ArtemisURBAN cause too large speed deviations for the 60% scale factor and lower. Also for the HighwayII car it is LA92(UC), NYCC, ArtemisURBAN, SC03, and ArtemisRURAL that cause too large speed deviations for the 60% scale factor and lower.

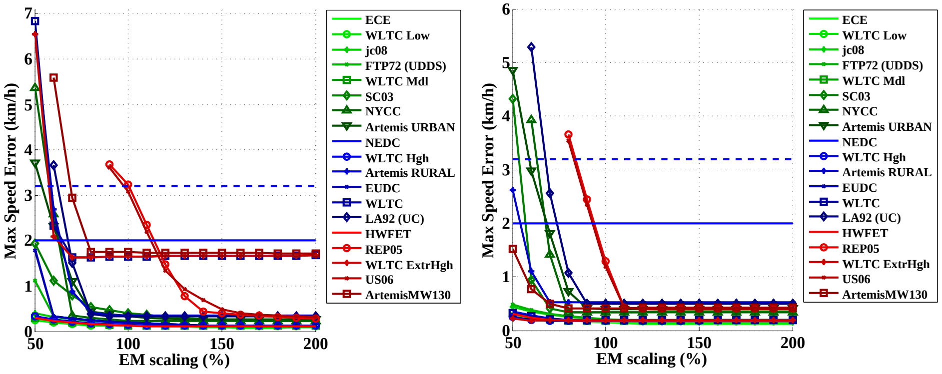

(a) CityII. (b) HighwayII.

Figure 7.4 Max speed error per single Test drive cycle, as a function of powertrain system scaling factor. The horizontal lines represent the max allowed speed deviations of 2 km/h (solid), and 3.2 km/h (dashed).

The resulting net battery energy consumption per driven distance for each cycle and vehicle is presented in Figure 7.5. In the figure, results that adhere to too large max speed deviations are omitted. As in Chapter 5, the consumption is the highest for Highway cycles, and the lowest for Urban cycles. In general, the energy consumption decreases with decreasing system scaling. For some cycles, there is a minimum energy consumption for a certain down scaled value. The reason is that many cycles most often operate relatively far from the systems max force limit, which thus benefits the systems of lower scaling factors.

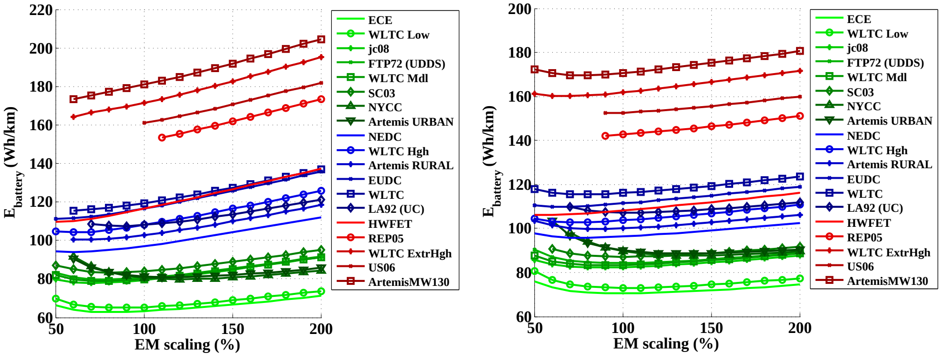

(a) CityII. (b) HighwayII.

Figure 7.5 Battery net energy consumption per driven distance per single drive cycle, as a function of powertrain system scaling factor.

Figure 7.6, presents the results from Figure 7.5 which are all normalized by the consumption with 100% scale factor. It can be noted for both cars that the optimum scale factor for most cycles is below 100%, with the exceptions of the acceleration intense NYCC and ArtemisURBAN. For those cycles the lowest consumption is at 120% scale factor for the CityII car and 140% for the HighwayII car.

For the CityII car, down scaling to 80% gives the lowest consumption for most Urban cycles, that is 98-99% of the consumption with 100% scale factor. A further down scaling will instead increase the energy consumption. For Rural cycles, a scale factor of 60% generally gives the lowest consumption (96%-98% of the reference system), and even lower with a 50% scale factor for EUDC and WLTC (95%-96%). The largest decrease in consumption is noted for the Highway cycles HWFET and WLTC ExtrHgh: 94% of consumption with the reference system.

The noted gains in energy consumption for re-scaling of the HighwayII car are generally smaller compared to the CityII car, as they are 98%-100%. Also here a lower scale factor (90%) gives the lowest consumption for the Urban cycles, whereas 70%-80% gives the lowest for the Rural cycles, and 60% for the Highway cycles. The largest gain in energy consumption is noted for NYCC.

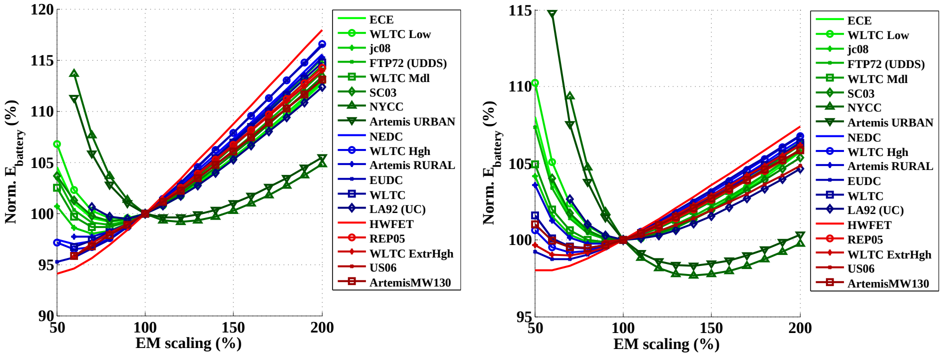

(a) CityII.

(b) HighwayII.

Figure 7.6 Normalized battery net energy consumption per driven distance per single drive cycle, as a function of powertrain system scaling factor. The normalization is done with respect to the reference lengths.

The same results are also reflected when studying the average net propulsion powertrain efficiency in Figure 7.7. For the CityII car, the highest efficiency levels are generally seen for the Urban cycles (up to 81%), whereas Rural and Highway cycles give similar results (up to 79%). The lowest efficiency, 76%, is seen for HWFET. For the HighwayII car, several cycles from all categories are amongst the ones with the highest efficiency (up to 88%). In the same time some of the Urban cycles result in the lowest levels of average efficiency (down to 85%). To conclude, the average net propulsion efficiencies are higher for the HighwayII car compared to the CityII car.

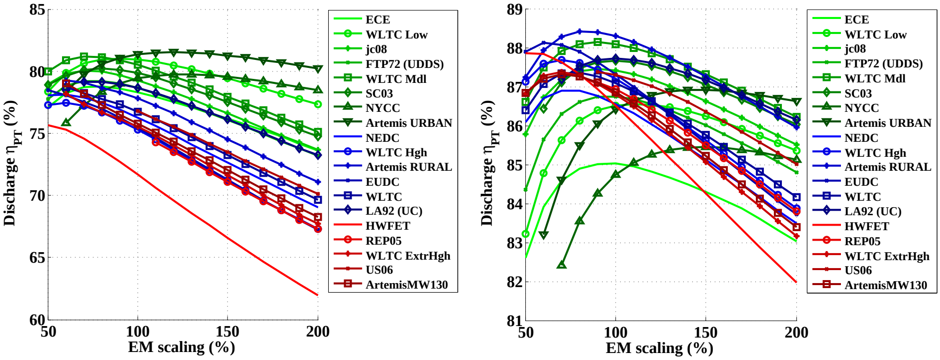

(a) CityII.

(b) HighwayII.

Figure 7.7 Powertrain cycle average propulsion (battery discharge) efficiency per single drive cycle, as a function of powertrain system scaling factor.

Chapter 8

Lumped-Parameter Thermal Model of HighwayII V-shaped Reference PMSM

Electric machines in BEVs experience highly dynamic load cycles, which cause similarly varying internal losses, and therefore strongly time dependent temperature fluctuations. High temperatures can degrade the winding insulation and shorten the machine lifetime, or if high enough even cause immediate winding failure, whereas permanent magnets risk demagnetization [19, 46].

If the machine is sized to be able to continuously operate at the peak power needed in the application, it will result in an unnecessary large and expensive motor. In addition, the available space for electric machines in automotive applications, is often limited. Therefore, a trade-off has to be found between performance, volume and cost, so that the machine is not unnecessarily thermally over dimensioned.

In practice, often a lower level of torque and power is specified which the motor can handle continuously, whereas it can handle a higher level for a shorter period of time, i.e. intermittently. Hence, BEV electric machines utilize temporary over-loading that is limited by the thermal capability of the machine.

A lumped-parameter transient thermal network is here presented for the HighwayII motor with the four different slot areas, such that the temperature development in key machine components can be estimated in various operating points and during load cycles.

8.1 Implemented thermal network

A wide range of suggested thermal networks can be found in literature with varying complexity and node configurations. However, since the object under consideration here is a concept machine where only the active parts are geometrically determined with a high accuracy, the level of complexity of the implemented network is to be adjusted accordingly. The implemented lumped-parameter network should include main heat transfer paths, and be able to predict the transient temperature development in crucial machine parts such as the windings and magnets, while considering losses in bulk regions e.g.: stator yoke, stator teeth, active winding, end-winding, rotor yoke and magnets.

A suitable 10-node network for TEFC IMs (totally enclosed fan cooled induction machines) is proposed in [19], where the T-equivalent node configuration is implemented. It assumes a uniform frame temperature, includes both radial and axial heat transfer in laminations and winding, as well as a speed dependent air gap convection and fan speed dependent convection in the end cap region. A similar fan cooled IM 8-node network is presented in [20], however without the T-equivalent node configuration. Furthermore, the axial heat transfer in the laminations are considered negligible, whereas bearing heat transfer is added. This network was later adjusted to a water cooled inset PMSM presented in [53], by mainly modifying the rotor modelling. Here, the network has been further adjusted for the used IPM rotor design. It is presented in Figure 8.1. Similar adjustments to the rotor parts are also reported in [101, 114, 115]. Another modification here, is the added consideration of convection heat transfer to the cooling media.

Furthermore, it is assumed that the internal heat generation is uniformly distributed in each region, as is also assumed in [47, 56, 116]. Axial heat transfer is considered in the copper windings and the shaft, whereas only radial heat transfer is considered for the laminations and magnets, as is also done in [47]. Moreover, axial symmetry around the midpoint is assumed, as well as cylindrical symmetry both geometrically and thermally.

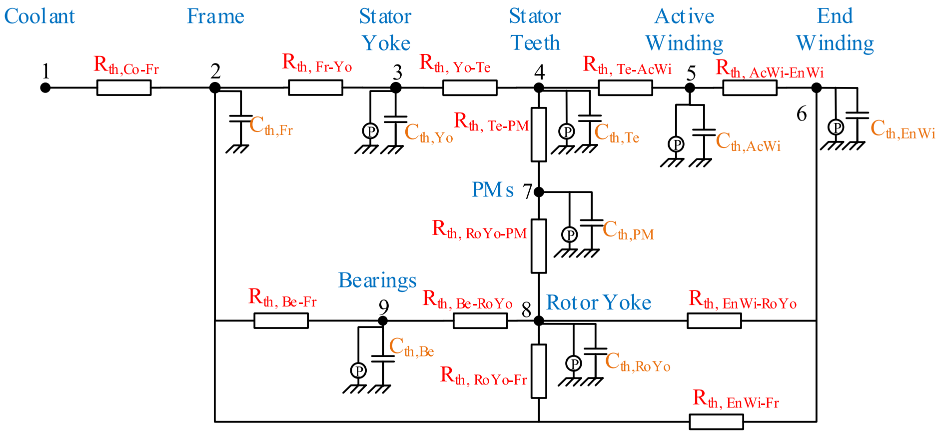

Figure 8.1 Implemented Thermal Network.

8.1.1 Frame and cooling

Since the rms current densities are expected to reach around 15-28 A/mm^2 in the different slot areas described in Section 6.7, a liquid cooling system is implemented as recommended in [34, p.90]. Additionally, liquid cooling is found to be frequently used in current BEV models on the market, as shown in Table A.3 in Appendix A.

The intention is here to find a reasonable estimation of the thermal resistance between the coolant and the frame nodes: $R_{th,Co-Fr}$. That is the sum of the resistances for the two main heat transfer modes involved: convection between the coolant medium and the aluminum frame, and conduction inside the aluminum. Thus both natural convection and radiation to the ambient air are considered negligible compared to the forced convection [52]. It is also desired to find an approximate value of the convection resistance for the specific coolant temperatures $20°C$ and $65°C$, as well as for certain flow rates. The higher of the two temperatures is here considered as the dimensioning temperature for the machines' thermal capability, which is studied in Chapter 9. In order to estimate these resistances a geometrical representation of the cooling channel is needed, as well as material data of the coolant.

The cooling medium in current BEV models is found to typically consist of about 50% deionized water and 50% ethylene-glycol, as stated for Ford Focus and Toyota RAV4 EV in [117, 118] (it was also seen for Fiat 500e, Mercedes B-Class, Mitsubishi i-MiEV, Nissan Leaf and Smart fortwo). The ethylene-glycol is added to prevent overheating, freezing and corrosion. The cooling medium used here is assumed to be a mixture of 48% (by volume) water and 52% mono ethylene glycol [119]. Its material parameters varies with temperature such that the density, thermal conductivity and dynamic viscosity decreases with increasing temperature, whereas the specific heat increases. The temperature dependencies are shown in Figure D.1 in Appendix D.

Various cooling circuits are possible for this application. However, for simplicity the cooling channel is assumed to form a spiral of four laps inside the aluminum frame, as illustrated in Figure 8.2. The cooling ducts have rectangular cross sections with a width w_{duct} of 30 mm, and a height h_{duct} of 5 mm, and are separated by 10 mm. The radial distances from the inner and outer frame boundaries $l_{Fr,lower}$ to the ducts are 3 mm on each side. Similar cooling channels with rectangular ducts are also used in BMW's i3 model with six laps [120], and in Nissan's 2011 Leaf model with three parallel laps (i.e no spiral) [94].

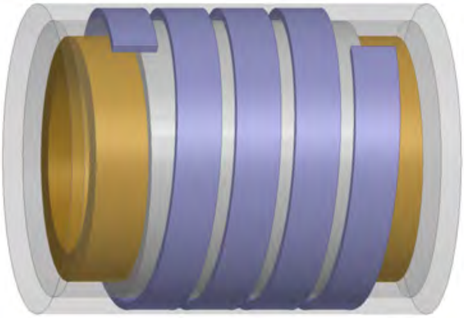

Figure 8.2 The four laps spiral cooling channels with rectangular ducts, along with simplified frame, stator core and end windings.

8.1.1.1 Frame conductive thermal resistance

For simplicity, only one network node is used for the whole frame. Another simplification is to only consider the radial heat transfer between the stator back surface and the inner cooling duct surface. Therefore, the frame node is placed at half the radial distance between these two boundaries. This part can be considered to be a hollow cylinder with the inner and outer radii $r_{Fr,in}$ and $r_{Fr,in} + l_{Fr,lower}$, and the length is here taken to be that of the active core length l_{stk}, of 150 mm. The conductive thermal resistance can then be expressed as

$$R_{th,Fr} = \frac{ln(\frac{r_{Fr,in}+l_{Fr,lower}}{r_{Fr,in}})}{2\pi\lambda_{Al}l_{stk}} \tag{8.1}$$

8.1.1.2 Cooling convection thermal resistance

In order to estimate the thermal convection resistance between the cooling media and the frame (2.45), the heat transfer coefficient is approximated. Preferably measurements or CFD methods are to be used for this purpose. Here, however, a rough empirical approach to find suitable Reynolds and Nusselt numbers is considered accurate enough. A detailed description of the approach is given in Appendix E.

The average heat transfer coefficient h_{cool} as a function of flow rate in liters per minute is presented in Figure 8.3 for four different coolant tempreatures. For laminar flow h_{cool} is almost constant for all flow rates and temperatures: around 290 W/m^2K. In contrast to laminar flow, for turbulent flow, h_{cool} increases with both flow rate and temperature and reach a few thousand W/m^2K in the studied range. It is assumed that a turbulent flow is prefered. Therefore, in the case of 65°C coolant, a flow rate of 6 L/min is chosen, which gives an h_{cool} of 1988 W/m^2K. In the case of 20°C coolant the flow rate is set to 12 L/min, which gives an h_{cool} of 1537 W/m^2K. A similar value for the high coolant temperature is also noted to be used in BMW's i3 model in [120], where the coolant is said to reach up to 70°C at inlet and 85°C at outlet, when the flow rate is 6 L/min. Here the temperature change of the coolant medium along the cooling channel is ignored, even though it may be up to 17°C, as pointed out in Appendix E.

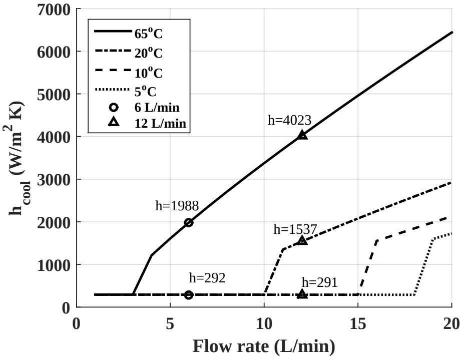

Figure 8.3 The estimated average heat transfer coefficient of the coolant, as a function of flow rate and temperature.

Furthermore, it is assumed that 50% of the total heat flux between the stator back and the cooling channel will pass through the inner duct surface. Therefore, a correction factor $k_{conv,corr}$ of 0.5 is added to the convection thermal resistance of the cooling channel

$R_{th,cool}$, which is

$$R_{th,cool} = \frac{k_{conv,corr}}{h_{cool}A_{cool}} \tag{8.2}$$

where A_{cool} is the surface area of the inner cooling duct boundaries, as in

$$A_{cool} = 4 \times 2\pi w_{duct}(r_{Fr,in} + l_{Fr,lower}) \tag{8.3}$$

8.1.1.3 Thermal resistance between coolant and frame

The thermal resistance between the frame temperature node point and the cooling channel's average temperature is thus the sum of the cooling convection thermal resistance and half of the conductive thermal resistance of the frame, as in

$$R_{th,Co-Fr} = R_{th,cool} + R_{th,Fr}/2 \tag{8.4}$$

8.1.2 Stator yoke

As in [53, p.85], the stator yoke is modeled as a hollow cylinder consisting of stacked laminated sheets of electrical steel with perfect insulation, thereby assuming a strictly radial heat flow.

The thermally conductive core length $l_{stk,cond}$ is the product of the total core stack length l_{stk}, and the stacking factor k_{sf}, which is here assumed to be 0.95, as in

$$l_{stk,cond} = k_{sf}\, l_{stk} = 0.95\ \times\ 0.150 = 0.1425m \tag{8.5}$$

The thermal resistance of the stator yoke, for radial heat flow thus depend on the inner and outer yoke radii: $r_{Yo,in}$ and $r_{Yo,out}$ respectively, as in

$$R_{th,StYo} = \frac{ln(\frac{r_{Yo,out}}{r_{Yo,in}})}{2\pi\lambda_{Fe}l_{stk,cond}} \tag{8.6}$$

8.1.2.1 Contact resistance between frame and stator yoke

Small air pockets inevitably exist between the aluminum frame and the stator back, who's size partly depend on the manufacturing process and surface roughness [19, 102]. Due to the relatively low thermal conductivity of air they need to be considered. The air pockets can be modeled as a small equivalent air gap [102]. According to [102], the interface cap between iron and aluminum is typically $0.6 - 6\mu m$. However, further presented measurements on electric machines give an average gap between lamination and aluminum housing of $0.037mm$ for different machine size, and the range $0.01 - 0.077mm$. It is here assumed that the gap distance, $l_{contFr-Yo}$ is 10 μm, i.e. the lower limit in the measurement series.

The contact resistance is modeled as a hollow cylinder, as in

$$R_{th,ContFr-Yo} = \frac{ln(\frac{r_{Yo,out}+l_{contFr-Yo}}{r_{Yo,out}})}{2\pi\lambda_{Air}l_{stk}} \tag{8.7}$$

8.1.2.2 Thermal resistance between frame and stator yoke

The yoke node is placed radially in the middle of the yoke. The thermal resistance between the frame and the yoke nodes thus consist of half of the frame and yoke conductive resistances, as well as the contact gap resistance, as in

$$R_{th,Fr-Yo} = R_{th,Fr}/2 + R_{th,ContFr-Yo} + R_{th,StYo}/2 \tag{8.8}$$

8.1.3 Stator teeth

The assumed radial heat transfer in all of the stator teeth leads to parallel thermal resistances. The same method as in [20, p.69-70] and in [53, p.87-88] is here used to find the total radial thermal resistance of the teeth $R_{th,Te}$.

Ideally, the total thermal resistance of the teeth is found by integrating the radial cross sectional area of the teeth in the radial direction, as in

$$R_{th,Te} = \int_{r_{St,in}}^{r_{Yo,in}} \frac{1}{\lambda_{Fe}\, Q_s\, l_{stk,cond}\, w_{tooth}(r)} dr \tag{8.9}$$

where Q_s is the number of teeth (and slots) and w_{tooth} is the tooth width which varies in the radial direction. In [20] and [53], however, the integration in (8.9) is replaced by an analytical expression, in which the axial cross sectional view of one tooth is segmented into four indexed geometrical pieces in a non-curvature xy-plane. The y-components denote the height of the segments (which represent the radial direction in the machine), and the x-components denote the width.

The fist segment (with xy-components indexed 1) belong to the rim rectangle. The second component is a trapezoid placed above the rim, where the y-component denote its height and the x-component its top width. The latter is also the lower tooth width. The third segment is the rectangular part of the tooth until the top curvature begins, at which its width is taken. The forth segment is the top of the tooth including a curvature on both sides until the tip of the slot, and its width is the distance between two slot tips. The resulting expression for the thermal resistance is

$$\begin{aligned} R_{th,Te} = \frac{1}{\lambda_{Fe}\, Q_s\, l_{stk,cond}} \Bigg[& \frac{y_1}{x_1} + \frac{y_3}{x_3} + \frac{y_2}{x_1 - x_2} \left(ln \left| \frac{x_1 y_2}{x_1 - x_2} \right| - ln \left| y_2 - \frac{x_1 y_2}{x_1 - x_2} \right| \right) - \\ & - \frac{\pi}{4} + \frac{a}{\sqrt{a^2-1}} \arctan \left(\frac{a+1}{\sqrt{a^2-1}} \right) \Bigg] \end{aligned} \tag{8.10}$$

where a is

$$a = \frac{x_3 + 2y_4}{2y_4} \tag{8.11}$$

8.1.3.1 Thermal resistance between stator yoke and teeth

The teeth node is placed radially in the middle of the teeth. Consequently, the thermal resistance between the yoke and teeth node is half of the thermal resistance for each part, as

$$R_{th,Yo-Te} = R_{th,StYo}/2 + R_{th,Te}/2 \tag{8.12}$$

8.1.4 Stator winding

As copper losses are one of the main loss components in the motors the heat flow from the winding is large. This heat flow will pass through, not only the copper wires, but also the wire insulation, the impregnation, air pockets and the slot liner. Since the winding is not geometrically well determined a specific geometrical representation is not possible.

Again, the same method as in [20, p.59-63] and [53, p.88-93] is here used, where the slot for simplicity is converted to an equivalent rectangular shape. The equivalent slot is then divided into two thin surface layers representing the slot liner $d_{slotliner}$ of 0.2 mm and a thin air film $d_{slotair}$ of 10 μm, and where the rest of the volume consist of an equivalent winding mix representing copper and impregnation which is assumed to have a uniform heat generation.

The width of the winding mix's part of the equivalent rectangular slot $w_{slot,eq}$, is taken as the average of an upper and lower slot width ($w_{slot,upper}$ and $w_{slot,lower}$) minus two times the sum of the slot liner and air film, as in

$$w_{slot,eq} = \frac{w_{slot,upper} + w_{slot,lower}}{2} - 2(d_{slotliner} + d_{slotair}) \tag{8.13}$$

The height of the winding mix's part of the rectangular slot $h_{slot,eq}$, is the slot area divided by the average of an upper and lower slot width minus two times the sum of the slot liner and air film, as in

$$h_{slot,eq} = \frac{2A_{slot}}{w_{slot,upper} + w_{slot,lower}} - 2(d_{slotliner} + d_{slotair}) \tag{8.14}$$

The slot liner's and the winding impregnation's thermal conductivities $\lambda_{slotliner}$ and λ_{impreg} are here assumed to be 0.2 W/mK, and that of the winding mix $\lambda_{WindMix}$ is assumed to be 0.55 W/mK. The latter is approximated as 2.75 times that of the impregnation material, as suggested in [20, p.60] for a 45$\%$ slot fill factor.

8.1.4.1 Thermal resistance between active winding and teeth

The thermal resistance between the active winding and teeth is estimated as in [53, p.89-91]

$$R_{th,Te-ActWi} = \frac{R_x R_y}{Q_s\, l_{stk,cond}\,(R_x + R_y)} \left(1 - \frac{R_{x0} R_{y0}}{720(R_{x0} + R_{y0})}\right) \tag{8.15}$$

where Q_s is the number of slots, and R_x, R_y, R_{x0} and R_{y0} represent thermal resistances per unit length in the width (x) and height (y) directions of the rectangular equivalent slot. The resistances R_x are R_y are found as

$$R_x = 0.5(R_{ix} + \frac{R_{x0}}{6}) \tag{8.16}$$

$$R_y = 0.5(R_{iy} + \frac{R_{y0}}{6}) \tag{8.17}$$

where R_ix and R_iy represent the per unit length thermal resistances of the slot liner and air film, as in

$$R_{ix} = \frac{d_{slotliner}}{\lambda_{slotliner}\, h_{slot,eq}} + \frac{d_{slotair}}{\lambda_{air}\, h_{slot,eq}} \tag{8.18}$$

$$R_{iy} = \frac{d_{slotliner}}{\lambda_{slotliner}\, w_{slot,eq}} + \frac{d_{slotair}}{\lambda_{air}\, w_{slot,eq}} \tag{8.19}$$

The per unit length thermal resistances of the slot winding mix: R_{x0} and R_{y0} are found as in

$$R_{x0} = \frac{w_{slot,eq}}{\lambda_{WindMix}\, h_{slot,eq}} \tag{8.20}$$

$$R_{y0} = \frac{h_{slot,eq}}{\lambda_{WindMix}\, w_{slot,eq}} \tag{8.21}$$

Since R_{y0} is about ten times larger than R_{x0} the heat flow from the slot to the yoke is assumed negligible.

8.1.4.2 Thermal resistance between the active winding and end winding nodes

The thermal resistance between the active winding and end winding is found as in [53, p.91-93]. The heat flow from the active part of the winding to the end winding is axial, with the cross sectional area of the copper A_{Cu} (m^2)in each slot. Since the heat flow occurs in parallel in the slots, the thermal resistance between the active and end winding network nodes is found as in

$$R_{th,AcWi-EnWi} = \frac{l_{av}}{6Q_s A_{Cu} \lambda_{Cu}} \tag{8.22}$$

where Q_s is the number of slots, l_{av} is the average conductor length of half a turn, and is approximated as the sum of the active and passive winding length's by (5.3). The end winding axial extension outside of the lamination stack d_{ext} is here assumed to be 35 mm on each side.

8.1.5 Air gap

Various suggested models of the air gap heat transfer can be found in publications, e.g. [19–22,47,53,102,121]. Many are based on the early work by Taylor 1935 [122], Gazley 1958 [123] and Becker and Kaye 1962 [124]. Usually the axial heat flow is omitted for machines with no internal forced air gap convection. The radial heat transfer is then dependent on the rotor speed, such that it is laminar i.e. conductive at low speed levels and transitional and turbulent at higher speed levels. The speed dependence is calculated by the Taylor number for which different critical values are set that represent laminar or turbulent flows. Different calculation methods are then given for the Nusselt number depending on the flow type.

The difference between the found models are usually the critical levels for the Taylor number which dictate the type of flow, and the approximation of the Nusselt number.

Here the method described in [124] is used, which is also used in [20–22, 53, 121], however with varying critical Taylor values.

The thermal resistance across the air gap is

$$R_{th,AirGap} = \frac{1}{h_{airgap}\,A_{airgap}} \tag{8.23}$$

where h_{airgap} (W/m^2K) is the air gap convection heat transfer coefficient, and A_{airgap} (m^2) the cylinder surface area in the air gap $(A_{airgap} = 2\pi r_{airgap} l_{stk})$, and r_{airgap} (m) is the average air gap radius.

The heat transfer coefficient and the Nusselt number are related as in

$$h_{airgap} = \frac{Nu\,\lambda_{air}}{2\,l_{airgap}} \tag{8.24}$$

where l_{airgap} is the air gap length.

The Nusselt number is approximated for different ranges of the modified Taylors number as

$$\begin{array}{lrr} Nu = 2 & T_{am} < 1790 & \text{laminar flow} \\ Nu = 0.128 * T_{am}^{0.367} & 1790 < T_{am} < 10^4 & \text{transitional flow} \\ Nu = 0.409 * T_{am}^{0.241} & 10^4 < T_{am} < 10^7 & \text{fully turbulent flow} \end{array}$$

In [124] the critical value of the modified Taylors number between laminar and transitional flow is 1700, however, here the value is adjusted somewhat to avoid discontinuity at this transition.

Taylor's number T_a is

$$T_a = \frac{\rho_{air}^2\,\omega_{rotor}^2\,r_{airgap}\,l_{airgap}^3}{\mu_{air}^2} \tag{8.25}$$

where ρ_{air} (kg/m^3) and μ_{air} (kg/ms) is the mass density and dynamic viscosity of air, respectively, and ω_{rotor} (rad/s) is the angular speed of the rotor.

The Modified Taylors number $T_{am} = \frac{T_a}{Fg}$, is

$$T_{am} = Ta\frac{1697[0.0056 + 0.0571(\frac{2r_{airgap}+2.304l_{airgap}}{2r_{airgap}-l_{airgap}})^2][1 - \frac{l_{airgap}}{2r_{airgap}}]}{\pi^4(\frac{2r_{airgap}-2.304l_{airgap}}{2r_{airgap}-l_{airgap}})} \tag{8.26}$$

where the geometrical correction factor $F_g^{-}1$ is close to unity, and therefore often neglected.

The material parameters of air are temperature dependent, as shown in Figure D.2 in Appendix D [48]. The air gap Nu number, heat convection coefficient, and resulting thermal resistance for the two temperatures $20°C$ and $100°C$ are presented in Figure 8.4, as a function of rotor speed. Since the air temperature is not calculated by the thermal network, the values at 100°C are used in all cases.

Additionally, the air gap length due to thermal expansion of the machine. At 80 °C, the air gap length may decrease to 85% of the value at 0 °C. This effect is however ignored here.

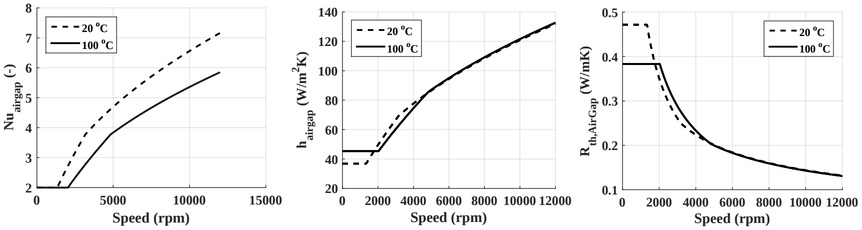

(a) Nu. (b) h_{airgap}. (c) $R_{th,AirGap}$.

Figure 8.4 Speed dependence of Nu, h_{airgap} and $R_{th,AirGap}$.

8.1.6 Rotor core and magnets

As for the stator, only radial heat flow is considered in the rotor. For simplicity, the rather complex magnet v-shape is replaced by an equivalent geometry with arced magnets, which is only used in the calculation of the thermal resistance, as shown in Figure 8.5 for one 8$^{\text{th}}$ of the rotor. Similar conversions methods are also seen in [101, 115, 125]. Additionally, a small air gap under the magnet is included with an assumed thickness of 150 μm l_{MagGap}. The equivalent thermal resistance is then a mix of series and parallel connections in the rotor.

The equivalent rotor is divided into seven different segments: one lamination segment that is above the arced magnet (S4), and one that is below (S1); one that is the arced magnet (S7); one small air segment on each side of the magnet with same height as the magnet (S5, S6); and two lamination segments outside of the air segments (S2, S3).

The heat flow is assumed to be radial i all segments. Segment S1 and S4 are modelled as hollow cylinders, resulting in the expression

$$R_{th,RoS:1,4} = \frac{ln(\frac{r_{out}}{r_{in}})}{2\pi\,\lambda\,l_{stk}} \tag{8.27}$$

The heat flow in segment S2, S3, and S5-S7 as well as the small air gap under the magnet are modeled as pieces of a hollow cylinder based on (2.43), rendering

$$R_{th,RoS:2,3,5-7} = \frac{ln(\frac{r_{out}}{r_{in}})}{\phi\,n_{pole}\,\lambda\,l_{stk}} \tag{8.28}$$

where n_{pole} is the number of poles. Furthermore, the radial heat flow in segment S2,S3, and S5-S7 is assumed to occur in parallel, and their equivalent resistance is $R_{th,MagArcEq}$. The radii and angles used in the conversion is presented in Table 8.1, as noted in Figure 8.5.

Table 8.1 Parameters in the equivalent rotor geometry used in the thermal network.

	r_{out}	r_{in}	ϕ	
Lamination	$R_{th,RoS1}$	r_1	$r_{Rot,in}$	2π
Lamination	$R_{th,RoS2}$	r_2	r_1	$2\phi_1$
Lamination	$R_{th,RoS3}$	r_2	r_1	ϕ_5
Lamination	$R_{th,RoS4}$	$r_{Rot,out}$	r_2	2π
Air	$R_{th,RoS5}$	r_2	r_1	$2\phi_2$
Air	$R_{th,RoS6}$	r_2	r_1	$2\phi_4$
Magnet	$R_{th,RoS7}$	r_2	r_1	$2\phi_3$
Air	$R_{th,MagAirgap}$	$r_1 + l_{MagGap}$	r_1	$2\phi_3$

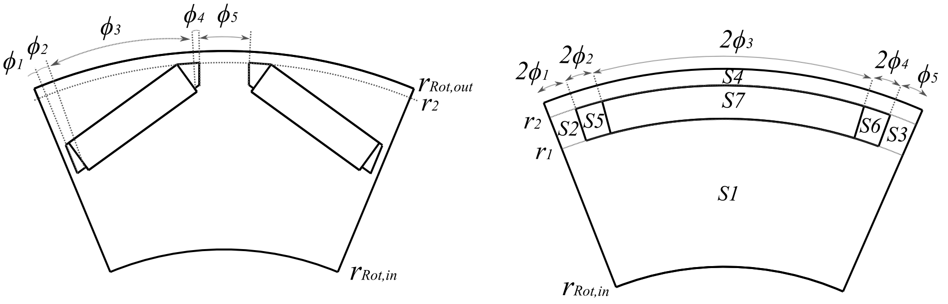

(a) Electromagnetic rotor geometry.

(b) Thermal equivalent rotor geometry outline.

Figure 8.5 Rotor geometries in electromagnetic and thermal equivalent models.

8.1.6.1 Thermal resistance between tooth and magnets

The magnet node is placed in the radial middle of the arced equivalent magnet. The thermal resistance between the stator tooth network node and the magnet node is thus found as

$$R_{th,Te-PM} = R_{th,Te}/2 + R_{th,AirGap} + R_{th,RoS4} + R_{th,MagArcEq}/2 \tag{8.29}$$

8.1.6.2 Thermal resistance between magnets and rotor yoke

The rotor yoke node is placed in the radial middle of the lower rotor part. The thermal resistance between the magnet network node and the rotor node then becomes

$$R_{th,RoYo-PM} = R_{th,MagArcEq}/2 + R_{th,MagAirgap} + R_{th,RoS1}/2 \tag{8.30}$$

8.1.7 Shaft

The shaft is assumed to be a lossless solid with only axial heat conduction, as also done in [47,53]. Furthermore, it is assumed to have a homogenous temperature distribution as in [53]. The shaft thermal resistance is divided into two sections depending on the shaft radius. Within the length of the lamination stack l_{stk} the shaft radius equals the rotor yoke inner radius $r_{RoYo,in}$. Outside of the lamination stack the shaft radius $r_{sh,ext}$ is 20 mm, and the distance to the bearings $l_{sh,ext}$ is 45 mm on each side.

Similarly as in [53], the shaft thermal resistance $R_{th,Sh}$ is then

$$R_{th,Sh} = \frac{l_{stk}}{\pi r^2_{RoYo,in}\lambda_{steel}} + \frac{2l_{sh,ext}}{\pi r^2_{sh,ext}\lambda_{steel}} \tag{8.31}$$

where λ_{steel} is the thermal conductivity of the shaft steel material.

8.1.8 Bearings

The thermal resistance of the bearings $R_{th,Be}$ is modeled as in [53], which is based on empirical data of IMs in [20], but where the speed dependent term is neglected for simplicity.

$$R_{th,Be} = 0.45 * 33(0.12 - d_b) \tag{8.32}$$

where d_b is the average bearing diameter (54 mm).

Another approach is suggested in [52, 102], where the bearing thermal resistance is approximated to that of an equivalent interface gap. Empirical data is presented for four small IMs, with equivalent gaps between 0.23-0.4 mm. This method is not used here.

Also bearing losses are included in the thermal model. For simplicity they are assumed to only depend on motor torque [126], as

$$P_{loss,Be} = \frac{r_{Be}\,\mu_{Be}\,T_{rq,e}\,w_m}{r_{Rot,out}} \tag{8.33}$$

where $T_{rq,e}$ is the motor torque, w_m is the motor angular speed, r_{Be} is the bearing bore radius (which equals the radius of the extended part of the shaft), μ_{Be} is the bearing friction coefficient which is here assumed to be 0.0015 as typical for deep groove ball bearings in [126].

8.1.8.1 Contact resistance between rotor yoke and shaft

A 10 μm air film $l_{contRoYo-Sh}$ is assumed between the rotor yoke and the shaft contact surfaces. The thermal resistance $R_{th,ContRoYo-Sh}$ is here modelled as a hollow air cylinder.

8.1.8.2 Thermal resistance between bearings and frame

As suggested in [20, 53], the thermal resistance between the bearing and the frame is

$$R_{th,Be-Fr} = R_{th,Be}/4 \tag{8.34}$$

8.1.8.3 Thermal resistance between rotor yoke and bearings

The thermal resistance between rotor Yoke and the bearings end up in

$$R_{th,Be-RoYo} = R_{th,YokeLower}/2 + R_{th,ContRoYo-Sh} + R_{th,Sh}/2 + R_{th,Be}/4 \tag{8.35}$$

8.1.9 Internal air

The internal air is the air inside the frame except the air gap between the stator and rotor. Analytical modelling expressions are not applicable, rather empirical data must be used due to the complicated air flow paths in the geometrically complex region. Therefore, there are many published suggestions for modelling of the convective heat transfer in this region [19, 20, 127]. A comparison between different heat transfer coefficient expressions that are suggested in various publications, along with experimental results of end winding convection, are presented in [127] (and partly in Figure 8.6). A fairly similar linear dependence on rotor speed is typically noted for the suggested heat transfer coefficients, with an offset which represents natural convection.

As suggested for the simple network in [20] and also used in [53], three separate convective heat transfer coefficients to the internal air are here implemented: one to the inner frame surface, one to the rotor end shields and one to the end windings.

The heat transfer coefficient between the **inner frame surface** and the internal air is via measurements empirically approximated in [20], as

$$h_{Fr,in} = 15 + 6.75 v_r^{0.65} \tag{8.36}$$

where v_r (m/s) is the rotor peripheral speed. It should be noted that the approximation is a curve fit to data with a relatively large spread [20].

The inner frame surface area consist of the two inner end cap surfaces and the inner frame shell surface that extends outside both sides of the lamination stack.

The heat transfer coefficient between the **rotor end shield surface** and the internal air in [20], is approximated as

$$h_{Ro} = 16.5 v_r^{0.65} \tag{8.37}$$

The rotor end shield area is approximated by the circular surface area with the average air gap radius.

The heat transfer coefficient between the **end winding surface** and the internal air is via measurements empirically approximated in [20], as

$$h_{EnWi} = 6.5 + 5.25 v_r^{0.6} \tag{8.38}$$

Also this approximation is based on data with a relatively large spread.

As in [20], the surface area of the end winding is approximated as

$$A_{EnWi} = \pi \, l_{passive} \, r_{EnWi,ave} \tag{8.39}$$

where $l_{passive}$ is the average end winding conductor length as from (5.3), $r_{EnWi,ave}$ is the average radial distance for the end winding.

A comparison between different found suggested values of convection heat transfer coefficient is shown in Figure 8.6. The speed range of found data are all up to 20 m/s, which represent about 3144 rpm of the here used HighwayII motor. The rotor speed dependence in the right part of Figure 8.6 is based on extrapolation of the velocity profiles. The Kylander [EW] data are similar to the Schubert [EW] data, whereas the Boglietti data seem to have a larger speed proportionality coefficient. The Kylander [Fr] data are very similar to the Stokum data for higher speed levels. The Kylander [Ro] data have the weakest speed dependence between all.

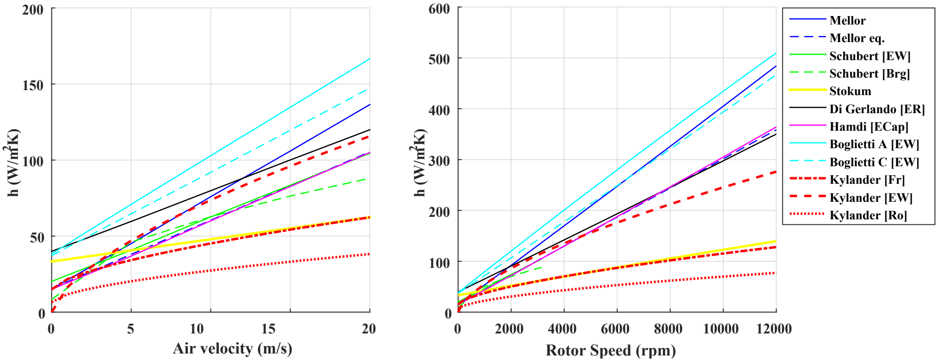

Figure 8.6 Comparison of suggested internal air convection heat transfer coefficients. Graphs in the left part of the figure are original data from references, whereas graphs in the right part are extrapolated data for the HW machine speed range. Mellor eq. from [19], Kylander from [20], the rest from [127].

The three thermal resistances to the internal air, are then converted from a Y to a Δ, since the internal air temperature is not a desired network node. The net thermal conductance is

$$G_T = \frac{1}{R_{th,InAir-Fr}} + \frac{1}{R_{th,InAir-Ro}} + \frac{1}{R_{th,InAir-EnWi}} \tag{8.40}$$

8.1.9.1 The Δ-nodes thermal resistances

The thermal resistance between the rotor yoke network node $R_{th,RoYo-Fr}$ and the frame node is

$$R_{th,RoYo-Fr} = R_{th,InAir-Fr} R_{th,InAir-Ro} G_T/2 \tag{8.41}$$

The thermal resistance between the end winding node $R_{th,EnWi-RoYo}$ and the rotor yoke is

$$R_{th,EnWi-RoYo} = R_{th,InAir-Ro} R_{th,InAir-EnWi} G_T/2 \tag{8.42}$$

And finally, the thermal resistance between end winding and frame $th, EnWi - Fr$ nodes is

$$R_{th,EnWi-Fr} = R_{th,InAir-Fr} R_{th,InAir-EndWi} G_T/2 \tag{8.43}$$

8.1.10 Thermal capacitances

The thermal capacitance of each motor part is the product of its mass and the specific heat of the material, and the mass is the product of its mass density and volume (2.47).

For the thermal capacitance of the frame, the volume includes the two end caps and the whole frame cylinder, while excluding the volume of the cooling channel. Since the end winding extent varies between the motors with different slot areas, so does the length of the cylindrical part of the frame. This is to still keep a 10 mm distance from the end winding to the inner side of the end cap. Therefore, the frame mass is somewhat lower for the Small slot geometry, and higher for the Large and High slot geometries.

The thermal capacitance of the yoke is modeled as a hollow cylinder.

The thermal capacitance of the teeth is found via the geometrical surface area from the FEA software, and the stack length.

The thermal capacitance of the active part of the winding is found by taking the sum of the active winding mass and the slot impregnation mass. The two volumes are found via the axial copper and slot cross sectional areas, the number of slots and the stack length.

The thermal capacitance of the end winding is found in a similar way as the active part of the winding, but the winding length is instead the passive part of half a turn, $l_{passive}$.

The thermal capacitance of the magnets and the rotor laminations is found in the same way as the stator laminations.

The shaft thermal capacitance is here neglected. This is considered a valid simplification as its thermal time constant is about 1 h and thus have little effect on the rotor and magnet temperatures, and even smaller on the stator laminations and windings.

The thermal capacitance of the bearings is found by using the mass in Section 6.2.5, and assuming that the specific heat is the same as for the shaft material.

The resulting network thermal capacitances are presented in Table 8.2, and in Figure 8.7. The values adhere to material parameters at $100°C$. As shown, the thermal capacitance of the end winding is generally lower than it is for the active winding.

Table 8.2 Thermal capacitances in J/K in the thermal network for the four slot sizes.

		Small	**Original**	**Large**	**High**
Frame	$C_{th,Fr}$	4403	4568	4729	4636
Stator yoke	$C_{th,Yo}$	4039	3345	2631	2631
Stator teeth	$C_{th,Te}$	2686	2725	2695	3136
Active winging and impreg.	$C_{th,AcWi}$	1247	1716	2251	1934
End winding	$C_{th,EnWi}$	576	871	1250	1026
Magnets	$C_{th,PM}$	501	501	501	501
Rotor yoke	$C_{th,RoYo}$	3717	3717	3717	3717
Bearings	$C_{th,Be}$	169	169	169	169

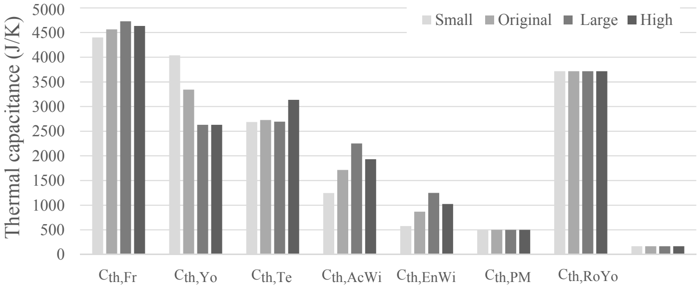

Figure 8.7 Thermal network node capacitances for the different slot areas.

8.1.11 Summary of thermal network node resistances

The resulting network thermal resistances are presented in Table 8.3. The values adhere to a coolant temperature of $65°C$, a flow rate of 6 L/min and a rotor speed of 4000 rpm. The thermal resistance values are considered to be well in line with the values in [53].

Relative changes between the slot geometries per resistance is shown in Figure 8.8.

Table 8.3 Thermal resistances ($W/m\,K$) in the thermal network for the four slot sizes.

	Small	**Original**	**Large**	**High**
$R_{th,Co-Fr}$	0.0037	0.0037	0.0037	0.0037
$R_{th,Fr-Yo}$	0.0066	0.0060	0.0055	0.0055
$R_{th,Yo-Te}$	0.0098	0.0115	0.0112	0.0115
$R_{th,Te-AcWi}$	0.0092	0.0084	0.0079	0.0076
$R_{th,AcWi-EnWi}$	0.0889	0.0669	0.0526	0.0603
$R_{th,EnWi-RoYo}$	1.3527	1.3002	1.2540	1.2665
$R_{th,Te-PM}$	0.2459	0.2482	0.2483	0.2483
$R_{th,RoYo-PM}$	0.1446	0.1446	0.1446	0.1446
$R_{th,EnWi-Fr}$	0.3422	0.3080	0.2796	0.3507
$R_{th,Be-RoYo}$	1.2464	1.3301	1.4123	1.3649
$R_{th,RoYo-Fr}$	0.5153	0.5150	0.5153	0.5169
$R_{th,Be-Fr}$	0.2450	0.2450	0.2450	0.2450

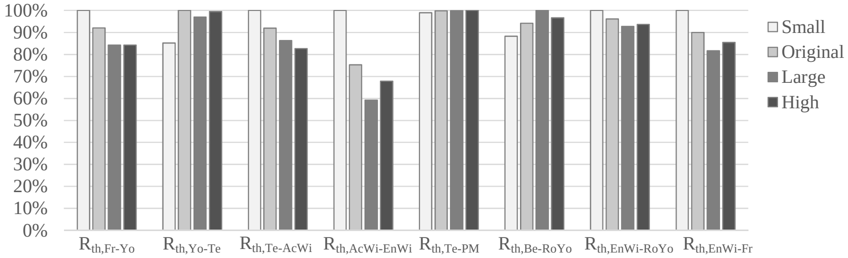

Figure 8.8 Relative thermal resistances for the different slot areas, normalized by the largest value.

8.2 Calculation set-up of lumped-parameter thermal model

The thermal network calculation algorithm is presented in Figure 8.9. The calculations are done for a specific coolant temperature and flow rate, which are treated in Section 8.1.1. The second type of input is the motor's torque and speed operating points that are under consideration. For these operating points, the electromagnetic losses in the six motor parts for the three different magnet and copper temperatures are extracted, as well as the bearing losses.

In the steady state solution for each operating point, an initial guess of the temperature in the magnet and winding network nodes is first used when updating the motor losses for the current temperatures, which is done via linear interpolation. Then follows an iterative loop in which both the temperatures and the losses are updated with respect to each other, until the temperature difference between the last to iterations fall below a specified threshold value.

In the transient solution, an initial temperature guess for the first value of the losses is done similarly as in the steady state case. However, then the temperature increase during one time step is calculated. In the next time step the losses are temperature corrected by using the temperatures from the previous time step.

In both the steady state and the transient solution, some temperature depending parameters are also updated. These are the copper and laminations' thermal conductivity and specific heat, and the thermal conductivity of steel, which is used in the shaft and bearings. The time dependencies of these parameters are presented in Appendix D.

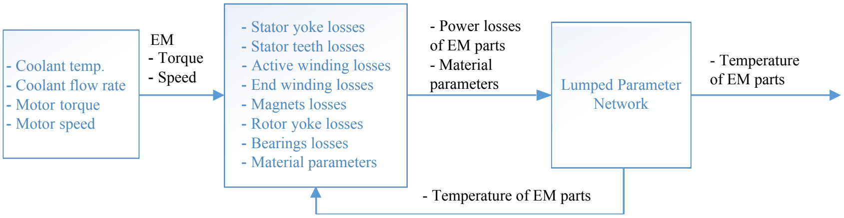

Figure 8.9 Calculation loop for thermal performance of EM.

8.3 Steady state comparison of lumped network and FEA

As a frame of reference, a steady state comparison is here presented between the lumped parameter network (LPN) and thermal simulation results from a 2D implementation of the motor in the FEA software Ansys Mechanical. Two motor operating points are considered: 100 Nm at 4000 rpm, and 50 Nm at 12000 rpm. The former represent a medium load situation where the total loss is 1.7 kW, and the latter a high load situation where the total loss is 3.6 kW. In both cases, the coolant temperature was set to $65°C$ and the flow rate to 6 L/min.

In Ansys Mechanical the losses are implemented as averaged over the same motor regions as was used in the electromagnetic simulations. In order to make the two calculation procedures comparable the following set-up was used in the Ansys Mechanical 2D calculation. Both the active and the end winding parts of the copper losses are applied in the windings, since the end winding node is not possible to represent in the 2D structure. Moreover, the other z-direction heat flows, through the shaft as well as through the internal air, also had to be represented using an alternative approach. These heat flows were calculated with the LPN, and then moved from the sending to the receiving regions manually. Moreover, the air gap is modeled as a conductive solid that has an equivalent thermal conductivity. This equivalent is found from the LPN air gap thermal resistance, the air gap thickness and a surface area in the middle of the air gap.

The results are presented in Table 8.4, along with illustrations of the temperature distribution in each case from Ansys Mechanical in Figure 8.10 and Figure 8.11.

For the medium load case the LPN temperatures are at most $3.7°C$ (4%) higher than the FEA solution. The largest deviation is seen for the stator teeth, the magnets, rotor yoke and the winding, which are over estimated by the LPN by 1.1%.

At the high load, the LPN winding temperatures are up to 3.8$^\circ C$ (3.1%) higher compared to the FEA solution. The largest deviations are seen in the same motor segments as for the medium load. The temperature agreement is quite good, which is positive since their temperatures are important for the study of the thermal performance of the motor.

Table 8.4 Steady state temperature comparison in $^\circ C$ between the LPN and FEA software.

	100 Nm at 4000 rpm			**50 Nm at 12,000 rpm**		
Motor Part	LPN	FEA	(Diff.)	LPN	FEA	(Diff.)
Frame	71.3	71.3	(0)	78.1	78.5	(-0.4)
Stator yoke	80.4	80.2	(0.2)	95.5	96.8	(-1.3)
Stator teeth	95.6	91.9	(3.7)	126.4	122.6	(3.8)
Active winding	103.2	102	(1.2)	138.0	139	(-1)
End winding	127.2	-	(-)	164.2	-	(-)
Magnets	93.9	91.7	(2.2)	123.7	120	(3.7)
Rotor yoke	92.9	91.4	(1.5)	120.2	118.1	(2.1)

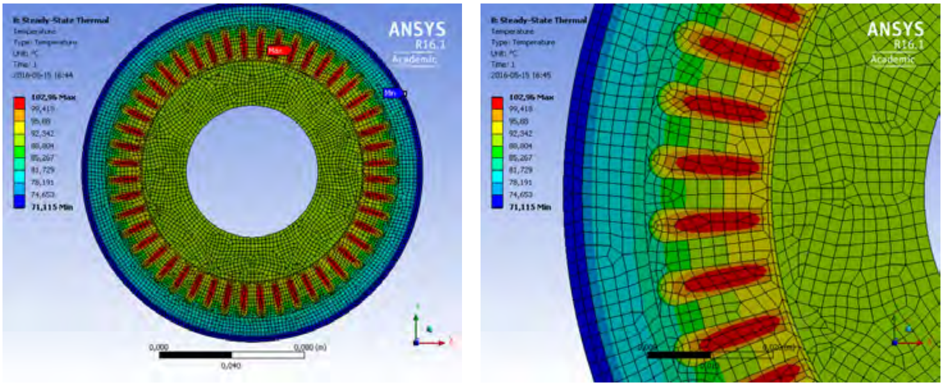

(a) Full cross section.

(b) Zoom in.

Figure 8.10 Temperature distribution in the motor's axial cross section, at 4000 rpm and 100 Nm load, with 65$^\circ C$ coolant and 6 L/min.

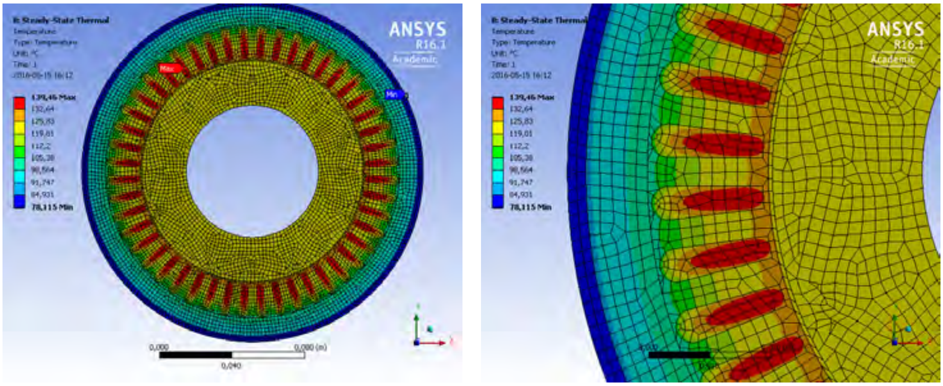

(a) Full cross section.

(b) Zoom in.

Figure 8.11 Temperature distribution in the motor's axial cross section, at 12,000 rpm and 50 Nm load, with 65$^\circ C$ coolant and 6 L/min.

8.4 Steady state sensitivity analysis for selected parameters

Some of the assumptions made when forming the thermal network are based on empirical reference data. It is not clear how representative these assumptions are for this type of motor. Contact air gaps between materials are for example highly dependent on the production process [102], which are not treated here. The thermal conductivity of the winding mix depends both on the fill factor and on the distribution pattern of the conductors, as investigated between ideal hexagon and square patterns in [128]. Furthermore, various suggested approximations of the convection heat transfer coefficients to the internal air showed to vary quite much.

Therefore, a sensitivity analysis with the original slot geometry is here presented, which gives the difference in temperature in the network nodes when varying selected uncertain parameters. The study is done with a coolant temperature at 65$^\circ C$ and a flow rate at 6 L/min. The motor was operated at 50 Nm at 12000 rpm and the total losses are 3.5 kW.

Initially, two different values of the cooling convection coefficient h_{cool} (1000 and 3000 $W/m^2\ K$) and the correction factor $k_{conv,korr}$ (0.4 and 0.6) are implemented. Then two contact air gaps are varied: between frame and stator yoke (5 μm and 15 μm), and between magnet and rotor yoke (10 μm and 200 μm). Also two values for the thermal conductivity of the winding mix is implemented, one that is $\lambda \times 0.5$ and one that is $\lambda \times 1.5$. Furthermore, two values of the thermal resistance of the bearing is studied (as $R_{th} \times 0.5$ and $R_{th} \times 1.5$). Finally, the internal air heat transfer coefficients are varied (as $h \times 0.5$ and $h \times 1.5$). The resulting temperature difference compared to the non-modified network solution is presented in Table 8.5.

Table 8.5 Change in steady state temperature in $^\circ C$ between the modified network and the non-modified, for the Original slot geometry at 50 Nm and 12000 rpm.

	Fr	StYo	StTe	AcWi	EnWi	PM	RoYo	Be
Reference temperatures	78.1	95.5	126.4	138.0	164.3	123.7	120.2	91.1
$h_{cool} = 1000$	12.7	12.7	12.1	12.5	13.9	12.3	12.5	12.7
$h_{cool} = 3000$	-4.3	-4.2	-3.8	-3.9	-4.4	-3.9	-4.1	-4.3
$k_{conv,korr} = 0.4$	-2.6	-2.5	-2.3	-2.3	-2.6	-2.3	-2.4	-2.5
$k_{conv,korr} = 0.6$	2.6	2.5	2.3	2.3	2.6	2.3	2.4	2.5
$l_{contFr-Yo} = 5\mu m$	0.0	-5.2	-4.3	-4.2	-3.3	-3.2	-2.0	-0.3
$l_{contFr-Yo} = 15\mu m$	0.0	5.1	4.3	4.3	3.3	3.2	2.1	0.3
$l_{MagGap} = 10\mu m$	0.0	0.0	-0.1	0.0	0.1	-1.3	1.5	0.2
$l_{MagGap} = 200\mu m$	0.0	0.0	0.0	0.0	0.0	0.3	-0.4	-0.1
$\lambda_{WindMix} = 0.275m$	0.1	0.0	-0.1	5.0	3.8	0.3	0.6	0.1
$\lambda_{WindMix} = 0.825m$	0.0	0.0	0.0	-1.7	-1.3	-0.1	-0.2	-0.1
$R_{th,Be} \times 0.5$	0.0	0.0	0.0	0.0	-0.1	-0.4	-0.7	-5.7
$R_{th,Be} \times 1.5$	0.0	0.0	0.0	0.0	0.1	0.3	0.6	4.7
$h_{Fr,in} \times 0.5$ (64 W/m^2K)	0.0	0.7	2.1	2.9	9.4	6.7	11.3	1.8
$h_{Fr,in} \times 1.5$ (192 W/m^2K)	0.0	-0.3	-0.9	-1.3	-4.1	-2.9	-4.9	-0.8
$h_{Ro} \times 0.5$ (138 W/m^2K)	0.0	0.0	0.1	0.1	-0.3	3.2	6.3	1.0
$h_{Ro} \times 1.5$ (414 W/m^2K)	0.0	0.0	-0.1	0.0	0.2	-1.7	-3.2	-0.5
$h_{EnWi} \times 0.5$ (39 W/m^2K)	0.2	1.3	3.4	5.2	18.9	0.5	-2.4	-0.2
$h_{EnWi} \times 1.5$ (115 W/m^2K)	-0.1	-0.7	-1.9	-2.8	-10.3	-0.3	1.3	0.1

Setting the coolant heat transfer coefficient h_{cool} to 1000 $W/m^2\ K$ gives a temperature increase in all network nodes of around 12-14$^\circ C$. When setting it to 3000 $W/m^2\ K$, the temperature decrease is 4$^\circ C$ in all points. Hence, the temperature change when going from 1000 $W/m^2\ K$ to 2000 $W/m^2\ K$ is almost three times larger, compared to going from 2000 $W/m^2\ K$ to 3000 $W/m^2\ K$. Thus it seems that it is important to be able to maintain a flow rate that can give a sufficient coolant heat transfer coefficient.

In the reference case, it is assumed that half (0.5) of the heat flux to the cooling channels pass through the lower duct surfaces. When instead setting the share to 0.1 more and less, the change in temperature in all network nodes is around 2-3$^\circ C$.

When the contact air gap between the magnet and rotor yoke is set to $10\mu m$ the magnet node temperature becomes about 1.3$^\circ C$ colder, and the rotor yoke node 1.5$^\circ C$ warmer. The other nodes are very little affected from this change, and are even less affected in the case of a $200\mu m$ gap length.

The same weak dependence is also noted for changes in the thermal resistance of the bearing, except in the bearing node itself.

When varying the contact gap length between the frame and stator yoke, on the other hand, the stator yoke temperature changes about $1^\circ C$ per μm gap length. The other node temperatures also change, however, the values decrease in the motors inward radial direction. The end winding and active winding temperatures changes about 0.8-0.9 $^\circ C$ per μm gap length. In [102], gap lengths of up to $77\mu m$ are reported for some machines. Such a gap length in this operating point would lead to winding temperatures of around 200$^\circ C$.

The temperature changes are notable when varying the internal air heat coefficients to $h \times 0.5$ and $h \times 1.5$. The changes are the smallest for h_{Ro} and the largest for h_{EnWi}.

For h_{Ro} the largest temperature changes of around 3%-5% is naturally seen in the rotor yoke, which is the closest node. The second closest node, the magnet, changes 1-2%. The temperature differences in the windings are very small and about the same in both cases.

When varying $h_{Fr,in}$ the largest temperature changes are noted in the rotor yoke node, and the second largest in the end winding node. The end winding increases about 6% in the $h \times 0.5$-case, and it decreases around 3% in the $h \times 1.5$-case. The magnet temperature increase about 5% in the $h \times 0.5$-case, and decreases around 2% in the $h \times 1.5$-case.

The largest changes in the end wining temperatures are noted for changes of h_{EnWi}. In the $h \times 0.5$-case the temperature increase is about 12%, and in the $h \times 1.5$-case the decrease is around 6%. The effect on the active winding temperature is 2%-4%, on the stator teeth 1%-3%, and on the magnets it is less than half a percent.

When it comes to the studied contact gap lengths, winding mix thermal conductivity, and internal air heat transfer coefficients, it is difficult to analytically find assumptions that are more applicable than the empirical data presented in the references. However, if experimental results are available from a physical machine, it it highly recommended to calibrate such network parameters towards measurements in order for the lumped parameter network to better fit the specific machine.

8.5 Transient thermal response to load step

The transient thermal response at two different load steps: 100 Nm at 4000 rpm, and 50 Nm at 12000 rpm, with a coolant temperature of 65°C and a flow rate of 6 L/min, are presented in Figure 8.12 and Figure 8.13, for the Original slot.

At the lower speed level, mainly the copper losses increase with increasing winding temperatures. Only minor changes can be seen for the lamination losses. At the higher speed level, the lamination losses decrease somewhat with increasing temperature.

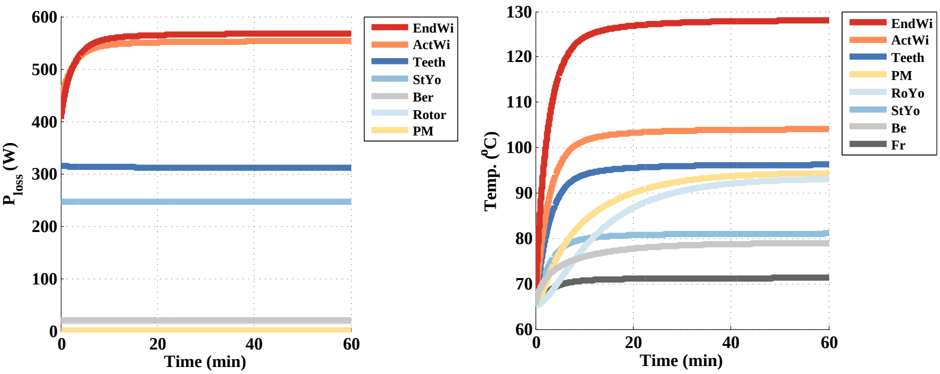

(a) Losses.

(b) Temperatures.

Figure 8.12 Losses and temperatures as a function of time, during a load step of 100 Nm at 4000 rpm with a coolant temperature of 65°C and a flow rate of $6L/min$, for the Original slot geometry.

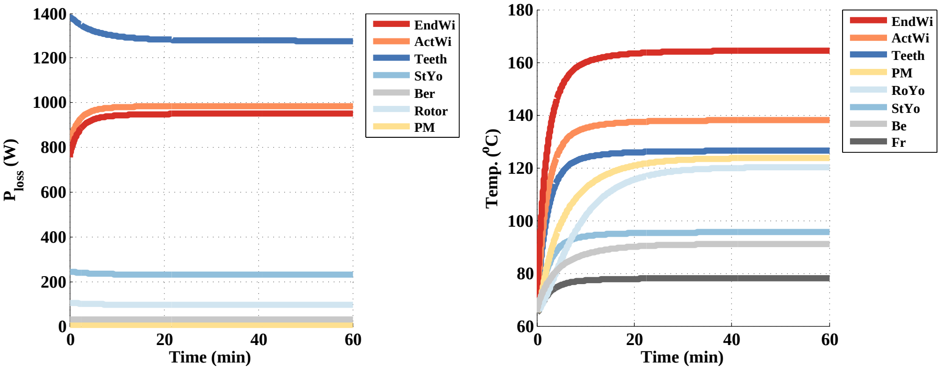

(a) Losses.

(b) Temperatures.

Figure 8.13 Losses and temperatures as a function of time, during a load step of 50 Nm at 12000 rpm with a coolant temperature of 65$^\circ C$ and a flow rate of $6L/min$, for the Original slot geometry.

The thermal time constants for the two load cases at two different coolant temperatures (20$^\circ C$ and 65$^\circ C$) and related flow rates (12 L/min and 6 L/min), are presented in Table 8.6. The time constants are a bit longer in the case of the lower motor speed compared to the higher. Furthermore, the time constants at one speed level are only slightly longer for the case of the cold coolant compared to the warm. It should be noted that the time constants of the rotor and magnets would be a bit longer if also the shaft thermal capacitance was included in the lumped network.

Table 8.6 Thermal time constants of lumped-parameter network nodes in minutes.

	100 Nm at 4000 rpm		**50 Nm at 12,000 rpm**	
	20$^\circ C$	65$^\circ C$	20$^\circ C$	65$^\circ C$
Stator yoke	3.6	3.3	3.1	2.8
Stator teeth	3.4	3.2	2.6	2.4
Active winding and impreg.	3.3	3.0	2.6	2.4
End windings	3.1	2.7	2.6	2.3
Magnets	9.8	9.9	5.9	5.8
Rotor yoke	14.0	14.6	9.1	9.3
Bearings	5.2	5.1	4.8	4.4

Chapter 9

Thermal Performance for HighwayII PMSM with Four Different Slot Areas

A comparison between the the performance when using different slot area geometries, which were introduced in Section 6.7, is here presented regarding thermal steady state, over load capability and transient load cycle performance. The purpose is to investigate the differences between the various slot geometries.

9.1 Steady state performance

As was noted in Chapter 8, the four parts in the motor with the highest temperatures are the two parts of the windings, the stator teeth, and the magnets. The steady state temperature development as a function of torque and speed in these motor parts for the Original slot motor geometry, is presented in Figure 9.1, along with the road load of the HighwayII concept BEV. It can be noted, that the highest temperatures are reached along the max torque trajectory. When driving at the top speed on a flat road, the winding temperature becomes around $120°C$, and the magnet temperature about $100°C$.

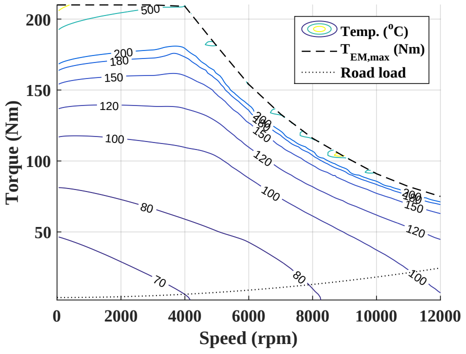

(a) Stator teeth.

(b) Active winding.

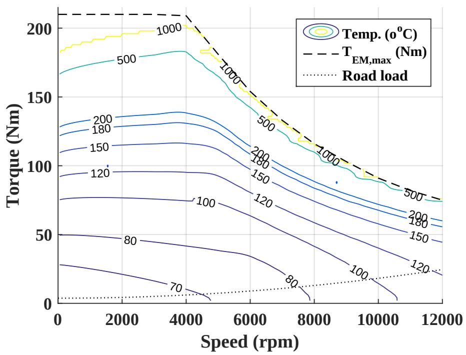

(c) End winding.

(d) Magnets.

Figure 9.1 Steady state temperature contour lines in selected motor parts as a function of torque and speed, for the Original slot geometry, with a coolant temperature of $65^{\circ}C$ and a flow rate of 6 L/min. The road load of the HighwayII BEV is also included as a reference.

In order for the lifetime of the motor to be as long as possible it is desired to limit the max temperature in the windings of an electric machine. The chosen critical temperature depends both on the winding insulation class and the number of working hours that is the design target [46]. It is here assumed that the winding temperature should not exceed $150^{\circ}C$ in transient mode, and be limited to $120^{\circ}C$ in continuous operation mode.

At the same time the magnet temperature should not exceed $140^{\circ}C$, as noted in Section 6.2.3.

The torque-speed levels for when the winding reach its critical temperatures $120^{\circ}C$ and $150^{\circ}C$, and the magnet reach $100^{\circ}C$ and $140^{\circ}C$, are presented for all four slot geometries in Figure 9.2. As expected, it can be noted that the motor with the Small slot will reach both the critical winding and magnet temperatures at lower torque levels compared to the other slot geometries. The highest torque levels for the specified critical temperatures can be reached with the Large slot geometry. This is due to the lower losses, especially copper losses, in a large part of the motor operating area with the Large slot compared to the other geometries (presented in Figure 6.18), and the higher losses for the Small slot.

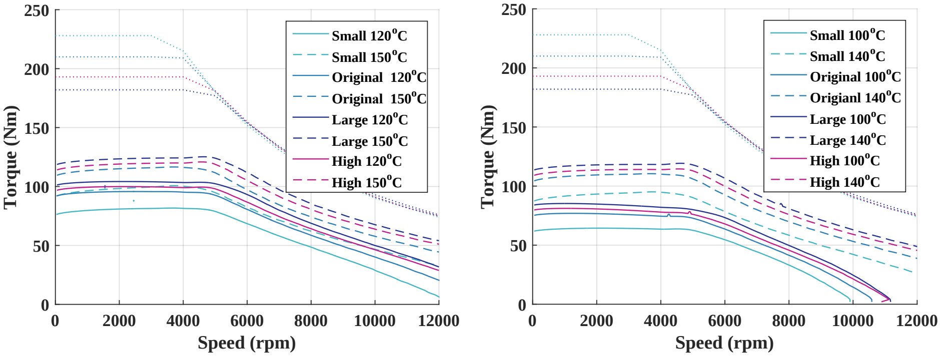

(a) End winding.

(b) Magnets.

Figure 9.2 Steady state temperature development in end windings and magnets for all slot geometries, at a coolant temperature of 65°C and a flow rate of 6 L/min.

The max torque levels reached at the studied critical temperatures above, are presented in Table 9.1. The magnet reaches the max temperature at lower torque levels compared to the torque levels at which the end winding reaches the max temperature. It seems that the magnet's temperature capability is not enough for this design and application, and perhaps it should be replaced by one that has a higher thermal capability. When considering the max torque at 120°C, the ratio of peak to continuous torque is around 2.8 for the Small slot, 2.2 for the Original, 1.8 for the Large, and 1.9 for the High slot. As a frame of reference it is around 1.2-2 times for nine existing BEVs (as presented in Figure A.4).

Table 9.1 Max torque reached at winding and magnet critical temperatures, for all slot geometries, at a coolant temperature of 65°C and a flow rate of 6 L/min.

	Small	**Original**	**Large**	**High**
Max torque at 120°C end winding	81.7 (88%)	95.7 (100%)	104.2 (104%)	99.9 (99%)
Max torque at 150°C end winding	100.7 (86%)	116.6 (100%)	125.2 (107%)	120.8 (104%)
Max torque at 100°C magnets	64.4 (84%)	76.9 (100%)	85.3 (111%)	81.1 (105%)
Max torque at 140°C magnets	95.1 (86%)	110.5 (100%)	119.3 (108%)	114.5 (104%)

9.2 Transient over load

Here the max time duration in a certain operating point in the torque-speed-plane is calculated, caused by a load step at a certain speed level. All load steps originates from the torque level where the end winding has already reached $120°C$ in steady state. The initial steady state temperatures of the other motor parts at this torque level are used as a starting point. Then load steps in the torque level are taken, whereupon the time until the end winding reaches $150°C$ is found via the transient thermal response. The results are presented in Figure 9.3.

As expected from the steady state results, the longest time at high torque levels can be reached with the Large slot geometry. With a load step up to the peak torque level for the Large slot geometry, 182 Nm (at 2000 rpm), it takes 33s until the end winding reaches the critical temperature of $150°C$. For the High slot it takes 27s, for the Original 25s, and for the Small slot 13s. Considering that 80% of all accelerations in the Test and Logged cycles are around 9s-13s (Section 3.4), and that this is a worst case approach by using a very high coolant temperature, the Small slot geometry may still be viable. It should also be noted that the comparison is done for a fixed max phase current. In case of a larger current, even larger torque levels could be thermally possible with the Original, Large and High slot geometries.

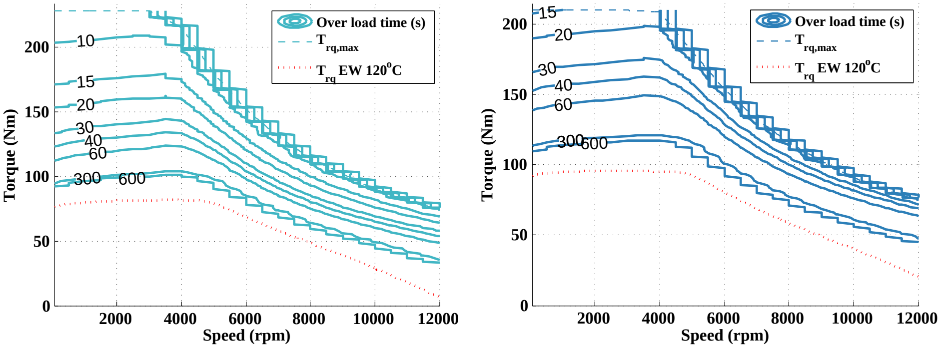

(a) Small slot area.

(b) Original slot area.

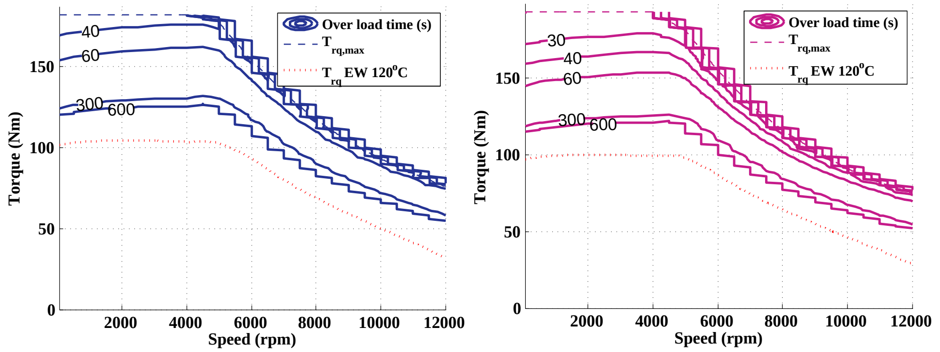

(c) Large slot area.

(d) High slot area.

Figure 9.3 Time spent in different operating points, before end winding reach 150 $°C$, at 20 $°C$ coolant temperature, for two slot sizes.

9.3 Performance during drive cycles

The motor's temperature development during selected Urban, Rural and Highway Test drive cycles are investigated and compared between the different stator geometries. The cycles are repeated several times in order to reach thermal steady state. As an example, the motor part losses and temperature development during NEDC is presented in Figure 9.4, and during ArtemisMW130 in Figure 9.5. It can be noted that the teeth losses are the highest during high speed driving in both cycles. Large power loss peaks are reached during breaking in the ArtemisMW130 cycle, which cause a temperature rise in the end winding of around 4-6$^\circ C$ during 4s each. The peak end winding temperatures are the highest in all cycles.

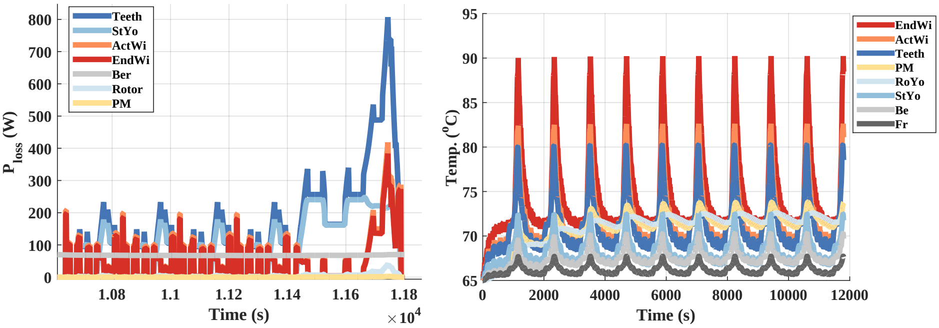

(a) Losses during one cycle.

(b) Temperature during ten consecutive cycles.

Figure 9.4 Losses and temperature development during the NEDC cycle with the original slot, at a coolant temperature of 65$^\circ C$ and a flow rate of 6 L/min.

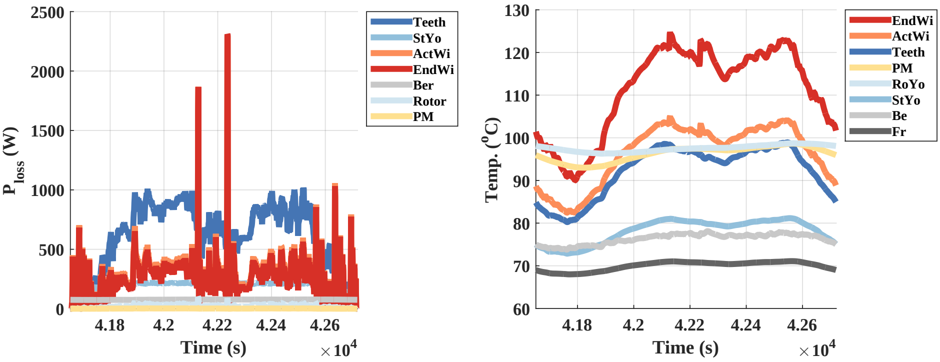

(a) Losses.

(b) Temperature.

Figure 9.5 Losses and temperature development during the ArtemisMW130 cycle with the original slot, at a coolant temperature of 65$^\circ C$ and a flow rate of 6 L/min.

The peak and cycle average power losses, normalized to the values of the Original slot geometry, are presented in Figure 9.6. The highest peak losses can be noted for the Small slot geometry, and the lowest for the Large slot, except in the ECE case. The cycle average losses are the lowest for the Small slot during all cycles except the acceleration intense ArtemisURBAN, UCLA92, and US06, as well as in the high speed cycle ArtemisMW130. In these cycles the losses are instead the highest for the Small slot, except in UCLA92 where the High slot cause the largest losses. Otherwise, the losses with the Large slot are the highest in most cycles. The largest difference between the highest and lowest cycle average losses are noted for the HWFET cycle, which includes high speed levels but relatively low acceleration levels.

The fact that the machine with the Small slot area has the lowest average cycle losses was slightly unexpected. This in combination with the highest peak torque and least amount of copper (which is more expensive than laminations per unit mass [128]), makes it a rather attractive design solution.

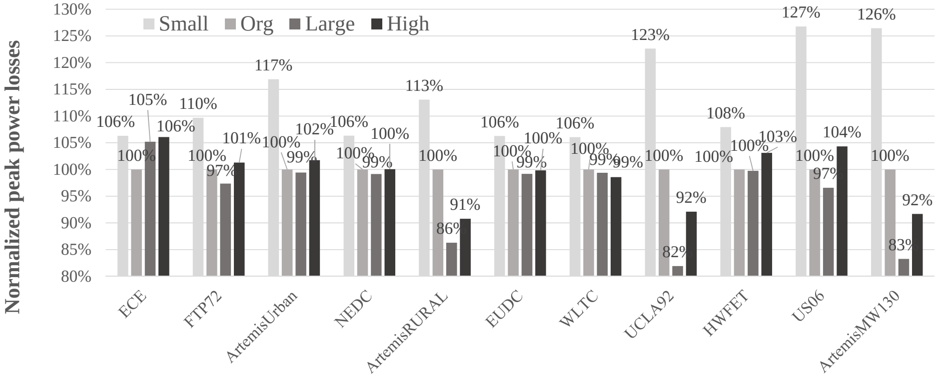

(a) Normalized peak losses.

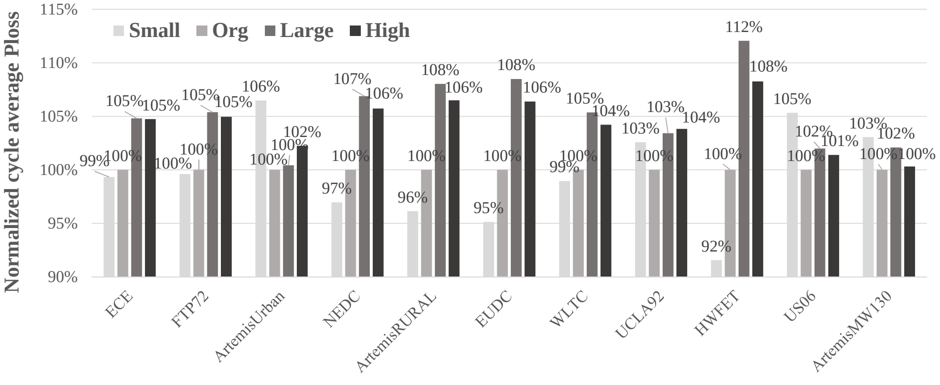

(b) Normalized cycle average losses.

Figure 9.6 Peak and cycle average losses during drive cycles, where all values are normalized by the results for the Original slot size, at a coolant temperature of $65^\circ C$ and a flow rate of $6\ L/min$.

The max magnet and end winding temperatures during the selected drive cycles are presented in Figure 9.7. The max magnet temperature differ $2°C$ or less between the different slot geometries for the investigated drive cycles. The highest magnet temperatures are seen for the two cycles with the highest average speed levels, but still they do not reach more than $99°C$.

The max winding temperature is the highest for the Small slot geometry for all cycles, followed by the Original slot, and the lowest for the Large slot geometry. As with the magnet, the largest peak temperatures are noted for the cycles with the highest speed levels, and are close to the critical for the Small slot geometry.

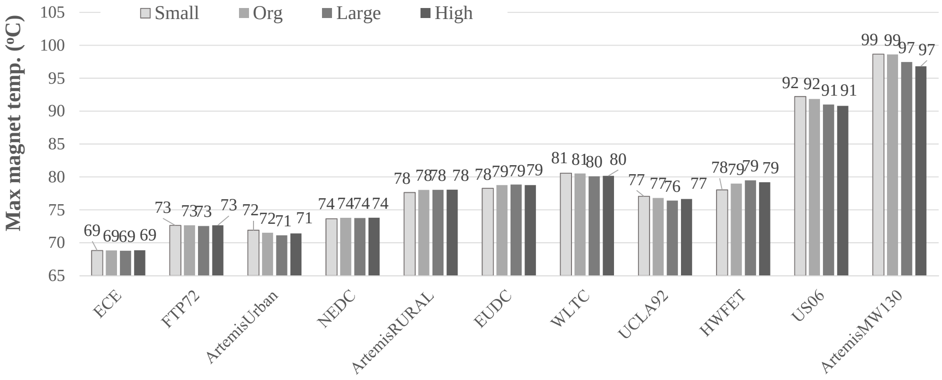

(a) Max magnet temperature.

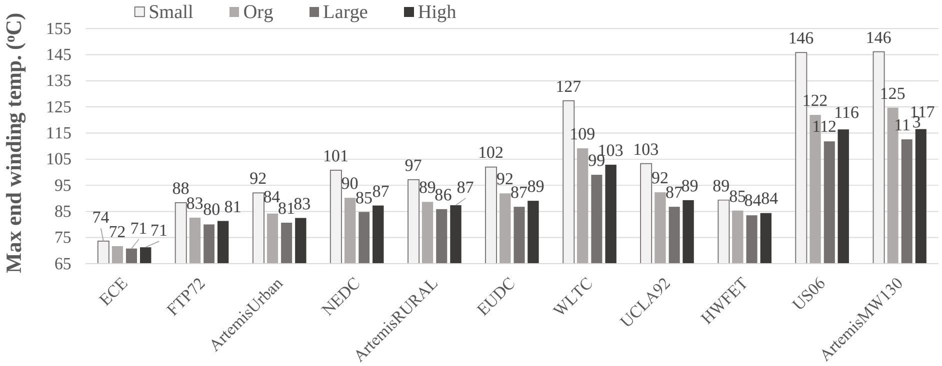

(b) Max end winding temperature.

Figure 9.7 Max magnet and end winding temperatures during drive cycles, at a coolant temperature of $65°C$ and a flow rate of 6 L/min.

Chapter 10

Conclusions and Future Work

10.1 Conclusions

In this thesis, various drive cycles, legislative, official real-world and measured within the frame of the project, have been studied and characterized in terms of speed and acceleration cycle parameters, as well as acceleration and speed distribution. The objective was to assess typical vehicle usage on different road types, but also to study the implication on vehicle energy consumption due to the drive cycle's characteristics. For this evaluation, three reference vehicles (a City car, a Highway car and a Sport car) were designed after different set performance requirements, with data on existing BEVs as a frame of reference. An available traction motor, power electronic module and traction battery were utilized. Furthermore, the electromagnetic efficiency of two v-shaped PMSM reference motors (CityII and HighwayII) were evaluated when scaling the active length. Then the consequence on acceleration performance, drive cycle fulfilment and energy consumption during re-scaling of the electric drive system was studied. Moreover, the electromagnetic losses for four different slot areas were compared (for the HighwayII motor), along with the thermal steady state and transient over load as well as temperature development during drive cycles.

Since most of the legislative drive cycles were developed a few decades ago, when the performance of passenger cars were generally lower than today's cars, the drive cycles are not fully representative for today's typical driving. Through comparison with measured drive cycles, it was found that the measured cycles report higher peak levels of acceleration for a certain speed level, and a larger number of speed fluctuations. On the other hand, when studying the relative time spent at certain levels of acceleration and speed, the measured cycles spend only slightly more time at higher levels of acceleration compared to the official cycles, at least on average over a group of similar cycles.

From a literature study, various estimation methods of vehicle frontal area were found. These were compared with available manufacturer data from nine models. It was found that a suitable approximate estimation of the area is 86 % of the product of vehicle track width and height. Furthermore, different, often referred to, estimations regarding the speed dependency of tire rolling resistance were found to deviate from each other rather much.

Through the mapping of existing BEVs it was found that there is a wide spread regarding their top speed and acceleration performance, as well as driving range, which made a categorization ambiguous.

When comparing the three reference City, Highway, and Sport cars their road load per mass while driving at a constant speed, it was found that the City car has a stronger speed dependency than the other two, due to its relatively higher aerodynamic drag. This causes it to have a higher road load relative to its mass for speed levels greater than $66\,km/h$, compared to the Highway and Sport cars.

The needed wheel force and power, due to performance requirements regarding top speed, time to accelerate to $100\,km/h$, take off at $25\,\%$ grade, and driving at a high grade in a high speed were studied. In a comparison it turned out that the acceleration requirement was the dominating one, hence the only one considered when specifying the needed output from the powertrain.

Furthermore, it was found that the time to accelerate can be achieved with various combinations of initial maximum force and maximum power. For a higher initial maximum force, the needed maximum power to reach $100\,km/h$ at the specified time is lower. This will lead to shorter time to accelerate to $50\,km/h$, but longer time to accelerate from 50 to $100\,km/h$. The conclusion is that a requirement of time to accelerate from 0 to $100\,km/h$ is not enough to describe the desired performance of a vehicle, there must also be an expressed requirement on low and high speed performance, respectively.

Another important finding is that the time resolution of the speed time traces, that defines the official cycles, is relatively low compared to the rate of change of speed. Then the estimated correlated acceleration is highly dependent on the method used for calculation, whether it is a forward and backward looking method or a simpler just backward looking method. The consequence on cycle energy consumption per distance is then highly sensitive to the method used for estimation of acceleration, where the difference may be as large as $15\,\%$ for some cycles.

The resulting average cycle powertrain efficiency are fairly similar for the City and Highway cars, and indicate slightly lower values for the Urban cycles, 77%-86%, compared to the Rural 85%-88% and highway cycles 87%-89%. The Sport model give lower average efficiencies due to the higher power rating of the powertrain. Moreover, the average efficiency values are very similar for both the test cycles and the logged cycles, within the same road-type category. For the two road-type categories with the lowest speed levels, the logged cycles indicate a larger spread compared to the test cycles regarding energy consumption per driven distance. Also within the same road-type category, those cycles that spend most time at high acceleration and speed levels are those that consume the most energy per distance during propulsion. At the same time, in these cycles more braking energy is also available for regenerative braking, which makes the total energy consumption a bit less sensitive to speed fluctuations and high acceleration levels, still the tendency is a higher energy consumption per driven distance.

The effect on acceleration due to re-scaling of motor active length, is largest for the shortest stack lengths and smallest for the longest. For the acceleration time 0-100km/h, the difference between the scale factors 50% and 80% is 12s for the CityII car, and 8s for the HighwayII, whereas the difference between the scale factors 120% and 150% is only about 2s for both cars.

Both the CityII and HighwayII concept BEVs can fulfill the speed reference of most

Test cycles down to 70% of the original stack length. Also, for both cars, the energy consumption per driven distance decreases with decreasing stack length, except for the two acceleration intense urban cycles NYCC and ArtemsURBAN whose minimum is reached with a up-scaled stack length. For the CityII car, the lowest values are down to 94% of the consumption with the original stack length, and for the HighwayII car the lowest values are 98% of the original stack length. With both cars, the largest decrease is noted for cycles with higher speed levels.

When varying the slot size for the v-shaped PMSM HighwayII reference motor while keeping the same max phase current and voltage, the amount of copper and core losses are shifted. For a smaller slot area, the copper losses increase and the core losses decrease, whereas the opposite applies to a larger slot and copper area. The resulting total losses are then largest for the smaller slot geometry in a large part of the motor operating area. Due to this, during thermal steady state, the small slot geometry reaches the chosen continuous end winding temperature at lower torque levels compared to the other slot geometries. The largest continuous torque levels are reached with the large slot area. During a transient over load step which originates from the steady state torque level, the motor version with the largest slot area is capable of staying at its peak torque for 33s. The high, original high and small slot geometries are able to stay at the same operating point for 27s, 25s, and 13s, respectively.

The small slot geometry had the highest peak losses during the drive cycles, however, on a cycle average it had the lowest losses for 7 of the 11 studied cycles. This fact, in combination with the highest peak torque and lowest material cost, makes it a very interesting option as an electric vehicle traction motor.

10.2 Future Work

As the presented results are valid under the assumptions made and models used during the study, perhaps it would be valuable to assess the consequence on energy consumption while improving the level of detail regarding some of the assumptions and models used. For example, by modeling the rolling resistance as a function of speed, and by implementing a wheel slip model, the change in energy consumption could be assessed in order to be able to draw conclusions on the necessary level of detail in the modeling of these phenomena. Also, a sensitivity study on the influence on energy consumption due to different values of vehicle frontal areas and aerodynamic drag coefficients would be interesting.

The accuracy of the battery losses and the dynamic voltage trajectory modeling could be improved by also implementing capacitive terms, although then perhaps a different battery cell should be modeled where more data is available.

Apart from energy consumption, range and acceleration performance, aspects such as life cycle cost and environmental effects of the BEV powertrain design choices, e.g. recycling, are of vital importance and could be included in future studies.

A more detailed investigation of various cooling channel geometries, preferably in combination with CFD simulations would be highly valuable in order to assure a reasonable cooling solution. Additionally, CFD simulations of the motor's internal air convection would be valuable to better estimate the heat transfer coefficients. Furthermore, in the lumped parameter network, perhaps the air temperatures could also be evaluated and it's parameters temperature adjusted for a higher accuracy.

Moreover, it would be interesting to also study the temperature development during the Logges real-world drive cycles for the different slot areas, in order to determine the effect on temperature for a larger number of speed fluctuations and various grade levels.

Finally, the derived drive cycles from the measured GPS and accelerometer signals, could perhaps be improved using more advanced filtering techniques.

References

[1] (2012, may) Regulation no 101, official journal of european union. Economic Commission for Europe of the United Nations. Accessed 2012-10-31. [Online]. Available: http://eur-lex.europa.eu/LexUriServ/LexUriServ.do?uri=OJ:L:2012:138:0001:0077:en:PDF

[2] A. Nordelöf, M. Messagie, A.-M. Tillman, M. Ljunggren Söderman, and J. Van Mierlo, "Environmental impacts of hybrid, plug-in hybrid, and battery electric vehicles—what can we learn from life cycle assessment?" *The International Journal of Life Cycle Assessment*, vol. 19, no. 11, pp. 1866–1890, 2014. [Online]. Available: http://dx.doi.org/10.1007/s11367-014-0788-0

[3] (2015) Global ev outlook 2015. IEA, International Energy Agency, EVI, Electric Vehicles Initiative. Accessed 2015-04-27. [Online]. Available: http://cleanenergyministerial.org/Portals/2/pdfs/EVI-GlobalEVOutlook2015-v14-landscape.pdf

[4] P. Mock. (2014) European vehicle market statistics, 2014. The International Council of Clean Transportation (ICCT).

[5] K. Rajashekara, "Present status and future trends in electric vehicle propulsion technologies," *Emerging and Selected Topics in Power Electronics, IEEE Journal of*, vol. 1, no. 1, pp. 3–10, March 2013.

[6] E. Ericsson. (2000) Driving pattern in urban areas - descriptive analysis and initial prediction model. Lund Institue of Technology, Department of Technology and Society, Traffic Planning. Accessed 2013-12-11. [Online]. Available: http://www.lunduniversity.lu.se/o.o.i.s?id=12683&postid=627123

[7] (2006, dec) Final technical support document, fuel economy labeling of motor vehicle revisions to improve calculation of fuel economy estimates. US Environmental Protection Agency (EPA), Office of Transportation and Air Quality. Accessed 2013-12-09. [Online]. Available: http://www.epa.gov/carlabel/documents/420r06017.pdf

[8] E. Ericsson, "Independent driving pattern factors and their influence on fuel-use and exhaust emission factors," *Transportation Research Part D: Transport and Environment*, vol. 6, no. 5, pp. 325 – 345, 2001. [Online]. Available: http://www.sciencedirect.com/science/article/pii/S1361920901000037

[9] S. Samuel, L. Austin, and D. Morrey, "Automotive test drive cycles for emission measurement and real-world emission levels - a review," *Proceedings of the Institution of Mechanical Engineers, Part D: Journal of Automobile Engineering*, vol. 216, no. 7, pp. 555–564, 2002, cited By (since 1996)34. [Online]. Available: http://www.scopus.com/inward/record.url?eid=2-s2.0-0036964445&partnerID=40&md5=7dfe8159f1a6d5b00f7a8e1153ee5aa4

[10] (2012) Advanced powertrain research facility, avta nissan leaf testing and analysis. Idaho National Laboratory (INL), Advanced Vehicle Testing Activity (AVTA). Accessed 2013-10-17.

[11] S. Williamson, A. Emadi, and K. Rajashekara, "Comprehensive efficiency modeling of electric traction motor drives for hybrid electric vehicle propulsion applications," *Vehicular Technology, IEEE Transactions on*, vol. 56, no. 4, pp. 1561–1572, July 2007.

[12] A. Boretti, "Analysis of the regenerative braking efficiency of a latest electric vehicle," in *SAE Technical Paper*. SAE International, 11 2013.

[13] J. G. Hayes and K. Davis, "Simplified electric vehicle powertrain model for range and energy consumption based on epa coast-down parameters and test validation by argonne national lab data on the nissan leaf," in *Transportation Electrification Conference and Expo (ITEC), 2014 IEEE*, June 2014, pp. 1–6.

[14] F. An, M. Barth, and G. Scora, "Impacts of diverse driving cycles on electric and hybrid electric vehicle performance," in *SAE Technical Paper*. SAE International, 08 1997.

[15] M. D. Gennaro, E. Paffumi, G. Martini, U. Manfredi, H. Scholz, H. Lacher, H. Kuehnelt, and D. Simic, "Experimental investigation of the energy efficiency of an electric vehicle in different driving conditions," in *SAE Technical Paper*. SAE International, 04 2014.

[16] J.-M. Zaccardi and F. Le Berr, "Analysis and choice of representative drive cycles for light duty vehicles, case study for electric vehicles," *Proceedings of the Institution of Mechanical Engineers, Part D: Journal of Automobile Engineering*, 2012.

[17] H. Neudorfer, A. Binder, and N. Wicker, "Analyse von unterschiedlichen fahrzyklen für den einsatz von elektrofahrzeugen," *Elektrotechnik und Informationstechnik*, vol. 123, no. 7-8, pp. 352–360, 2006.

[18] X. Wu, D. Freese, A. Cabrera, and W. A. Kitch, "Electric vehicles energy consumption measurement and estimation," *Transportation Research Part D: Transport and Environment*, vol. 34, no. 0, pp. 52 – 67, 2015.

[19] P. Mellor, D. Roberts, and D. Turner, "Lumped parameter thermal model for electrical machines of tefc design," *Electric Power Applications, IEE Proceedings B*, vol. 138, no. 5, pp. 205–218, Sept 1991.

[20] G. Kylander, "Thermal modelling of small cage induction motors," Thesis for the degree of Doctor of Philosophy in Engineering, Technical Report No. 265, Chalmers University of Technology, Feb 1995.

[21] J. Nerg, M. Rilla, and J. Pyrhonen, "Thermal analysis of radial-flux electrical machines with a high power density," *Industrial Electronics, IEEE Transactions on*, vol. 55, no. 10, pp. 3543–3554, Oct 2008.

[22] G. Demetriades, H. De La Parra, E. Andersson, and H. Olsson, “A real-time thermal model of a permanent-magnet synchronous motor,” *Power Electronics, IEEE Transactions on*, vol. 25, no. 2, pp. 463–474, Feb 2010.

[23] J. Fan, C. Zhang, Z. Wang, Y. Dong, C. E. Nino, A. R. Tariq, and E. G. Strangas, “Thermal analysis of permanent magnet motor for the electric vehicle application considering driving duty cycle,” *IEEE Transactions on Magnetics*, vol. 46, no. 6, pp. 2493–2496, June 2010.

[24] J. M. Miller, *Propulsion Systems for Hybrid Vehicles*. Institution of Engineering and Technology, London, United Kingdom, 2010. [Online]. Available: http://digital-library.theiet.org/content/books/rn/pbrn007e

[25] T. D. Gillespie, *Fundamentals Of Vehicle Dynamics*, 1st ed. Society of Automotive Engineers, Inc., 1992.

[26] (2014, jan) Density of air. English Wikipedia, the free encyclopedia. Accessed 2014-01-03. [Online]. Available: http://en.wikipedia.org/wiki/Density_of_air

[27] J. Y. Wong, Ed., *Theory of Ground Vehicles*, 4th ed. John Wiley & Sons , Inc., 2008.

[28] W.-H. Hucho, Ed., *Aerodynamics of Road Vehicles, From Fluid Mechanics to Vehicle Engineering*, 4th ed. Society of Automotive Engineers, Inc., 1998.

[29] R. B. GmbH, *Automotive Handbook*, 8th ed. John Wiley Sons, 2011.

[30] (2006, feb) The pneumatic tire, dot hs 810 561. NHTSA, National Highway Traffic Safety Administration, U.S. Department of Transportation. Accessed 2014-02-19. [Online]. Available: http://www.nhtsa.gov/staticfiles/safercar/pdf/PneumaticTire_HS-810-561.pdf

[31] L. Guzzella and A. Sciarretta, *Vehicle Propulsion Systems - Introduction to Modeling and Optimization*, 2nd ed. Springer, 2007.

[32] M. Ehsani, Y. Gao, and A. Emadi, *Modern Electric, Hybrid Electric, and Fuel Cell Vehicles: Fundamentals, Theory, and Design*, 2nd ed. CRC Press, Taylor & Francis Group., 2010.

[33] *Tires and Passenger Vehicle Fuel Economy: Informing Consumers, Improving Performance – Special Report 286*. Washington, DC: The National Academies Press, 2006. [Online]. Available: http://www.nap.edu/

[34] J. Hendershot and T. Miller, *Design of Brushless Permanent-Magnet Machines*. Motor Design Books LLC, 2010.

[35] A. Rabiei, “Energy efficiency of an electric vehicle propulsion inverter using various semiconductor technologies,” Thesis for the degree of Licentiate of Engineering, Chalmers University of Technology, 2013. [Online]. Available: http://publications.lib.chalmers.se/records/fulltext/187097/187097.pdf

[36] O. Wallmark, “On control of permanent-magnet synchronous motors in hybrid-electric vehicle applications,” Thesis for the degree of Licentiate of Engineering, Chalmers University of Technology, 2004. [Online]. Available: http://publications.lib.chalmers.se/records/fulltext/2386.pdf

[37] A. Wintrich, U. Nicolai, W. Tursky, and T. Reimann. (2011) Application manual power semiconductors. Semikron International GmbH. [Online]. Available: http://www.semikron.com/skcompub/en/SEMIKRON_Application_Manual_Power_Semiconductors_.pdf

[38] O. Josefsson, “Energy efficiency comparison between two-level and multilevel inverters for electric vehicle applications,” Thesis for the degree of Licentiate of Engineering, Chalmers University of Technology, 2013. [Online]. Available: http://publications.lib.chalmers.se/records/fulltext/174182/174182.pdf

[39] V. Johnson, “Battery performance models in {ADVISOR},” *Journal of Power Sources*, vol. 110, no. 2, pp. 321 – 329, 2002. [Online]. Available: http://www.sciencedirect.com/science/article/pii/S0378775302001945

[40] T. Reddy and D. Linden, *Handbook of batteries*, 4th ed. Mcgraw-Hill, 2011.

[41] J. Croes and S. Iqbal. D2.1 document 1: Literature survey: Gearlosses. ESToMaD, Energy Software Tools for Sustainable Machine Design. Accessed 2014-04-25. [Online]. Available: http://www.estomad.org/documenten/D2_1/D2_1%20Document%201%20%20Literature%20survey%20gears.pdf

[42] E. Nam. (2004) Advanced technology vehicle modeling in pere. EPA, United States Environmental Protection Agency, Office of Transportation and Air Quality. Accessed 2014-04-15. [Online]. Available: http://www.epa.gov/otaq/models/ngm/420d04002.pdf

[43] T. Hofman and C. H. Dai, “Energy efficiency analysis and comparison of transmission technologies for an electric vehicle,” in *Vehicle Power and Propulsion Conference (VPPC), 2010 IEEE*, Sept 2010, pp. 1–6.

[44] M. A. M. Chris Mi and D. W. Gao, *Hybrid Electric Vehicles: Principles and Applications with Practical Perspectives*, 1st ed. John Wiley & Sons , Inc., 2011.

[45] F. Incropera, D. Dewitt, T. Bergman, and A. Lavine, *Fundamentals of Heat and Mass Transfer*. John Wiley & Sons, 2007.

[46] J. Soparat and C. na Benyajati, “Liquid cooled induction motor: Computational design, heat transfer analysis, parametric study, and performance testing,” *SAE Int. J. Alt. Power.*, vol. 2, pp. 1–6, 03 2013.

[47] A. Boglietti, A. Cavagnino, M. Lazzari, and M. Pastorelli, “A simplified thermal model for variable-speed self-cooled industrial induction motor,” *Industry Applications, IEEE Transactions on*, vol. 39, no. 4, pp. 945–952, July 2003.

[48] Y. A. Çengel, *Introduction to Thermodynamics and Heat Transfer*. Mcgraw-Hill, 2008.

[49] Y. Chin and D. Staton, “Transient thermal analysis using both lumped-circuit approach and finite element method of a permanent magnet traction motor,” in *AFRICON, 2004. 7th AFRICON Conference in Africa*, vol. 2, Sept 2004, pp. 1027–1035 Vol.2.

[50] A. F. Mills, *Heat Transfer*. Prentice-Hall Inc., 1999.

[51] D. Staton, S. PICKERING, and D. LAMPARD, “Recent advancement in the thermal design of electric motors,” in *SMMA 2001 Fall Technical Conference "Emerging Technologies for the Electric Motion Industry", Raleigh-Durham, North Carolina, USA*, Oct 2001.

[52] A. Boglietti, A. Cavagnino, and D. Staton, “Determination of critical parameters in electrical machine thermal models,” *Industry Applications, IEEE Transactions on*, vol. 44, no. 4, pp. 1150–1159, July 2008.

[53] J. Lindström, “Development of an experimental permanent-magnet motor drive,” Licentiate of Engineering, Technical Report No. 312L, Chalmers University of Technology, apr 1999.

[54] I. J. PEREZ and J. G. KASSAKIAN, “A stationary thermal model for smooth air-gap rotating electric machines,” *Electric Machines & Power Systems*, vol. 3, no. 3-4, pp. 285–303, 1979. [Online]. Available: http://dx.doi.org/10.1080/03616967908955346

[55] D. Kuehbacher, A. Kelleter, and D. Gerling, “An improved approach for transient thermal modeling using lumped parameter networks,” in *Electric Machines Drives Conference (IEMDC), 2013 IEEE International*, May 2013, pp. 824–831.

[56] G. Dajaku and D. Gerling, “An improved lumped parameter thermal model for electrical machines,” in *17th International conference on electrical machines (ICEM2006)*, 2006.

[57] F. Sprei, S. Karlsson, and J. Holmberg, “Better performance or lower fuel consumption. technological development in the swedish new-car fleet...” *Transportation Research Part D: Transport and Environment*, vol. 13:2, s. 75-85, 2008.

[58] S. Karlsson. (2013) The swedish car movement data project final report. Division of Physical resource Theory, Chalmers University of Technology. [Online]. Available: http://publications.lib.chalmers.se/records/fulltext/187380/local_187380.pdf

[59] H. Watson. (1978) Vehicle driving patterns and measurement methods for energy and emission assessment. Bureau of Transport Economics, Canberra. Accessed 2014-01-15. [Online]. Available: http://www.bitre.gov.au/publications/1978/files/op_030.pdf

[60] I. M. Berry, “The effects of driving style and vehicle performance on the real-world fuel consumption of u.s. light-duty vehicles,” Master of Science in Mechanical Engineering and Master of Science in Technology and Policy,

Massachusetts Institute of Technology, feb 2010, accessed 2011-12-20. [Online]. Available: http://web.mit.edu/sloan-auto-lab/research/beforeh2/files/IreneBerry_Thesis_February2010.pdf

[61] (1995, jan) Final technical report on aggressive driving behavior for the revised federal test procedure notice of proposed rulemaking. US Environmental Protection Agency (EPA), Office of Transportation and Air Quality and U.S. Department of Transportation, National Highway Traffic Safety Administration (NHTSA). Accessed 2014-01-21. [Online]. Available: http://www.epa.gov/OMS/regs/ld-hwy/ftp-rev/ftp-us06.pdf

[62] (2011) Final rule, federal register, vol. 76, no. 129, part ii, 40 cfr parts 85, 86 and 600. EPA, United States Environmental Protection Agency, Office of Transportation and Air Quality. Accessed 2013-12-10. [Online]. Available: www.gpo.gov/fdsys/pkg/FR-2011-07-06/pdf/2011-14291.pdf

[63] Council. (1970, march) Council directive 70/220/eec of 20 march 1970 on the approximation of the laws of the member states relating to measures to be taken against air pollution by gases from positive-ignition engines of motor vehicles. Official Journal of the European Communities. Accessed 2014-01-15. [Online]. Available: http://ec.europa.eu/enterprise/sectors/automotive/documents/directives/motor-vehicles/

[64] (2014, january) Emission standards, summary of wolrdwide engine emission standards. DieselNet, Ecopint Inc., Canada. Accessed 2014-01-16. [Online]. Available: http://www.dieselnet.com/standards/

[65] A. Faiz, C. S. Weaver, and M. P. Walsh. (1996) Air pollition from motor vehicles - standards and technolgies fro controlling emissions. The International Bank for Reconstruction and Development, The World Bank, Washington, D.C. Accessed 2014-01-15. [Online]. Available: http://www.un.org/esa/gite/iandm/faizpaper.pdf

[66] M. André. (2004, jun) Real-world driving cycles for measuring cars pollutant emissions, part a: The artemis european driving cycles. ARTEMIS - Assessment and reliability of transport emission models and inventory systems. Accessed 2014-01-10. [Online]. Available: http://inrets.fr/ur/lte/publi-autresactions/fichesresultats/ficheartemis/road3/method31/Artemis_cycles_report_LTE0411.pdf

[67] (2013, nov) Development of a world-wide worldwide harmonized light duty driving test cycle (wltc), draft technical report. United Nations Economic Commission for Europe, Working Party on Pollution and Energy (GRPE), Worldwide harmonized Light vehicles Test Procedure (WLTP), WLTP Sub-group on the Development of the Harmonized driving Cycle (DHC). Accessed 2013-11-14. [Online]. Available: https://www2.unece.org/wiki/download/attachments/15237269/WLTP-DHC-draft_technical_report_ver131101-4.doc?api=v2

[68] (2013, feb) Dynamometer drive schedules. EPA, United States Environmental Protection Agency, Transportation and Air Quality. Accessed 2011-12-19. [Online]. Available: http://www.epa.gov/nvfel/testing/dynamometer.htm#vehcycles/

[69] (2013, jan) Finalized test cycle, wltc. UNECE, United Nations Economic Commission for Europe, Worldwide harmonized Light vehicles Test Procedure (WLTP). Accessed 2013-11-14. [Online]. Available: https://www2.unece.org/wiki/download/attachments/5801079/WLTP-DHC-16-06e_rev.xlsx?api=v2

[70] (2012) Krav för vägars och gators utformning. Trafikverket. Accessed 2013-10-01. [Online]. Available: http://publikationswebbutik.vv.se/shopping/ShowItem.aspx?id=5848

[71] (2005) A policy on design standards interstate system. American Association of State Highway and Transport Officials. Accessed 2013-10-01. [Online]. Available: http://www.dot.state.fl.us/rddesign/qa/Data/AASHTO-InterstateDesignStandards.pdf

[72] (2013) Pmsv3 database. Trafikverket. Accessed 2013-10-01. [Online]. Available: https://pmsv3.trafikverket.se/Pages/EnkelSok/EnkelSokView.aspx

[73] (2009, nov) San fransisco, ca, usa, streets colored by slope. Data Pointed. Accessed 2013-10-01. [Online]. Available: http://www.datapointed.net/visualizations/maps/san-francisco/streets-slope/

[74] N. S. Pearre, W. Kempton, R. L. Guensler, and V. V. Elango, "Electric vehicles: How much range is required for a day's driving?" *Transportation Research Part C: Emerging Technologies*, vol. 19, no. 6, pp. 1171 – 1184, 2011. [Online]. Available: http://www.sciencedirect.com/science/article/pii/S0968090X1100012X

[75] (2011) Summary of travel trends: 2009 national household travel survey. US Department of Transportation, Federal Highway Administration. Accessed 2013-10-09. [Online]. Available: http://nhts.ornl.gov/2009/pub/stt.pdf

[76] (2007) Res 2005-2006, den nationella resvaneundersökningen. SIKA Statistik, Statens institut för kommunikationsanalys. Accessed 2010-12-21. [Online]. Available: http://trafa.se/PageDocuments/ss_2007_19_1.pdf

[77] (2007) Körsträckor øor 2006. SIKA Statistik, Statens institut för kommunikationsanalys. Accessed 2010-12-21. [Online]. Available: http://www.scb.se/Statistik/TK/_dokument/Korstr_2006.pdf

[78] (2012) Driving and parking patterns of european car drivers, a mobility survey. European Commission. Accessed 2013-10-10. [Online]. Available: http://publications.jrc.ec.europa.eu/repository/handle/111111111/26994/1/

[79] (2010) Ample driving range for everyday deeds. Nissan Motor Corporation. Accessed 2013-04-02. [Online]. Available: http://www.newsroom.nissan-europe.com/download/media/specialfile/41486_3_6.aspx

[80] S. Karlsson and E. Jonson, "The importance of car movement data for determining design, viability and potential of phevs," *Proceedings of International Advanced Mobility Forum (IAMF) 2011, Geneva Switzerland*, 2011.

[81] L.-H. Kullingsjö and S. Karlsson. (2012) The swedish car movement data project. Division of Physical resource Theory, Chalmers University of Technology. [Online]. Available: http://publications.lib.chalmers.se/records/fulltext/local_165497.pdf

[82] (2007) Resvanor i göteborgsregionen 2005. Göteborgs Stad, Vägverket and Västtrafik. Accessed 2011-10-11. [Online]. Available: http://www2.trafikkontoret.goteborg.se/resourcelibrary/Resvanor.pdf

[83] J. Krumm, "How people use their vehicles: Statistics from the 2009 national household travel survey," *SAE 2012 World Congress & Exhibition*, 04 2012. [Online]. Available: http://dx.doi.org/10.4271/2012-01-0489

[84] (2007) Axp course design - baseline driving statistics. Automotive Xprice. Accessed 2011-10-08. [Online]. Available: http://www.progressiveautoxprize.org/files/downloads/auto/AXP_FHWA_driving_stats.pdf

[85] R. van Haaren. (2012) Assessment of electric car's range requirements and usage pattern based on driving behavior recorded in the national household travel survey of 2009. Automotive Xprice. Accessed 2011-10-07. [Online]. Available: http://www.solarjourneyusa.com/HowFarWeDrive_v1.3.pdf

[86] E. A. Grunditz, "Bev powertrain component sizing with respect to performance, energy consumption and driving patterns," Thesis for the degree of Licentiate of Engineering, Chalmers University of Technology, 2014. [Online]. Available: http://publications.lib.chalmers.se/records/fulltext/198921/198921.pdf

[87] (1999, oct) 1999 ev america technical specifications. Electric Transportation Applications. Accessed 2014-02-04. [Online]. Available: http://avt.inl.gov/fsev.shtml

[88] (2014) Igbt modules up to 600v, 650v. Infineon. Accessed 2014-03-20. [Online]. Available: http://www.infineon.com/cms/en/product/power/igbt/igbt-module/igbt-module-600v-650v/

[89] (2014, jan) Aesc home page. AESC, Automotive Energy Supply Corporation. Accessed 2014-03-14. [Online]. Available: http://www.eco-aesc-lb.com/en/aboutus/company/

[90] (2011) 2011 nissan leaf - vin 0356. Idaho National Laboratory (INL), Advanced Vehicle Testing Activity (AVTA). Accessed 2014-02-04. [Online]. Available: http://avt.inel.gov/pdf/fsev/batteryleaf0356.pdf

[91] J. Hellsing, "Design and otimization of a permanent magnet motor for a hybrid electric vehicle," Licentiate of Engineering, Technical Report No. 282L, Chalmers University of Technology, mar 1998.

[92] A. Rabiei, T. Thiringer, and J. Lindberg, "Maximizing the energy efficiency of a pmsm for vehicular applications using an iron loss accounting optimization based on nonlinear programming," in *Electrical Machines (ICEM), 2012 XXth International Conference on*, Sept 2012, pp. 1001–1007.

[93] M.-F. Hsieh, Y.-C. Hsu, D. Dorrell, and K.-H. Hu, “Investigation on end winding inductance in motor stator windings,” *Magnetics, IEEE Transactions on*, vol. 43, no. 6, pp. 2513–2515, June 2007.

[94] Y. Sato, S. Ishikawa, T. Okubo, M. Abe, and K. Tamai, “Development of high response motor and inverter system for the nissan leaf electric vehicle,” in *SAE Technical Paper*. SAE International, 04 2011. [Online]. Available: http://dx.doi.org/10.4271/2011-01-0350

[95] S. Oki, S. Ishikawa, and T. Ikemi, “Development of high-power and high-efficiency motor for a newly developed electric vehicle,” *SAE Int. J. Alt. Power.*, vol. 1, pp. 104–111, 04 2012. [Online]. Available: http://dx.doi.org/10.4271/2012-01-0342

[96] H. Shimizu, T. Okubo, I. Hirano, S. Ishikawa, and M. Abe, “Development of an integrated electrified powertrain for a newly developed electric vehicle,” in *SAE Technical Paper*. SAE International, 04 2013. [Online]. Available: http://dx.doi.org/10.4271/2013-01-1759

[97] T. Nakada, S. Ishikawa, and S. Oki, “Development of an electric motor for a newly developed electric vehicle,” in *SAE Technical Paper*. SAE International, 04 2014. [Online]. Available: http://dx.doi.org/10.4271/2014-01-1879

[98] T. Burress and S. Campbell, “Benchmarking ev and hev power electronics and electric machines,” in *Transportation Electrification Conference and Expo (ITEC), 2013 IEEE*, June 2013, pp. 1–6.

[99] B. Ozpineci. (2014) Annual progress report for the power electronics and electric motors program. Oak Ridge National Laboratory. Accessed 2015-04-23. [Online]. Available: http://info.ornl.gov/sites/publications/Files/Pub52422.pdf

[100] T. A. B. et. al. (2011) Evaluation of the 2010 toyota prius hybrid synergy drive system. Oak Ridge National Laboratory. Accessed 2013-11-27. [Online]. Available: http://info.ornl.gov/sites/publications/files/Pub26762.pdf

[101] A. EL-Refaie, N. Harris, T. Jahns, and K. Rahman, “Thermal analysis of multi-barrier interior pm synchronous machine using lumped parameter model,” *Energy Conversion, IEEE Transactions on*, vol. 19, no. 2, pp. 303–309, June 2004.

[102] D. Staton, A. Boglietti, and A. Cavagnino, “Solving the more difficult aspects of electric motor thermal analysis in small and medium size industrial induction motors,” *Energy Conversion, IEEE Transactions on*, vol. 20, no. 3, pp. 620–628, Sept 2005.

[103] B. Zhang, R. Qu, W. Xu, J. Wang, and Y. Chen, “Thermal model of totally enclosed water-cooled permanent magnet synchronous machines for electric vehicle applications,” in *Electrical Machines (ICEM), 2014 International Conference on*, Sept 2014, pp. 2205–2211.

[104] (2015) Hi-lite no30 data sheet. Cogent. Accessed 2015-05-19. [Online]. Available: http://cogent-power.com/cms-data/downloads/Hi-Lite_NO30.pdf

[105] M. D. Magnus Lindenmo and T. C. Support, "No30 hi-lite material data," Cogent Power / Surahammars Bruks AB, private Communication 2016-03-01.

[106] S. Constantinides. (2015) The important role of dysprosium in modern permanent magnets. Arnold Magnetic Technologies Corp. Accessed 2016-03-18. [Online]. Available: http://www.arnoldmagnetics.com/en-us/Technical-Library/Technical-Publications

[107] (2011) Critical materials strategy. U.S. Department Of Energy. Accessed 2016-03-18. [Online]. Available: http://energy.gov/sites/prod/files/DOE_CMS2011_FINAL_Full.pdf

[108] S. Hoenderdaal, L. T. Espinoza, F. Marscheider-Weidemann, and W. Graus, "Can a dysprosium shortage threaten green energy technologies?" *Energy*, vol. 49, pp. 344 – 355, 2013. [Online]. Available: http://www.sciencedirect.com/science/article/pii/S0360544212008055

[109] (2014) Hitachi review vol. 63, no. 3, p.113. Hitachi Metals, Ltd. Accessed 2015-05-28. [Online]. Available: http://www.hitachi.com/rev/specialissue/2014/ebook/index.html#page=1

[110] (2014) Neomax series, data sheets. Hitachi Metals, Ltd. Accessed 2015-05-29. [Online]. Available: http://www.hitachi-metals.co.jp/e/products/auto/el/pdf/nmx_a.pdf

[111] (2015) Neodymium-iron-boron magnets neomax, home page. Hitachi Metals, Ltd. Accessed 2015-05-27. [Online]. Available: http://www.hitachi-metals.co.jp/e/products/auto/el/p03_21.html

[112] (2016) Ball bearings. SKF. Accessed 2016-03-30. [Online]. Available: http://www.skf.com/group/products/bearings-units-housings/ball-bearings/index.html

[113] (2012, oct) Federal report, vol. 77, no. 199, final rule. US Environmental Protection Agency (EPA), Department of Transportation, National Highway Traffic Safety Administration (NHTSA). Accessed 2013-12-08. [Online]. Available: http://www.epa.gov/otaq/climate/regs-light-duty.htm#new1

[114] P. Juris, A. Brune, and B. Ponick, "A coupled thermal-electromagnetic energy consumption calculation for an electric vehicle with wheel hub drive considering different driving cycles," in *Vehicle Power and Propulsion Conference (VPPC), 2012 IEEE*, Oct 2012, pp. 28–31.

[115] A. Abdelli, "Optimal design of an interior permanent magnet synchronous motor for wide constant-power region operation: Considering thermal and electromagnetic aspects," *SAE Int. J. Alt. Power.*, vol. 3, pp. 129–138, 04 2014. [Online]. Available: http://dx.doi.org/10.4271/2014-01-1889

[116] J. Fan, C. Zhang, Z. Wang, and E. Strangas, “Thermal analysis of water cooled surface mount permanent magnet electric motor for electric vehicle,” in *Electrical Machines and Systems (ICEMS), 2010 International Conference on*, Oct 2010, pp. 1024–1028.

[117] “2015 focus electric owner’s manual,” Ford Service Content, 2014, accessed 2015-06-26. [Online]. Available: http://www.fordservicecontent.com/Ford_Content/Catalog/owner_information/2015-Focus-Electric-Owners-Manual-version-1_om_EN-US_11_2014.pdf

[118] “Rav4 ev 2012, quick reference guide,” Toyota, 2012, accessed 2015-05-17. [Online]. Available: http://www.myrav4ev.com/docs/RAV4EV_Owners_Manual.pdf

[119] (1991) Table 8-3-1 - properties of mixture water/glycol. Detector Cooling. Accessed 2016-02-02. [Online]. Available: https://detector-cooling.web.cern.ch/detector-cooling/data/Table%208-3-1.htm

[120] “Technical training. product information. bmw service i01 high-voltage components,” Bayerische Motorenwerke Aktiengesellschaft, 2014, accessed 2015-06-25. [Online]. Available: http://www.kneb.net/bmw/I01/06_I01High-voltageComponents.pdf

[121] G. Li, J. Ojeda, E. Hoang, M. Gabsi, and M. Lecrivain, “Thermal-electromagnetic analysis for driving cycles of embedded flux-switching permanent-magnet motors,” *Vehicular Technology, IEEE Transactions on*, vol. 61, no. 1, pp. 140–151, Jan 2012.

[122] G. I. Taylor, “Distribution of velocity and temperature between concentric rotating cylinders,” *Proceedings of the Royal Society of London A: Mathematical, Physical and Engineering Sciences*, vol. 151, no. 874, pp. 494–512, 1935. [Online]. Available: http://rspa.royalsocietypublishing.org/content/151/874/494

[123] C. Gazley, “Heat transfer characteristics of rotational and axial flow between concentric cylinders,” *Transactions of the ASME*, vol. 80, no. 1, pp. 79–90, 1958.

[124] K. M. Becker and J. Kaye, “Measurements of diabatic flow in an annulus with an inner rotating cylinder,” *Journal of Heat Transfer*, vol. 84, no. 2, pp. 97–104, may 1962. [Online]. Available: http://dx.doi.org/10.1115/1.3684335

[125] B. Zhang, R. Qu, J. Wang, W. Xu, X. Fan, and Y. Chen, “Thermal model of totally enclosed water-cooled permanent-magnet synchronous machines for electric vehicle application,” *Industry Applications, IEEE Transactions on*, vol. 51, no. 4, pp. 3020–3029, July 2015.

[126] (2013) Ball bearings catalogue. SKF. Accessed 2016-04-30. [Online]. Available: http://www.skf.com/binary/138-121486/SKF-rolling-bearings-catalogue.pdf

[127] A. Boglietti and A. Cavagnino, “Analysis of the endwinding cooling effects in tefc induction motors,” *Industry Applications, IEEE Transactions on*, vol. 43, no. 5, pp. 1214–1222, Sept 2007.

[128] C. Du-Bar, “Design of a fault-tolerant fractional slot pmsm for a vehicle application,” Thesis for the degree of Licentiate of Engineering, Chalmers University of Technology, 2014. [Online]. Available: http://publications.lib.chalmers.se/records/fulltext/206039/206039.pdf

[129] (2015) New pc registrations or sales. OICA, Organisation Internationale des Constructeurs d’Automobiles. Accessed 2015-04-27. [Online]. Available: http://www.oica.net/wp-content/uploads//pc-sales-2014.pdf

[130] (2015) More than 740,000 cars worldwide powered by electricity. ZSW, Zentrum für Sonnenenergie- und Wasserstoff-Forschung, Baden-Württemberg. Accessed 2015-04-27. [Online]. Available: http://www.zsw-bw.de/uploads/media/pi06-2015-ZSW-E-Mobility.pdf

[131] (2015) New electric vehicle registrations in the european union. ACEA, European Automobile Manufacturers Association. Accessed 2015-04-24. [Online]. Available: http://www.acea.be/press-releases/article/electric-vehicle-registrations-2014

[132] Electric vehicle sales. EVs Rock EVs Roll. [Accessed: Apr. 24, 2015]. [Online]. Available: http://evsroll.com

[133] Usa december 2015. ev-sales.blogspot.com. [Accessed: Apr. 19, 2016].

[134] Europe december 2015, europe december 2014. ev-sales.blogspot.com. [Accessed: Apr. 19, 2016, and Nov. 6, 2015].

[135] Japan december 2015, japan december 2014. ev-sales.blogspot.com. [Accessed: Apr. 19, 2016, and Nov. 6, 2015].

[136] “Simply electric. smart fortwo electric drive.” Smart UK, 2013, accessed 2015-03-23. [Online]. Available: http://uk.smart.com/uk/en/index/smart-fortwo-electric-drive.html

[137] “Electric drive, frequently asked questions,” Smart USA, 2014, accessed 2015-03-26. [Online]. Available: http://www.smartusa.com/models/electric-drive/faq.aspx

[138] “Plug in. peel out, smart fortwo electric drive,” Smart USA, 2015, accessed 2015-06-30. [Online]. Available: http://www.smartusa.com/Downloads/2015-smart-electric-drive-brochure.pdf

[139] M. Anderman. (2014) The tesla battery report. Advanced Automotive Batteries, (AAB). Accessed 2015-03-31. [Online]. Available: https://www.advancedautobat.com/industry-reports/2014-Tesla-report/Extract-from-the-Tesla-battery-report.pdf

[140] “Smart brabus electric drive,” Smart, 2015, accessed 2015-03-23. [Online]. Available: https://www.smart.com/en/en/index/smart-fortwo-electric-drive/BRABUS.html

[141] "Paris 2012," Toyota Motor Europe, 2012, accessed 2015-03-23. [Online]. Available: http://toyotamedia.iconicweb.com/mediasite/specs/Paris_MS_2012_EN.pdf

[142] "Scion iq ev electric 2013 model emergency response guide," 2012 Toyota Motor Corporation, 2012, accessed 2015-03-23. [Online]. Available: http://afvsafetytraining.com/erg/Scion-IQEV-2013.pdf

[143] "2014 scion iq specifications," Scion USA, 2014, accessed 2015-03-23. [Online]. Available: http://www.scion.com/cars/iQ2014/specs/

[144] "2015 fiat 500e specifications," Fiat Chrysler Automobiles, 2014, accessed 2015-03-20. [Online]. Available: http://www.media.chrysler.com/

[145] "Fiat 500e," Fiat USA, 2013, accessed 2015-03-26. [Online]. Available: http://www.fiatusa.com/assets/pdf/brochures/fiat_500e.pdf

[146] "Citroen c-zero caracterisyiques techniques et equipements," Citroen France, 2014, accessed 2015-03-20. [Online]. Available: http://www.citroen.fr/vehicules/citroen/citroen-c-zero.html

[147] "Citroen c-zero," Citroen France, 2015, accessed 2015-03-27. [Online]. Available: http://www.citroen.fr/vehicules/citroen/citroen-c-zero.html#sticky

[148] "Peugeot ion, preise, ausstattungen und technische daten," Peugeot Germany, 2015, accessed 2015-03-27. [Online]. Available: http://www.peugeot.de/showroom/ion/5-turer/

[149] "2014 i-miev specs," Mitsubishi Canada, 2014, accessed 2015-03-27. [Online]. Available: http://www.mitsubishi-motors.com/en/showroom/i-miev/specifications/

[150] "2014 fuel economy datafile," Office of Transportation & Air Quality, U.S. Environmental Protection Agency, U.S. Department of Energy, 2014, accessed 2015-03-20. [Online]. Available: http://www.fueleconomy.gov/feg/download.shtml

[151] "2014 i-miev specs," Mitsubishi Canada, 2014, accessed 2015-03-27. [Online]. Available: http://www.mitsubishi-motors.ca/en/vehicles/i-miev/2014/specs/

[152] "Tekniska data nya e-up!" Volkswagen Sweden, 2013, accessed 2015-03-18. [Online]. Available: http://personbilar.volkswagen.se/sv/models/up/broschyrer.html

[153] "e-up specifications," Volkswagen Japan, 2015, accessed 2015-03-13. [Online]. Available: http://web.volkswagen.co.jp/cms4/trimlevel/e-up_specs.html#url=

[154] "10 fragen zum e-up!" Volkswagen Das Auto Magazin, 2015, accessed 2015-07-02. [Online]. Available: http://magazin.volkswagen.de/e-up-elektromobilitaet-technik.html

[155] “2015 chevrolet spark specifications,” Chevrolet News, GM Media, 2015, accessed 2015-03-25. [Online]. Available: http://media.gm.com/media/us/en/chevrolet/vehicles/spark-ev/2015.tab1.html

[156] “Bluecar la citadine 100% electrique,” Bluecar France, 2015, accessed 2015-05-15. [Online]. Available: http://www.bluecar.fr/sites/bluecar/files/medias/bluecar_plaquette-vf.pdf

[157] “Minicab miev specifications,” Mitsubishi Motors Japan, 2014, accessed 2015-05-17. [Online]. Available: http://www.mitsubishi-motors.co.jp/minicab-miev/spec/pdf/minicab-miev_spec.pdf

[158] “Mitsubishi motors to launch new minicab-miev commercial electric vehicle in japan,” Mitsubishi Motors, 2011, accessed 2015-07-01. [Online]. Available: http://www.mitsubishi-motors.com/publish/pressrelease_en/products/2011/news/detail0817.html

[159] “Specifications of the bmw i3, valid from 03/2014,” BMW Group PressClub Global, 2014, accessed 2015-03-26. [Online]. Available: https://www.press.bmwgroup.com/global/showTextTopic.html?left_menu_item=node__8601

[160] “Srvice and warranty information, 2014 bmw i3,” BMW Service and Warranty Books, 2014, accessed 2015-07-02. [Online]. Available: http://www.bmwusa.com/Standard/Content/Explore/BMWValue/BMWUltimateService/ServiceandWarrantyBooks.aspx

[161] “Press kit, the bmw i3,” BMW Group, BMW Media Information, 2013, accessed 2015-03-26. [Online]. Available: https://www.press.bmwgroup.com/global/pressDetail.html?title=the-bmw-i3&outputChannelId=6&id=T0148284EN&left_menu_item=node__8601

[162] “Renault zoe, simply revolutionary,” Renault UK, 2015, accessed 2015-06-30. [Online]. Available: https://www.renault.co.uk/brochures/brochure-download.html

[163] “Renault zoe,” Renault Sweden, 2015, accessed 2015-06-30. [Online]. Available: http://www.renault.se/bilar/elbilar/ZOE/ZOE/Versioner.jsp

[164] “Volvo c30 electric in cooperation with siemens,” Volvo Car Sverige AB, 2013, accessed 2013-09-02. [Online]. Available: https://www.media.volvocars.com/se/sv-se

[165] “Tekniska data 2012 volvo utg 3,” Volvo Car Sverige AB, 2011, accessed 2015-03-20. [Online]. Available: http://az685612.vo.msecnd.net/pdfs/fa036e925b36a32206104ac267a1e460b6eed952/P1-1148-C30_Electric_TP_14620-Web.pdf

[166] “2015 e-golf technical specifications,” Volks Wagen US Media Newsroom, 2015, accessed 2015-03-26. [Online]. Available: http://media.vw.com/model/pack/92/

[167] "Media information, 2015 volkswagen e-golf," Volkswagen US Media Newsroom, 2015, accessed 2015-03-26. [Online]. Available: http://media.vw.com/model/pack/92/

[168] "Saljstart for eldrivna volkswagen e-golf," Volkswagen Group Sweden, 2014, accessed 2015-05-25. [Online]. Available: http://www.volkswagengroup.se/sv/Mediarummet/Pressrelease---visningsida/?pid=887747

[169] "Nissan leaf," Nissan UK, 2015, accessed 2015-03-27. [Online]. Available: http://www.nissan.co.uk/dam/services/gb/brochure/Nissan_Leaf_technical_specs.pdf

[170] "Nissan leaf prislista," Nissan Sweden, 2015, accessed 2015-03-27. [Online]. Available: http://www.nissan.se/etc/medialib/nissaneu/_SE_sv/_Other_pdf/pricelists.Par.47200.File.dat/LEAF_Kundprislista__01-01-15_0509.pdf

[171] M. Ikezoe, N. Hirata, C. AMEMIYA, T. Miyamoto, Y. Watanabe, T. Hirai, and T. Sasaki, "Development of high capacity lithium- ion battery for nissan leaf," in *SAE Technical Paper*. SAE International, 04 2012. [Online]. Available: http://dx.doi.org/10.4271/2012-01-0664

[172] "2016 leaf 30kwh, and technical specifications," Nissan Newsroom Europe, 2015, accessed 2015-10-21. [Online]. Available: http://newsroom.nissan-europe.com/EU/en-gb/media/presskit.aspx?mediaid=138556&topicid=0&mediatypeid=2

[173] "2016 nissan leaf press kit," Nissan Newsroom USA, 2015, accessed 2015-10-21. [Online]. Available: http://nissannews.com/en-US/nissan/usa/presskits/us-2016-nissan-leaf-press-kit

[174] "Fit ev 2014 specifications," American Honda Motor Co., Inc., 2014, accessed 2015-02-14. [Online]. Available: http://automobiles.honda.com/fit-ev/specifications.aspx

[175] "2013 smart fortwo electric drive vs 2013 honda fit ev," AutoBlog, 2013, accessed 2015-04-22. [Online]. Available: http://www.autoblog.com/cars-compare?cur_page=details&v1=USC30SMC021A0&v2=&v3=&v4=&v5=&v6=&v7=&v8=&v9=&state=&mileage=

[176] "Renault fluence z.e. drive the change," Renault Ireland, 2012, accessed 2015-03-30. [Online]. Available: http://www.renault.ie/media/e-brochures/att00426864/e-brochureFluenceZ.E..pdf

[177] "Renault fluence z.e." Wikipedia, 2015, accessed 2015-03-30. [Online]. Available: http://en.wikipedia.org/wiki/Renault_Fluence_Z.E.

[178] "2015 focus specifications," Ford USA, 2015, accessed 2015-03-30. [Online]. Available: http://www.ford.com/cars/focus/specifications/view-all/

[179] "14 focus electric," Ford, 2013, accessed 2015-01-18. [Online]. Available: http://www.ford.com/services/assets/Brochure?make=Ford&model=FocusElectric&year=2014

[180] “2013 model year ford hybrid car and electric vehicle warranty guide,” Ford, 2013, accessed 2015-07-02. [Online]. Available: http://www.ford.com/resources/ford/general/pdf/2013HybridWarranty.pdf

[181] “Kia soul ev faktablad,” Kia Motors Sweden AB, 2015, accessed 2015-04-02. [Online]. Available: https://www.kia.com/se/-/media/se/forms/brochure/pdf/faktablad/2015/20150216-soul-ev-faktablad.pdf

[182] “Kia soul ev technical specification,” Kia Motors UK, 2015, accessed 2015-04-02. [Online]. Available: http://www.kia.co.uk/new-cars/range/compact-cars/soul-ev/specification/technical%20specification.aspx

[183] “All-new 2015 soul ev,” Kia Motors America, 2014, accessed 2015-06-30. [Online]. Available: http://cdn.dealereprocess.com/cdn/brochures/kia/2015-soulev.pdf

[184] “Mercedes-benz b-klasse electric drive: Technische daten,” Mercedes-Benz Germany, 2015, accessed 2015-04-02. [Online]. Available: http://www.mercedes-benz.de/content/germany/mpc/mpc_germany_website/de/home_mpc/passengercars/home/new_cars/models/b-class/w242/facts/technicaldata/model.html

[185] “The mercedes-benz b-class electric drive: Electric driving without compromises,” Daimler Global Media Site, 2014, accessed 2015-04-02. [Online]. Available: http://media.daimler.com/dcmedia/0-921-1740090-1-1751040-1-0-0-1751123-0-1-12759-614216-0-0-0-0-0-0-0.html

[186] “2014 bmw i3 vs. 2014 mercedes benz b-class electric drive, final scoring, performance data, and complete specs,” Car And Driver, 2014, accessed 2015-04-02. [Online]. Available: http://www.caranddriver.com

[187] “Byd e6 specs,” BYD Latin America, 2015, accessed 2015-04-10. [Online]. Available: http://www.byd.com/la/auto/e6.html

[188] “Byd e6,” BYD North America, 2015, accessed 2015-04-10. [Online]. Available: http://www.byd.com/na/auto/e6.html

[189] “Byd e6 specifications,” BYD AUTO, 2015, accessed 2015-04-4. [Online]. Available: http://www.byd.com/na/auto/e6.html#p2

[190] “Nissan e-nv200 combi, evalia,” Nissan Sweden, 2015, accessed 2015-05-15. [Online]. Available: http://www.nissan.se/etc/medialib/nissaneu/_SE_sv/_Other_pdf/pricelists.Par.67618.File.dat/e-NV200_Kundprislista_Combi_Evalia_03-03-15_0522.pdf

[191] “Nissan e-nv200,” Nissan UK, 2015, accessed 2015-05-18. [Online]. Available: http://www.nissan.co.uk/GB/en/tool/brochure/e-nv200.html

[192] “2014 rav4 ev,” Toyota, 2014, accessed 2015-05-17. [Online]. Available: http://www.toyota.com/content/ebrochure/2014/rav4ev_ebrochure.pdf

[193] "Rav4 ev,electric vehicle dismantling manual," Toyota, 2012, accessed 2015-05-17. [Online]. Available: https://techinfo.toyota.com/techInfoPortal/staticcontent/en/techinfo/html/prelogin/docs/rav4evdisman2nd.pdf

[194] "Tesla model s," Tesla Motors USA, 2015, accessed 2015-10-20. [Online]. Available: http://www.teslamotors.com/models

[195] "Tesla model x," Tesla Motors USA, 2015, accessed 2015-10-20. [Online]. Available: http://www.teslamotors.com/modelx

[196] "Roadster features & specifications," Tesla Motors, 2012, accessed 2012-04-17. [Online]. Available: http://www.teslamotors.com/roadster/specs

[197] "Tesla roadster, emergency responder guide," Tesla Motors, 2009, accessed 2015-03-31. [Online]. Available: https://www.teslamotors.com/sites/default/files/downloads/Tesla_Roadster_Emergency_Responder_Guide.pdf

[198] "Roadster, technology, battery," Tesla Motors, 2015, accessed 2015-03-31. [Online]. Available: http://my.teslamotors.com/roadster/technology/battery

[199] "Concept one, specifications," Rimac Automobili, 2015, accessed 2015-07-01. [Online]. Available: http://www.rimac-automobili.com/concept_one/specifications-10

[200] "Rimac automobili and vredestein at top marques monaco," Rimac Automobili, 2012, accessed 2014-02-12. [Online]. Available: http://www.rimac-automobili.com/press/rimac-automobili-and-vredestein-at-top-marques-monaco-p8

[201] "Sls amg electric drive, accumulated data," Mercedes-Benz, 2015, accessed 2015-03-20. [Online]. Available: http://www.mercedes-amg.com/webspecial/sls_e-drive/eng.php

[202] "Mercedes-benz sls amg coupé electric drive, electrifying the world's most powerful electric super sports car," Daimler Media, 2012, accessed 2015-03-20. [Online]. Available: http://media.daimler.com/dcmedia/0-921-614307-1-1535313-1-0-0-0-0-0-11702-0-0-1-0-0-0-0-0.html

[203] "Mercedes-benz sls amg coupé electric drive," Daimler Press Information, 2013, accessed 2015-03-13. [Online]. Available: www.daimler.com/Projects/c2c/channel/documents/2292390_PM_SLS_AMG_en.doc

[204] "Lightning gt," Lightning Car Company, 2015, accessed 2015-04-10. [Online]. Available: http://www.lightningcarcompany.co.uk/Lightning/home.html

[205] "Lightning gt," Car body design, 2008, accessed 2015-07-02. [Online]. Available: http://www.carbodydesign.com/archive/2008/07/25-lightning-gt/

[206] "Sp:01," Detroit Electric, 2015, accessed 2015-07-01. [Online]. Available: http://detroit-electric-group.com/sp01.html

[207] “Fetish,” Venturi, 2015, accessed 2015-07-02. [Online]. Available: http://en.venturi.fr/vehicles/venturi-range/fetish/overview

[208] “America technical specifications,” Venturi, 2015, accessed 2015-07-02. [Online]. Available: http://en.venturi.fr/venturi/documents/vehicules/america/eBrochure_America.pdf

[209] “America,” Venturi, 2015, accessed 2015-07-02. [Online]. Available: http://en.venturi.fr/vehicles/venturi-range/america/overview

[210] “The coupe, production prototype,” Renovo Motors, 2015, accessed 2015-07-02. [Online]. Available: http://renovomotors.com/the-coupe/

[211] T. Lehner-Ilsanker, “Audi presents the new r8: The sporty spearhead just got even sharper,” Audi Media Info, 2015, accessed 2015-07-06. [Online]. Available: https://www.audi-mediacenter.com/en/press-releases/audi-presents-the-new-r8-the-sporty-spearhead-just-got-even-sharper-391

[212] “Audi r8 e-tron,” Audi Technology Magazine, 2013, accessed 2015-07-06. [Online]. Available: http://www.audi.com/content/dam/com/EN/corporate-responsibility/product/audi_technology_magazine.pdf

[213] “Innovative technologies in the new audi r8 model family,” Audi AG Product Communications, 2015, accessed 2015-07-06. [Online]. Available: https://www.audi-mediacenter.com/en/press-releases/audi-presents-the-new-r8-the-sporty-spearhead-just-got-even-sharper-391

[214] “Lampo 3 specifications,” Protoscar, 2012, accessed 2015-07-06. [Online]. Available: http://www.protoscar.com/pdf/LAMPO3/LAMPO3_Technical_Specifications.pdf

[215] “Roadster 3.0,” Tesla Motors Blog, 2014, accessed 2015-03-31. [Online]. Available: http://www.teslamotors.com/blog/roadster-30

[216] “Vehicle coefficient of drag list,” EcoModder Wiki, 2015, accessed 2015-03-23. [Online]. Available: http://ecomodder.com/wiki/index.php/Vehicle_Coefficient_of_Drag_List

[217] “2012 mitsubishi i-miev - features & specs,” Edmunds, 2012, accessed 2015-03-30. [Online]. Available: http://www.edmunds.com/mitsubishi/i-miev/2012/features-specs.html

[218] “Viavision march 2014 - volkswagen - shaping the future of mobility,” Volkswagen Media Services, 2014, accessed 2015-05-25. [Online]. Available: https://www.volkswagen-media-services.com/documents/10541/1091571/ViaVision_2014_March.pdf

[219] W. Steiger, “Future mobility, volkswagen group’s solutions for sustainable mobility,” Volkswagen, 2014, accessed 2015-10-24. [Online]. Available: http://www.volkswagenag.com

[220] “2014 chevrolet spark ev vs. 2013 fiat 500e, 2014 ford focus electric, 2013 honda fit ev, 2013 nissan leaf sl, 2013 smart fortwo ed cabriolet, final scoring, performance data, and complete specs,” Car and Driver, 2013, accessed 2015-03-30. [Online]. Available: http://www.caranddriver.com

[221] “2015 chevrolet spark product information,” Chevrolet News, GM Media, 2015, accessed 2015-03-25. [Online]. Available: http://media.gm.com/media/us/en/chevrolet/vehicles/spark-ev/2015.html

[222] “Bmw i3 models,” BMW USA, 2015, accessed 2015-07-08. [Online]. Available: http://www.bmwusa.com/bmw/bmwi/i3

[223] “Bmw i3 and i3 with range extender (i01),” BMW UK, 2013, accessed 2015-03-26. [Online]. Available: https://www.press.bmwgroup.com/united-kingdom/download.html?textId=190985&textAttachmentId=234889

[224] “Overview: Renault at the paris motor show,” Under the Skin, Automotive Technology Online, 2010, accessed 2014-02-13. [Online]. Available: http://under-the-skin.org.uk/news_renault_1010.html

[225] “Tekniska data 2012 volvo utg 3,” Volvo Car Sverige AB, 2011, accessed 2015-03-20. [Online]. Available: https://www.media.volvocars.com/se/sv-se

[226] “Volvo c30 electric, siemens fleet in cooperation with volvo car corporation,” Siemens AG, Digital Factory, eCar Powertrain Systems, Feb 2015. [Online]. Available: www.siemens.com/electriccar

[227] “World premieres of the e-up! and e-golf, international motor show (iaa) frankfurt, september 2013,” Volkswagen, 2013, accessed 2015-10-24. [Online]. Available: http://www.smmt.co.uk/wp-content/uploads/sites/2/Innovation-Stream-public-3.pdf

[228] “Nissan releases specs for the 2011 leaf ev,” Nissan in the News, 2010, accessed 2015-03-27. [Online]. Available: http://www.nissaninthenews.com/nissan-releases-specs-for-the-2011-leaf-ev/

[229] “2013 honda fit ev (model since july 2012 for north america u.s.) specifications & performance data review,” Automobile catalog, 2014, accessed 2015-03-30. [Online]. Available: http://www.automobile-catalog.com/car/2013/1761020/honda_fit_ev.html

[230] “Renault fluence z.e.” Renault Denmark, 2014, accessed 2014-02-07. [Online]. Available: http://www.renault.co.uk/cars/electric-vehicles/fluence-ze/fluence-ze/specifications/index.jsp

[231] “Renault fluence z.e. drive the change,” Renault UK, 2013, accessed 2015-03-30. [Online]. Available: http://motorline.co.uk/renault/pdfs/fluence-ze.pdf

[232] “Ford focus electric,” Miljofordon.se, 2014, accessed 2014-03-13. [Online]. Available: http://www.miljofordon.se/fordon?view=detalj&id=43532

[233] “Streamlined all-new ford focus significantly reduces aerodynamic drag, adding fuel efficiency,” The Ford Motor Company Media Center, 2011, accessed 2014-03-13. [Online]. Available: https://media.ford.com/content/fordmedia/fna/us/en/news/2011/01/24/streamlined-all-new-ford-focus-significantly-reduces-aerodynamic.html

[234] “Kia soul electric, pris - pris - utstyrsoversikt - tekniske data - tilbehor,” Kia Motors Norway AB, 2015, accessed 2015-04-02. [Online]. Available: http://www.kia.com/no/modeller/soul-electric/

[235] “Kia soul ev eco electric,” Kia Motors Sweden AB, 2014, accessed 2015-04-02. [Online]. Available: https://www.kia.com/se/-/media/se/forms/brochure/pdf/broschyrer/2014/150529-broschyr-soul-ev-final-swe.pdf

[236] “2015 kia soul ev review,” Automobile Magazine, 2014, accessed 2015-04-02. [Online]. Available: http://www.automobilemag.com/reviews/driven/1409-2015-kia-soul-ev-review/

[237] “2014 tesla model s - owner’s manual (north america),” Car Manuals, 2014, accessed 2015-06-12. [Online]. Available: https://carmanuals2.com/get/tesla-model-s-2014-owner-s-manual-north-america-36741

[238] “Model s, specifikationer,” Tesla Motors Sweden, 2014, accessed 2014-02-07. [Online]. Available: http://www.teslamotors.com/sv_SE/models/specs

[239] “Drag queens: Aerodynamics compared,” Car and Driver, 2014, accessed 2015-03-31. [Online]. Available: http://www.caranddriver.com

[240] “Model s efficiency and range,” Tesla Motors USA, Blog, 2012, accessed 2015-03-31. [Online]. Available: http://www.teslamotors.com/blog/model-s-efficiency-and-range

[241] “Owners manual, roadster 2, roadster sport,” Tesla Motors, 2009, accessed 2013-06-29. [Online]. Available: http://maben.homeip.net/static/auto/tesla/teslaroadster2ownersmanual.pdf

[242] “Tesla roadster review,” Edmunds, 2010, accessed 2013-06-29. [Online]. Available: http://www.edmunds.com/tesla/roadster/

[243] “Concept one, propulsion system,” Rimac Automobili, 2015, accessed 2014-02-11. [Online]. Available: http://www.rimac-automobili.com/concept_one/propulsion-system-8

[244] “Official: Mercedes-benz sls amg coupé electric drive,” GT Spirit, 2012, accessed 2015-03-18. [Online]. Available: http://www.gtspirit.com/2012/09/27/official-mercedes-benz-sls-amg-coupe-electric-drive/

[245] “Lightning gt,” Wikipedia English, 2015, accessed 2015-04-10. [Online]. Available: http://en.wikipedia.org/wiki/Lightning_GT

[246] “Lightning gt,” TwinRev, 2008, accessed 2015-07-02. [Online]. Available: http://twinrev.com/supercar/Lightning-GT

[247] “Audi r8 coupe v10,” Audi Sweden, 2015, accessed 2015-07-06. [Online]. Available: http://www.audi.se/se/brand/sv/models/r8/r8-coupe/technical-data/dimensions.html

[248] “Fit ev,” Honda Japan, 2015, accessed 2015-07-08. [Online]. Available: http://www.honda.co.jp/FITEV/usability/

[249] “Lightning gt,” Lightning Car Company, 2015, accessed 2015-11-18. [Online]. Available: http://www.lightningcarcompany.co.uk/Lightning/home.html

[250] “2013 smart fortwo electric drive,” AutoBlog, 2012, accessed 2015-03-23. [Online]. Available: http://www.autoblog.com/2012/10/10/2013-smart-fortwo-electric-drive-first-drive-review/

[251] “2013 fiat 500e ev - first drive review,” Car and Driver, 2013, accessed 2015-03-20. [Online]. Available: http://www.caranddriver.com/reviews/2013-fiat-500e-ev-first-drive-review

[252] “Bosch smg 180/120 electric motor: compact powerhouse,” BOSCH Media Service, 2013, accessed 2015-06-30. [Online]. Available: http://www.bosch-presse.de/presseforum/details.htm?txtID=6226&tk_id=108&locale=en

[253] “First uk electric car club powered by renault,” My Renault ZOE electric car, 2013, accessed 2015-03-26. [Online]. Available: http://myrenaultzoe.com/index.php/2013/10/

[254] W. Steiger, “Driving the future, volkswagen group’s solution for sustainable mobility,” Volkswagen, 2013, accessed 2015-10-20. [Online]. Available: http://www.smmt.co.uk/wp-content/uploads/sites/2/Innovation-Stream-public-3.pdf

[255] “Der e-golf, technik und preise,” Volkswagen Germany, 2015, accessed 2015-03-26. [Online]. Available: https://app-ssl.volkswagen.de/de/dialog_center/infomaterial_anfordern/produktbroschueren.htx

[256] H. Shimizu, T. Okubo, I. Hirano, S. Ishikawa, and M. Abe, “Development of an integrated electrified powertrain for a newly developed electric vehicle,” in *SAE Technical Paper*. SAE International, 04 2013. [Online]. Available: http://dx.doi.org/10.4271/2013-01-1759

[257] W. Hackman, “Electrical traction drives: Hev e-drive development and products,” Continental AG, 2012, accessed 2015-10-24. [Online]. Available: http://myrenaultzoe.com/Docs/2012_wien_vortrag_uv.pdf

[258] “Renault fluence z.e. and kangoo express z.e.: Finalized designs revealed and pre-reservations open,” Renault Denmark, 2010, accessed 2015-07-09. [Online]. Available: http://large.stanford.edu/courses/2010/ph240/smillie1/docs/renault.pdf

[259] "2015 fuel economy datafile," Office of Transportation & Air Quality, U.S. Environmental Protection Agency, U.S. Department of Energy, 2015, accessed 2015-07-16. [Online]. Available: http://www.fueleconomy.gov/feg/download.shtml

[260] "Introducing the byd e6 electric car," Tree Hugger, 2008, accessed 2015-04-10. [Online]. Available: http://www.treehugger.com/cars/introducing-the-byd-e6-electric-car.html

[261] "Byd e6a auto owner's manual," BYD AUTO, 2009, accessed 2015-04-10. [Online]. Available: http://www.produktinfo.conrad.com/datenblaetter/250000-274999/251704-in-01-en-BYD_LITHIUM_FE_BLOCK_12V_10_AH_B_BMS.pdf

[262] "Model s specifications," Tesla Motors USA, 2015, accessed 2015-03-31. [Online]. Available: http://www.teslamotors.com/support/model-s-specifications

[263] "Tesla model s 60kwh," Miljofordon.se, 2015, accessed 2015-03-31. [Online]. Available: http://www.miljofordon.se/fordon

[264] "Model s," Tesla Motors Sweden, 2015, accessed 2015-03-20. [Online]. Available: http://www.teslamotors.com/sv_SE/models

[265] "2013 tesla model s overview," Hybrid Cars, 2013, accessed 2015-03-31. [Online]. Available: http://www.hybridcars.com/2013-tesla-model-s-overview/

[266] "2013 fuel economy datafile," Office of Transportation & Air Quality, U.S. Environmental Protection Agency, U.S. Department of Energy, 2013, accessed 2013-09-05. [Online]. Available: http://www.fueleconomy.gov/feg/download.shtml

[267] "Operator's manual, smart fortwo coupÃ© and smart fortwo cabriolet electric drive," Smart USA, 2013, accessed 2015-05-25. [Online]. Available: http://owners.smartusa.com/userfiles/file/2014-smart-electric-drive-owners-manual.pdf

[268] "Innovative charge management," Smart, 2015, accessed 2015-07-06. [Online]. Available: http://int.smart.com/en/en/index/smart-fortwo-electric-drive/charge-management.html

[269] "2012 toyota iq ev," Top Speed, 2012, accessed 2015-07-07. [Online]. Available: http://www.topspeed.com/cars/toyota/2012-toyota-iq-ev-ar136554.html

[270] "2016 fuel economy datafile," Office of Transportation & Air Quality, U.S. Environmental Protection Agency, U.S. Department of Energy, 2015, accessed 2015-10-21. [Online]. Available: http://www.fueleconomy.gov/feg/download.shtml

[271] E. N. Zongguang Wang, Tetsuji Ukita and Y. Masuda, "Prediction of air cooling system for ev/hev battery pack," in *SAE Technical Paper*. SAE International, 05 2011.

[272] "Viavision, electromobility, the e-up! made by volkswagen," Volkswagen, 2013, accessed 2015-10-24. [Online]. Available: http://www.volkswagenag.com/content/vwcorp/info_center/en/publications/2013/09/VIAVISION7.bin.html/binarystorageitem/file/VIAVISION_E.pdf

[273] "2015 chevrolet spark ev hatchback review," Edmunds, 2015, accessed 2015-07-07. [Online]. Available: http://www.edmunds.com/chevrolet/spark-ev/2015/hatchback/review/

[274] (2015) Chademo-compatible evs. CHAdeMO. Accessed 2015-07-06. [Online]. Available: http://www.chademo.com/wp/chademo-ev/

[275] "The new bmw i3," BMW Group, BMW UK Ltd., 2013, accessed 2014-02-26. [Online]. Available: https://www.press.bmwgroup.com/united-kingdom/download.html?textId=190985&textAttachmentId=234890

[276] "The high voltage batteries of the bmw i3 and bmw i8," BMW Group, BMW Media Information, 2014, accessed 2015-03-26. [Online]. Available: https://wiki.aalto.fi/download/attachments/91692283/high_voltage_batteries_of_bmw_vehicles.pdf?version=1&modificationDate=1398446470505&api=v2

[277] "Charging the bmw i3," BMW UK Corporate Communications, 2013, accessed 2015-07-07. [Online]. Available: https://www.press.bmwgroup.com/united-kingdom/download.html?textId=190985&textAttachmentId=234885

[278] "Renault zoe," Renault France, 2015, accessed 2015-06-30. [Online]. Available: http://www.renault.fr/e-brochure/ZOE_1/pdf/fullPDF.pdf

[279] "Brusa 22 kw charger for new volvo c30 electric," BRUSA, 2013, accessed 2015-07-07. [Online]. Available: www.brusa.eu/no_cache/en/news/news/article/brusa-22-kw-ladegeraet-im-neuen-volvo-c30-electric.html

[280] Y. Kinoshita, T. Hirai, Y. Watanabe, Y. Yamazaki, R. Amagai, and K. Sato, "Newly developed lithium-ion battery pack technology for a mass-market electric vehicle," in *SAE Technical Paper*. SAE International, 04 2013. [Online]. Available: http://dx.doi.org/10.4271/2013-01-1543

[281] "Soul ev 2015," Kia Motors USA, 2015, accessed 2015-04-02. [Online]. Available: http://www.kia.com/us/en/vehicle/soul-ev/2015/features

[282] "2014 mercedes b-class ed battery much bigger than previously stated," AutoBlog, 2014, accessed 2015-04-08. [Online]. Available: http://www.autoblog.com/2014/06/23/2015-mercedes-b-class-ed-battery-much-bigger-than-we-knew/

[283] "Byd e6a auto owner's manual," BYD AUTO, 2015, accessed 2015-04-10. [Online]. Available: http://www.byd-auto.net/medias/Owner'sManual/BYDE6Owner'smanual2011.6.22-usethis_en-update.pdf

[284] "Charging solutions," BYD Europe, 2015, accessed 2015-07-07. [Online]. Available: http://www.bydeurope.com/innovations/technology/index.php

[285] B. Fleming, "Electric vehicle collaboration-toyota motor corporation and tesla motors [automotive electronics]," *Vehicular Technology Magazine, IEEE*, vol. 8, no. 1, pp. 4–9, March 2013.

[286] "Rav4 ev 2012, warranty and maintenance guide," Toyota, 2012, accessed 2015-05-17. [Online]. Available: http://www.myrav4ev.com/docs/RAV4EV_Warranty_and_Maintenance.pdf

[287] "Supercharger," Tesla Motors USA, 2015, accessed 2015-07-07. [Online]. Available: http://www.teslamotors.com/supercharger

[288] "2016 detroit electric sp:01 - on-sale date, specs, pictures," Green Car Congress, 2013, accessed 2015-07-08. [Online]. Available: http://www.greencarcongress.com/2013/04/sp01-20130404.html

[289] "Electric renovo coupe is an ev performance revolution," Gas2, 2014, accessed 2015-07-08. [Online]. Available: http://gas2.org/2014/08/15/electric-renovo-coupe-is-an-ev-performance-revolution/

[290] "Renovo coupe shapes high-performance electric car future," CNET, 2014, accessed 2015-07-08. [Online]. Available: http://www.cnet.com/news/renovo-coupe-shapes-high-performance-electric-car-future/

[291] "2011 mitsubishi minicab miev van," Top Speed, 2012, accessed 2015-07-01. [Online]. Available: http://www.topspeed.com/trucks/truck-reviews/mitsubishi/2011-mitsubishi-minicab-miev-van-ar131865.html

[292] "Honda begins lease sales of fit ev in japan," Honda World News Releases 2012, 2012, accessed 2015-03-27. [Online]. Available: http://world.honda.com/news/2012/4120831Lease-Sales-Fit-EV-Japan/

[293] "Renault has already halted european production of fluence z.e. electric car," Renault Denmark, 2014, accessed 2015-07-07. [Online]. Available: http://www.renault.dk/brochurer/att00200958/B-Fluence-ZE-Better-Place-DK-PDF_BD2.pdf

[294] "Focus electric prestanda och effektivitet," Ford Sweden, 2015, accessed 2015-03-30. [Online]. Available: http://www.ford.se/Personbilar/Focus-Electric/Prestanda-och-effektivitet

[295] "Byd aoto, a thriving star," BYD Auto Co. LTD, 2015, accessed 2015-04-10. [Online]. Available: http://www.byd.com/la/auto/images/e6/download/BYD_Car_Series_Introduction.pdf

[296] "Tesla model s," Tesla Motors Sweden, 2015, accessed 2015-10-20. [Online]. Available: http://www.teslamotors.com/sv_SE/models

[297] "Tesla model s," Tesla Motors USA, 2015, accessed 2015-07-14. [Online]. Available: http://www.teslamotors.com/models

[298] “Tesla model x,” Tesla Motors Sweden, 2015, accessed 2015-10-20. [Online]. Available: http://www.teslamotors.com/modelx

[299] “Tesla roadster,” Miljofordon.se, 2013, accessed 2013-09-05. [Online]. Available: http://www.miljofordon.se/fordon/detalj?id=37824

[300] “Production schedule and achievement of critical milestones on crash tests and range testing,” Tesla Motors Blog, 2010, accessed 2013-06-29. [Online]. Available: http://www.teslamotors.com/blog/tesla-motors-announces-2008-roadster-production-schedule-and-achievement-critic

[301] “Official: Mercedes-benz sls amg coupé electric drive,” Mercedes-Benz Sweden, 2012, accessed 2014-02-12. [Online]. Available: http://www2.mercedes-benz.se/content/sweden/mpc/mpc_sweden_website/sv/home_mpc/passengercars/home/new_cars/models/sls_amg/_c197/facts_/drivetrain/alternativetransmission.html

[302] (2009, apr) Regulation (ec) no 1222/2009, on the labelling of tyres with respect to fuel efficiency and other essential parameters. European Parliament, Council of the European Union. Accessed 2015-11-06. [Online]. Available: http://eur-lex.europa.eu/legal-content/EN/ALL/?uri=CELEX:32009R1222

[303] G. Pannone. (2015) Technical analysis of vehicle load reduction potential for advanced clean cars. CONTROLTEC, LLC. Accessed 2015-11-11. [Online]. Available: http://www.arb.ca.gov/research/apr/past/13-313.pdf

[304] (2013) Regulation no. 85. United Nations Economic Commission for Europe (UNECE). Accessed 2015-10-21. [Online]. Available: http://www.unece.org/fileadmin/DAM/trans/main/wp29/wp29regs/2013/R085r1e.pdf

[305] J. P. Holman, *Heat Transfer, Ninth Edition.* Mcgraw-Hill, 2002.

[306] D. A. Staton and A. Cavagnino, “Convection heat transfer and flow calculations suitable for electric machines thermal models,” *IEEE Transactions on Industrial Electronics*, vol. 55, no. 10, pp. 3509–3516, Oct 2008.

Appendix A

Sales and Specification BEV data

A.1 Top selling BEVs 2014 and 2015

During 2014 about 65 million passenger cars were sold world wide [129]. Out of these about 320,000 [130] or 0.5% are estimated to have been electric vehicles (EVs), and 57% of those are estimated to have been BEVs as opposed to PHEVs [3]. That is about 180,000 BEVs or less than 0.3% of the global total passenger car sales.

The same year the absolute majority, about 94%, of all EVs (BEVs and PHEVs) were sold in the USA (37%), Europe (31%), China (17%) and Japan (10%) [130, 131]. In the USA and Japan about half of the sales were BEVs, whereas the share was about 60% in China [3]. During 2014 the largest number of BEVs in Europe were sold in Norway (around 18,100), France (10,600), Germany (8,500) and the UK (7,400) [131]. Together these four countries accounted for about 77% of the total European BEV sales that year.

The top selling highway capable (≥110km/h) BEVs during 2014 and 2015 in USA, Europe and Japan are presented in Figure A.1.

It should be noted that found sales data is not complete and differs somewhat between sources as some figures are based on estimates, such as the Tesla data. Furthermore, it is not clear whether the sales data for i3 adheres to the BEV or the range extended version. Additionally, some top selling models are here ignored due to their low top speed, e.g. Renault Twizy. Additionally, a few 2-seat vans are omitted since they are aimed for transport of goods rather than of people. Moreover, the Fiat 500e and Chevrolet Spark EV are only for sale in California and Oregon.

All of the models mentioned in Figure A.1 are included in this paper. Toyota Scion iQ EV, Volvo C30 Electric, and ten 2-seat sport models are also included.

A.2 Specification BEV data

The gathered BEV specifications are presented in the following tables. The vast majority of the data originates from vehicle manufacturer specifications, advertising brochures and media information, as well as governmental organisations such as EPA. A small part of the data are found in car magazines and similar web sites. These figures are printed in

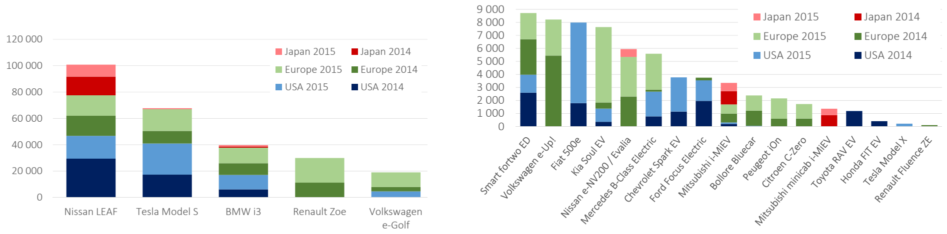

(a) Top 5.

(b) Top 6-22.

Figure A.1 Top 22 of highway capable BEV sales in USA, Europe and Japan during 2014 and 2015, [132–135].

gray color in the tables, which indicates a somewhat lower level of confidence. SI units are used throughout the tables, hence unit conversions have been made for some of the data.

Through a deal between Mitsubishi Motors (Japan) and PSA Peugeot Citroën (France) Mitsubishi is manufacturing both Peugeot iOn and Citroen C-Zero similarly as Mitsubishi i-MiEV. Therefore, the three BEVs can be expected to have similar specifications. It was however found that advertised specifications differ between countries on the manufactures' web sites even for the same model. The deviations regard: the curb weight (1065-1185 kg), the motor maximum torque (180 Nm or 196 Nm), the speed at which maximum torque and power is reached (4 and 5 different data respectively), and the battery energy capacity (14.5kWh or 16kWh). In contrast, data of the top speed and time to accelerate 0-100km/h does not differ. The here presented data is assumed to be fairly representative for the latest models.

A.2.1 Brand, model and miscellaneous data

Available data regarding: brand, model, model year, number of seats, drive, standard tire size on driving wheel pair, powertrain and battery warranty and battery type is shown in Table A.1, including a yes or no to whether or not the BEV model is derived from an existing combustion engine vehicle (CEV) model under the same brand.

A.2.2 Dimensional specifications

Dimensional data regarding weight, track width, external measures, area and aerodynamic drag coefficient is presented in Table A.2. The curb weight is here presented as without driver and extra cargo whenever possible. The average track width is the average between front and rear. The width is without side mirrors, when data was available. For C30 Electric the C_d value is assumed to be the same as for c30 DRIVe and for the Ford Focus Electric the C_d value is assumed to be the same as for Ford Focus. The Nissan Leaf is said to have different C_d values depending on tire rim: 0.291 for 16", and 0.289 for 17" [169]. The coming updated Tesla Roadster 3.0 will have a C_d value of 0.31 for the version that comes with a "retrofit aero kit" [215].

Table A.1 Brand, model, drive, tire, warranty and battery type data.

Brand	Model	Model year	Conv. from CEV?	Seats	Drive	Standard Tire size on driving wheel pair	Powertrain Warranty Distance/ Years	Battery Warranty Distance/ Years	Battery Type
Smart	fortwo el.dr. Coupe	2014 [136] 2015 [138]	Yes	2 [136]	Rear [136]	175/55R15 [136]	50kmi/4yrs [137]	50kmi/4yrs [137]	Li-ion [136] Pol. [139]
Smart	fortwo BRABUS El.Dr. Coupe	2014 [140]	Yes	2 [140]	Rear [140]	225/35R17 [140]			Li-ion [140]
Toyta Scion	iQ EV	2012 [141]	Yes	4 [142]	Front [141]	175/60R16 [143]			Li-ion [141]
Fiat	500e	2015 [144]	Yes	4 [144]	Front [144]	185/55R15 [144]	50kmi/4yrs [145]	100kmi/8yrs [145]	Li-ion [144] Pri. [139]
Citroën	C-ZERO	2014 [146]	Yes	4 [146]	Rear [146]	175/55R15 [146]		100kkm/8yrs [147]	Li-ion [146]
Peugeot	iOn	2014 [148]	Yes	4 [148]	Rear [148]	175/55R15 [148]	50kkm/5yrs [148]	50kkm/5yrs [148]	Li-ion [148]
Mitsubishi	i-MiEV	2014 [149]	Yes	4 [149]	Rear [150]	175/60R15 [151]	100kkm/5yrs [151]	160kkm/8yrs [151]	Li-ion [151] Pri. [139]
Volkswagen	e-up!	2013 [152]	Yes	4 [153]	Front [152]	165/65R15 [152]		160kkm/8yrs [154]	Li-ion [152]
Chevrolet	Spark EV	2015 [155]	Yes	4 [155]	Front [155]	185/55R15 [155]	100kmi/5yrs [155]	100kmi/8yrs [155]	Li-ion [155]
Bollore	Bluecar	2015 [156]		4 [156]					Li-ion Pol. [156]
Mitsubishi	MiniCab MiEV	2014 [157]	Yes	4 [157]	Rear [158]	145R12 [157]			Li-ion [158]
BMW	i3	2014 [159]	No	4 [159]	Rear [159]	155/70R19 [159]	50kmi/4yrs [160]	100kmi/8yrs [160] 62kmi/8yrs [161]	Li-ion [159] Pri. [139]
Renault	Zoe	2015 [162]	No	5 [162]	Front [163]	185/65R15 [162]	100kmi/5yrs [162]	60kmi/5yrs [162]	Li-ion [162] Pol. [139]
Volvo	C30 Electric	2013 [164]	Yes	4 [164]		205/55R16 [165]			Li-ion [164]
Volkswagen	e-Golf	2015 [166]	Yes	5 [166]	Front [166]	205/55R16 [166]	60kmi/5yrs [167]	100kmi/8yrs [167] 160kkm/8yrs [168]	Li-ion Pri. [167]
Nissan	Leaf (Visia)	2015 [169]	No	5 [169]	Front [169]	205/55R16 [169]	100kkm/5yrs [170]	100kkm/5yrs [170]	Li-ion Lam. [171]
Nissan	Leaf (Acenta,SV)	2016 [172]	No	5 [172]	Front [172]	205/55R16 [172]		160kkm/8yrs [172]	Li-ion Lam. [173]
Honda	FIT EV	2014 [174]	Yes	5 [174]	Front [174]	185/65R15 [174]	60kmi/5yrs [175]	60kmi/5yrs [175]	Li-ion [174] Pri. [139]
Renault	Fluence Z.E.	2012 [176]	Yes	5 [176]	Front [177]	205/55R16 [176]	100kkm/5yrs [176]		Li-ion [176]
Ford	Focus EV	2015 [178]	Yes	5 [178]	Front [178]	225/50R17 [179]	100kmi/8yrs [180]	100kmi/8yrs [180]	Li-ion [178]
Kia	Soul Electric	2015 [181]	Yes	5 [182]	Front [181]	205/60R16 [181]	100kmi/10yr [183]	100kmi/10yrs [183] 150kkm/7yrs [181]	Li-ion Pol. [181]
Mercedes-Benz	B-Class El. Dr.	2015 [184]	Yes	5 [184]	Front [184]	205/60R16 [184]		100kkm/8yrs [185]	Li-ion [184] Cyl. [186]
BYD	e6	2015 [187]	No	5 [187]	Front [150]	235/65R17 [187]		10yrs [188]	LiFePO4 [189]
Nissan	e-NV200 (Evalia)	2015 [190]	Yes	5 [190]	Front [190]	185/65R15 [190]	100kkm/5yrs [190]	100kkm/5yrs [190]	Li-ion [191]
Toyota	RAV4 EV	2014 [192]	Yes	5 [192]	Front [192]	225/65R17 [192]	60kmi/5yrs [192]	100kmi/8yrs [192]	Li-ion [192] Cyl. [193]
Tesla	Model S	2015 [194]	No	5 [194]	Rear/AWD [194]	245/45R19 [194]	unlim./8yrs [194]	unlim./8yrs [194]	Li-ion [194] Cyl. [139]
Tesla	Model X	2015 [195]	No	6/7 [195]	AWD [195]		unlim./8yrs [195]	unlim./8yrs [195]	
Tesla	Roadster	2012 [196]	No	2 [196]	Rear [197]	225/45R17 [196]		100kmi/7yrs [196]	Li-ion [198] Cyl. [139]
Rimac	Concept One	2015 [199]	No	2 [199]	AWD [199]	F:245/35R20 [20 R:295/30R20			LiFePO4 [199]
Mercedes-Benz	SLS AMG El.Dr.	2015 [201]	Yes	2 [201]	AWD [201]	F:265/35R19 [202] R:295/30R20			Li-ion [203]
Lightning	Lightning GT	2015 [204]	No	2 [204]	Rear [204]	245/45R20 [205]			Li-titan [204]
Detroit Electric	SP:01 Pure	2015 [206]	No	2 [206]	Rear [206]	225/45R17 [206]			
Detroit Electric	SP:01 Perf.	2015 [206]	No	2 [206]	Rear [206]	225/45R17 [206]			
Venturi	Fetish	2015 [207]		2 [207]					Li-ion Pol. [207]
Venturi	America	2014 [208]		2 [209]	Rear [209]	275/45R20 [208]			Li-ion Pol. [209]
Renovo	Coupe	2015 [210]							Li-ion [210]
Audi	R8 e-tron	2015 [211]	Yes	2 [212]	Rear [213]	275/40R19 [213]			Li-ion [213]
Protoscar	LAMPO 3	2011 [214]		2+2 [214]	AWD [214]	F:245/40R18 [214] R:295/35R18			Li-ion Pri. [214]

Table A.2 Dimensional data.

Model	Curb weight (kg)	Max. cargo (kg)	Max. Weight (kg)	Weight Front/ Rear (%)	Average Track Width (mm)	Width (mm)	Height (mm)	Length (mm)	Front Area (m^2)	Air drag coeff. Cd	A*Cd (m2)
fortwo	900 [136]	250 [136]	1150 [136]		1334 [136]	1559 [136]	1565 [136]	2695 [136]		0.29 [175]	
BRABUS	925 [140]	150 [140]	1150 [140]		1317 [140]	1559 [140]	1565 [140]	2727 [140]			
iQ EV	1100 [142]				1468 [143]	1680 [141]	1505 [141]	3120 [141]	2.15 [216]	0.299 [216]	0.64 cal.
500e	1355 [144]			57/43 [144]	1402 [144]	1627 [144]	1527 [144]	3617 [144]		0.311 [144]	
C-ZERO	1065 [146]	385 [146]	1450 [146]	44/56 [146]	1290 [146]	1475 [146]	1608 [146]	3475 [146]			
iOn	1065 [148]	310 [148]	1450 [148]		1290 [148]	1475 [148]	1610 [148]	3480 [148]	2.14 cal.	0.33 [148]	0.706 [148]
i-MiEV	1085 [149]	365 cal.	1450 [149]	46/54 [151]	1290 [149]	1475 [149]	1615 [151]	3675 [151]		0.35 [217]	
e-Up!	1139 [152]	361 cal.	1500 [152]		1426 [152]	1645 [152]	1489 [152]	3540 [152]	2.09 cal.	0.308 [218]	0.644 [219]
Spark EV	1300 [155]			52/48 [220]	1401 [155]	1627 [155]	1590 [155]	3720 [155]		0.326 [221]	
Bluecar	1120 [156]	230 [156]	1350 cal.			1700 [156]	1610 [156]	3650 [156]			
MiniCab MiEV	1110 [157]	200 [157]	1310 cal.		1303 [157]	1475 [157]	1810 [157]	3395 [157]			
i3	1195 [159]	425 [159]	1620 [159]	47/53 [159]	1573 [222]	1775 [159]	1578 [159]	3999 [159]	2.38 [159]	0.29 [159]	0.69 [223]
Zoe	1468 [162]	475 cal.	1943 [162]	59/41 [162]	1511 [162]	1730 [162]	1562 [162]	4084 [162]	2.59 cal.	0.29 [224]	0.75 [162]
C30 El.	1725 [164]				1546 [225]	1782 [226]	1447 [226]	4266 [226]	2.18 [225]	0.28 [225]	0.61 cal.
e-Golf	1510 [166]	422 [166]	1960 [166]		1528 [166]	1799 [166]	1450 [166]	4270 [166]	2.19 cal. [227]	0.27 [166]	0.59 cal. [227]
Leaf'15	1474 [169]	471 cal.	1945 [169]		1538 [169]	1770 [169]	1545 [169]	4445 [169]	2.27 [228]	0.291 [169]	0.66 cal.
Leaf'16	1516 [172]	454 cal.	1970 [172]	58/42 [173]	1537 [173]	1770 [172]	1550 [172]	4445 [172]		0.29 [172]	
FIT EV	1475 [174]			55/45 [174]	1474 [174]	1721 [174]	1579 [174]	4114 [174]		0.34 [229]	
Fluence Z.E.	1535 [230]	388 cal.	2023 [176]	46/54 [176]	1546 [176]	1809 [231]	1458 [176]	4748 [176]			0.67 [231]
Focus EV	1642 [178]	365 [232]	2007 cal.		1525 [178]	1823 [178]	1478 [178]	4391 [178]		0.295 [233]	
Soul Electric	1490 [234]	470 cal.	1960 [181]		1582 [235]	1800 [181]	1593 [181]	4140 [181]		0.35 [236]	
B-Class El. Dr.	1650 [184]	445 [184]	2170 [184]		1548 [184]	1812 [184]	1599 [184]	4358 [184]		0.28 [184]	
e6	2380 [187]	375 [187]	2755 cal.		1573 [187]	1822 [187]	1645 [187]	4560 [187]			
e-NV200	1571 [191]	483 [190]	2220 [190]	48/52 [190]	1530 [190]	1755 [190]	1858 [190]	4560 [190]			
RAV4 EV	1828 [192]				1559 [192]	1816 [192]	1684 [192]	4574 [192]		0.30 [192]	
ModelS	2108 [194]	482 cal.	2590 [237]	48/52 [194]	1680 [194]	1963 [194]	1445 [238]	4978 [194]	2.34 [239]	0.24 [240]	0.56 cal.
ModelX										0.24 [195]	
Roadster	1235 [196]	249 cal.	1484 [241]	35/65 [242]	1482 [196]	1851 [196]	1126 [196]	3939 [196]		0.36 [215]	
Concept One	1950 [243]			42/58 [199]		1997 [243]	1198 [243]	4548 [243]			
SLS AMG El.Dr.	2110 [203]	250 [203]	2435 [203]	47/53 [244]	1667 [203]	1939 [203]	1262 [203]	4638 [203]			
Lightning GT	1850 [245]				1668 [246]	1940 [245]	1200 [245]	4445 [245]			
SP:01 Pure	1155 [206]					1751 [206]	1117 [206]	3880 [206]			
SP:01 Perf.	1175 [206]					1751 [206]	1117 [206]	3880 [206]			
Fetish	1200 [207]										
America	1525 [209]					2060 [209]	1450 [209]	4125 [209]			
Coupe	1474 [210]										
R8 e-tron	1841 [213]			40/60 [213]	1617 [247]	1929 [247]	1252 [212]	4431 [212]		0.28 [211]	
LAMPO 3	1700 [214]					1998 [214]	1307 [214]	4687 [214]			

A.2.3 Powertrain specifications

Specifications found regarding the electric machine and battery are shown in Table A.3 and Table A.4.

The Roadster has a max voltage of 420V [197]. The coming Roadster 3.0 will be fitted with a 70kWh battery energy capacity [215]. The Japanese version of Honda Fit EV comes with a CHAdeMO connection [248]. According to [249], the Lightning GT is currently undergoing a major powertrain update.

A.2.4 Performance specifications

Specifications found regarding the performance such as top speed and acceleration, and also energy consumption and range according to type approval tests in the US and Europe is presented in Table A.5. The presented EPA energy consumption and range data adhere to the adjusted values.

According to [169], the Nissan Leaf top speed is 140km/h on the 16" tire rims and 144km/h on the 17" rims.

A.2.5 Terminated and coming BEV models

BEV models that are no longer on the market for new sales and models that are expected to be introduced to the market or as concepts shortly, are presented in Table A.6.

A.3 Comments on selected data

A.3.1 Area and aerodynamic drag coefficient, C_d

Based on data for nine of the BEV models the fractions between the area and the product of height and width, as well as height and track width, are shown in Table A.7. Here the range is 82%-96% of the height and width, and 96%-110% of the height and track width (from the driving wheel pair), with mean values of 86% and 99% respectively.

Data on area, C_d and C_dA relative to curb weight for small, medium-large, high performing and sport BEVs is shown in Fig. A.2. The figure also shows estimates of area, ranging from 80%-100% of height×width, as well as resulting C_dA values as lines where marked dots represent the case of using an estimation factor of 86%. Low C_d values are more often seen for medium-large models compared to small models, whereas the small models are seen to have slightly lower area values. The resulting C_dA values are thus rather similar for both small and medium-large models, but they are the lowest for the high performing Model S.

A.3.2 Rolling resistance coefficient, (C_r)

The rolling resistance depends on the tire and road material as well as the tire operating conditions. Hence C_r varies for different tires and tire types. In the EU (European Union), tires are subject to the fuel efficiency classification regulation No. 1222/2009, where the

Table A.3 Electric Motor Data

Model	EM Motor type	EM Max. Torque (Nm)	EM Max. Power (kW)	EM Cont. Power (kW)	EM Speed at max. Torque (rpm)	EM Speed at max. power (rpm)	EM Max. Speed (rpm)	EM Cooling	Transm. Ratio
fortwo	PM [136]	130 [136]	55 [136]	35 [136]				Water [138]	9.922 [250]
BRABUS	PM [140]	135 [140]	60 [140]	35 [140]					
iQ EV	PMSM [142]	163 [141]	47 [141]					Air [141]	
500e	PMSM [251]	200 [144]	83 [144]				12’800 [252]	Water [252]]	9.59 [144]
C-ZERO	PMSM [146]	196 [146]	49 [146]		300 [146]	4’000-8’800 [146]			
iOn	PMSM [148]	196 [148]	49 [148]	35 [148]	300 [148]	4’000-8’800 [148]	9’500 [148]		
i-MiEV	PMSM [151]	196 [151]	49 [151]		300 [151]	4’000-8’800 [151]	9’900 [151]	Water [151]	7.065 [151]
e-Up!	PMSM [152]	210 [152]	60 [152]		2’800 [152]	2’800 [152]	12’000 [152]		8.162 [153]
Spark EV	PMSM [155]	444 [155]	105 [155]					Liquid [155]	3.87 [155]
Bluecar			50 [156]	35 [156]					
MiniCab	PMSM [158]	196 [157]	30 [157]	25 [157]	3’000 [158]	2’500-6’000 [158]			7.065 [157]
i3	HPMSM [161]	250 [159]	125 [159]	75 [159]	5’000 [120]		11’400 [161]	Liquid [120]	9.7 [159]
Zoe	SM, w.r. [162]	220 [162]	65 [162]		2’500 [162]	3’000-11’300 [162]	11’300 [162]		9.32 [253]
C30 El.		250 [164]	89 [164]						
e-Golf	PMSM [166]	270 [166]	85 [166]	50 [254]	3’000 [255]	3’000 [255]	12’000 [166]		9.747 [166]
Leaf’15	IPMSM [256]	254 [169]	80 [169]		3’008 [169]	3’008-10’000 [169]	10’500 [169]	Water [256]	8.1938 [169]
Leaf’16	SM [172]	254 [172]	80 [172]		3’008 [172]	3’008-10’000 [172]	10’500 [172]		8.1938 [172]
FIT EV	PMSM [174]	256 [174]	92 [174]		3’056 [174]	3’695-10’320 [174]	10’320 [174]		8.058 [174]
Fluence.	SM, w.r. [176]	226 [176]	70 [176]	35 [257]	2’500 [231]	3’000-8’900 [231]	11’000 [258]		9.34 [176]
Focus EV	PMSM [259]	250 [178]	107 [178]			5’500 [220]		Liquid [179]	7.82 [220]
Soul El.	IPMSM [182]	285 [181]	81.4 [235]		2’730 [181]	2’730-8’000 [181]		Liquid [235]	8.206 [181]
B-Class El.Dr.	IM [184]	340 [184]	132 [184]	65 [184]		9’900-12’500 [184]		Liquid [185]	9.73 [186]
e6	PMSM [187]	450 [187]	90 [187]				7’000 [260]	Liquid [261]	6.844 [260]
e-NV200	IPMSM [191]	254 [190]	80 [190]				10’500 [191]		7.938 [190]
RAV4 EV	IM [192]	370 [192]	115 [192]					Liquid [118]	9.73 [192]
ModelS 60	IM Cu. [262]	430 [263]	283 [264]		5’000 [263]	5’000-8’000 [265]	16’000 [237]	Liquid [237]	9.73 [262]
ModelS 70	2 IM Cu. [194]	441 [194]	285 [194]					Liquid [194]	
ModelS 70D	2 IM Cu. [194]	525 [194]	F,R:193 [194]					Liquid [194]	
ModelS 85	2 IM Cu. [194]	441 [194]	285 [194]		5’800 [263]	6’000-9’500 [265]	16’000 [237]	Liquid [194]	9.73 [262]
ModelS 85D	2 IM Cu. [194]	658 [194]	F,R:193 [194]		5’800 [263]		16’000 [237]	Liquid [194]	9.73 [262]
ModelS P85D	3 IM Cu. [194]	967 [194]	F:193 [194] R:375		5’100 [263]	5’000-8’600 [265]	16’000 [237]	Liquid [194]	9.73 [262]
ModelX 90D			F,R: 193 [195]						
ModelX P90D			F:193 [195] R:375 [195]						
Roadster	IM [196]	370 [196]	225 [196]		5’400 [196]	5’000-6’000 [196]	14’000 [196]	Air [196]	8.28 [196]
Concept One	4 PMSM [199]	1600 [199]	800 [199]		6’500 [199]		12’000 [199]	Oil [199]	3.5 [243]
SLS AMG El.Dr.	4 PMSM [201]	1000 [201]	552 [201]				13’000 [201]	Liquid [203]	
Lightning GT	2 EM [204]	4000 [204]	300 [204]						5.5 [245]
SP:01 Pure		280 [206]	150 [206]						
SP:01 Perf.		280 [206]	210 [206]						
Fetish	PMSM [207]	380 [207]	220 [207]						
America	2 PMSM [208]	480 [209]	300 [209]		6’000 [208]		10’500 [208]		
Coupe	2 Ax.Flux [210]	1355 [210]	368 [210]						
R8 e-tron	2 EM [213]	920 [211]	340 [211]						
LAMPO 3	3 HSM [214]	900 [214]	420 [214]		4’500 [214]			Water [214]	6.4 [214]

Table A.4 BEV Battery and Charging Data

Model	Battery Energy Capacity (kWh)	Battery Charge Capacity (Ah)	Battery voltage (V)	Battery (Cont.) Max. Power (kW)	Number of cells	Battery weight (kg)	Battery Specific Energy (Wh/kg)	Battery Cooling	Standard (Optional) AC Charge Power (kW)	DC Fast Charging Method/ Peak Power (kW)
fortwo el.dr.	17.6 [136]	52 [266]	339 [266]		93 [136]	178 cal.	98,9 [266]	Liquid [267]	3.3 [138] (22) [268]	
fortwo BRABUS	17.6 [140]				93 [140]				3.3 (22) [140]	
iQ EV	12 [141]	43 [266]	277.5 [141]		150 [141]	220 [142]	54.7 [266]	Air [141]	3 [141]	CHA [269]
500e	24 [144]	63 [259]	364 [144]		97 [144]	291 [251]	88 [259]	Liquid [144]	6.6 [144]	
C-ZERO	14.5 [146]		300 [146]		80 [146]				3.2 [146]	50 [146]
iOn	14.5 [148]				80 [148]	221 [148]	66 cal.		3.2 [148]	50/CHA [148]
i-MiEV	16 [151]	50 [150]	330 [151]			145 cal.	110 [270]	Air [271]	3.7 [149]	CHA [149]
e-Up!	18.7 [152]		374n [152]	75 [272]	204 [152]	230 [152]	81 cal.	Passive [272]	3.6 [152]	40/CCS [152]
Spark EV	18.4 [155]	54 [155]	400t [155]	120 [155]	192 [155]	215 [155]	85 [270]	Liquid [155]	3.3 [273]	CCS [155]
Bluecar	30 [156]		410n [156]	45 [156]		300 [156]	100 cal.			
MiniCab	16 [157]		330 [157]						3 [158]	CHA [274]
i3	22.0 [159]	60 [259]	360n [120]	(40) [120] 147 [276]	96 [275]	233 [276]	93 [259]	Refrig. [120]	7.4 [277]	50/CCS [277]
Zoe	22 [162]		400n [162]		192 [162]	290 [162]	76 cal.		43 [278]	
C30 El.	24 [164]					330 [164]	73 cal.		22 [279]	
e-Golf	24.2 [166]	75 [270]	323n [166]		264 [166]	318 [166]	76.1 [270]	Passive [167]	7.2 [218]	50/CCS [218]
Leaf'15	24 [169]	66 [259]	360 [169]	90 [280]	192 [169]	273 cal.	87.9 [259]	Passive [171]	3.6 (6.6) [169]	50/CHA [169]
Leaf'16	30 [172]	83 [270]	360 [270]		192 [172]	294 cal.	102 [259]		3.6 (6.6) [172]	50/CHA [172]
FIT EV	20 [174]	20 [150]	330 [150]	100 [174]		224 cal.	89.3 [150]		6.6 [174]	CHA [248]
Fluence	22 [176]	65 [176]	398 [176]		192 [231]	280 [231]	79 cal.		3.5 (43) [177]	
Focus EV	23 [178]	75 [259]	350 [259]			287 cal.	80.2 [259]	Liquid [178]	6.6 [178]	
Soul El.	27 [181]	75 [259]	360 [181]	90 [235]	192 [182]	274.5 [182]	98.4 [281]	Air [183]	6.6 [181]	50/CHA [181]
B-Class El.Dr.	36 [282]	120 [259]	367 [259]			222 cal.	125.9 [259]	Liquid [185]	10 [186]	
e6	61.4 [187]	200 [150]	307 [150]	(162) [283] 270 [283]		624 cal.	98.4 [150]	Air [283]	40 [284]	100 [188]
e-NV200	24 [190]		360 [191]		192 [191]				3.6 (6.6) [190]	CHA [190]
RAV4 EV	41.8 [192]	130 [150]	386m [192]	129 [192]	4500 [285]	383.5 [192]	110.3 [150]	Liquid [286]	10 [192]	
ModelS 60	60 [264]	245 [259]	400 [259]			353 cal.	170 [259]			
ModelS 85	85 [264]	245 [264]	400 [259]			500 cal.	170 [259]	Liquid [237]	10 (20) [262]	120/Spr [287]
ModelX	90 [195]	250 [270]	350 [270]			600 cal.	150 [270]			
Roadster	56 [198]		366n [197]	215 [198]	6 831 [196]	450 [198]	121 [198]	Liquid [198]	16.8 [241]	
Concept One	82 [199]		650n [199]	(1000) [199]	1 400 [243]			Liquid [199]	22 [199]	50/CCS [199]
SLS AMG El.Dr.	60 [201]		400 [201]	600 [202]	864 [203]	548 [202]	109 cal.	Liquid [203]	22 [202]	
Lightning GT	44 [204]		450 [204]						9 [204]	50 [204]
SP:01	37 [206]								7.7 [288]	
Fetish	54 [207]									
America	53 [209]								22 [208]	
Coupe	30 [289]		740 [210]							CHA [290]
R8 e-tron	90.3 [213]		385n [213]		7488 [213]	595 [213]	152 [213]	Liquid [213]	7.2 [213]	50/CCS [213]
LAMPO 3	32 [214]	80 [214]	400n [214]		216 [214]	360 [214]	89 cal.	Water [214]	22 [214]	CHA [214]

Table A.5 Performance data.

Model	**Top speed (km/h)**	**Acc. Time 0-100 km/h (s)**	**Acc. Time 0-60 mph (s)**	**Acc. Time (0-X) km/h (s)**	**Energy p. dist. NEDC (Wh/km)**	**Energy p. dist. EPA City eq.(Wh/km)**	**Energy p. dist. EPA Highw. eq.(Wh/km)**	**Energy p. dist. EPA Comb. eq.(Wh/km)**	**Range NEDC (km)**	**Range EPA Comb. eq.(km)**
fortwo Coupe	126 [136]	11.5 [136]		4.8 (60) [136]	151 [136]	172 [259]	225 [259]	196 [259]	145 [136]	109 [266]
BRABUS Coupe	130 [140]	10.2 [140]			163 [140]				145 [140]	
iQ EV	125 [141]	14 [141]	13.4 [143]		134 [141]	151 [266]	200 [266]	173 [266]	85 [141]	61 [266]
500e	137 [144]		8.9 [251]			171 [259]	194 [259]	181 [259]		140 [259]
C-ZERO	130 [146]	15.9 [146]		5.9 (50) [146]	126 [146]				150 [146]	
iOn	130 [148]	15.9 [148]			126 [148]				150 [148]	
i-MiEV	130 [149]	15.9 [149]			125 [149]	166 [150]	212 [150]	187 [150]	160 [149]	100 [150]
e-Up!	130 [152]	12.4 [152]		8.1 (80) [152]	117 [152]				160 [152]	
Spark EV	145 [155]		7.2 [221]	3 (48) [155]		163 [259]	192 [259]	176 [259]		132 [259]
Bluecar	120 [156]			6.3 (60) [156]						
MiniCab MiEV	114 [291]									
i3	150 [159]	7.2 [159]	7.0 [222]	3.7 (60) [223]	129 [159]	152 [259]	188 [259]	168 [259]	190 [159]	130 [259]
Zoe	135 [162]	13.5 [162]		4 (48) [162]	133 [278]				240 [162]	
C30 El.	125 [164]	10.7 [164]		5.9 (70) [164]	175 [164]				163 [164]	
e-Golf	140 [255]	10.4 [255]		6.9 (80) [255]	127 [255]	167 [259]	199 [259]	181 [259]	190 [255]	134 [259]
Leaf'15	140 [169]	11.5 [169]			150 [169]	166 [259]	207 [259]	184 [259]	199 [259]	135 [259]
Leaf'16	144 [172]	11.5 [172]			150 [169]	170 [270]	207 [270]	186 [270]	250 [172]	172 [270]
FIT EV	148 [292]		8.5 [220]	3.1 (48) [220]		159 [150]	200 [150]	177 [150]		132 [150]
Fluence Z.E.	135 [176]	13.7 [176]			140 [293]				185 [176]	
Focus EV	137 [294]	11.4 [232]			154 [232]	190 [259]	211 [259]	200 [259]	162 [294]	122 [259]
Soul Electric	145 [181]	11.2 [181]	10.8 [182]		147 [181]	175 [181]	228 [259]	199 [259]	212 [181]	150 [259]
B-Class El. Dr.	160 [184]	7.9 [184]		3.9 (60) [184]	166 [184]	245 [259]	256 [259]	250 [259]	200 [184]	140 [259]
e6	140 [187]	9.2 [295]		7.7 (60) [188]		341 [150]	322 [150]	333 [150]		204 [150]
e-NV200 / Evalia	122 [191]	14 [190]			165 [191]				170 [191]	
RAV4 EV	161 [192]		7.0 [285]			267 [150]	285 [150]	275 [150]		166 [150]
ModelS 60	190 [264]	6.2 [264]	5.9 [262]		188 [263]	222 [259]	217 [259]	219 [259]	390 [264]	335 [259]
ModelS 70	225 [194]	5.8 [296]	5.5 [194]						442 [296]	386 [194]
ModelS 70D	225 [194]	5.4 [296]	5.2 [297]						420 [296]	370 [194]
ModelS 85	225 [194]	5.6 [296]	5.4 [194]		170 [263]	238 [259]	232 [259]	235 [259]	502 [296]	426 [259]
ModelS 85D	249 [194]	4.4 [296]	4.2 [194]		170 [263]	220 [259]	198 [259]	210 [259]	528 [296]	435 [259]
ModelS P85D	249 [194]	3.3 [296]	3.1 [194]		188 [263]	234 [259]	215 [259]	225 [259]	491 [296]	407 [259]
ModelX 90D	249 [195]	5.0 [298]	4.8 [195]			232 [270]	222 [270]	227 [270]		414 [270]
ModelX P90D	249 [195]	4.0 [298]	3.8 [195]			236 [270]	233 [270]	235 [270]		402 [270]
Roadster	201 [196]		3.9 [196]		160 [299]				340 [299]	393 [300]
Concept One	305 [200]	2.8 [199]							600 [243]	
SLS AMG El.Dr.	250 [201]	3.9 [201]			268 [301]				250 [201]	
Lightning GT	209 [204]		5 [204]						241 [204]	
SP:01 Pure	170 [206]	5.6 [206]	5.3 [206]						288 [206]	
SP:01 Perf.	250 [206]	3.9 [206]	3.7 [206]						288 [206]	
Fetish	200 [207]	4 [207]								
America	220 [209]	4.5 [209]		14 (200) [209]						
Coupe	193 [210]		3.4 [210]							
R8 e-tron	250 [213]	3.9 [211]							450 [211]	
LAMPO 3	220 [214]	4.5 [214]							200 [214]	

Table A.6 Terminated and coming BEV models.

Terminated	Coming
Scion iQ EV	Chevrolet Bolt EV
Renault Fluence Z.E.	Porsche Concept Study Mission E
RAV4 EV	Audi e-tron Quattro Concept
Tesla Model S 60kWh	Tesla Roadster 3.0
Tesla Roadster 2.5	Renovo Coupe
	Detroit Electric SP:01
	Tesla Model 3

Table A.7 Front area vs. height times width or track width.

Model	iQ	iOn	e-Up!	i3	Zoe	C30	e-Golf	Leaf	ModelS
$\frac{A}{w\,h}$	85%	90%	85%	85%	96%	85%	84%	83%	82%
$\frac{A}{tw\,h}$	97%	103%	98%	96%	110%	97%	99%	96%	96%

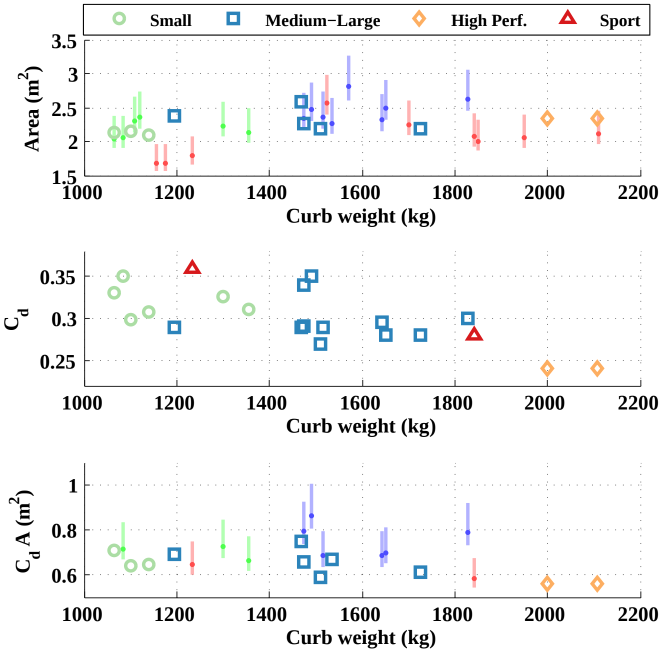

Figure A.2 Data on area, C_d and C_dA, as well as estimates of area and C_dA, using the found C_d values and area estimates of 80-100% of height and width, all as functions of curb weight.

classes are labeled A-G. Class A represent tires with the lowest coefficients ≤0.0065, class B 0.0066-0.0077, C 0.0078-0.009, as so on up to G ≥0.0121 [302].

Still, neither original tire brand and model, nor it's rolling resistance coefficient are generally provided in BEV model specifications. Nevertheless, many manufacturers claim to use low rolling resistance tires on their BEV models; 500e, iMiEV, Spark EV,

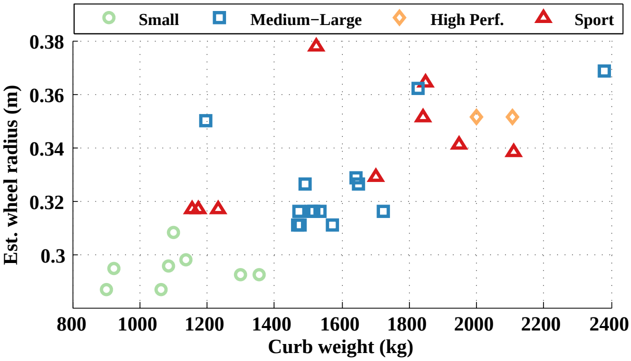

Figure A.3 Tire radius estimation vs. curb weight.

i3, Zoe, e-Golf, Fluence, Focus, and Soul ("super low") [145,149,155,162,167,179,183, 223,258,277]. In fact, only three references have been found that mentions a value; e-Up! 0.007 [219], e-Golf 0.0065 [227], and Tesla Roadster 0.011, whereas the next Roadster version (3.0) will have 0.0089 [215].

Furthermore, few public sources of measured rolling resistance data exist. Yet in [33], data provided by a few different actors such as the US EPA (Environmental Protection Agency) and some of the major tire manufacturers (e.g. Michelin, Goodyear and Bridgestone) is presented. In one of the later and largest data sets (from 2005), the C_r values range from 0.0065-0.0133, with a mean value of 0.0102. It is also mentioned that due to different factors, there is a tendency of higher average C_r values for groups of tires made for higher speed levels; for tires up to 180-190 km/h it was 0.0098, for tires up to 210-240 km/h it was 0.0101, and for tires above 240km/h it was 0.0113. The tendency of lower C_r values for fuel economy focused vehicles and higher for performance focused models is also reflected in [303], where estimated C_r values are analysed.

A.3.3 Wheel radius estimation from tire dimensions

Estimated wheel radius values for BEVs with found tire data are shown in Figure A.3 as function of curb weight. Generally the small cars have a wheel radius below 0.3 m (with one exception: iQ), medium-large cars have a wheel radius between 0.31-0.37, while most values are within 0.31-0.32 m. The spread is quite large for the sport cars; 0.32-0.38 m. It should be noted that the real tire radius naturally varies both by tire load and inflation pressure. It also varies during driving, since speed, acceleration and deceleration all affect the load forces on the tires. The presented data can thus be thought of as maximum values.

A.3.4 Traction Electric Machine data

It is here noted that the most dominating EM **type** in current BEVs is the permanent magnet synchronous machine (PMSM), which can be found in at lest 22 models. In some models, like Soul EV [182] and Leaf [256], it is specifically mentioned that interior mounted permanent magnet machines (IPMSMs) are used. Five models; (B-Class, RAV4, ModelS, ModelX and Roadster) utilize induction machines (IMs), however, these have all been provided by Tesla Motors [185, 194, 285]. Renault's two models Zoe and Fluence are equipped with their wound rotor synchronous machine (SM w.r.) [162, 176]. In i3 the in-house developed hybrid permanent magnet synchronous machine (HPMSM) is used, i.e. a synchronous reluctance machine with added permanent magnets. A hybrid synchronous machine (HSM) by Brusa is also used in Lampo3. Renovo claim to use an axial flux machine in Coupé [210].

Data on maximum torque and power is presented for almost all models while data on continuous power is presented for 9 models. It is, however, quite unclear under what circumstances these values have been determined. The maximum and continuous torque is typically strongly influenced by the machine's cooling system design. Additionally, the maximum power level changes with the dc voltage level during driving. Some manufacturers refer to the European type approval regulation UNECE R85 [304] in which the motor power measurement over a time duration of 30 min. is regulated as is a full load test over a non specified time duration of a motor that has first been run warm for three minutes at 80% of full load. Still, the regulations leave room for interpretation, and this should be kept in mind when comparing data on BEV motors.

The range of maximum output torque levels are from about 130-1600 Nm (up to 440 Nm for single motors), and the combined EM power range is 30-800 kW (up to 285 kW for single motors). These are quite wide ranges. In Fig. A.4, it is shown that the maximum power is about 1.2-2 times that of the continuous power for 9 of the models.

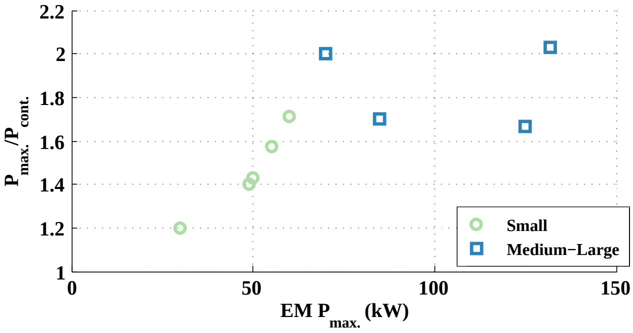

Figure A.4 Max-to-continuous ratio of EM power vs. max power.

Appendix B

GPS-accelerometer Measurement System

B.1 Description of the measurement system

The measurement system is called MX3 and was delivered by HostMobility in Gothenburg. Two units were purchased. Each unit includes a GPS along with a roof top mountable antenna, a 3D accelerometer and 2 temperature sensors attached to the end of extension cables of 1m and 3 m respectively. The GPS module is an IT500, by FasTrax. The accelerometer is a MMA7455L, by Freescale[1], with a range of $\pm 2g$, and a resolution of $g/64 = 0.15328(m/s^2)$. The temperature sensors are SMT16030 by Smartec.

The unit is strapped on a flat surface in the test vehicle, with the accelerometer coordinate frame aligned with the vehicle's coordinate frame. An external voltage source is needed to power the unit, e.g. the vehicles $12V$ outlet or an external battery, see Figure B.1.

Data is then logged on a PC via a RS232/USB connection and a terminal software. The sampling frequency of the GPS signal is $5\,Hz$, that of the accelerometer signal is $20\,Hz$ and that of the temperature signal is $1\,Hz$.

GPS data regarding GPS time, position (latitude, longitude and altitude), speed, dilution of precision (hdop, vdop and pdop), nuber of satelites in fix etc. is received according to the NMEA format, from the GGA, GSA, GSV, and RMC packages. That is, no raw data from the satellite communication (e.g distance to satellite) are available. According to FasTrax, the GPS position accuracy is $1.8\,m$, and the velocity accuracy is $0.1\,m/s$. DGPS has not been utilized.

---

[1] The data sheet can be found at http://www.freescale.com/files/sensors/doc/data_sheet/MMA7455L.pdf

(a) One of the measurement units.

(b) The measurement unit strapped in a car.

Figure B.1 The measurement unit and an example of usage.

B.2 Filtering of measurement Data

The speed and altitude signals are low pass filtered with a cut off frequency of $0.5\,Hz$, and the acceleration signal with a frequency of $2\,Hz$. Then both speed and altitude are resampled to $20\,Hz$. Traveled distance was calculated as the time integral of the speed signal.

Road slope was estimated as the inverse sine of the ratio between a change in altitude (dh) and a change in traveled distance dS, for each sample ($\alpha = \arcsin(\frac{dh}{dS})$). It proved to be rather difficult to attain a fair estimate of the road slope, especially at low speed levels close to stand still where with very small values of dh and dS, causing an unstable grade value. In order to deal with this, a few different limiting strategies were applied, e.g. to smooth the grade within a time frame of $2\,s$ during the mentioned situations.

Finally the estimated grade was utilized to compensate that part of the accelerometer signal that is caused by road grade, see Figure B.2.

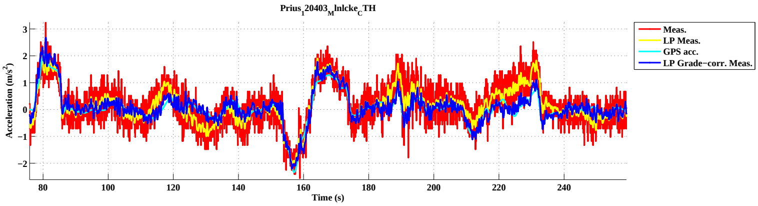

Figure B.2 Example of correction for road grade of acceleration.

B.3 Ambiguity of measurements

Even though the same driver was using the same car, drove the same route, at similar times of the day, the logs are different, as can be seen in Table B.1, and Figure B.3 to B.5.

Table B.1 Cycle data for all CTH - Kålltorp logs.

V744 CTH-Klltrp Cycles	Cycle duration (s)	Driven distance (m)	Max. speed (km/h)	Average speed (km/h)	Average running speed (km/h)	Std. speed (km/h)	Max. pos. acc. (m/s^2)	Max. neg. acc (m/s^2)	Average pos. acc. (m/s^2)	Average neg. acc. (m/s^2)	Std. pos. acc. (m/s^2)	Std. neg. acc. (m/s^2)	RPA (m/s^2)	Time share pos. acc. (%)	Time share neg. acc. (%)	Time share standing (%)
120306	897	8 023	57	32	32	17	2.98	-3.10	0.42	-0.37	0.49	0.48	0.18	46	54	0.7
120307	769	7 937	63	37	37	15	2.17	-3.96	0.39	-0.40	0.36	0.47	0.18	51	49	0.2
120320	844	7 930	53	34	34	15	3.48	-3.60	0.38	-0.35	0.44	0.44	0.15	47	53	1.3
120325	737	7 854	60	38	38	16	3.28	-3.33	0.42	-0.41	0.51	0.49	0.16	45	55	0.1
120327	806	7 932	64	35	36	18	2.99	-2.70	0.43	-0.45	0.43	0.48	0.21	54	46	1.5
MEAN	**811**	**7 935**	**59**	**35**	**36**	**16**	**2.98**	**-3.34**	**0.41**	**-0.40**	**0.45**	**0.47**	**0.18**	**49**	**51**	**0.8**

As can be seen in Figure B.3, the exact same route was driven.

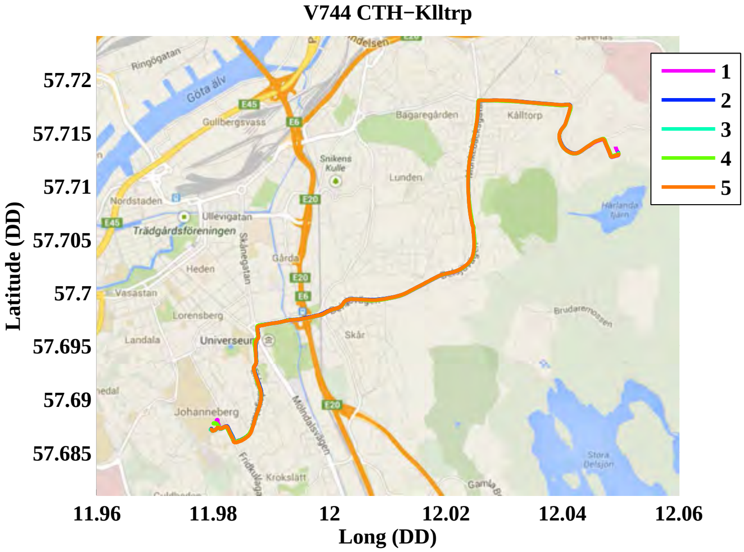

Figure B.3 Logs on map.

As can be seen in the upper right subplot in Figure B.4, the speed varies from log to log. The difference may be about 20 km/h.

As can be seen in the lower right subplot in Figure B.4, the estimated road grade may also vary from log to log. But there is a fair level of consistency.

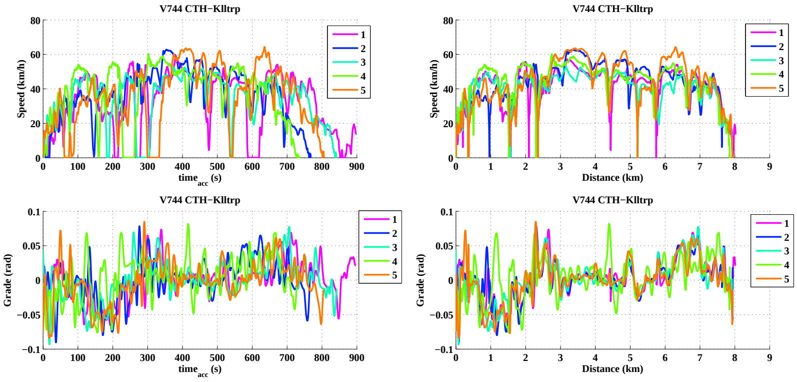

Figure B.4 Logged Speed and road grade.

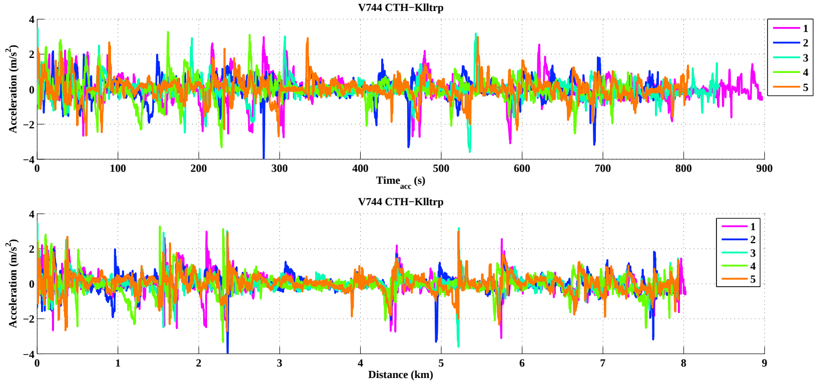

Figure B.5 Logged Acceleration.

B.4 Logged vehicles

Curb weight, powertrain power and the resulting power-to-weight-ratio for the vehicles used during logging can be seen in Table B.2.

Table B.2 Selected data on logged vehicles.

Brand	**Model**	**Fuel type**	**Curb weight** ***(kg)***	**Max. Power** ***(kW)***	**Power-to-weight ratio** ***(kW/kg)***
E CAR	500 EV	El.	1165	30	26
Nissan	Leaf	El.	1613	80	50
Tesla	Roadster	El.	1235	225	182
Toyota	Prius	Gasoline	1365-1425	73	53
Volvo	C30 D2	Diesel	1428	84	59
Volvo	C30 Electric	El.	1660	82	49
Volvo	V744	Gasoline	1370	86	63
Volvo	V70	Gasoline	1640	125	76
Volvo	XC60	Diesel	1920	120	63
Volvo	V60 PHEV	Diesel & El.	2000	160+50	80 or 105

Appendix C

Speed and Acceleration Dither

In order to get an idea of the total and relative time spent at different speed and acceleration operating points for the Urban, Rural and Highway cycles, each cycle value is attributed to a certain acceleration and speed bin, of $0.5\,m/s^2$ and $5\,km/h$, see Figure C.1(a) for the Urban Test cycles. The result can also be visualized in a contour plot, see Figure C.2(a) for total time in each bin and Figure C.2(b) for the share of total time in each bin.

In order to get a more smooth looking contour plot, a random gaussian noise (with zero mean, and $0.5\,m/s^2$ respectively $1\,m/s$ standard deviation) was added to each operating point, so called dithering. Furthermore, each drive cycle with the added noise is looped 100 times, after which the total and relative time spent in each bin is divided by the number of loops. The results can be seen in Figure C.1(b) and C.3(b), for the Urban cycles, and in Figure C.4 and C.5 for the Rural and Highway cycles respectively.

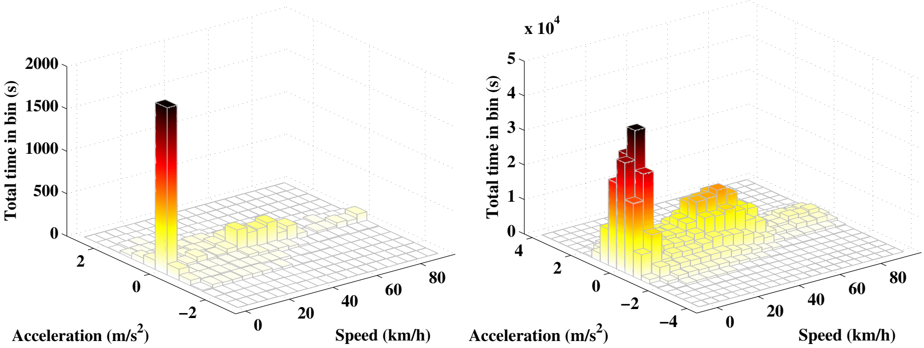

(a) No added noise.

(b) With added noise during 100 loops.

Figure C.1 Share of total time $(\%)$ of operation in acceleration bins of $0.5\ m/s^2$ and speed bins of $5\ km/h$, for all Urban test cycles.

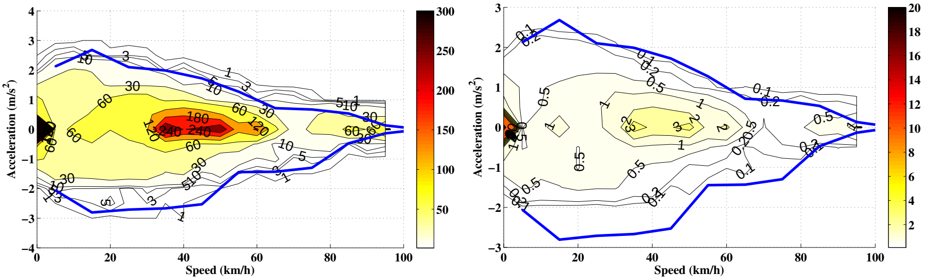

(a) Total time.

(b) Share of total time.

Figure C.2 Total time (s) vs. Share of total time $(\%)$ of operation in acceleration bins of $0.5\ m/s^2$ and speed bins of $5\ km/h$, for all Urban test cycles, no added noise.

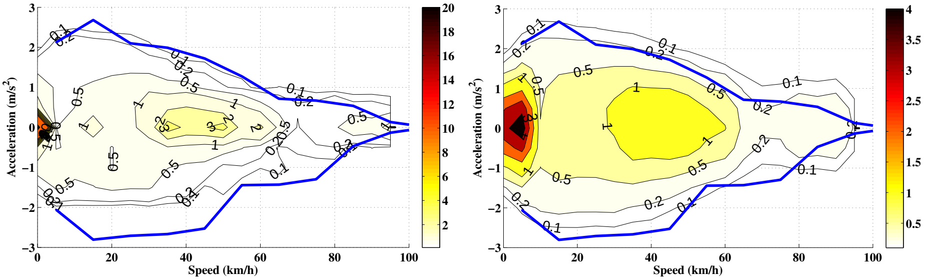

(a) No added noise.

(b) With added noise during 100 loops.

Figure C.3 Share of total time $(\%)$ of operation in acceleration bins of $0.5\ m/s^2$ and speed bins of $5\ km/h$, for all Urban test cycles.

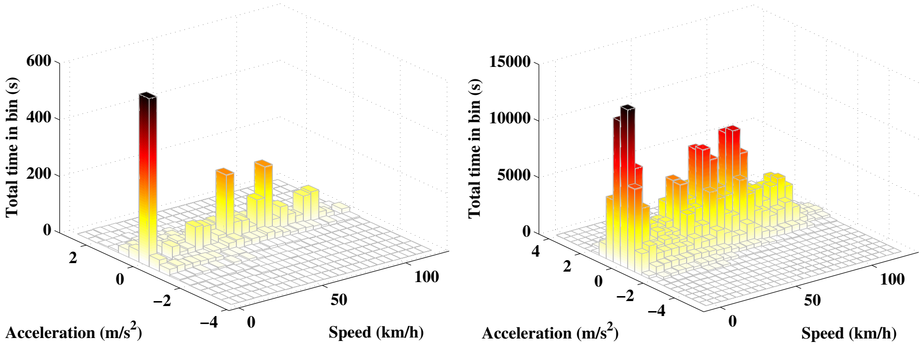

(a) No added noise.

(b) With added noise during 100 loops.

Figure C.4 Share of total time (%) of operation in acceleration bins of $0.5\ m/s^2$ and speed bins of $5\ km/h$, for all Rural test cycles.

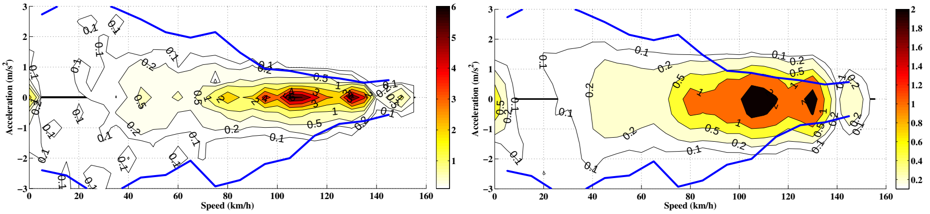

(a) No added noise.

(b) With added noise during 100 loops.

Figure C.5 Share of total time (%) of operation in acceleration bins of $0.5\ m/s^2$ and speed bins of $5\ km/h$, for all Highway test cycles.

Appendix D

Temperature Dependence of some Material Parameters

Cooling medium (ethylene-glycol) material parameters as a function of temperature, is presented in Figure D.1 (data from [119]). Figure D.1 also include material parameters for water [48] as a reference.

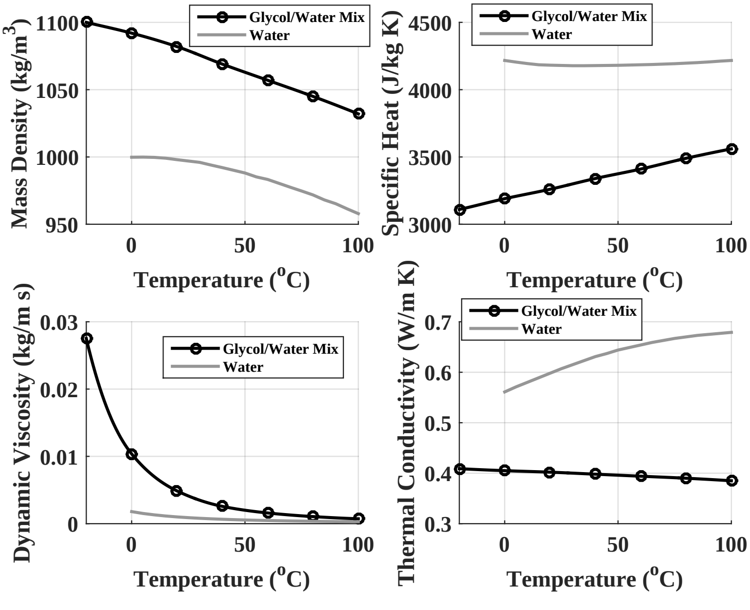

Figure D.1 Glycol/water mixed coolant material properties as a function of temperature [119]. The properties of water are also included as a reference [48]

The temperature dependence of material parameters of air is presented in Figure D.2.

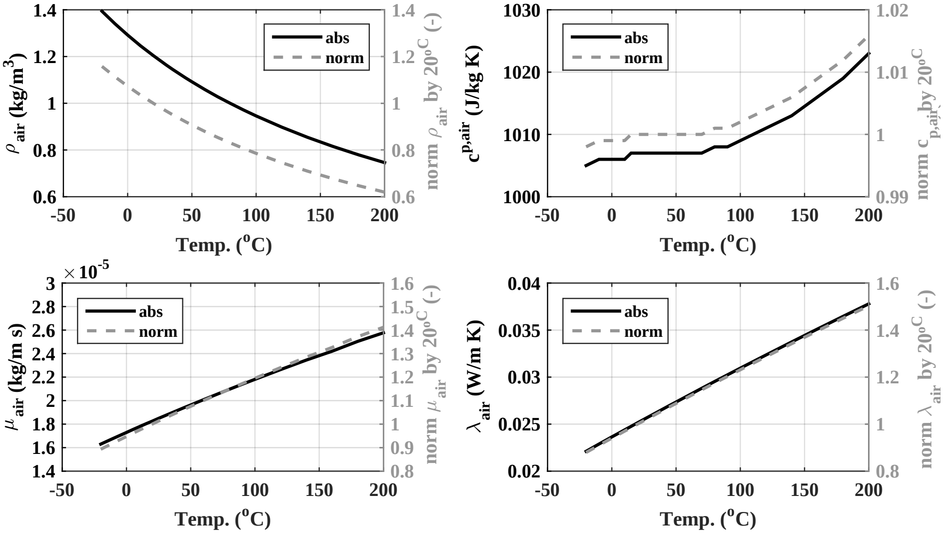

Figure D.2 Air material properties as a function of temperature, both absolute values and normalized to the value at $20°C$. [48]

The temperature dependence of thermal conductivity and specific heat, for the used lamination core material is presented in Figure D.3.

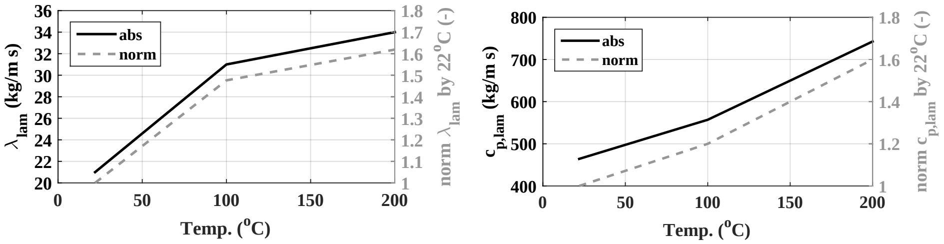

(a) Thermal conductivity.

(b) Specific heat.

Figure D.3 Thermal conductivity and specific heat of lamination material (NO30) as a function of temperature [105], both absolute values and normalized to the value at $22°C$.

The temperature dependence of thermal conductivity and specific heat, for copper (the used winding material) is presented in Figure D.4.

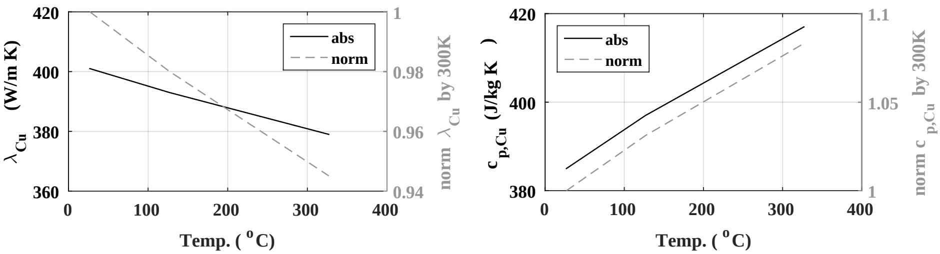

(a) Thermal conductivity.

(b) Specific heat.

Figure D.4 Thermal conductivity and specific heat of winding copper as a function of temperature [48], both absolute values and normalized to the value at 300 K.

Finally, the temperature dependence of thermal conductivity for the used shaft material (carbon-silicon steel) is presented in Figure D.5.

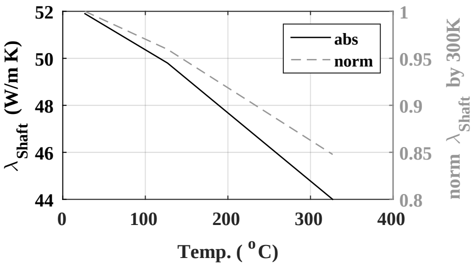

Figure D.5 Shaft material thermal conductivity as a function of temperature, both absolute values and normalized to the value at 300 K. [48]

Appendix E

Cooling Channel Modelling

The Prandtl number of the coolant is much larger than one in the whole temperature range, as is shown in Figure E.1. This means that convection heat transfer is likely to dominate over conductive heat transfer in the coolant medium.

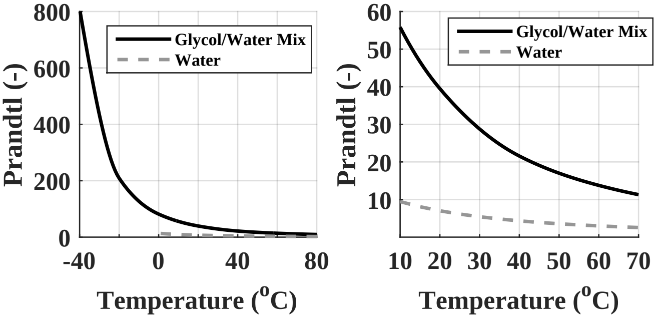

Figure E.1 The Prandtl number of the coolant as a function of temperature.

As mentioned in section 2.8.1, the heat transfer coefficient is often found via empirical approximations of the Nusselt number (Nu). There exist a number of different Nu approximations for circular tubes in literature, for the three flow types: laminar, transitional and turbulent, which is determined by the Reynolds number (Re). The flow can be assumed to be laminar for $Re \leq 2300$, and fully turbulent for $Re \geq 10,000$ [45,48,50]. According to [45], these critical values can also be assumed for non-circular tubes. In practice, the critical Re values additionally depend on factors such as surface roughness and vibrations [48], which makes them difficult to predict.

For these non-circular tubes, the hydraulic diameter D_h is used when calculating Nu and Re [48,305]. It is four times the cross sectional area divided by the perimeter. For a rectangular tube, with side a and b, D_h is

$$D_h = \frac{2ab}{a+b} \tag{E.1}$$

The Reynolds number Re_D is here depending on the hydraulic diameter D_h, and the average flow velocity v_{ave} (m/s), which in turn depends on the flow rate $fl_{L/min}$ (liters/min), as

$$Re_D = \frac{\rho\, D_h\, v_{ave}}{\mu} = \frac{2\rho}{\mu(a+b)}\frac{fl_{L/min}}{60\times 10^3} \tag{E.2}$$

The Re number as a function of flow rate is presented in Figure E.2, for four different coolant temperatures. The flow rate needed to reach the Re value for critically turbulent flow is lower when the coolant is warmer, and higher when the coolant is colder.

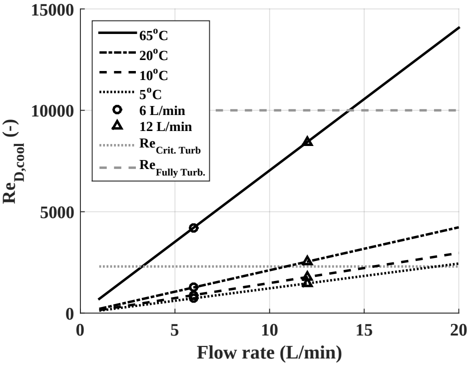

Figure E.2 The Reynolds number of the coolant as a function of flow rate and temperature.

For fully developed **laminar** flow the Nusselt number can be approximated as a constant that only depends on the cross sectional geometry [45, 48, 50, 305]. For rectangular tubes with width-to-height ratio of 6 ($30/5 = 6$), and under the assumption of a constant heat flux, Nu is **6.05** [48]. There are also expressions for how the Nu decays to that of the fully developed laminar flow value as a function of tube length, which also include entrance effects [50, 306]. For simplicity, the entrance effect is here neglected, even though it was noted that it could result in up to three times larger Nu values.

For **turbulent** flow with Re_D $3000 - 5\times 10^6$ and Prandtl (Pr) 0.5-2000, the Nusselt number can be approximated to a reasonable accuracy [45, 48, 50, 306], as

$$Nu = \frac{(f/8)(Re_D - 1000)Pr}{1 + 12.7(f/8)^{1/2}(Pr^{2/3} - 1)} \tag{E.3}$$

where the friction factor f, for smooth tubes can be approximated as

$$f = (0.790\, ln(Re_D) - 1.64)^{-2} \tag{E.4}$$

The surface roughness for die cast aluminum is here estimated to approximately 5 μm. This gives a relative roughness (i.e. ratio of surface roughness to hydraulic diameter) of 0.00006. According to a so called Moody diagram in e.g. [45], the friction factor for this level of relative roughness may be approximated as that of a smooth surface for Re_D values lower than 10^6, i.e. well within the expected Re_D range. Therefore, (E.4) is here used.

The resulting Nu number as a function of flow rate is shown in Figure E.3, for different coolant temperatures. Similarly to the Re_D, the Nu number increases with both temperature and flow rate for turbulent flows.

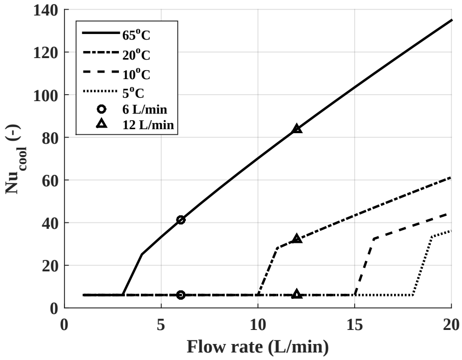

Figure E.3 The Nusselt number of the cooling circuit as a function of flow rate and temperature.

The temperature increase of the coolant is proportional to the amount of losses P_{loss} absorbed and inversely proportional to the flow rate [116], as in

$$\Delta T_{cool} = \frac{P_{loss}}{\rho_{cool}\, c_{p,cool}\, \frac{fl_{L/min}}{60\times 10^3}} \tag{E.5}$$

The temperature increase of the coolant for different levels of total losses and flow rates is presented in Figure E.4, for the initial coolant temperature of 65°C. Only minor differences were noted for different initial coolant temperatures. For the highest losses in the Original slot HighwayII motor: 6 kW, with a flow rate of 6 L/min, the coolant temperature increase is at most 17°C, and for moderate losses of 3 kW the temperature increase is 8°C at most. At 12 L/min the temperature increase is 8°C with 6 kW losses, and 4°C with 3 kW.

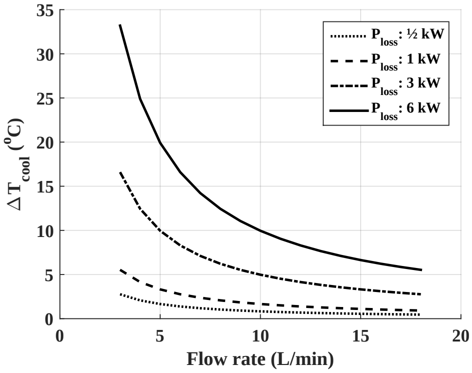

Figure E.4 The expected increase in coolant temperature for different heat absorptions.